University of Southampton

Faculty of Engineering and Physical Sciences

Electronics and Computer Science

Spectrophotometric Analysis of Stochastic Hybrid Black Silicon Nanostructures for Crystalline Silicon Photovoltaic Cells

by

Jack James Tyson

A thesis submitted for the degree of

Doctor of Philosophy

October 2023

University of Southampton

Abstract

Faculty of Engineering and Physical Sciences

Electronics and Computer Science

Doctor of Philosophy

Spectrophotometric Analysis of Stochastic Hybrid Black Silicon Nanostructures for Crystalline Silicon Photovoltaic Cells

by Jack James Tyson

Black silicon nanotextures offer exceptionally low levels of reflectance and are of interest to the field of solar photovoltaics. The nanowires that form this texture create a graded refractive index, allowing light to be absorbed with high efficiency. Explored here is the application of these nanotextures on top of conventional microscale pyramids, combining the advantages forwarded by the latter, predominantly being a second chance for absorption, and the former, being light steering. These structures are known as hybrid black silicon. Variations on the wet chemical etch parameters are explored and related to topological features, which can, in–turn, be related to front surface reflectance. The hybrid black silicon textures created are shown to exhibit reflectance as low as 0.7%.

An advanced hemispherical reflectometry system is reported, designed for measuring the optical characteristics of a variety of samples resolved against wavelength, angle of incidence, and polarisation. Variable angle reflectance data enables a new perspective on the interaction between electromagnetic waves and nanostructures, which do not interact with light in the same way as their microscale counterparts. The versatility of this data is demonstrated for photovoltaics when combined with geographic spectral irradiance data. Solar cell optical performance, when structured with the textures measured in the reflectometer, is successfully predicted should that cell be placed in Southampton, UK. This mathematical formulation is capable, alongside the appropriate angle–resolved reflectance data, of approximating the optical performance of a given sample when situated almost anywhere in the world.

Supporting the reflectance data gathered through this work is a black silicon nanowire model, pseudorandomised using custom–made algorithms against a set of desired surface features. The model uniquely generates complex surface topologies that meet the

requirements of electromagnetic wave optics simulations. The model reported showcases an accuracy within the ±2% relative error against measured reflectance, and offers a new, fast, and accurate way of simulating nanostructures without the need to manufacture them in bulk.

Contents

List of Figures

List of Tables

List of Abbreviations

AM	Air mass
ARC	Anti–reflectance coating
ARS	Angle–resolved spectrophotometer
a-Si	Amorphous silicon
BSE	Back scattered electron
b-Si	Black silicon
c-Si	Crystalline silicon
CdTe	Cadmium telluride
CIGS	Copper indium gallium selenide
EIM	Effective index method
EM	Electromagnetic
FDTD	Finite difference time domain
FEM	Finite element method
FsL	Femtosecond laser
hb-Si	Hybrid black silicon
KOH	Potassium hydroxide
LCoE	Levelised cost of energy
MACE	Metal assisted chemical etching
mc-Si	Multicrystalline silicon
NIR	Near infra–red
NOA	Norland optical adhesive
NUV	Near ultraviolet
NWs	Nanowires
PDE	Partial differential equation
PF	Planar fraction
PTFE	Polytetrafluoroethylene

PV	Photovoltaic
QDR	Quick dump rinse
RAT	Reflectance, absorption, and transmission
RIE	Reactive ion etching
RT	Ray tracing
SAR	Standard angle reflectance
SDK	Software development kit
SEM	Scanning electron microscopy
SOP	Standard operating procedure
SPEX	Specular excluded
SPIN	Specular included
STA	Scans to average
TMM	Transfer matrix method
VAR	Variable angle reflectance

Declaration of Authorship

I, Jack James Tyson, confirm with the submission of this thesis entitled *"Spectrophotometric Analysis of Stochastic Hybrid Black Silicon Nanostructures for Crystalline Silicon Photovoltaic Cells"*, that all content enclosed herein are of my own work, and/or derived from my own research. I confirm that:

- This work was done wholly or mainly while in candidature for a research degree at this University;
- Where any part of this thesis has previously been submitted for a degree or any other qualification at this University or any other institution, this has been clearly stated;
- Where I have consulted the published work of others, this is always clearly attributed;
- Where I have quoted from the work of others, the source is always given. With the exception of such quotations, this thesis is entirely my own work;
- I have acknowledged all main sources of help;
- Where the thesis is based on work done by myself jointly with others, I have made clear exactly what was done by others and what I have contributed myself;
- Parts of this work have been published as outlined in Research Outputs on page xxv.

Print Name: .....

Signature: .....

Research Outputs

J. J. Tyson, T. Rahman, and S. A. Boden, "Optical simulation of black silicon surfaces using geometric randomisation and unit-cell based averaging," in *15th Photovoltaic Science, Application and Technology Conference*, Apr. 2019.

Q. R. Islam, **J. J. Tyson**, S. Islam, T. Rahman, S. A. Boden, and M. Hossain, "Bunched silicon nanowires for enhanced light trapping in solar cells," in *15th Photovoltaic Science, Application and Technology Conference*, Apr. 2019.

E. Khorani, T. E. Scheul, **J. J. Tyson**, T. Rahman, and S. A. Boden, "Boron–doped silicon growth via Hot Wire CVD towards emitter formation for interdigitated back-contact solar cells," in *15th Photovoltaic Science, Application and Technology Conference*, Apr. 2019.

J. J. Tyson, T. Rahman, and S. A. Boden, "Multiphysics simulations for robust computational modelling of stochastic nanostructures," in:

- *2019 COMSOL Conference in Cambridge*, Sep. 2019.
- *2019 IET Innovation Awards*, Nov. 2019.

J. J. Tyson, T. Rahman, and S. A. Boden, "A new mathematical interpretation of disordered nanoscale material systems for computational modelling," in *Computer Physics Communications*, Oct. 2020.

J. J. Tyson, T. Rahman, and S. A. Boden, "Ray tracing coupled with electromagnetic wave optics for nanoscale light propagation studies," in *2020 COMSOL Conference in Europe*, Oct. 2020.

J. J. Tyson, T. Rahman, and S. A. Boden, "Angle-resolved hemispherical reflectometry for the optical characterisation of solar photovoltaics," in *SuperSolar Annual Conference 2021*, Jun. 2021.

J. J. Tyson, T. Rahman, and S. A. Boden, "Angle-resolved spectrophotometry for the optical characterisation of material surfaces," in *IEEE Transactions on Instrumentation and Measurement*, Jan. 2022.

J. J. Tyson, T. Rahman, and S. A. Boden, "A ground-breaking new system to accurately measure light reflection from a shifting source," in *Future Worlds: Labs*, Mar. 2022.

J. J. Tyson, T. Rahman, and S. A. Boden, "Hybrid Black Silicon Nanotextures and their Implications on the Time-varying Performance of Solar Photovoltaic Technologies in the Real World," in *16th Photovoltaic Science, Application and Technology Conference*, Apr. 2022.

Y. Musleh, **J. J. Tyson**, C. Cao, S. A. Boden, and T. Rahman, "Developing Outdoor Testing Equipment for Insolation Measurement of Bifacial Solar Tracking Systems for Evaluation Purposes," in *16th Photovoltaic Science, Application and Technology Conference*, Apr. 2022.

J. J. Tyson, T. Rahman, and S. A. Boden, "Analysing the optical performance of hybrid black silicon surface textures under variable angle illumination," in *SuperSolar Annual Conference 2022*, Sept 2022.

J. J. Tyson, T. E. Scheul, T. Rahman, and S. A. Boden, "Characterising the broadband, wide–angle reflectance properties of black silicon surfaces for photovoltaic applications," in *Optics Express*, Aug. 2023.

Acknowledgements

I would like to start by expressing my deepest appreciation to my supervisory team, Stuart Boden and Tasmiat Rahman. Your guidance, support, and patience has been invaluable to me over the last few years. I would not have been able to make it to this point without them, as well as your unwavering personal support through some very difficult times for me. I also want to show my appreciation to Tudor, Edris, Yazan, and Chen for all of your support and friendship throughout my PhD. A special thanks to Tracey for her friendship and support in the cleanroom, as well as for our good chats during long and arduous days. I would also like to thank Owain and Xiangjun for their supplementary support within the SNC.

I had the pleasure of working as part of the CDT throughout my PhD, but particularly in 2018/19 during our residential placements. I'm sending my thanks, love, and best wishes to all of C5. You've been like another family to me over the years, and I look forward to seeing you all again in the years to come. Many thanks to Ken Durose, Alison Walker, Asim Mumtaz, and Alan Dunbar for making the CDT what it was. Thanks should also go to Adam, Connor, Matt, Mike, Nabeel, and Teodor for your friendship, care, and interest in my work. A special mention goes to Charlie and Rohan for the chats, laughs, and good times we have had over the years.

To my fiancée, Laura, and our wonderful Schrödinger, Jasper, and Mayo, thank you for bringing me endless entertainment and a surplus of coffee when I needed it most. I also thank my whole family for their love and support throughout my PhD.

This work has been supported by the Centre for Doctoral Training in New and Sustainable Photovoltaics (EPSRC grant number EP/L01551X/1), and completed as part of Black Silicon Photovoltaics (EPSRC grant number EP/R005303/1). The author of this work also acknowledges the use of the IRIDIS compute cluster, and associated support services at the University of Southampton, in the completion of this work.

To my late grandparents Eve and Ron, this is for you.

Chapter 1

Introduction

1.1 Motivation

Amid an energy crisis, innovative and sustainable sources present themselves in various forms. Fossil fuels are not sustainable, and come paired with significant, often irreversible environmental changes to our planet. Using either disadvantage as a driving force, research into 'renewable' energy sources has ramped-up considerably over the past couple of decades. The impact potential of these renewables on the science, technology, and engineering sectors is high; alongside their rapid adoption within residential, commercial, and industrial settings, the inevitable transition between the traditional fossil and progressive renewable fuels is already under way.

Techniques have been developed to harvest wind, tidal, wave, solar, vibrational, and thermal energies with varied efficiencies and points of application. Nuclear reactions are also habitually referred to as being within the renewables family despite having an inherently limited, albeit extensive, supply of reactants. One could argue that the greatest source of energy, delicately utilised by all forms of life on the planet, comes directly from the sun. Solar radiation provides an average surface power density of 1.361 kW/m^2 [5] at the outer limit of Earth's atmosphere. Adjusted accordingly for atmospheric attenuation, this average power density yields a figure of approximately 1 kW/m^2 at sea level across the world, all of which is available for direct solar energy harvesting using photovoltaic (PV) devices. Over three generations, these technologies have seen many advances in their structure, formulation, and manufacture, yielding many different forms of solar PV. Despite this, each is designed to operate based on the same principles outlined by the quantum theory of light and semiconductor physics.

The three generations of solar PV, and their respective technologies, are outlined in table 1.1. The advantages and disadvantages of each are also listed for reference.

Table 1.1: An overview of the three types of solar PV. Shorthand expansions: amorphous Si (a-Si) [1], cadmium telluride (CdTe) [2], copper indium gallium selenide (CIGS) [3], organic PV (OPV) [4].

Technologies	Comments
a-Si	+ Inexpensive
	– Poor efficiency
c-Si, mc-Si	+ Tried and tested
	+ Long service life
	– High optical losses
CdTe, CIGS	+ Inexpensive
	– Elemental scarcity (In, Te)
	– High toxicity (Cd)
Perovskites, OPV	+ Efficiency to rival Si
	+ Simple to manufacture
	– Poor stability

The objective of this research is to improve the anti-reflectivity of silicon-based solar cells using novel nanoscale surface texturing techniques. Over time the improvement of both crystalline (c-Si) and multi-crystalline silicon (mc-Si) based PV has slowed dramatically due to the Shockley-Queisser limit, though this has been increasing again in more recent years. This limit describes the maximum efficiency that can be obtained with a single junction semiconductor substrate based on its band gap energy. For silicon, with a band gap of 1.17 eV [6], this limit is widely accepted to be between 32% and 33% [7]. The current leading research-grade c-Si cell holds an efficiency of 26.8% [8] and can be seen on the National Renewable Energy Laboratory's best research cell efficiencies chart in figure 1.1.

Given that the quality of solar grade silicon (SG-Si) for manufacturing solar cell technologies is already high, with a purity metric of 6 N[1], other methods of increasing the efficiency must be explored separate from substrate preparation in developments where only one junction is being employed. The use of higher purity substrates such as electronic grade silicon (EG-Si) is not warranted for solar applications [9]. This is due to

[1]The 'N' metric is a value representative of purity. For example, 6 N or six nines' is 99.9999% pure.

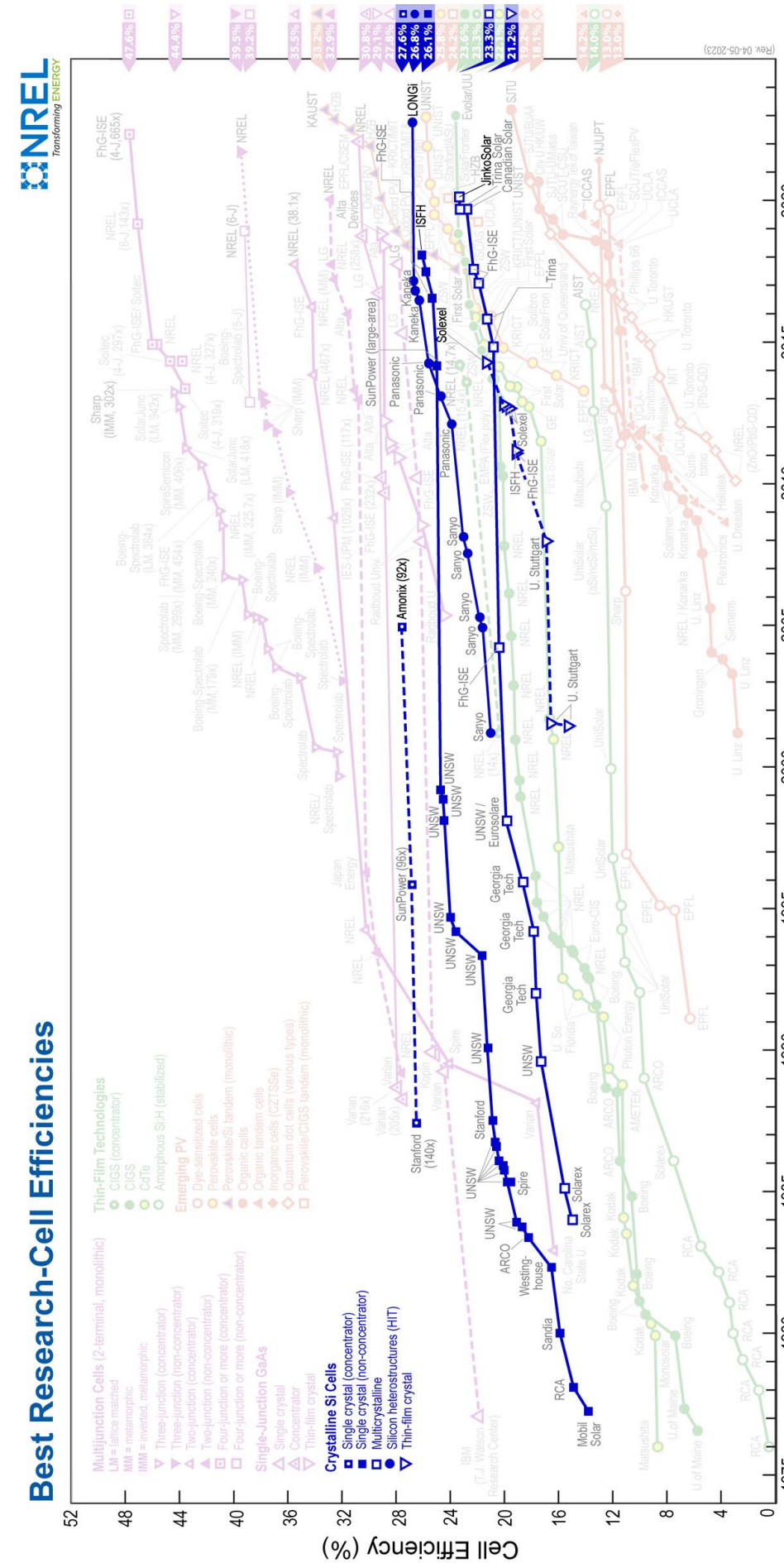

Figure 1.1: The best research cell efficiencies; a time-lapse visualisation on the progression of single junction c-Si and mc-Si PV technologies. This plot is courtesy of the National Renewable Energy Laboratory, Golden, CO. (2022).

the fact that there is very little to gain in overall efficiency, and that the cost of producing the large substrates required for solar PV would be extortionate at this purity level. There has been the development of multi-junction devices that are capable of exceeding the single junction Shockley-Queisser limit [10]. One of the first examples of such a device arose in 1982 in the form of a two-junction aluminium gallium arsenide to gallium arsenide cell with an efficiency surpassing 21% [11]. However, despite its potential offerings, it is arguably one of the most expensive cell structures to manufacture due to its complexity and layer-by-layer fabrication method [12–14]. Surface texturing techniques have, as an alternative, become the next step in increasing this efficiency further by enabling as much light to be drawn into the device as possible.

1.2 Solar Photovoltaics: A Retrospective

1.2.1 Solar Energy Prospects

Notably hindered for varying periods throughout their development, the adoption of solar PV as a modern energy source has never seen consistency. Despite this, the growth of the sector can be fit with a modest degree of accuracy against an exponential trend [15]. This demonstrates not only a drive to shift to solar energy and renewables in general, but also the market and investment value for these technologies. As one would expect, solar energy has both a time and a place where its performance can be considered to be maximal. Solar irradiation varies dramatically throughout each day, month, and season, whilst peaking at different levels around the world. Figure 1.2 demonstrates how this differs with respect to geographical location.

From the data shown in figure 1.2, solar 'hotspots' can be identified whereby incident irradiation is of significant magnitude to permit high solar power generation rates. Statistically, one of the best places to host solar PV devices is Australia, with a relatively uniform irradiation of approximately 8 kW/m^2 per hour across the entire country. As a point of comparison, this is a level approximately 10× that of the United Kingdom. Despite this, Australia generated approximately 6.2 TWh of solar energy in 2016, leaving it 10^{th} in the world; three places *behind* the United Kingdom. This data is visualised in figure 1.3a. Figure 1.2 demonstrates that direct normal irradiance is at its highest around parts of Chile, Peru, Bolivia, and Argentina. This opens an opportunity for these countries to update their existing infrastructure to accommodate solar energy as a dominant source, provided their drive to use such resources are sufficient. The impli-

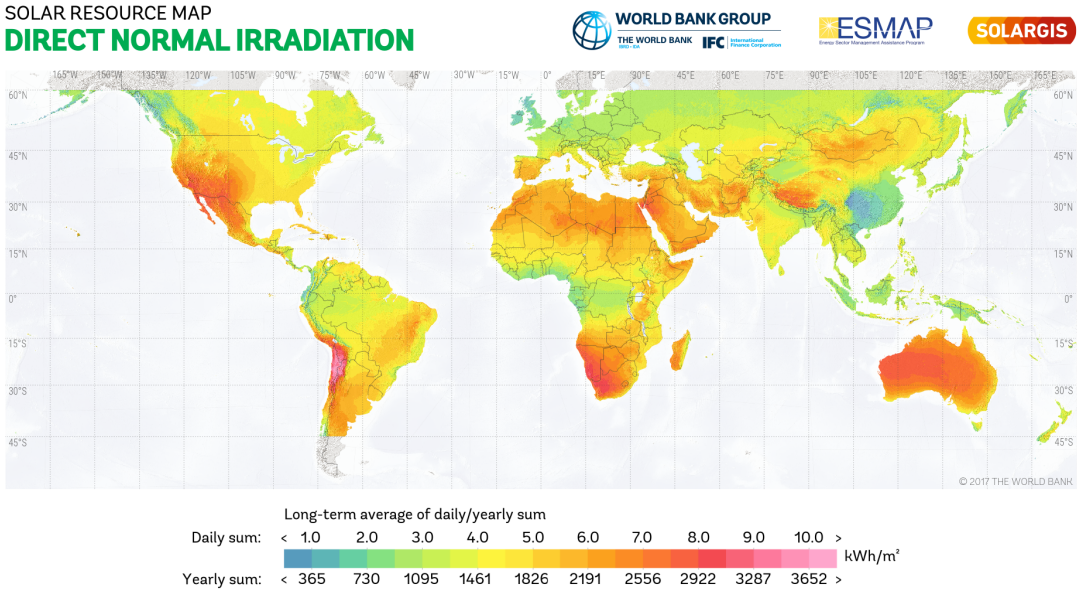

Figure 1.2: Solar energy potential made apparent by direct normal solar irradiation levels reported worldwide. Solar resource data obtained from the Global Solar Atlas and provided by Solargis (2019).

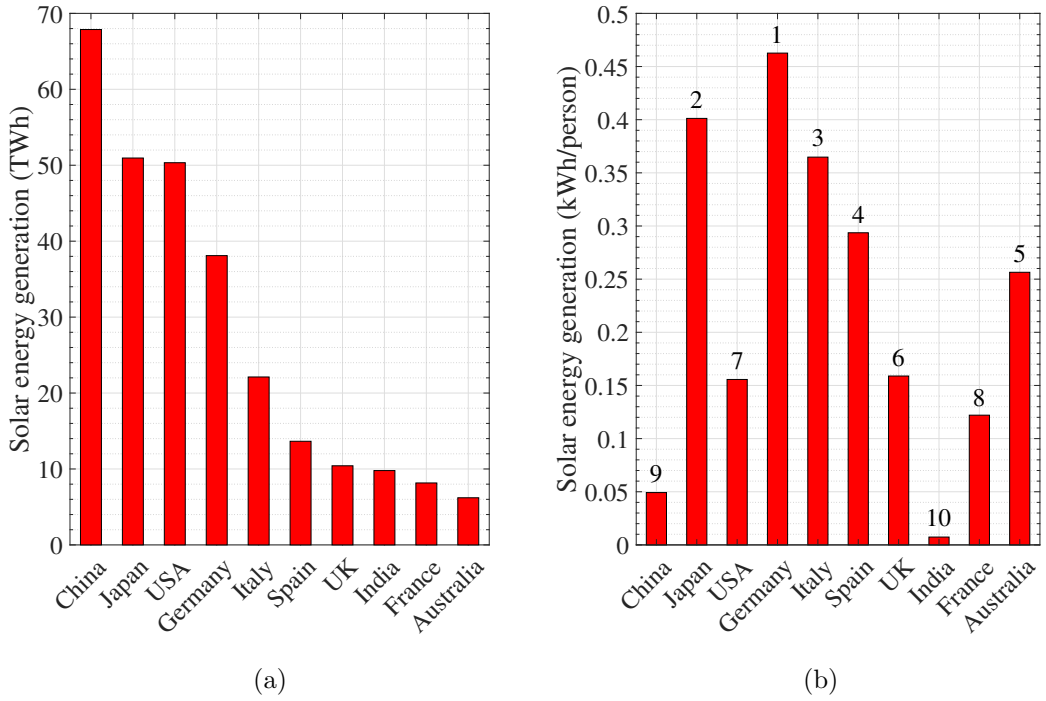

Figure 1.3: Solar energy generation statistics relating to the total solar energy generation of the top 10 countries worldwide (a) and the solar energy generated per person by these countries (b). Generation and population data provided by IRENA and the World Bank Group (2018).

cation of this data is that, regardless of the irradiation metrics showcased in figure 1.3a, the adoption of solar PV is unpredictable from this data alone. Other factors come into play such as research drive, resources, and population. Countries with a high population density are far more reliant on fossil fuels for reliable energy generation. Consequently, the demand for renewables in these locations is high [16, 17].

Generation data, with respect to the population of that country, is shown in figure 1.3b where it can be seen that Germany and Japan generate the most solar energy per capita. Crucially, as previously stated, solar energy is highly variable and, consequently, no single 'optimal' design exists – nor can one exist. Although this may seem undesirable, it has been the driving force for the parallel development of a huge variety of form-factors over the years; from concentrator PV [18] to silicon–, organic–, and perovskite–based technologies, each can be shown to have their own relative strengths and weaknesses when deployed around the world, though only Si-based technologies, and to a lesser degree, CIGS and CdTe, have few enough disadvantages overall to be considered widely deployable [19].

The cost of energy, particularly during the 2022 cost of living crisis, is often noted as the biggest area of concern for consumers when it comes down to the adoption of a specific energy source. This is true for all parties, be it those situated within the residential, commercial, or industrial sectors. Interest in a particular energy generation method comes down to one's ability to afford it, and whether it will prove cost-effective in the long-term. To quantify the overarching, impactful cost of deploying a specific type of energy, a metric was designed to consolidate this information into a single figure: the levelised cost of energy (LCoE) [20]. Equation (1.1) is the formula used to calculate the LCoE and yields an average cost representative of that energy source over its lifetime. Here, C is the total cost per unit time, D is the discount rate, and E is the energy generated per unit time. The value for time, t, is expressed in years, making the lifetime of the product n years. The discount rate, D, is a financial term given to the rate at which future expenses will decrease against the original value at $t = 0$. The units of LCoE are £/kWH in the UK.

$$\text{LCoE} = \frac{\sum_{t=1}^{n} \left(\frac{C_t}{(1+D)^t} \right)}{\sum_{t=1}^{n} \left(\frac{E_t}{(1+D)^t} \right)} \tag{1.1}$$

It should be noted how the LCoE for solar energy has dropped by approximately 90% in the past 10 years alone, with further plummeting costs expected for the forthcoming

years [21]. Such decreases in LCoE can be attributed to reductions to the associated costs of solar PV technologies: sourcing, manufacturing, and system complexity, for example. The cost of energy storage, essential in solar and wind energy generation, has also dropped considerably over the same period, although it should be noted that this is not as considerable as that outlined previously. The remaining influential factors on the overall cost of solar PV relate to cell-level research and development that includes factors like optical and electronic efficiency, as well as the research into the other aforementioned cell structures and technologies.

1.2.2 Crystalline Silicon

Upon reflection of the information shown in table 1.1, whereby all solar cells built upon this material are considered first generation, Si has often become viewed as anachronistic in a world of next-generation technological developments. Such technologies include perovskites and the OPV cell. Despite this, Si dominates the industry as much today as it has since its conception; basking in a 93% market share [17]. The implication of this being that solar cells will seldom appear in any other form, gaining the material a reputation for its unmatched reliability, durability, and purity. Si was first openly showcased in a "light–sensitive" device in 1941 [22]. The device embodied by this record was noted as having an efficiency of less than 1% [23]. Fast–forward to the present, and this efficiency is edging ever–closer to 30% by the year.

At present, global solar generation is contributed to by c-Si, mc-Si, and thin film technologies with a ratio of approximately $32 : 61 : 5$ respectively. The proportion of mc-Si and thin films has been dropping to the gain of c-Si consistently since 2015 [17]. This gain comes as a result of unexpected changes to the solar PV market causing a dramatic drop in the costs of c-Si [24], as well as a shift in priorities towards higher cell efficiencies. This has led to a reduction in the use of cheaper, less pure mc-Si substrates. Furthermore, c-Si cells are said to have a longer lifespan and that, due to a decrease of the market price of c-Si, mc-Si has been forced to also become cheaper to remain competitive. This is problematic since there has been a low demand and an oversupply of mc-Si for some time[2]. In early 2022, a team at Fraunhofer ISE noted that 95% of PV module production was c-Si, and followed that the LCoE for this form of PV was dropping consistently by approximately 15% every year since 2012.

[2] As reported by M. Willuhn in the article "Ingot, wafer prices dropping; market momentum needed" for PV Magazine, Oct. 2018.

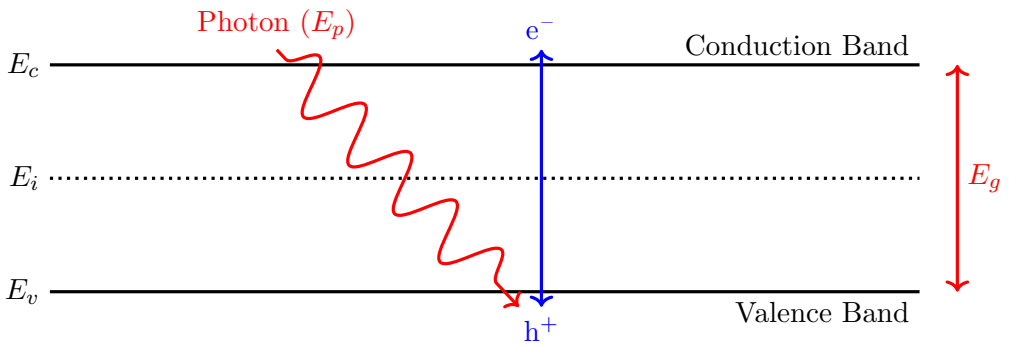

Figure 1.4: Outlining semiconductor energy bands and the generation of an electron-hole pair for a single incident photon of energy E_p, whereby $E_g \leq E_p$, the band gap energy.

Si is a widely used group IV semiconductor credited for significant technological advances over the past century. It works as a photoelectric material by absorbing incident photonic energy and generating electron-hole (e-h) pairs. These e-h pairs recombine after some transient period, the average of which is referred to as the carrier lifetime, τ. This process works when a Si atom absorbs a photon of some energy, E_p. Provided this energy is greater than or equal to the material's band gap energy, E_g, an electron will be excited from the valence band to the conduction band, leaving a hole in its place. This process is shown in figure 1.4. Given the conservation of energy, on the recombination of an e-h pair some form of energy is given off, usually in the form of a new photon of energy, E_g, whereby the excess energy of the initial photon above the band gap energy, E_x, is released in the form of a phonon; a lattice vibration resulting in heat generation within the substrate itself. This is typical of band–to–band recombination, particularly for semiconductors featuring an indirect band gap like Si.

$$E_p \rightarrow E_g + E_x \qquad \text{for } E_g < E_p \tag{1.2}$$

$$E_p = hf = \frac{hc}{\lambda} \tag{1.3}$$

$$\lambda_c = \frac{hc}{E_g} \tag{1.4}$$

$$\therefore \lambda_c \approx 1,060 \text{ nm} \qquad \text{for Si} \tag{1.5}$$

For solar applications the aim is to separate these e-h pairs as quickly as possible, preventing spontaneous recombination. This separation creates a photovoltage; a potential difference that can be held across some external load. This pair can recombine upon flowing through this load, allowing power to be dissipated through an electronic circuit,

for example. In the case of incident photons of energy less than the band gap energy, E_g, the semiconductor will not respond with the generation of e-h pairs. Instead, a material becomes transparent to wavelengths of light that are beyond those indicative of such energy levels. The wavelength at which a material becomes transparent to incident light is referred to herein as the critical wavelength, λ_c, where the relation between energy and wavelength is outlined in equation (1.3). Light below this wavelength can either pass directly through a material, or, more likely, generate lattice vibrations and, subsequently, heat as it does so.

Electrons that are elevated to the conduction band eventually lose their energy and recombine with the hole left in the valence band. Such carrier recombination comes in three forms: radiative, defect, and Auger. The two latter types are most prevalent in c-Si substrates. During radiative recombination, an e-h pair will recombine directly from the valence and conduction bands. Defect recombination is where a defect energy level, which sits between these two bands, acts as an intermediary in the recombination process, trapping either an electron or hole within the defect state, and allowing recombination to occur more readily. Trap states are effective at aiding recombination when they are more central to the intrinsic energy level; the middle of the band gap. Auger recombination, unlike the other two types, involves three charge carriers. When the recombination of an e-h pair occurs, the excess energy, E_x, is transferred to another electron as opposed to being released as heat.

1.3 Electromagnetic Wave Theory and Propagation

EM waves comprise of two major components: an electric field, $\vec{E}$, and a magnetic field, $\vec{B}$. The two of these fields are always present and perpendicular with respect to one another. An example of this is shown in figure 1.5. In this case, the $\vec{E}$-field is parallel with the x-z plane, and the $\vec{B}$-field is parallel with the x-y plane.

EM waves can also be represented arithmetically. An EM wave, with oscillatory components spanning all three spatial axes, x, y, and z, as well as having variance over time, t, has a definition as shown in equation (1.6). Here, A is the amplitude of the wave at time period, t, along wave vector, $\vec{r}$. The temporal angular frequency, ω, spatial angular frequency, k, and phase difference, ϕ, and peak amplitude, A_0, also form part of this formulation and subsequently the characteristics of the wave itself. Equation (1.6) also

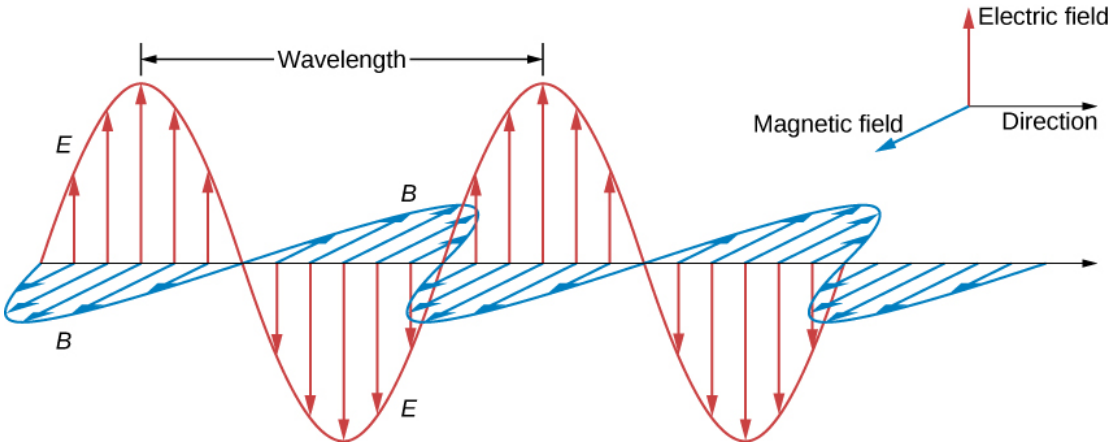

Figure 1.5: An exemplar EM wave travelling in a left to right direction displaying the composite $\vec{E}$ (red) and $\vec{B}$ (blue) fields. Image provided courtesy of OpenStax and attributed authors [25].

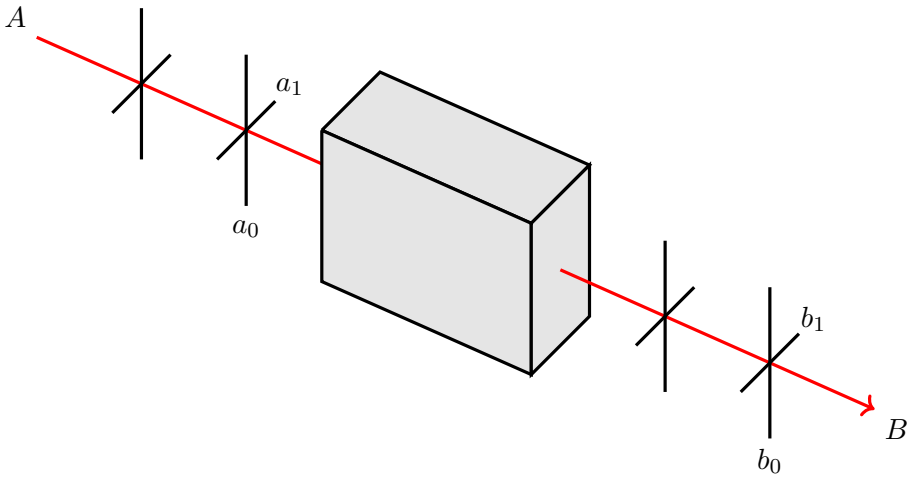

Figure 1.6: A ray of light (red) passing from points A to B, through a black-box optical medium experiencing some degree of reflection, refraction, and absorption. If the source is point A and the observer is point B, or vice versa, the light observed will be the same.

applies identically to both $\vec{E}$ and $\vec{B}$ fields.

$$A(\vec{r},t) = A_0 \cos\left(\vec{k}\cdot\vec{r} - \omega t + \phi\right) \tag{1.6}$$

The reflection and refraction resulting from an interaction with some given surface is dependent on the polarisation of the incident EM wave. There are two types of polarisation, referred to as senkrecht (S; German for 'perpendicular'), and parallel (P). These represent the transmission of light in the TE or TM modes, respectively, and are defined by their relation to the plane of incidence. Light from most sources is said to be unpolarised. This is an inaccurate definition since the term itself implies a wave of light is travelling with no transient directionality to the electric or magnetic field components, which is not possible. More accurately, it can be said that the direction of both fields are changing constantly, yielding an indistinguishable mode of polarisation over time. In an instant, a distinct mode will be detectable however: S, P, or a mixture of the two, implying it is travelling with more than one mode simultaneously. This is referred to herein as hybrid polarisation light, as opposed to unpolarised light.

It has been noted that reflectance, refraction, and absorption of light with some passive media is described by the Helmholtz reciprocity principle [26]. Helmholtz states that light travelling between two points is subject to some arbitrary number of reflections, refractions, and some degree of absorption. This can be thought of as an optical black box, as shown in figure 1.6. Crucially, it outlines how a ray of light travelling between these two points, regardless of the direction, will be optically identical. This implies that the ray will be the same before and after interaction with a series of media independent of the direction it travels through them: in short, the source and observation points can be swapped with no difference to what the observer sees. This is key in the design of optical manipulation systems, such as a series of lenses, as explored here.

1.4 Anti-reflectance Coatings and Textures

1.4.1 Planar Coatings

1.4.1.1 Single Layer Coatings

Top surface reflectance, a key cause of the optical losses in solar cells, has been addressed through the use of microscale texturing and anti–reflectance coatings (ARCs) [30]. ARCs are appropriate for a wide variety of applications and are made out of dielectric materials. By tuning the thickness, d, of such a coating, with a refractive index,

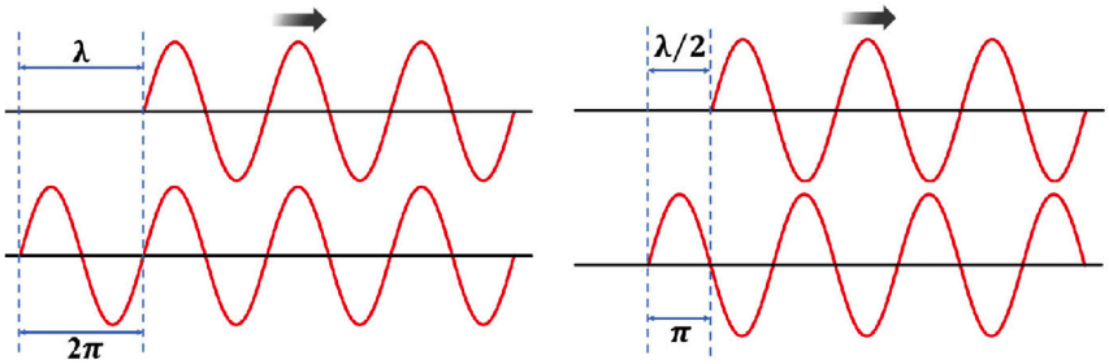

Figure 1.7: Visualising constructive (left) and destructive (right) interference. ARCs are tuned to a thickness of $d = \frac{\lambda}{4}$ to enable secondary reflected rays, which travel a distance of $2d$ between the air-ARC and ARC-substrate interfaces, to be out of phase at the air-ARC interface by $\frac{\lambda}{2}$, summing to no reflected component at a wavelength of λ. Image sourced from [27].

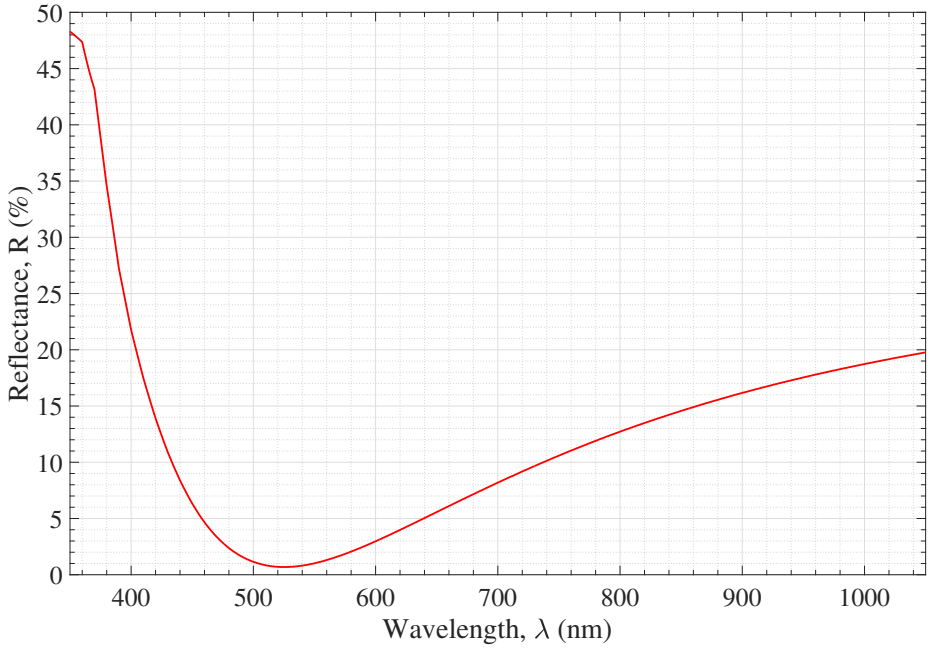

Figure 1.8: The reflectance spectrum, at an angle of incidence of 8°, of polished silicon coated with a 69 nm thick Si_3N_4 ARC. The refractive index of Si_3N_4 was reported by M. R. Vogt [28] and surface reflectance was simulated using OPAL 2 [29].

n_c, it is possible to minimise the reflectance intensity for one wavelength of light, λ_0. The property λ_0 is a discrete wavelength that is selected during the design process, and is typically at some point in the visible portion of the EM spectrum for solar ARCs. This process works because, by setting the thickness of a dielectric coating as in equation (1.7), incident light reflected at the air-ARC and ARC-Si interfaces are 180° out of phase. This causes the two to destructively interfere and have no magnitude at a wavelength of λ_0. Such a process is illustrated in figure 1.7, where reflected red light is cancelled out by itself, leaving no such component in the spectrum.

$$d(\lambda_0) = \frac{\lambda_0}{4n_c(\lambda_0)} \tag{1.7}$$

$$n_c(\lambda_0) = \sqrt{n_{\mathrm{Si}}(\lambda_0)} \tag{1.8}$$

Equations (1.7) and (1.8) assume normal incidence. The thickness of the ARC is not the only property that needs to be accounted for when optimising performance. By ensuring the refractive index of the coating, n_c, is the geometric mean of the refractive indices of the media it is sitting between, a further performance enhancement is attained. Under the assumption that this ARC is between air and Si, as with figure 1.7, we obtain equation (1.8). By taking $\lambda_0 = 555$ nm, the wavelength of light human eyes are most receptive to, and substituting this into equation (1.8), followed by equation (1.7), we get $n_c = 2.01$ and $d = 68.9$ nm respectively. The closest material matching the value for n_c is silicon nitride (Si_3N_4) where $n = 1.92$ for $\lambda = 550$ nm [28]. Using the calculated thickness and Si_3N_4 as the coating material, it is possible to simulate the optical response of such a coating [29]. The output of this is shown in figure 1.8.

1.4.1.2 Stacked Coatings

Thin film ARCs can also be stacked on top of one another, creating what has been dubbed as dual layer ARCs. These are more complicated than their single layer counterparts, however, when tuned properly, can offer exceptional anti–reflectance properties [33]. Dual layer ARCs require similar calculations in order to be correctly optimised. Similarly, distinct reflectance minima can be seen for each layer of the coating, often resulting in an oscillatory spectral response if these two wavelengths are further apart. Interesting to note is that ARC thickness can be accurately identified by non–destructive methods as simple as colour identification, making the automated manufacturing and characterisation of these coatings more viable for industrial settings [34]. This has resulted in a broad uptake of this anti–reflectance method across many streams of solar

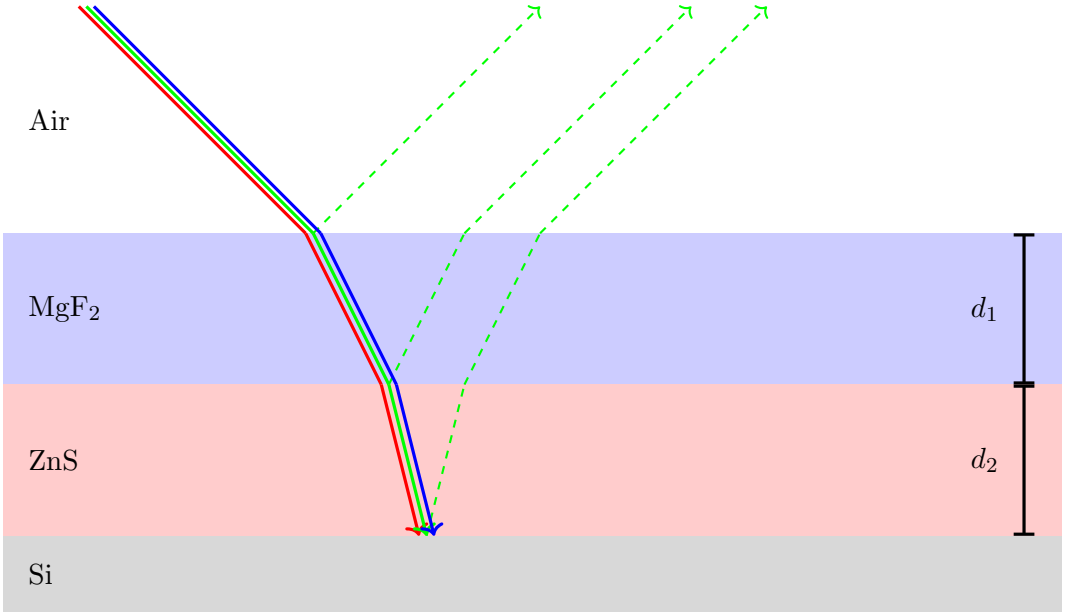

Figure 1.9: Showing how a dual-layer ARC eliminates the reflection of two wavelengths of light using two thin films of set thickness, d. Dashed lines represent secondary (reflected) rays. In this example only green light is reflected.

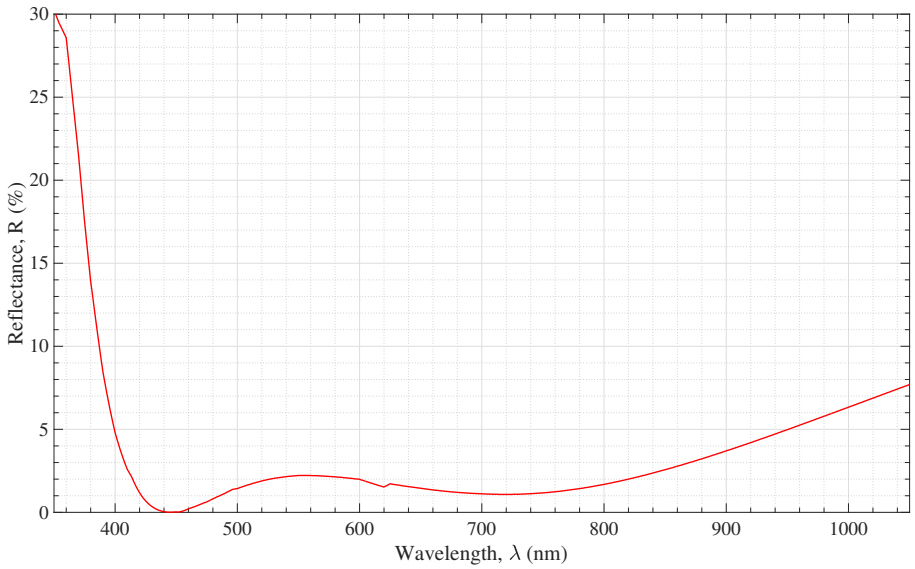

Figure 1.10: The reflectance spectrum, at an angle of incidence of 8°, of polished Si coated first with a 105 nm thick ZnS layer, followed by a 55 nm thick MgF_2 layer, together forming a dual-layer ARC. The refractive indices of ZnS and MgF_2 were reported by E. D. Palik [31] and M. J. Dodge [32], respectively. Surface reflectance was simulated using OPAL 2 [29].

PV research.

For ARCs inclusive of more than one layer, each layer must be ordered appropriately with respect to the part of the EM spectrum they are anti–reflective towards. The reason for this relates to the Beer-Lambert law. This law describes how light is attenuated as it passes through some medium. In general, higher energy EM waves are unable to travel far into certain media whilst waves of lower energies can. High energy waves are able to interact with the electrons orbiting atoms, promoting them to higher energy states and losing energy themselves, subsequently losing the ability to penetrate the medium further. Lower energy waves do not elicit such a response with electron orbitals as readily as their high energy counterparts, and thus can pass much deeper and sometimes straight through with no interaction at all. This means that ARCs should be stacked from substrate (semiconductor) to superstrate (encapsulation) in an order respective of their decreasing tuned wavelength. For example, this is to say ARCs tuned for the colour red should be closest to the substrate, and those tuned for blue colours should be closest to the surface or encapsulation layer. An example of a dual layer ARC, alongside its reflectance spectrum, can be seen in figures 1.9 and 1.10, respectively.

1.4.2 Surface Texturing

1.4.2.1 Microscale Textures

Aside from thin film ARCs, the application of microscale pyramidal textures has proven particularly beneficial for reducing surface reflectance not only at normal incidence, but at wider angles as well. They help to ensure light can be collected efficiently at many different angles of incidence; a property invaluable to solar PV devices given the Sun's constant movement. Pyramidal textures can also be covered with an ARC to further enhance optical performance. Examples of both can be seen in figure 1.11 inclusive of incident rays. They are capable of providing such anti-reflectance due to light reflected off the inclined facets of the pyramids being subsequently directed toward an adjacent facet. This gives the ray of light another chance to be coupled into the substrate. There is also the added benefit of light trapping with these structures through the change in the propagation direction of light as it enters the substrate, resulting in an optical path length enhancement. This is another key benefit for PV as it increases the absorption of light, and as a result the likelihood of e-h pair generation.

At present, this is the most widely used anti–reflectance mechanism in solar PV. There are several varieties of the texture, including uniform, random, and inverted. It should

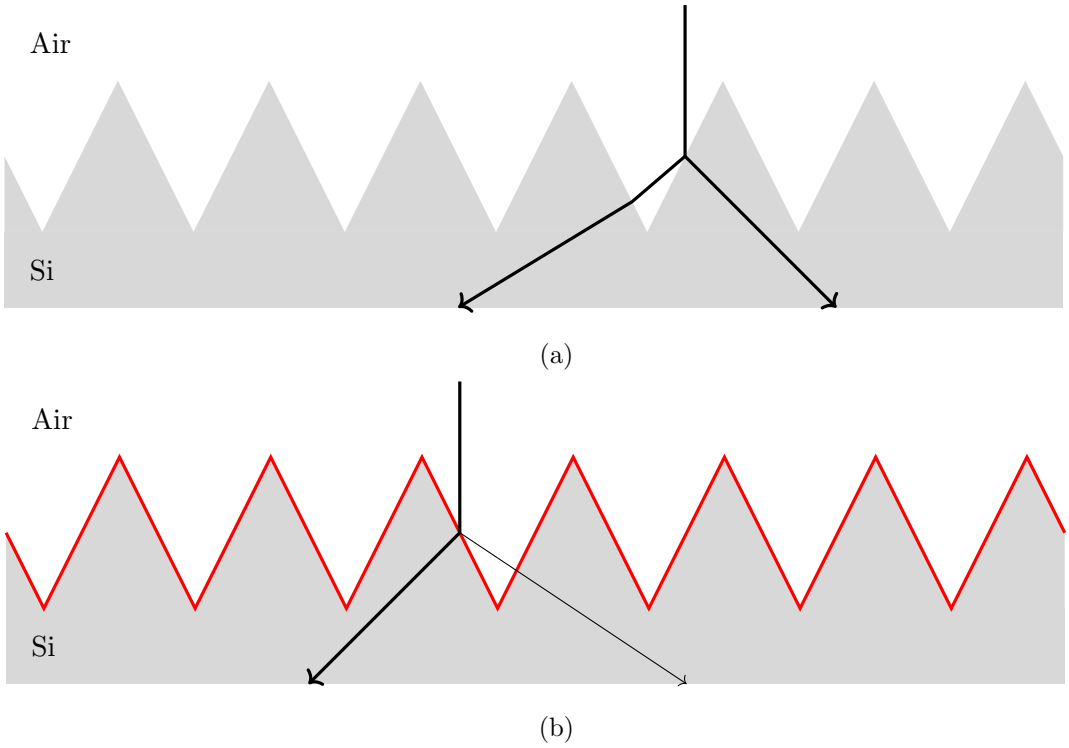

Figure 1.11: Showing how pyramidal texturing interacts with incident rays of light both without (a) and with (b) and ARC. It can be seen that the application of an ARC does not change the way light interacts with the structures, but does decrease the intensity of the secondary reflection, absorbing more of the primary ray's intensity into the substrate directly. Tertiary reflections have been omitted.

be noted that such microscale textures can be periodic or random. Random pyramids are most common here, and are formed readily by an industry-standard anisotropic potassium hydroxide (KOH) etch. The surface etchant is referred to as anisotropic due to the preferential etch rate along the <100> crystallographic plane.

Etching on mc-Si, which has multiple crystal orientations [35], does not produce the same pyramidal textures as on c-Si substrate cleaved along the <100> plane. Instead, mc-Si substrates require surface isotexturing via a combination of acidic and alkali solutions [36,37]. The use of hydrogen fluoride (HF) and nitric acid (HNO_3) are common in this regard. This can then be followed by the KOH solution aforementioned, or a sodium hydroxide (NaOH) based equivalent. Alternatively, a photolithographic–governed etch or surface ablation can be employed to create such structures on mc-Si, though these are far less common in practice. Surface ablation can be carried out using either mechanical means, such as a saw or abrasive contact, or by using a LASER to chip away at the surface via energy bombardment. These methods of creating microscale textures

for solar PV are notably slower, more complex, and carry greater cost than the wet chemical etches, limiting their applicability to large-scale production lines, where these three factors carry significant weight in the manufacture of solar panels.

1.4.2.2 Nanoscale Textures

Surface texturing for PV is not limited to the microscale. Several nanoscale textures, including pyramids, pits, pillars, spikes, wires, and general surface roughness have all been shown to work effectively at decreasing the optical reflectance from Si surfaces [38]. In particular, black silicon (b-Si) nanowires (NWs) have seen an uptake in recent years [39]. Originally discovered as an unwanted side effect of a chemical etching process, b-Si NWs are now formed through a variety of different methods, to be described later, and have an appearance strikingly similar to that of grass: vertically aligned and often splaying at slight angles from the normal, bunching together. This varies with manufacturing methodology and is outlined in chapter 2. NW structures are extremely delicate, with little force required to shear them from the Si surface on which they were situated. This makes handling them a more involved process than that of other textures, and becomes a consideration when looking at automated manufacturing — the manufacturing line could easily remove the surface texture during even the most basic automated movement from one stage to the next [40, 41].

Nanoscale surface texturing offers comparably greater optical performance for solar PV in lieu of those of the microscale. Often hailed as the way forward for all photovoltaics alike, where optical efficiency is always critical, nanoscale texturing is not only capable of scattering light, as opposed to merely reflecting and refracting it, but also forms a graded refractive index between the two media between which it sits. The result is overall reflectance levels are measurably lower, and thus have a far darker appearance to the naked eye.

1.5 Electrodynamics of Solar Cells

Key metrics outlining solar cell performance not only lie within the optical response of its surface, but in its electrical characteristics as well. Quantifying these characteristics permit formative comparisons to be made between devices, regardless of their respective central technologies. Behaviour relating to current and voltage generation under illumination is key here. This includes the current density (J), fill factor (FF), maximum power point ($P_{\max}$), minority carrier lifetime (τ), parasitic resistances (R_s

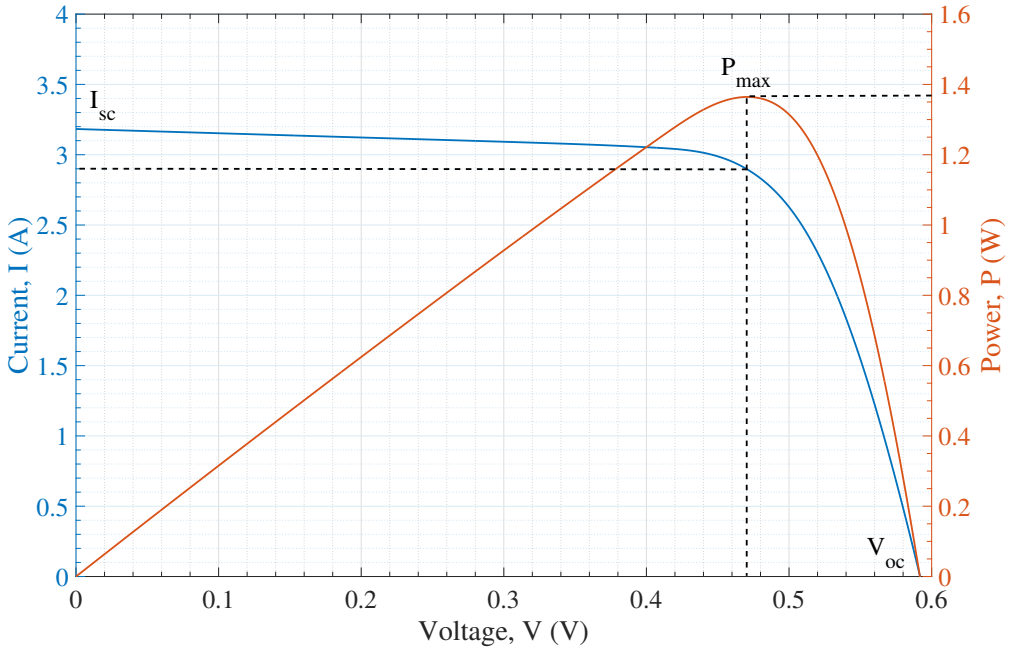

Figure 1.12: An exemplar I-V curve for a c-Si solar cell. Marked is the maximum power point, $P_{\max}$, short-circuit current, I_{sc}, and open-circuit voltage, V_{oc}.

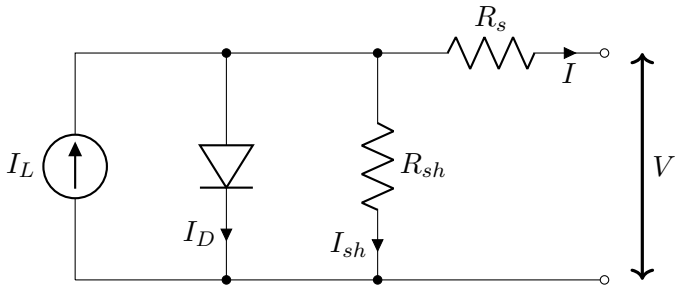

Figure 1.13: The circuit diagram representing the non-ideal electronic equivalent of a solar PV cell. Series (R_s) and shunt (R_{sh} resistances come into play, effective overall electrical performance characteristics. Notably, the former reduces the cell's output current (ideally $R_s = 0$), whilst the latter reduces the output voltage (ideally $R_{sh} = \infty$). The dark current, I_D, is a parasitic current draw through the device itself (ideally, $I_D = 0$).

and R_{sh}), power conversion efficiency (η), as well as the open-circuit voltage (V_{oc}), and short-circuit current (I_{sc}). A typical current-voltage (I-V) response curve for a c-Si solar PV device is shown in figure 1.12.

Many of the these electrical properties can be read directly from a graph such as the one shown in figure 1.12. For instance, let us take I_{sc}, where the cell voltage, V, is zero — that is to say the y-intercept. For the data shown in figure 1.12, this is shy of 3.20 A. Conversely, V_{oc} is apparent where the output current, I, is zero, implying that there is no connected load — the circuit voltage is floating. This value can be seen at the x-intercept, yielding a value of 0.59 V here. $P_{\max}$ is where the product of the cell's output current and voltage reaches its peak. Commonly, such as seen in figure 1.12, power-voltage (P-V) curves can be plotted within the same figure as I-V curves, in this case showing $P_{\max}$ to be at the maximum power voltage, V_{mp}, of 0.47 V. Looking back at the I-V graph, the value for the maximum power current, I_{mp}, at which the maximum power is 2.9 A. By determining the area between these points in the form a rectangle, we can determine the FF.

$$\mathrm{FF} = \frac{P_{\max}}{I_{sc}V_{oc}} = \frac{I_{mp}V_{mp}}{I_{sc}V_{oc}} \tag{1.9}$$

The FF is given as the ratio between the area of this rectangle over the area formed by a similar rectangle bound by the short-circuit current, I_{sc}, and open-circuit voltage, V_{oc}. This is demonstrated in equation (1.9) and always holds a value less than unity. Series, R_s, and shunt, R_{sh}, resistances have different but noticeable effects on I-V curves. To understand this fully, we must look at the electronic equivalent model of a PV cell as shown in figure 1.13.

$$I = I_L - I_D - I_{sh} \tag{1.10}$$

$$= I_L - I_0\left(e^{\frac{qV_D}{nkT}} - 1\right) - \frac{V_{sh}}{R_{sh}} \tag{1.11}$$

$$= I_L - I_0\left(e^{\frac{q(V+IR_s)}{nkT}} - 1\right) - \frac{V + IR_s}{R_{sh}} \tag{1.12}$$

$$= I_L - I_0\left(e^{\frac{qV}{nkT}} - 1\right) \qquad \text{for } R_s = 0 \text{ and } R_{sh} = \infty \tag{1.13}$$

The series resistance, R_s, can have a considerable impact on both the output voltage, V, and current, I, from the system when under load. This is because R_s is floating load-side in the absence of any connected device holding V across it. On the other hand, the shunt resistance, R_{sh}, only causes a drop in cell current across all voltages as current must

now be split between the R_s and load resistances connected in parallel with R_{sh} [42]. From figure 1.13, it is possible to derive I for non-ideal solar cells under light-induced current, I_L, by starting with Kirchhoff's current law and Ohm's law. This derivation is shown in equation (1.12). An ideal solar cell will have negligible R_s and infinite R_{sh}, yielding no effect on cell output current or voltage (see equation (1.13)) [42].

The power conversion efficiency, η, of a solar cell takes into account many of the factors discussed previously in this section and yields a single value in return. This property is defined as in equation (1.14).

$$\eta = \frac{P_{\text{max}}}{P_{\text{in}}} = \frac{I_{mp}V_{mp}}{P_{\text{in}}} \tag{1.14}$$

Power conversion efficiency is a measure determining the maximum output power, P_{max}, for the cell with a given input power, P_{in}. In order to make the value of η for different solar cells comparable to one another, P_{in} is made constant by adhering to a set of two standard testing conditions. These include holding the cell temperature constant at 25 °C, and ensuring the test is conducted under AM1.5G conditions for terrestrial devices, or AM0 for space-dwelling devices. The input power for AM1.5G conditions, as outlined in section 1.1, is 1 kW/m^2. The current record for efficiency is 47.1% [43] and was set by the National Renewable Energy Laboratory for their six junction III-V semiconductor concentrator cell illuminated under 143 Suns.

Quantum efficiency, a measurement of optoelectronic efficiency within a semiconductor, is important for solar PV technologies and comes in two classifications: internal (IQE) and external (EQE). EQE is a measure relating the number of e-h pairs *collected* from the semiconductor substrate (and thereby contribute to the current generated) to the number of photons originally incident upon it. Ideally, this ratio would be 1 : 1, but is not possible in practice for a number of reasons. Most notably, this 1 : 1 ratio is not achievable due to the limited spectral response range of all semiconductor materials. In the case of Si, with a band-gap energy yielding a critical wavelength, λ_c, of $\sim 1,060$ nm (equation (1.5)), the photon energy range that can be used is limited. A considerable amount of atmospheric irradiance, as measured at sea level, is in the infrared (IR) region of the EM spectrum – wavelengths that are beyond the band-gap of Si. Si is subsequently transparent to IR waves, meaning no photons are absorbed for e-h pair generation, causing the quantum efficiency to be essentially saturated at some level below 100%. Furthermore, high energy ultraviolet (UV) radiation penetrates only a small distance into the substrate before being absorbed. This means e-h pairs generated

as a result of UV radiation typically recombine before they can be collected by the cell, given this shallow generation is further from the junction and closer to the surface acting as a recombination site. However, very little UV waves penetrate Earth's atmosphere and reach sea level, so the impact of this region of the EM spectrum is far less significant than that of the IR region. The spectral radiance indicated by the AM1.5 standard is shown in figure 1.14.

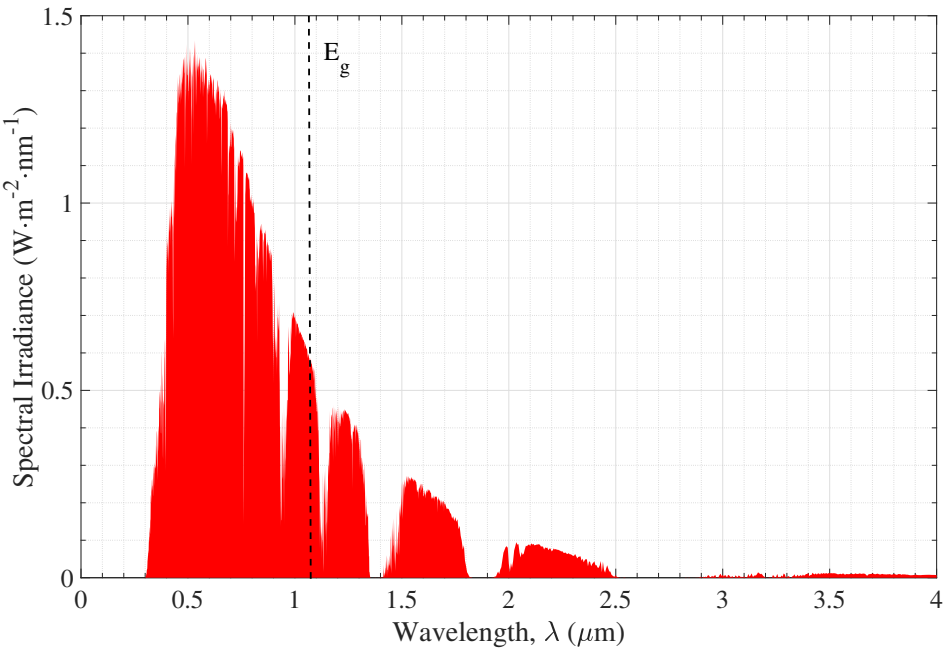

Figure 1.14: The AM1.5 spectral irradiance characteristics, at sea level, as reported by ASTM International [44]. E_g here represents the bandgap energy of Si.

By definition, IQE is a determinate of EQE, since the number of photons not reflected at the surface (that is EQE) yields the number of photons available to generate electron-hole (e-h) pairs. Subsequently, IQE is always higher than EQE by some amount. The smaller the difference between the two indicates a higher quality solar cell overall, with improved electrical characteristics, as well as low optical losses from the surface. Quantum efficiency is expressed with respect to wavelength because, for reasons outlined previously, different wavelengths of light interact differently with a given substrate; Si in this case.

1.6 Scope and Outline of Thesis

Increasing the optical efficiency of Si–based PV through the use of hb-Si textures such as those proposed here is of crucial importance and rooted in current global issues

and scientific principles. Global warming is an ever–increasing issue requiring new and effective energy generation to replace that of fossil fuels that release greenhouse gasses into the atmosphere. By increasing the efficiency of our solar cell technologies, we will reduce our dependence on fossil fuels and eliminate the harmful emission of these gasses. The cleaner energy generated from more efficient PV will significantly contribute to global efforts to combat climate change.

Our growing energy demands require a secure source of energy for the future, and solar PV is a key player in the solution to this problem. The efficiency of Si solar cells can be greatly improved through unique, effective, and careful application of optical media to increase quantum yield. This not only makes PV more reliable, but also more accessible in parts of the world not exposed to the highest levels of solar irradiance. Greater quantum yield also reduces the LCoE for solar PV, making it more economically competitive with other energy sources. It is important to note that such cost metrics will be critical to widespread adoption of the technology as a whole, as well as market competitiveness.

Furthermore, the production of c-Si solar cells relies on high–purity Si, crystals that are typically grown through methods such as float zone or the Czochralski method, which can be resource–intensive and costly. Hybrid black silicon nanotextures can improve the efficiency of these cells, enabling us to generate more electricity from the same sized substrate. These textures leverage the quantum principles of light. At the nanoscale, these textures trap incident light more effectively, increase the optical path length enhancement, and allow for higher absorption coefficients.

In summary, increasing the optical efficiency of our Si–based PV using hb-Si addresses pressing global issues related to climate change, energy security, resource scarcity, and reduction of LCoE. Moreover, it is firmly rooted in the principles of optics and materials science, offering a sustainable and technologically innovative solution to our energy challenges. In pursuing this avenue of research, we can move ever–closer to harnessing the full potential of solar energy, making it a more viable solution in our efforts to combat climate change and create a sustainable future for our energy needs.

A theoretical analysis, backed by a substantive review of literature, outlines the capabilities of nanoscale textures in the minimisation of surface reflectance. Black silicon (b-Si) is an easy–to–make, inexpensive, and robust way to achieve these optical properties in the field of solar PV. However, even nanoscale textures, employed on their own,

will have performance shortfalls in the wide-angles of incidence provided by a moving source: the Sun over the period of a solar day. By pairing microscale pyramids with nanoscale b-Si textures to create a hybrid topology, referred to herein as hybrid black silicon (hb-Si), the benefits of both can be carried forward to gain a significant reduction in both broadband and wide-angle reflectance. Several key areas need to be addressed, along with resulting questions raised, before these textures can be realised in a solar cell.

1. **Manufacturing.** A reliable, compatible, and controllable manufacturing process, based on the metal assisted chemical etch (MACE) process, is taken alongside a similarly qualified potassium hydroxide (KOH) etch, to create hb-Si surfaces. With these two proven recipes, etch time is scrutinised to yield the appropriate balance in terms of pyramid size and NW length, resulting in highly optically efficient structures that can be made reliably.

2. **Characterisation.** The key selling point for the proposed hb-Si textures over planar ARCs, pyramids (with or without ARCs), and b-Si, is that reflectance will remain low for high angles of incidence. This means that optical performance of hb-Si will be maintained throughout the day irrespective of the relative angle between the Sun and the solar panel coated with hb-Si. A comprehensive characterisation study is required to show the benefits raised by hb-Si, coupled with a comparative study with the remaining aforementioned anti-reflectance schemes.

3. **Modelling.** Models to accurately recreate and simulate the optics resulting from nanoscale textures, such as b-Si, are complex and computationally expensive. In having an accurate way to model these structures, it becomes possible to recreate b-Si in a number of different configurations simultaneously and measure the optical response of each. This can then be compared to measured data in a verification study, and used to reverse-engineer surfaces with low reflectance, balanced with high electrical performance.

This thesis is structured in respect to the order of the three areas outlined above. Chapter 3 explores the manufacturing workflows and implications when creating pyramids and b-Si textures, then taking this forward to merge these etching processes (KOH and MACE, respectively) in a sequential manner to form hb-Si. Various etch times as a factor on resultant surface properties are analysed. Reproducibility is studied in accordance with the industry-adoption scope of this project, ensuring textures of comparable

features are created for set compositions within the bounds of what stochastic etching processes will yield.

Variable angle reflectance (VAR) will be quantified through the use of an angle-resolved spectrophotometry (ARS) system, designed and built to address the gap in research for angle-dependant reflectance. This work is outlined in chapter 4. Thin film ARCs, pyramids, pyramids coated with ARCs, b-Si, and hb-Si are measured, compared, and analysed using the data from the ARS. Advanced spectrophotometric analyses are performed using this data, including optical efficiency mapped against location and time, and variable angle colorimetry, to show how the colour of a given surface changes based on the angle by which light is incident on its surface. Non-PV related samples are measured in this area of work to demonstrate the versatility of the technique and system, revealing new areas of research outside the scope of this work.

To support the experimental studies, also forming a validation for itself, a computational model is developed to determine the reflectance of b-Si NW structures using electromagnetic wave propagation optics, alongside mathematical algorithms to provide a high level of pseudo-randomisation. This work is showcased in chapter 6, and allows the model to be more representative of b-Si surfaces as manufactured in chapter 3. Scanning electron micrographs of these b-Si samples will form the basis of these mathematical algorithms, and subsequent comparisons between real and simulated reflectance aim to validate the model. A similar model for hb-Si is designed, but lacking the computational power to run such a dense model, remains an unexplored area for the time being. The theory behind the model and its simulation is outlined in-situ with the b-Si model shown in this chapter.

Chapter 2

Review of Literature

2.1 Traditional Mechanisms for Anti-reflectance

2.1.1 Anti-reflectance Coatings

ARCs, whether they be single or multi-layer, are robust dielectric material layers designed to coat an underlying medium in order to modify the way that medium's surface interacts with incident EM radiation. They are crucial for the efficient function of solar cells – particularly those built on a Si substrate that are susceptible to optical losses. This is due to the high reflectance of an uncoated, polished piece of c-Si, which is upwards of 30% when averaged over its operational range of approximately $300 \leq \lambda \leq 1,100$ nm [45]. The primary method of reducing reflectance is by obscuring the large difference in refractive index between the two materials [46] – Si and air, in this case.

In essence, the application of more than one ARC between the substrate and superstate layers creates a graded refractive index effect. This is the reason multi-layer ARCs are beneficial in systems where a large difference in refractive indices is present [46, 47]. Single layer ARCs are often tuned to minimise reflectance at a wavelength of $\lambda = 600$ nm, as this is the point where spectral irradiance is at its highest [48]. Today, manufacturers commonly use titanium oxide (TiO_2) [49], silicon nitride (SiN_x) [50], and silicon dioxide (SiO_2) [51] as a basis for these layers, with the former having the higher refractive index of the three, and the latter having the lowest. Boron nitride (BNx) is another coating used in Si-based PV, though this is not as typical. Aluminium oxide (Al_2O_3) is used as a passivation layer for solar cells, but can also be used as an ARC simultaneously.

2.1.2 Microscale texturing and Pyramids

The concept of creating surface roughness as a method of increasing the efficiency of solar cells has been around since the mid 20th century. However, the concept of using pyramids to increase the probability of light absorption into a semiconductor substrate did not surface until a time closer to the turn of the century [52]. Microscale pyramids were popularised by researchers at the University of New South Wales (UNSW) in Australia. In 1986, Patrick Campbell and Martin Green explained that traditional square-based pyramids were formed as a result of an anisotropic KOH etching process favouring the <100> crystallographic plane, leaving behind Si along intersecting <111> planes that result in the pyramid shapes on the surface [52]. Several variations of the basic structure have surfaced over the years, including the bipyramid and patch textures [53], however, the most notable variant of the original is the inverted pyramid structure. This is regarded as the most efficient microscale texture in respect to resultant optical path length enhancement [54].

2.2 Nanoporous Films

2.2.1 The Moth–eye Effect

The moth–eye effect is the result pertaining from the sub–wavelength surface patterns present in a moth's eyes [55]. These pseudo-regular protuberance arrays, create a natural highly anti–reflective interface resulting from a subtle graded refractive index formed by them between the eye and the air [56]. Due to their unique optical properties, these structures have been artificially recreated for a wide variety of uses including water–resistant coatings [56], light emitting diodes (LEDs) [57], as well as an effective ARC for the likes of glass [58], PV [57, 59], and low–light cameras[1]. The moth–eye protuberance arrays form the basis of the b-Si anti–reflectance coating, with both interacting with light in the same way.

2.2.2 Black Silicon

2.2.2.1 Summary

Vertically aligned, protruding Si NWs are of interest within the field of nanotechnology as a result of their broad set of applications. This is inclusive of areas within optics [60–

[1] As reported by L. Keesey in the article "Moth's Eye Inspires Critical Component on SOFIA's Newest Instrument" for NASA, Aug. 2017.

62], nanosensors [63], nanoelectronics [64], and solar PV [38,65–67]. These structures are commonly formed through either MACE [68], or one of the following three 'top down' fabrication methods: maskless reactive ion etching (RIE) [69], electron beam lithography (EBL) coupled with RIE [70], or femtosecond laser (FsL) treatment [71]. MACE is also referred to as metal catalysed chemical etching (MCCE), though these refer to the same oxidation-reduction (RedOx) reaction sequence. Each type of etch produces NWs with differing physical properties, though surface heterogeneity is observed consistently between them [72, 73], save EBL [74]. Variations between individual NWs, as well as their tendency to bunch together unpredictably, are visible across many distinct studies [40, 75–77]. Despite this, there have been occasions whereby researchers were able to chemically etch NWs with considerable uniformity through the use of a lower concentration MACE solution for longer periods of exposure [78].

The term 'black' silicon is derived solely from the appearance of said material; a matte black colouring representative of extremely low reflectance across a large proportion of the electromagnetic (EM) spectrum, and over a wider set of incidence angles than larger textures [79]. It has been noted that b-Si exhibits this level of anti–reflectivity due to the unique nanoscale structures being far smaller than the wavelength of incident light [80]. Black silicon can be etched onto any type of silicon wafer, whether that be c-Si or mc-Si. Visual differences are noted between b-Si on these two types of wafer however, where the use of c-Si wafers to host b-Si surfaces gives a uniform appearance and mc-Si gives a patterned look as a result of the non–uniform crystal orientation on the latter [81].

In 2019, Canadian Solar Inc. demonstrated the ability to increase the surface uniformity of mc-Si wafers by combining several etching steps in sequence [37]. It has been argued that extended process workflows significantly increases the cost of manufacturing lower quality devices [82]. Four years earlier, researchers working on this project preceded with a similar premise by creating nanoscale pyramids on mc-Si wafers as a substitute to conventional microscale pyramidal texturing [83]. This form of nanotexturing was shown to be a good compromise between optical and electronic performance; a balance frequently oppressing the adoption of b-Si.

Aside from its applications to solar PV technologies, b-Si proves useful for a variety of other applications. These include high efficiency photodetectors [84,85], high frequency electromagnetics [86], electrical contacts [87], anti-bacterial surfaces [88], and highly sensitive ammonia sensors [89].

2.2.2.2 Manufacturing Techniques

Femtosecond Laser Treatment. Femtosecond laser (FsL) surface treatments were first explored by Eric Mazur in the late 1990s. The work of his group, based at Harvard University, showcased a novel approach to texturing the surface of silicon at both the micro- and nano-scale using extremely short, consecutive, and high-power laser bursts [90]. Originally, this procedure was described as being able to create surface 'spikes' as opposed to the more common NW structures that researchers were familiar with. The observation of the tapered, tall, and nanoparticle-topped structures resulting from FsL led to this naming convention given conventional NWs do not exhibit physical properties like this. These structures are shown in figure 2.1.

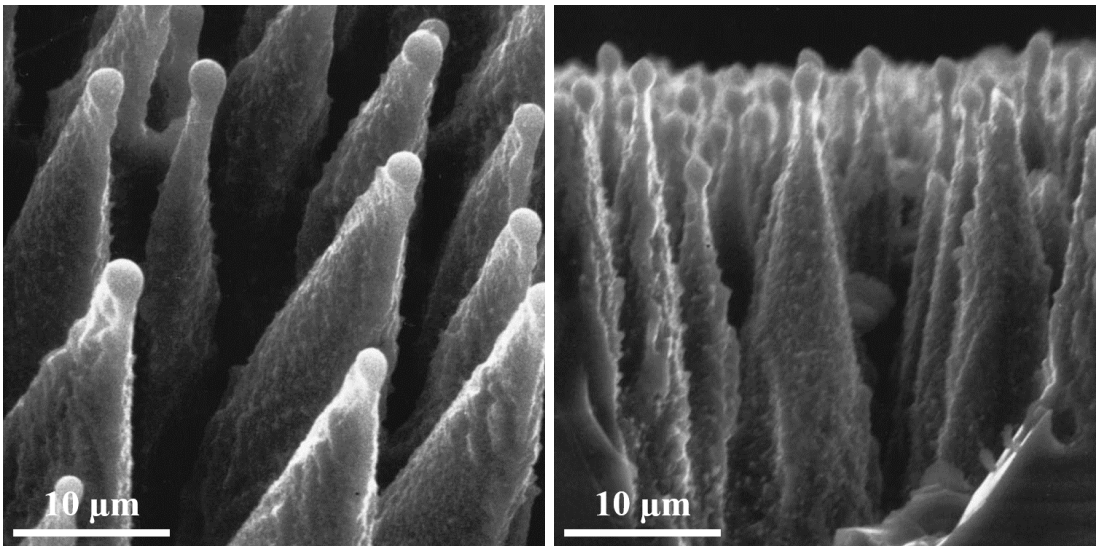

(a) (b)

Figure 2.1: FsL etched nanospikes from above (a) and side-on (b), as formed on <100> c-Si showing the nanoparticle–topped microscale textured features, with nanoscale roughness, resulting from the etch process. Images sourced from [90].

The FsL process works for creating textures like those in figure 2.1 due to the shortness of the laser pulse. Under these conditions the material being etched does not have enough time to respond to the stimulation thermally. Instead, in the case of silicon etching, electrons within the crystalline lattice structure are promoted to the conduction band, whilst the bulk remains unaffected. This causes the covalent bonds within the lattice structure to become unstable and subsequently deform under the stimulation of the laser pulse, resulting in nanoscale surface damage [90, 91].

FsL has been shown to have an impressive level of control over its surface etching

process: the height of the surface spikes [91], their pitch [91,92], surface roughness, and heterogeneity [92] can each be controlled by varying different properties of the inbound electromagnetic (EM) radiation. This level of control yields a significant number of applications resulting from the broad range of surface morphologies it can create. For instance, a great deal of research has gone into using FsL to create unique and strongly hydrophobic surfaces for a variety of different use cases [93,94], and has been used as a drill to create uniform nanoholes for diffraction gratings [95]. Aside from creating b-Si, FsL has been used to create various different Si surface colours aside from black as part of a process control demonstration [71].

Reactive Ion Etching. There are three core types of plasma-based etching; physical ion beam etching (IBE), chemical plasma etching (CPE) and synergetic RIE. In 1995, Henri Jansen discovered the application of RIE in the creation of b-Si [96]. The work reported by Jansen et al. demonstrated so-called nanoscale 'grass' representative of NWs manufactured using the top-down approach. The process uses sulphur hexafluoride (SF_6) alongside oxygen (O_2) and fluoroform (CHF_3), each in gaseous form, and typically at low temperatures. The material to be etched, silicon in this case, is applied with an electrical bias and is subsequently bombarded with ions causing nanoscopic damage to its surface; similar in principle to FsL techniques. It is possible to increase or decrease the etch rate of RIE by varying the applied bias, where higher bias values result in a greater attractive force, and therefore speed, of the ions creating deeper surface damage far quicker.

Work using RIE has shown the process as being able to create nanoscale pyramids, as opposed to the commonplace microscale versions, when methane (CH_4) is added to the SF_6/O_2 mixture [97]. It has been shown that good levels of anti-reflectance are present in b-Si samples created using RIE regardless of crystallographic orientation of the substrate material [98], suggesting greater applicability to creating uniform mc-Si wafers than other etching methods.

RIE systems are readily available and are generally compatible with industrial processes [99], whereby such systems allow for a high throughput of silicon at a large scale. It is important to realise that RIE causes significant damage to a silicon substrate during its use for nanoscale etching. The result of this damage is seen as a significant drop in minority carrier lifetime, τ, within around 20 nm of the substrate surface [72]. This notably creates issues with large scale process optimisation [100] and can cause

the costs associated with the use of RIE to rise dramatically. Furthermore, the use of SF_6, a dielectric medium with a breakdown potential far greater than air, raises significant environmental concerns regardless of its application [101]. SF_6 is an inert gas, used predominantly in the power and semiconductor industries, but has become highly regulated with its use significantly restricted. This is due to the gas's profound impact toward the greenhouse effect; SF_6 is almost $23,000\times$ better at trapping the heat-building IR region of the irradiance spectrum [101].

Metal Assisted Chemical Etching. The focus of this work is through the application of MACE, specifically with silver (Ag), to create NW structures given it is far more cost effective [73], controllable and faster than the previously outlined etching methods. It works with existing production flows with few modifications needed [76]. Copper (Cu) can be used in the MACE process in lieu of Ag. This holds a particular advantage over Ag as Cu produces far more uniform NWs across crystallographic orientations due to its lower ReDox potential. This makes it particularly advantageous to MACE on mc-Si wafers [102]. Conversely, Cu is not typically compatible with industrial processes as it is a considerable contaminant to other processes in a cleanroom environment. An example of Si NWs created using a MACE process featuring Ag can be seen in figure 2.2.

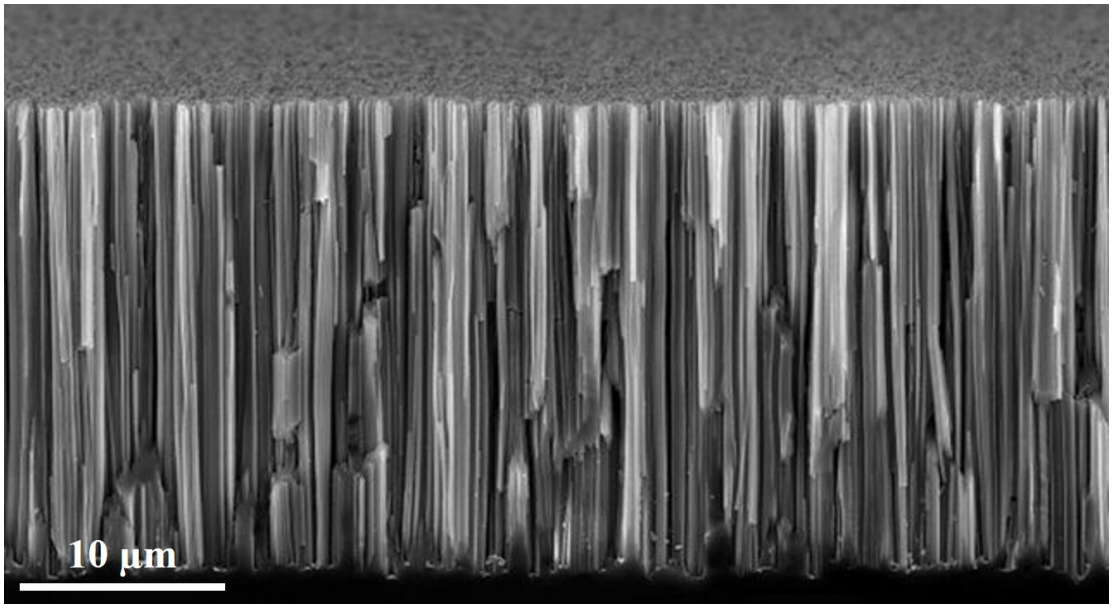

Figure 2.2: Side-on view of b-Si NWs created using an Ag-based MACE procedure. Image sourced from [103].

Despite the numerous advantages of MACE, it is considerably dangerous due to the

inclusion of hydrofluoric (HF) acid and nitric acid (HNO_3). It is not considered to be environmentally friendly due to the wastage of chemicals and the acidity of the HF and HNO_3 components of the etching solution [77]. It is also notable that the use of Ag makes Ag-based MACE for PV expensive. As an alternative, Cu has been used in-situ with Ag in an effort to reduce the costs associated with the process [104]. Outlined here is an exemplar MACE process as conducted by Li et al. [105]. Firstly, a polished Si wafer is cleaned using a HF acid bath for several minutes, before then being placed into an etching solution containing a mixture of HF acid and silver nitrate ($AgNO_3$). Here, the Ag acts as a catalyst for injecting positive charge into the Si substrate, causing the substrate beneath to dissolve and the Ag particle to sink into the surface. The structures remaining on the removal of the Ag dendrites are Si NWs created through the top-down approach. The chemical reaction for this process can be seen in equation (2.1).

$$18\,HF + 4\,HNO_3 + 3\,Si \longrightarrow 3\,H_2(SiF_6) + 4\,NO + 8\,H_2O \tag{2.1}$$

After etching with MACE for the desired time, the Si wafer is cleaned to remove the HF acid, preventing any further etching. This is achieved by first flushing the Si through a bath of deionised water (diH_2O) to prevent the dislocation of any surface NWs. To remove the Ag dendrites embedded on the surface, the wafer is then placed into a solution of 50% HNO_3 and 50% water (by volume). Finally, the surface is then flushed through another diH_2O bath to remove any remaining HNO_3.

MACE is reported to be dependent on temperature, whereby higher temperatures have been noted to cause a smoother appearance to the etched NWs, reducing their anti-reflectance properties considerably [106]. This same paper outlined that, above temperatures of 65 °C, a porous layer was observed in absence of any NWs. A further dependency for MACE-based etching onto Si is crystallographic orientation [107]. This is why Ag-MACE in particular does not perform sufficiently well without supplementary help on mc-Si wafers [81], where the crystal orientation varies throughout the substrate.

2.2.2.3 Black Silicon for Solar Photovoltaics

Despite its unmatched optical benefits, b-Si has been difficult to turn into a competitive PV device with efficiencies matching or exceeding the more common microscale pyramidal texturing. This is because b-Si suffers extensively from higher levels of carrier recombination at the surface as a result of its far larger surface area [65] and defects

resulting from the etching process. The use of interdigitated back contacts (IBCs) as opposed to front-contacts has been shown to prevent Auger recombination by moving the highly-doped regions away from the NWs [66,108]. When conventional passivation is sought after, such as thermal silicon dioxide (SiO_2) or plasma enhanced chemical vapour deposition (PECVD), issues arise with the complex nature of NW surface morphology. Alternatives have been explored to mitigate the issues presented in this situation.

Savin et al. [66] showcased an IBC b-Si cell with an efficiency of over 22%. This was achieved by exploring the impact of an applied aluminium oxide (Al_2O_3) passivation layer, 20 nm thick, via atomic layer deposition (ALD). The effects of the Al_2O_3 layer could be quantified by measuring the surface recombination velocity, S_{eff} (equation (2.2)). A low value for S_{eff} is critical for higher cell performance, and thus it can be said that lower values represent greater surface passivation quality.

$$S_{eff} = \frac{W}{2}\left(\frac{1}{\tau_{eff}} - \frac{1}{\tau_i}\right) \tag{2.2}$$

Here, W is the thickness of the silicon wafer, τ_{eff} is the measured effective carrier lifetime and τ_i is the intrinsic carrier lifetime. Similarly, Rahman *et al.* [67] also reported the successful application of Al_2O_3 via ALD on a MACE textured surface to achieve, in theory, a significant increase in solar cell efficiency to beyond 21%. It has been shown to become a balancing act between getting solid optical performance and good electronic performance however, given any method of surface passivation can negate against b-Si's anti-reflectivity [109]. Conversely, Savin *et al.* have also shown that, given an optimum thickness of the dielectric coating has been achieved, surface passivation can actually aid optical performance [66].

2.3 Computational Modelling of Solar Technologies

2.3.1 The Transfer Matrix and Ray Tracing

The transfer matrix method (TMM) is one of the simplest forms of modelling used in applications attaining to the wave propagation characteristics for both optics and acoustics. The Fresnel equations describe how a ray of light is reflected and transmitted at a single interface between two different media. However, with three or more media there are secondary reflections and transmissions that need to be considered. TMM functions along only one dimension, and subsequently any media with a textured surface cannot be modelled using this method. As a result, TMM is far less often used within

the field at present, with its application primarily for analysing the path of light and light-trapping within thin films and anti-reflectance coatings.

Ray tracing (RT) methods involve simulating the transient propagation of optical rays with respect to a given structure. Such structures can be of any shape, but must be a considerable degree larger in dimensions than the wavelength of light simulated. As with TMM, RT also uses the Fresnel equations to determine the response of light within both 2- and 3-D domains. It is also common to see RT methods incorporate the TMM into its computations. Such studies are highly beneficial for microscale structures in solar PV, such as pyramidal textures. The assumptions made using RT do not hold for sufficiently small structures like NWs and require the use of EM wave optics (EMWO) instead to ensure their correct modelling.

2.3.2 The Finite Methods

Modern computational and mathematical methods permit us to recreate many different physical conditions to model various systems accurately. The finite modelling methods are at the forefront of this area with unparalleled accuracy, robustness, and versatility. In particular, the finite element method (FEM) has been hailed as one of the most powerful tools in EMWO [110,111] due to the unmatched level of control over its simulation domains, yielded in-part due to its adaptive free-tetrahedral approach to meshing. The FEM has also been showcased to work well for fluid dynamics, thermal propagation, and structural mechanics [112]. Modelling such problems using this method heralded an interest in the late 1990s, whereby increasingly more complex structures needed to be modelled, and often in-place of their fabrication [112].

The finite difference time domain (FDTD) method is actively used within the field and is often referred to as the most preferred method by researchers. Unlike TMM and RT, FDTD is highly versatile and can approach far more complex physics and multiphysics problems with relative ease [111]. FDTD can use 3-D modelling techniques to create far more intricate structures making it the ideal choice for modelling the microscale and nanoscale surfaces present on patterned solar PV devices [113]. The rudimentary-by-comparison effective index method (EIM) has also been applied to NW structures; results were reported to be less accurate than FDTD [114].

The EIM assumes that EM waves propagate through a medium of approximated refractive index taken as a weighted spatial average of the surrounding area [115]. This modelling method is beneficial for nanophotonic applications. Such examples include

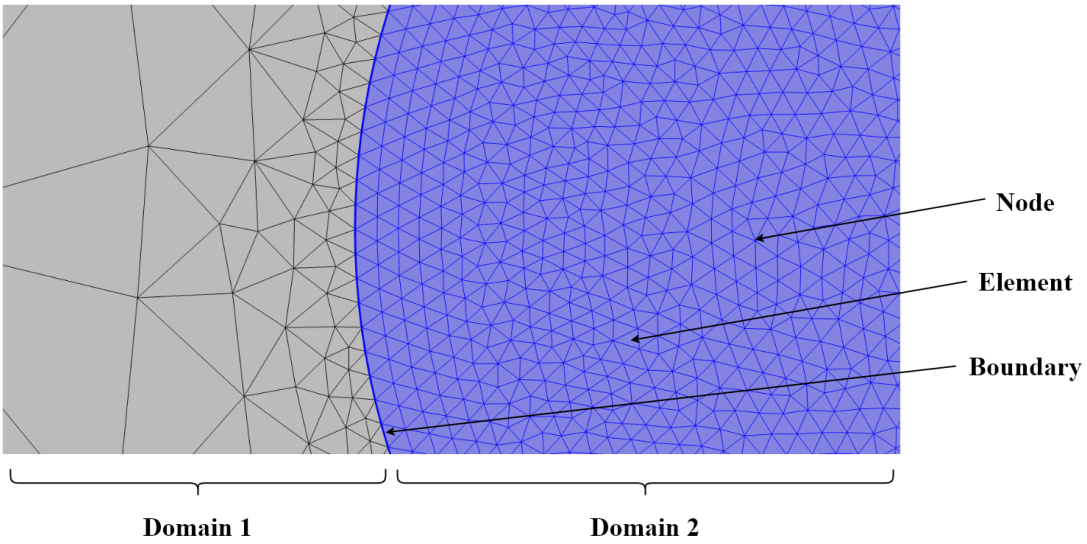

Figure 2.3: An example of a tetrahedral mesh employed using FEM modelling.

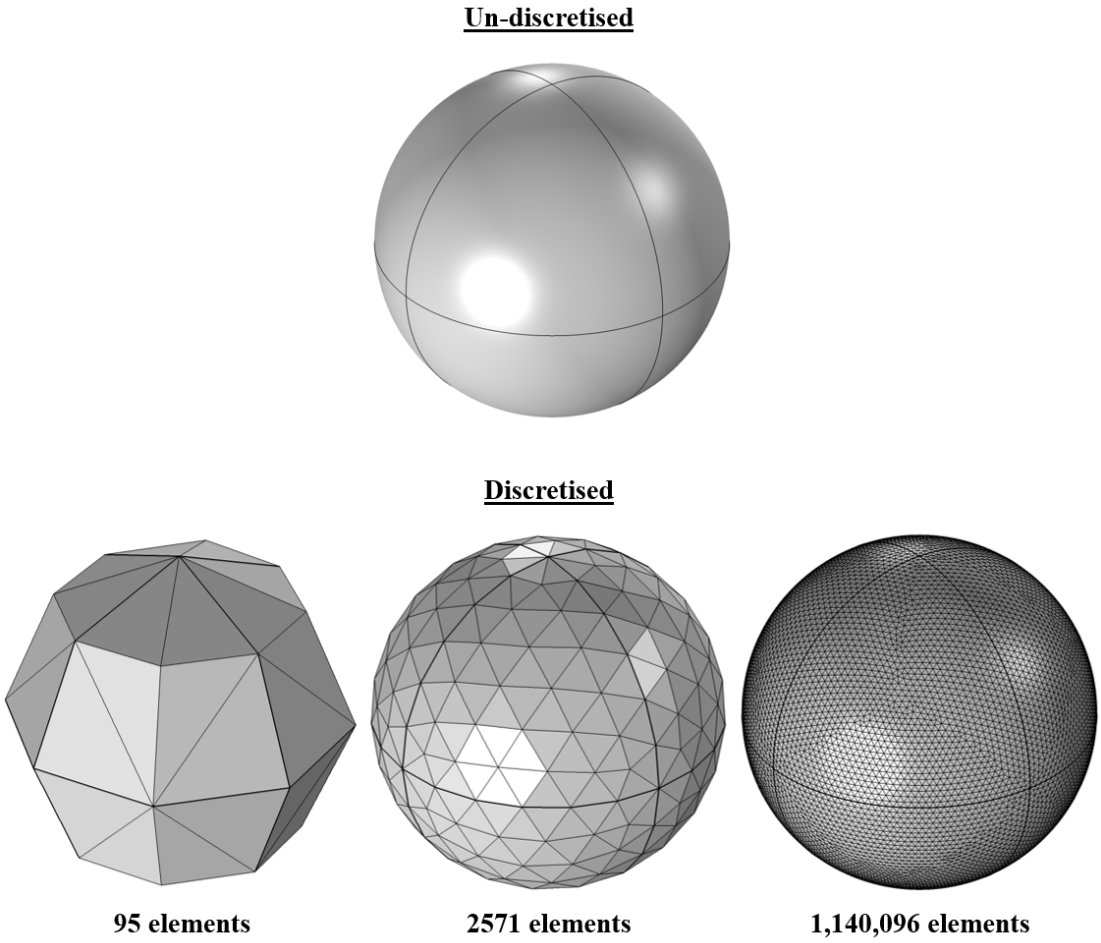

Figure 2.4: Discretising a completely spherical object, with infinite element regression, using a mesh overlay of varying element density.

optical waveguides [116–118], semiconductor lasers [119], and plasmonics [120,121]. This modelling method only accounts for a refractive index gradient in one dimension, making it useful in the simulation of nanoscale textures in the form of applied thin film coatings. An example of such was explored by Rahman and Boden for the anti-reflectivity of a hb-Si surface when coupled with FDTD methods, though showcased questionable accuracy [114].

Analytical approaches to understanding how the universe works introduces us to a vast array of mathematical problems representative of the laws of physics. These problems are often expressed as partial differential equations (PDEs). The FEM confronts many of these problems using a largely broken-down, estimated approach by employing various types of discretisation; methods used to approximate PDEs. Model geometries constructed for the FEM are, similarly to FDTD, mapped with a mesh used to break the geometry down into solvable components. In this case however, over using a cubic tensor grid like that employed by the FDTD method, a free and adaptive tetrahedral grid is used instead. Such a meshing strategy is noted to prevent aliasing from the discretisation process. Typically, a mesh consists of four key features: domains, elements, boundaries, and nodes. These features are outlined with respect to their descending comparative size, and is shown in figure 2.3.

The FEM is renowned for being sensitive to the density of this mesh, and thus the degree of discretisation used within the model. For instance, a mesh density set too low will result in a lack of simulation elements. Essentially, these elements can be compared in likeness to pixels on an electronic display. Too few elements (too little discretisation) will cause the model to alias and smooth shapes to be overly-deformed; pixelation causes identical issues in pictures and videos [122,123]. This is demonstrated in figure 2.4. Conversely, too many elements (or over-discretisation) will cause a huge number of elements in need of solving resulting in extensive simulation runtime and resource requirements [110].

Naturally, the more a given geometry is aliased, the lower the accuracy of the simulation. Finding a balance between accuracy and runtime is a critical component of the FEM, but it can still take considerable time to find the optimal combination through convergence analyses and trial-and-error. This balance can become complex to define since runtime also relies heavily on system architecture. Parallel or multi-parallel systems will always require a different level of optimisation given their utilisation of a far higher throughput. However, a linear relationship between mesh density and runtime can be seen for serial

systems. For example, as seen in figure 2.4, spherical likeliness is acceptable with only $2,571$ elements making up the model. The computation time of the model discretised to $1,140,096$ elements using a single-threaded setup will be in excess of $440\times$ more than that of only 95 elements. Critically, it is important to realise that no further accuracy is guaranteed once a critical number of elements has been reached [123].

The FEM, much like FDTD, can be either 2- or 3-D, and studied using eigenvalue, transient, or time-invariant studies. It was first reported to have been successfully used for modelling b-Si NWs in 2009 by Altermatt et al. using a partially pseudo-randomised geometry configuration [123]. This model was configured to have rounded-tops to each NW, and to tilt each one differently in a random direction. The position of each was also randomised but contained within a predefined area, and the injected wavelengths were only 600, 800, and $1,000$ nm due to computational restrictions. Furthermore, NWs were not rendered when intersecting the periodic boundary conditions.

Attempts have been made to model b-Si NWs with largely varying accuracy as a result of their apparent disorder. Such attempts include using the EIM [114], FDTD method [124], and FEM [123, 125]. All computational methods, due to their artificial mathematical constructs, rely on periodicity to some degree. Truly heterogeneous structures, much like Si NWs, are impossible to simulate with complete accuracy as a result of this dependency.

2.4 Reflectance, Absorption, and Transmission of Light

2.4.1 Quantification

Reflectance, absorption, and transmission (RAT) measurements have a considerable weighting on the performance metrics for all kinds of solar PV devices. All three of these characteristics are commonly grouped together due to their dependency on one another. This relationship is outlined in (2.3).

$$R + a + T = 1 \tag{2.3}$$

Here, R represents light reflected off the material surface, a represents the intensity of light absorbed in the supporting medium, and T is the intensity of light that passes through the medium, exiting on the other side. Each of these properties must sum to unity, that is to say the light originally incident on the medium is equal in intensity to the sum of that reflected from, absorbed by, and transmitted through that medium.

Spectrophotometry is a branch of optics relating to the measurement of these three properties, and there are several different technologies that can be used to accomplish this: integrating spheres [126], reflectance probes [127], charge-coupled devices (CCDs) [128], and photodiode arrays [129]. Which of these is used to determine the RAT metrics depends on the media being measured. For example, systems built around an integrating sphere are fundamentally limited to smaller samples – attempting to measure large solar or structured glass panels within a spherical body would require a very large diameter, resulting in an incredibly complex and expensive system. Instead, camera–based measurement or reflectance probes would be more applicable.

Integrating spheres, as the name suggests, collect light reflected from a sample and integrate it about the whole sphere. This creates a uniform illumination effect across the entirety of the inner surface, which in–turn can be sampled by a sensor. This sensor must be shielded by a baffle that prevents light from passing from the sample to the sensor without first being integrated. Allowing direct reflection to impact the sensor prior to integration will skew the sample's RAT data. Conversely, methods such as the CCD and reflectance probe offer a simple and cost–effective way to quantify reflectance resolved against relative coordinates. This means that reflectance can be mapped across a spatial geometry to determine uniformity or surface defects, not only for solar PV, but also for fields such as, ecology [130], biology, and medicine [131, 132]. These methodologies require movement of the sensor, manually or automatically, across the surface of a sample.

RAT measurements are notoriously difficult to perform due to the high degree of calibration and reference required to complete it accurately. Typically, a sample of known reflectance over a set wavelength range, ratified by a certification body, is required. This sample must be used as a reference in the determination of a sample's reflectance. Two approaches are available here dependant on what is being used as the reference. If the reference sample is of known reflectance, that is to say a reflectance standard, then the absolute reflectance of the measured sample can be quantified. If the reflectance of the reference sample is unknown, then the relative reflectance of the measured sample with respect to the reference can be shown instead. For instance, if the measured reflectance of the sample is 50% relative to a 10% reflectance standard, then the absolute reflectance of the sample is 5%. Conversely, if we were to measure the same sample against the same reference, but we did not know the reference had a reflectance of 10%, we can only show that the measured sample has a relative reflectance of 50% with respect to

the reference.

2.4.2 Resolution and Limitations

The accurate resolution of reflectance is dependent on the consideration of several different factors: polarisation, angle of incidence, and wavelength. Very few systems are capable of resolving against all simultaneously. Instead, a typical system will set one or two of these properties as a constant and vary those remaining. Notably, angle of incidence is held at 8° — an angle that has become a standard for all reflectance measurements. Holding samples in position permitting this angle, slightly offset from direct normal incidence, provides several benefits. It enables reflected light to be measured far easier, given that, at direct normal incidence, input light will be reflected straight back along the entry path, away from the sensor medium, on a return path to the source as per the Fresnel equations. While this has been shown to remove the direct component of reflection, leaving only scattered light in the system, it permits the reflected light to interfere with that of the input. In any system measuring one or more of the RAT metrics, stable input light intensity is essential for reliable data collection.

While measurements at 8° have become standard practice, those resolved against variable angles are rare. Very few systems are capable of performing variable angle measurements due to the complexity of the measurement process and incompatibility with the measurement medium [133]. Goniophotometric measurements are slightly better suited for variable angle reflectance in the absence of an equivalent spectrophotometry system, despite only being able to measure one angle of reflection at a time due to the lack of an integrating sphere. Reflectance probes tend to have a selection of two angles to use for incident light: direct normal and 45° [133, 134].

Measurement resolution in the wavelength domain, independent of system topology, is dictated by the type of light source used and whether a narrow–band filter (monochromator) is fitted between the source and system. A monochromator is an opto–mechanical device that takes light of distributed wavelength emission and passes one small window of wavelengths (typically a small range about a single wavelength) through it based on the spatial rotation of its diffraction grating. A diagram of this is shown in figure 2.5. The use of a monochromator in RAT measurements permits only a single wavelength of light to be present in the system at any one time, requiring the monochromator to cycle through the appropriate wavelength range (based on the emission spectrum of the light source present) in order to achieve a complete reflectance spectrum.

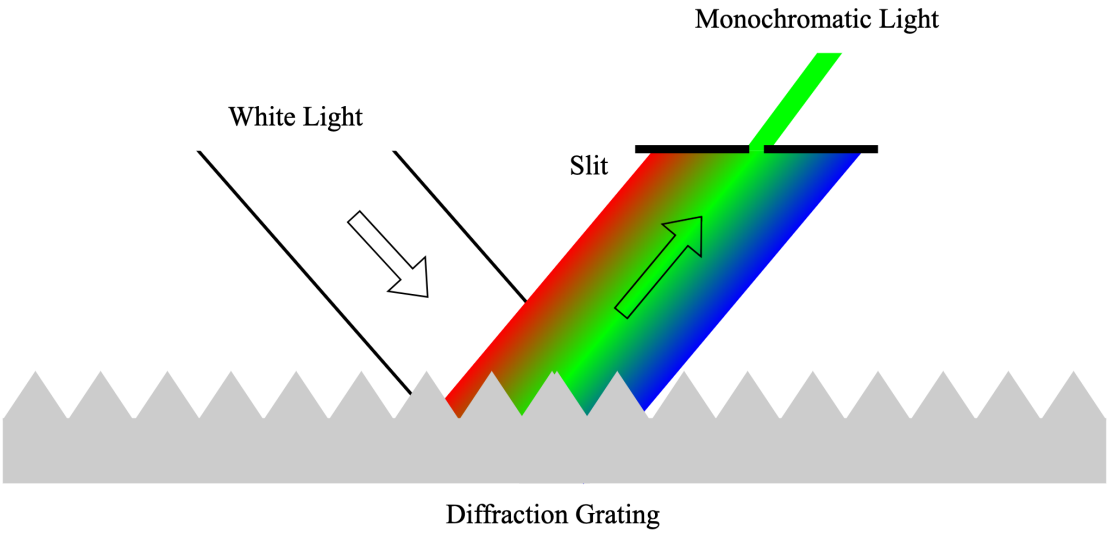

Figure 2.5: An overview of how a typical diffraction grating monochromator is able to split the wavelengths of light and transmit a single colour.

2.5 Conclusions

Reported here is a review of several key topics in literature, including: anti–reflectance for PV, b-Si fabrication methodologies, computational modelling for micro– and nano–scale domains, as well as current optical characterisation technologies and their associated characteristics. There are several of each technologies seen in circulation today, with the prospect of merging pyramids and b-Si textures to form hb-Si relatively unexplored. A summary of the three core manufacturing methods for b-Si can been seen in table 2.1.

A key note to take away from this review is the relationship between topology controllability and manufacturing expense; more controllability is considerably more expensive, and generally slower than other alternatives. We have seen that FsL is the most controllable process, whilst MACE is the least. Addressing the issue of controllability in MACE manufacturing workflows will open a newer, inexpensive avenue to manufacture specialised designs of b-Si, and subsequently hb-Si on the production line. Pyramid texturing for solar cells has been around for over half a century and is well–founded as an effective and efficient standard for creating highly anti–reflective surfaces when paired with an approrpiate ARC. This forms the main competition to hb-Si. The widely–used KOH etching process will be employed for the manufacture of all pyramids studied in this work, allowing the MACE processing to be 'dropped' onto the existing etching process already in–place in industry.

Table 2.1: Summarising the advantages and disadvantages of each b-Si manufacturing method as collated from the review of literature.

FsL	**RIE**
+ Variety of textures possible	– Expensive
– Very slow	– Complex
– Expensive	– Slower than MACE
– Incompatible with production lines	– Damages shallow substrate

MACE
+ Inexpensive
+ Easily integrated into production line
– Lacking controllability
– Wasteful by default

It can be seen from previous work that the FEM presents the best way to model the structures indicative of stochastic b-Si surfaces. Pseudo–randomisation and model size remains a key challenge for these structures, whereby wave–based optical models need to be used over ray tracing due to the relative scale between the EM radiation and feature size. Creating a larger simulation model, which would be more indicative of a b-Si texture, is extremely difficult due to the computational expense required of such a model. As such, very little work has been done in this regard and showcases the need to address the gap in research here.

Optical characterisation systems are vastly different from one another, and utilise different areas of optical physics in order to determine RAT characteristics. Literature has shown the versatility of these measurements, going far beyond the field of solar PV and into areas such as glass design, colour analysis, rapid ecological surveys, and spatial reflectance. Spectrophotometric RAT measurements resolved against angle are rare, with very few systems actively reported to be able to complete these complex measurements accurately. The adoption and uptake of nanoscale textures, such as b-Si, present a need to branch into these studies due to the unique way they have been shown to interact with light. Reflectance over angle is unique and distinctive for b-Si, and, as such, a key research topic and area of significance has come to light. It can be concluded that the angular response of b-Si, and hb-Si, is what would push the texture above its closest competition: the pyramidal texture with an ARC.

Chapter 3

Hybrid Black Silicon by Sequential Chemical Etching

3.1 Introduction

Showcased here is the process behind producing the multi-scale hb-Si surfaces that are the subject of this work. These surfaces comprise of a planar Si wafer etched to form a combination of both anisotropic pyramidal textures and stochastic vertically aligned NWs, in said order. Such surfaces offer remarkable levels of anti-reflectance through the combination of both offset reflection from the facets of the pyramids and the graded refractive index formed by the NW structures. A heated KOH etch is first used to form microscale pyramids – a typical and well known process in the manufacture of optically efficient PV. A subsequent top-down Ag-MACE process is then employed to etch NWs into the facets of those pyramids, yielding a 'grassy hill' like structure.

MACE works as either a single– or dual–step process. The former is a simplified version of the latter, whereby nucleation of the silicon surface, in this case by Ag, is performed in conjunction with the etching process in a single solution. Dual–step processes require nucleation of the surface to be performed before the sample is placed into an etching solution. This can be achieved via sputtering or evaporation techniques. In theory, nucleation of the surface through sputtering will enable greater control over the etched surface topology, with particular emphasis on surface uniformity. The single–step process arbitrarily attracts Ag particles to the Si surface resulting from fluctuations within the solution make–up. This causes parts of the surface to nucleate, and subsequently etch, faster than others. Despite this apparent pitfall, the single–step MACE process

is used to manufacture the samples shown here, being the more applicable to industry as a result of its simplicity, compatibility, and speed. Furthermore, heterogeneity offers enhanced optical response characteristics over homogeneous equivalents.

Each etching process, be it the alkali-based KOH etch, or the acid-based MACE, have several constituent properties that will have a considerable impact on the features of their resultant structures. This effect is amplified when combining the processes together, as with hb-Si. By using an industry standard and time–proven recipe for pyramidal textures, we are able to reliably manufacture these topologies whilst maintaining compatibility with existing manufacturing processes. Similarly, an optimal and functional recipe was determined for the manufacture of b-Si NWs using single–step MACE by T. E. Scheul [135] during the project preceding that reported here. In the case of the MACE, etch time can be varied reliably to adjust the average height of the NWs as seen through scanning electron microscopy (SEM).

A fixed, standard pyramid size, as used by Norwegian solar manufacturer NorSun[1], is subject to various periods of MACE, and the height of NWs recorded. This is subsequently compared back to a separate study, identical in principle, but instead carried out on planar c-Si. A differential relationship is formed between etching these nanostructures on the planar and pre-textured Si wafers, and effect on topology is recorded using SEM and surface uniformity evaluation by image processing. These samples will form the basis for the work reported in chapter 5, where advanced characterisation techniques showcase the unique optical characteristics of each topological hb-Si variant shown here. The primary area of interest post–manufacture for these surfaces is in their optical anti-reflectance properties. Specifically, how these surfaces respond over broadband EM illumination for different polarisations and angles of incidence. The wavelength range of interest relates to the electronic response of Si, which is predominant from the NUV below around 400 nm, to the NIR above around $1,050$ nm. At low photonic energy levels, Si becomes transparent to incident EM waves and subsequently does not interact with them. At sufficiently high energy levels however, Si appears opaque to incident waves and will either reflect them away from, or terminate them within a *very* small depth of, the surface. This causes e-h pair generation in an area considerably further away from the junction in which they must be collected than with other, longer wavelengths of light. The probability of recombination at the surface is also considerably higher at these shallow depths, greatly increasing the probability of

[1] https://www.norsun.no

carrier recombination, and subsequently lower power generation, at these high energy levels.

The surfaces of a Si substrate are important interfaces that need to be manufactured carefully when the aim of a device is to perform well electronically as well as optically. Due to the optical focus of these investigations, the requirement for high quality, appropriately doped EG-Si was moot. In consequence, the Si used here is double side polished (DSP), test grade (TG), <100> orientation c-Si. TG-Si wafers have significant impurities within their bulk and, as a result, are not suitable for use in electronic studies. Despite this, the ability to passivate the surface of the sample or wafer is important to consider at all times.

Mono-crystalline silicon contains a periodic crystalline lattice network, meaning that its surface will be the natural termination of this periodic structure. The result of this is are periodic vacant bonds – Si atoms unable to bond with a lack of neighbouring atoms [42]. This introduces discrete energy levels into the lattice system that sit between the valence, E_v, and conduction, E_c, bands' respective energy levels. Any e-h pairs generated are capable of using these inter–band energy levels to recombine far more readily through Shockley–Read–Hall recombination [42]. This is *highly* undesirable for PV applications, where carrier lifetime prior to recombination needs to be as long as possible, greatly increasing the chances of e-h pair collection. The presence of these energy levels reduces this likelihood, and as such, surface passivation is introduced to the surface to reduce the chances of unwanted recombination at the surface of the substrate.

It should be noted that the larger the surface area of a PV cell, the greater the need for this passivation layer. The etching of black silicon textures creates a very high surface area. This is also true, to a greater degree, for hb-Si surfaces. How readily any of the surface topologies created here can be passivated must be considered, paying particular attention as to whether one can be applied uniformly *around* the individual NWs, as well as on top of them. As found in chapter 2, ALD has shown significant promise in this area, and will be kept in mind going forward with these investigations.

3.2 Experimental Methodology

3.2.1 Wafer Preparation

Before any chemical etching occurs, the samples are subject to a peroxymonosulfuric acid (H_2SO_5) etch. This is often referred to as the 'piranha' etch and typically removes

any organic residue on the surface, as well as dust and other contaminants. Piranha is commonly a solution of 75 vol% sulphuric acid (H_2SO_4) and 25 vol% hydrogen peroxide (H_2O_2), *extremely* dangerous to organic matter, and highly explosive. H_2SO_5 is one of the strongest oxidisers known to exist. As a result, it increases the surface tension of processed samples considerably, resulting in a surface that is now hydrophilic.

High surface tension is counter-productive in regards to most chemical reactions, essentially slowing them down, or preventing them from working at all. Before any texturing takes place, the surface oxide, the cause of the surface tension, must be stripped. This is achieved through the use of an 6.25 vol% HF acid dip. It is important to note that water (H_2O) is a solvent and will cause the oxidation of the surface of any sample submerged within it. As a result, only deionised water (diH_2O) is used to considerably reduce the risk of reoxidation post-piranha etch. It is also crucial that any sample remains submerged and unexposed to air to prevent both particulates from settling on the surface, as well as accelerated re–oxidisation, subsequently interfering with subsequent etch processes.

3.2.2 Microscale Pyramids by Potassium Hydroxide Etching

The KOH etch is relatively standard across industry and routinely varies only in strength based on the required use. Higher concentrations of KOH erode the surface far more evenly, whilst lower concentrations exhibit the anisotropic etch on Si. In the realm of solar PV, the etch typically used to create the anti–reflectance textures seen on solar cells consists of 3 vol% KOH and 1 vol% isopropyl alcohol (C_3H_8O), with the remainder composed of diH_2O. C_3H_8O is used here as a wetting agent that decreases the surface tension present between the solution and the sample. By decreasing this surface tension, the solution in which a Si sample resides is capable of making greater contact with the surface.

High surface tension, in essence, 'pushes' the solution away from the surface to be etched. This in–turn causes significant uniformity issues with pyramidal coverage, where planar areas of the Si substrate can be seen alongside textured areas. The ratio between these two areas across the sample surface forms the planar fraction, PF, as shown in equation (3.1). Here, a_p and a_t are the planar and textured surface areas, respectively.

$$\mathrm{PF} = \frac{a_p}{a_p + a_t} \tag{3.1}$$

Equation (3.1) forms an important metric for pyramidal textures, whereby a planar surface would be denoted by PF = 1, and a wholly textured surface would be shown with a value of PF = 0, the latter being the ideal. In general, the lower the value of PF, the higher the quality of the sample, and the lower the average reflectivity. In the case of the pyramidal wafers used in this work, PF $\rightarrow$ 0 due to the robustness of the large–scale manufacturing and time–proven recipe employed in their creation. This has been corroborated with the use of SEM imagery, where a number of surface samples were captured and analysed to provide an overall approximation. Planar regions on the substrate can be a result of any combination of the following:

- Inadequate cleaning of the sample prior to the etch;
- Incorrect concentration of KOH;
- No C_3H_8O reagent present;
- Solution temperature is out of range;
- The etch time is insufficient.

The solution of KOH, C_3H_8O, and diH_2O must be heated to and maintained at a constant temperature of 75 °C – a point at which the anisotropic etch rate is easily anticipated. Automated mechanical stirring is also run constantly to prevent the disassociation of KOH and diH_2O, although heat-generated disturbances in the solution can also act as a passive mechanism to achieve the same (to a lesser degree).

3.2.3 Silicon Nanowires by Metal Assisted Chemical Etching

3.2.3.1 Oxidation–reduction Reactions

Oxidation–reduction reactions, commonly dubbed 'RedOx' reactions, are a primary source of energy for many systems of both natural and artificial origin. Such reactions are a chemical process by which electrons are transferred between different elements, involving the loss of electrons from one (now oxidised) element, and the subsequent gain of electrons in another (now reduced) element.

$$\begin{aligned} H_2 + F_2 &\longrightarrow 2\,H^+ + F_2 + 2\,e^- \\ &\longrightarrow 2\,H^+ + 2\,F^- \\ &\longrightarrow 2\,HF \end{aligned} \tag{3.2}$$

Equation (3.2) demonstrates how hydrogen fluoride (HF) is formed through a RedOx reaction between the separated elements, hydrogen (H) and fluorine (F). In this case, H atoms act as the reducing agent by losing a pair of electrons and allowing the F atoms to be reduced as a result. Meanwhile, F atoms act as the oxidising agent, given that they accept the electron pair yielded by the H atom, reducing itself, but allowing the H atoms to oxidise. Such principles are the backbone of the MACE process, and are what cause the resultant structures.

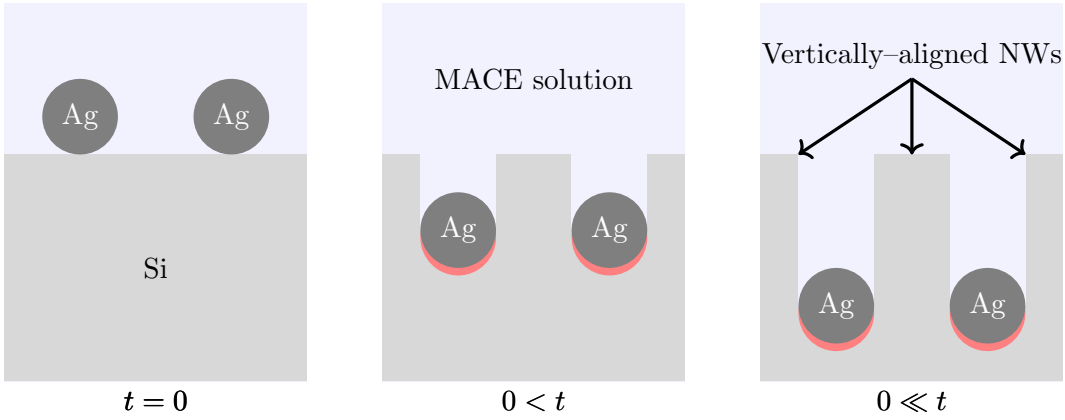

Figure 3.1: Demonstrating how Ag-based MACE acts on a planar Si surface to create b-Si NWs. The dissolution of Si is highlighted in red, underneath the Ag particle causing said dissolution.

In the case of MACE, a solution of HF acid, diH_2O, and $AgNO_3$ forms the basis of the reaction sequence. The oxidising and reducing agents in this situation are HF and Ag respectively, where the Ag particles catalyse the reaction at their surface. The result of this is an accelerated RedOx process about the silver, which also happen to be resting on the Si wafer's surface. As the oxidising agent, the HF in the MACE solution accepts electrons from the reducing agent, Ag, essentially exchanging holes in its place as per the conservation of charge. Now, with an excess of holes, the silver particles dissolve the Si beneath them, and subsequently sink into the surface. The reason for this dissolution comes from the Ag injecting the holes it has received into the crystallographic plane of Si, weakening it, and making it susceptible to the acidity of the HF acid. This process is visualised in figure 3.1. The etching will continue until the oxidising agent has been flushed from the solution. Removal of the Ag particles left in–situ require a separate instance of chemical processing.

3.2.3.2 Chemical Composition and Considerations

The chemical composition of the MACE recipe used in this work is held constant with the proportions 0.12 vol% $AgNO_3$, 24.97 vol% HF, and 74.91 vol% diH_2O. It should be noted that $AgNO_3$ is highly sensitive to light, and will deteriorate when subject to it for extensive periods of time. As a result of this, it is packaged in a light attenuating glass bottle with limited translucency, bordering on the opaque. With this in mind, $AgNO_3$ must be decanted as appropriate only when it is required to be added to the MACE solution. Decanting too soon would result in light–induced degradation that will have an adverse effect on the etch process.

The reagent in MACE, that is to say HF in this case, is an acid that is part of the hydrohalic group. Unlike the other members of this group, HF is a weak acid despite its pH of $\sim$ 3.2. Despite this, it is an extremely dangerous substance that must be handled with the strictest of control at all times. In the dispensing of HF for the MACE solution outlined above, a buffered and controlled volume of 10 ml/cycle is dispensed from a bottle using a Hirschmann Ceramus®[2] dispenser configuration. This allows for highly precise dispensing in–line with the recipe, but removes a large proportion of the risks associated with the handling of HF acid.

3.2.3.3 Sample Handling and Positioning

Samples subject to the MACE will have NW topological structures. The Si NW is *very* fragile, and can be damaged easily (typically unintentionally). Drying the sample post–etch using forced–air evaporation, picking the sample up using tweezers, and laying face–down in a sample container with excessive pressure, are all ways to rip, sheer, or crush the structures just made through MACE. Sample positioning is also important in relation to the outcome of MACE [135,136]. For instance, vertical alignment, as opposed to allowing the sample to fall face–down in the solution medium, allows for greater uniformity among the NWs etched. This is likely related to the transient separation between the Ag particles and diH_2O. Contrary to oil and water, whereby oil will separate and sit on top, Ag will sink underneath diH_2O. If a sample is permitted to remain face–down at the bottom of the etching medium, these particles will slowly accumulate on the surface throughout the etch, as opposed to only at the beginning. This will create significant disorder resulting in considerable non–uniformity. In order to address these points, several things need to be implemented both during and after

[2] https://www.hirschmann-laborgeraete.de/en/artikelgruppe/93100

the etch process.

To ensure the sample remains vertical for the duration of the etch, that is to say with the large surface area faces (the etch target) perpendicular to the level surface it is situated on, a small clamp is put into position as such it is in contact with the topmost trailing edge of the sample. This means the etching surfaces remain free of any obstruction, and the sample is held in the correct orientation by stiction.

In relation to the matter of sample handling, it is very difficult to avoid contact with the surface when the sample needs to be moved. As opposed to eliminating the prospect of surface damage, something well–nigh impossible, an approach of reducing the damage as much as reasonably possible was adopted. For instance, when moving the sample is required, only one (marked) corner will be subject to the tweezers. Localising the damage in this fashion means that this portion of the surface can be excluded from any measurements or imaging, if possible. The use of a quick dump rinse (QDR) chamber for all required rinsing steps is also beneficial, where the system is capable of purging etchants far more effectively and delicately than using a diH_2O tap and rinsing by hand.

3.2.3.4 Process Workflow

A standard process was required in order to achieve consistent etching results and limit the likelihood of error. Variations of the etch time, a key focus of this study, can be controlled and monitored with more consistency. The standard workflow used in the commencement of the anisotropic Ag-MACE process, for both b-Si and hb-Si samples forthcoming, is outlined below.

1. An appropriately cleaved sample of c-Si, either planar or pyramidally textured, is subject to the H_2SO_5 cleansing etch for a period of 15 minutes prior to any processing. This is to ensure all surface contaminants (debris, organic matter, and oxides, for example) are removed.

2. The sample is thoroughly rinsed–through using automated QDR bath as stated previously. This system allows for a very high level of solution removal in a consistent manner[3]

[3]Where QDR cleansing is referenced, two full tank purges and 10 minutes of filtration are carried out as part of the automated process. The QDR process remains constant throughout this work. di$-H_2O$ is the only cleaning agent in the QDR bath.

3. Subsequently, sample is dipped in the HF dip solution for a period of five minutes. This ensures the surface is completely hydrophilic before proceeding.

4. The sample is now placed in the Ag-MACE solution, for some discrete period of time referred to herein as the etch time, t_e.

5. Upon the elapsing of the selected etch time, t_e, the sample is pulled from the etch solution and *immediately* placed into the QDR bath for cleansing. The rapid transition between the MACE solution and the QDR is crucial to ensure the etch process does not continue on the surface after removal. Failure to adhere to this will result in deviation from the relationship between t_e and NW height.

6. Once the etch has been completed, the sample is rinsed once again with deionised water. It is then transferred into a solution containing 50 vol% nitric acid HNO_3 in order to remove the Ag dendrites from the surface. These are situated between the NWs and need to be removed to maintain low surface reflectance, given Ag is a relatively effective reflector.

7. Following this, the sample must be rinsed through the QDR one final time and dried carefully using nitrogen N_2, prior to being stored as appropriate for study.

An appropriate selection of etch times, t_e, were required in order to confirm and compare the etch rates for both planar and textured Si surfaces. These times are four, six, eight, and 10 minutes. Each sample, once processed in accordance to the outlined sequence, can then be imaged at the nanoscale to confirm the average height of the NWs across the surface.

3.2.4 Surface Uniformity

Surface uniformity, whilst capable of being approximated through SEM imaging, requires a consistent configuration for accurate quantification. All the operating parameters for an SEM system will typically vary based on the sample being measured, leading to changes in image brightness and contrast between samples, and even between different parts of the same sample. This is because the smallest deviation in distance between the sample surface and the SEM hardware, usually brought–on by moving the target, will require a refocus and thus variation of the operating parameters. This will introduce inconsistencies when looking to evaluate surface uniformity and conformity systematically.

In statistical analysis, the standard deviation, σ, of a set of data points is often used to

identify the dispersion of said data points with respect to their mean. The implication being that a dataset with values closer to one another, that is to say less dispersed, will have a lower value for standard deviation, and vice versa.

$$\sigma = \sqrt{\frac{1}{n}\sum_{i=1}^{n}(x_i - \bar{x})^2} \tag{3.3}$$

In equation (3.3), n is the total number of values in the set, x_i is a single data point for $1 \leq i \leq n$, and n is the mean value for all the data points within the set. It should be noted that, as shown in equation (3.3), standard deviation can only be positive. Here uniformity, U, is defined as unity minus the standard deviation, as shown in equation (3.4).

$$U = 1 - \sqrt{\frac{1}{n}\sum_{i=1}^{n}(x_i - \bar{x})^2} \tag{3.4}$$

This formula is valid due to the valuation of the data points, x. Any real system, as discussed further in chapter 6, can be viewed as an infinite number of data points. In order to be analysed systematically it must first be discretised. This can be achieved through photographing the surface in question. Pixels will be assigned to discrete surface areas depending on the resolution of the camera itself. This means that a higher resolution results in each pixel aliasing a smaller area of the surface. We then have an image with a distinct number of pixels, n, each with its own value for colour, x. Convert this image into an 8-bit binary image (greyscale), and the possible values of x are as defined in equation (3.5).

$$0 \leq x \leq 255 \tag{3.5}$$

$$0 \leq \frac{x}{255} \leq 1 \tag{3.6}$$

By converting these data points into fractions, as in equation (3.6), and inputting them into equation (3.4), σ can only hold values of $0 \leq \sigma < 1$. This results in uniformity being bound as $0 < U \leq 1$. It is possible, albeit highly unlikely, that a system can be completely uniform, that is to say $U = 1$. However, it is not possible for a real system to be infinitely variant, the implication being $U \neq 0$. This is down to the fact that $\sigma \to 0$ only for infinitely divergent values for x; where $x_1 = 0$ and $x_2 = \infty$, for example. This form of surface uniformity analysis has been developed specifically for the work reported here.

Photographs of samples are taken, under constant lighting conditions, and the images are automatically cropped to ensure both only the sample surface is visible, and that as much of the surface as possible is included. Else, the image backdrop will contribute to the uniformity determination, ultimately rendering the process of determining surface uniformity unfit for purpose. This inevitably does introduce an element of error given that parts of the sample are cropped out of the image, though the proportion of the surface removed is so low that its effect on the overall quantification is mute. Furthermore, edge artefacts, typically caused by movement damage post–manufacture, will also be discounted from the measurement, further reducing error given that these interfaces will typically not correspond to the primary surface.

3.3 Results and Analysis

3.3.1 Pyramids

Using the industry standard KOH recipe for pyramidal textures, as described in section 3.2.2, we expect to see a planar fraction, PF, of essentially unity (PF ≈ 1). Taking 10 samples, each having undergone the same etching process, it is possible to determine key topological features of the resultant surfaces, such as pyramidal base size, height, uniformity, the planar fraction, and inclination angle for this particular workflow. For reference, scanning electron micrographs showing one of these samples with pyramidal surface textures can be seen in figure 3.2 for reference. Note that each manufactured sample have comparable textures to those shown here.

For each of the 10 samples manufactured, five arbitrary areas of each surface were imaged using SEM and scrutinised for the information mentioned previously. Each arbitrary section encompassed an area in the order of 10^3 μm^2. It can be seen that PF ≈ 1, which is to say that the surface is completely covered in microscale pyramids. The justification for an approximate sign against this property comes from the *very* small regions of surface damage caused by sample handling, likely from metallic tweezers, and/or impact damage caused by sample movement.

Variance in pyramid base size is considerable, likely due to their ability to propagate randomly during the etching process, and yields sizes between $\sim 1\mu$m and $\sim 8\mu$m. The apparent presence of smaller pyramids is discounted as being a component of larger ones. Large pyramids envelop one or more facets of those smaller than them during the KOH etch, resulting in a single pyramid structure with, contrary to typical understand-

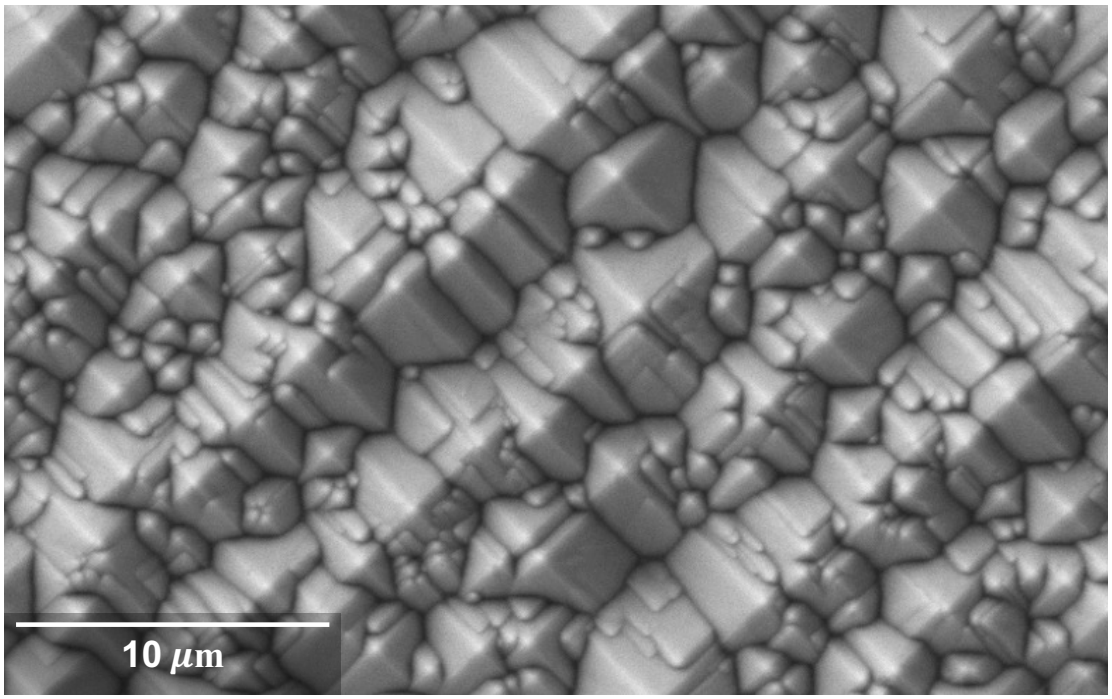

(a)

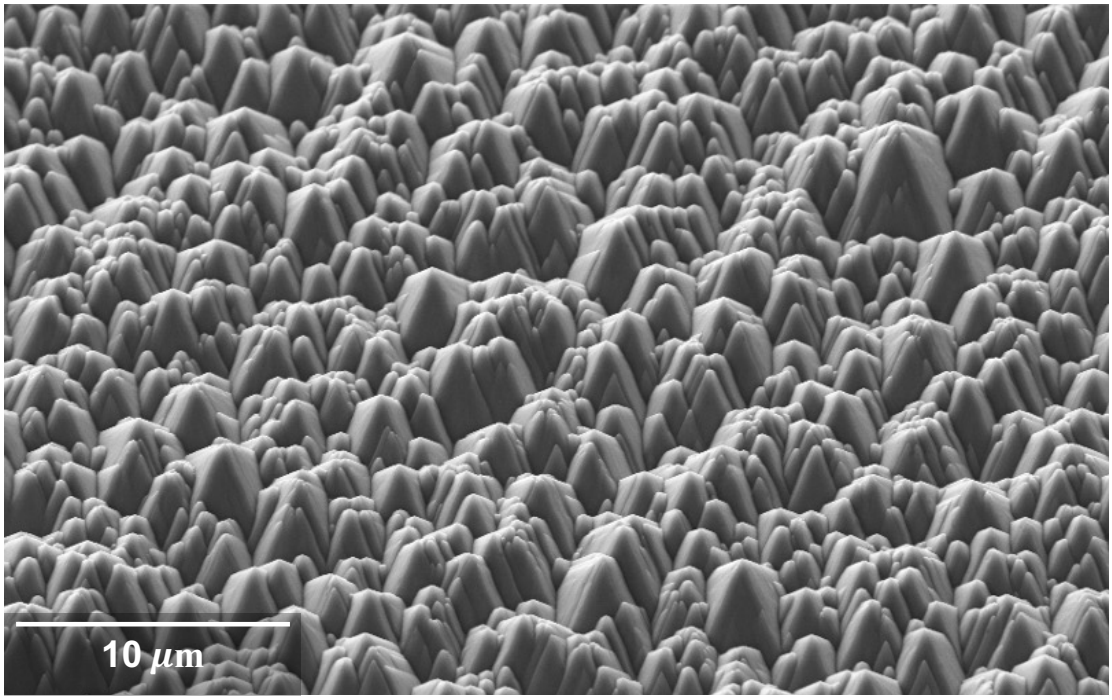

(b)

Figure 3.2: Pyramidal textures from top–down (a) and side–on at an angle of 30° from the horizontal (b) as formed by KOH etching for a period of 30 minutes and at a temperature of 75 °C.

ing, microscale pyramids with more than four facets. This is also apparent in figure 3.3.

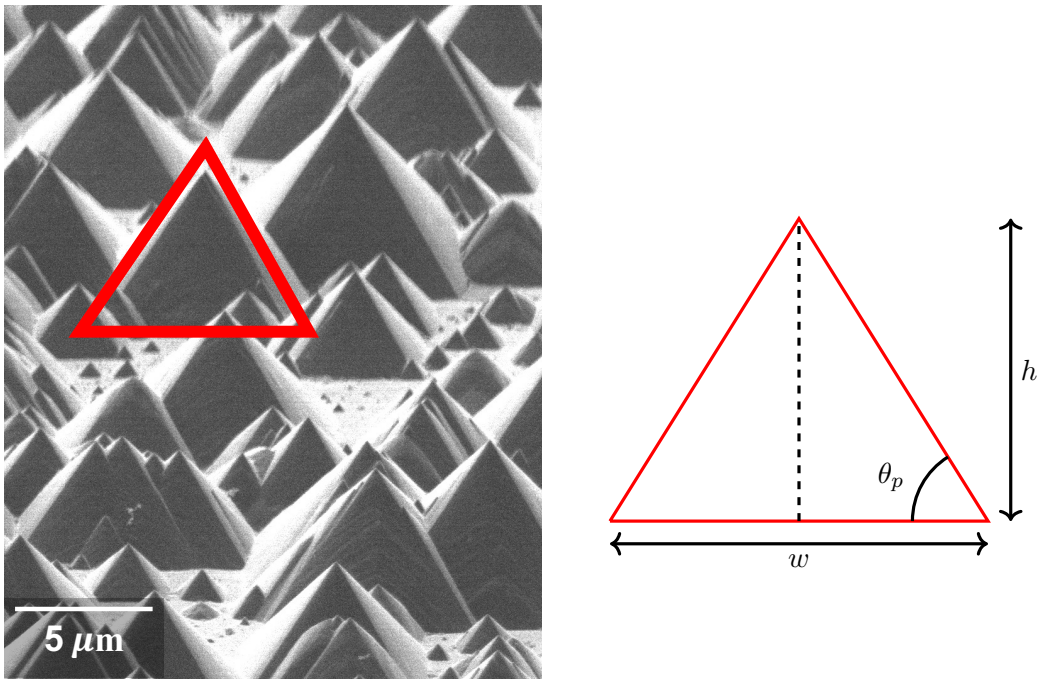

Figure 3.3: Interpreting topological information through SEM imagery including the pyramid angle of inclination, θ_p, height, h, and base width/depth, w. Figure shows base in only one direction, but is implicit along the z–axis (into the page).

The feature height, h, despite clearly being variable between pyramids as in figures 3.2b and 3.3, can be related to a significant degree of accuracy to its respective base dimensions, w. This is to say that the two properties are proportional to one another. Given the nature of this etch, the base of the texture is approximated to a square, resulting in dimensions across the surface spatial plane being the same; x–axis width, w_x, and z–axis depth, w_z, are identical ($w_x = w_z = w$).

$$\begin{aligned} h &= \frac{w \tan(\theta_p)}{2} \\ &\cong \frac{1.43w}{2} \\ &\cong 0.717w \end{aligned} \tag{3.7}$$

Through these analyses, it was found that $\theta_p \approx 55.1°$, and subsequently $h \cong 0.717w$, as in equation (3.7). This is to say that the height of each pyramid is approximately 72% that of the size of its base. Aligning this with the observations regarding variant base sizes from a top–down perspective, a height distribution for the same 10 sample surfaces can be determined. A collation of surface properties, averaged across these samples, is

listed in table 3.1. The determined value for θ_p is almost exactly the expected value of 54.7° expected for KOH etching on a c-Si wafer of $< 100 >$ crystallographic orientation. The difference here can be attributed to human error in manually reading the angle based on approximation from SEM imagery.

Table 3.1: Tabulated values of the surface properties across all of the KOH etched samples reported here.

Property	**Value**			
	Minimum	Maximum	Range	Mean
PF (1)	–	–	–	1
w (μm)	1	8	7	6.12
h (μm)	0.717	5.73	5.01	4.93
θ_p (°)	–	–	–	55.1
U (1)	0.941	0.976	0.035	0.963

Sample uniformity, U, as quantified using the methodology outlined in section 3.2.4, is a measure of the apparent uniformity of the surface as seen by the human eye. This is to say that it is a macroscale determination of uniformity, and subsequently the variation of individual pyramid size on the surface has a considerably smaller influence on the determined value of U. Instead, the average response of the surface as a whole will influence perceived unifomity, implying that PF will have more impact in this regard.

The planar fraction, PF, found for these samples and listed in table 3.1, can be attributed to the use of a wetting agent. Mentioned prior in section 3.2.2, the addition of isopropyl alcohol to the etching solution results in better sample–solution contact due to the reduction of surface tension. To demonstrate this experimentally, the etch described in section 3.2.2 was performed, with and without the C_3H_8O reagent. A direct comparison can then be made whereby the difference can be attributed solely to the change in surface tension between these etches. The resulting textures formed with and without C_3H_8O are shown in figures 3.4 and 3.5.

As seen in figure 3.5, the effect of high surface tension is considerable. Several islands of pyramids can be seen, subtly interconnected by much smaller standalone pyramids. Surrounding these are vast areas of planar Si with little–to–no texturing at all. In the top left–hand corner of the image, slight surface indentations can be seen, which are an indicator of limited etching within that area. Surface tension can be mapped against

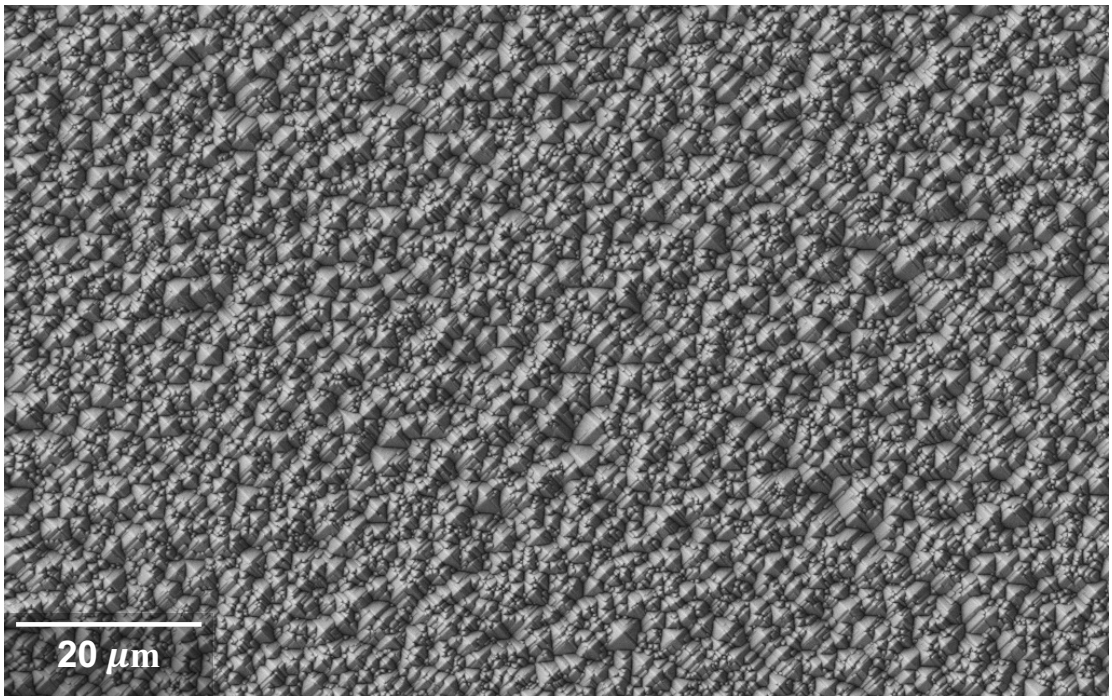

Figure 3.4: An SEM image of pyramidal textures created *with* the C_3H_8O wetting agent. For this sample, PF ≈ 1 (taken as an average over several SEM images aside from the one shown here).

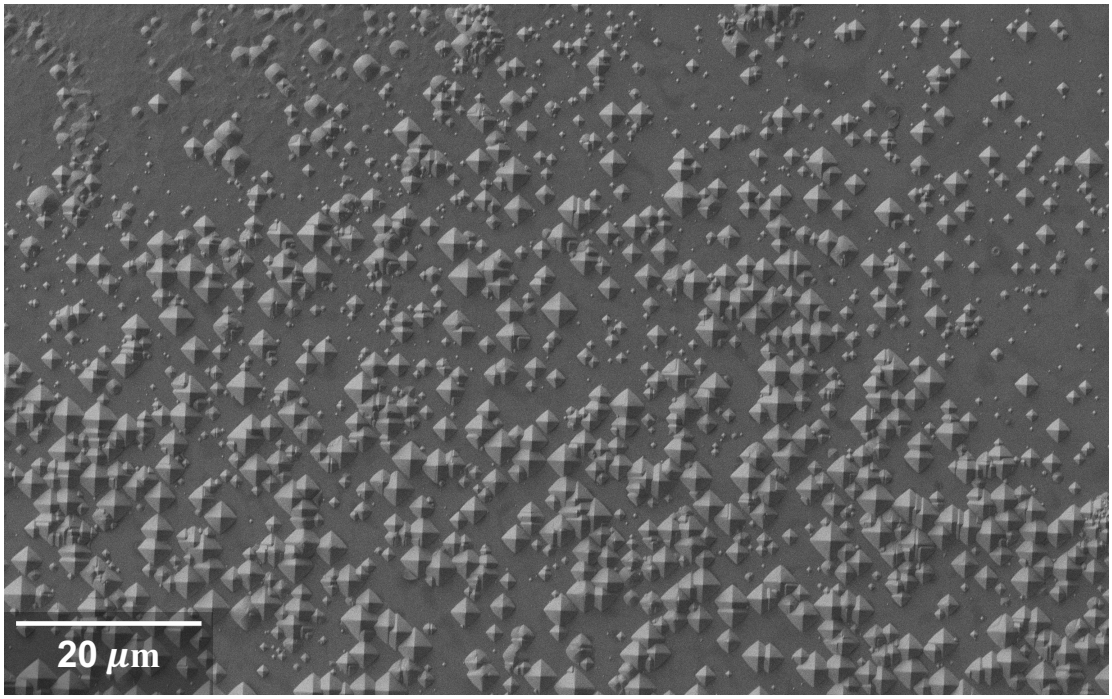

Figure 3.5: An SEM image of pyramidal textures created *without* the C_3H_8O wetting agent. For this sample, PF $\cong 0.487$ (taken as an average over several SEM images aside from the one shown here).

areas such as these, whereby the etching solution failed to make sufficient contact with the surface for the duration of the etch. It should be noted that C_3H_8O is not the only wetting agent capable of achieving approximately 100% surface coverage. Similar results can be achieved using a non–ionic surfactant such as polyethylene glycol tert-octylphenyl ether ($C_{28}H_{50}O_8$) or polyoxyethylene lauryl ether ($C_{58}H_{118}O_{24}$).

3.3.2 Black Silicon

In this section four b-Si samples are created using the recipe outlined in section 3.2.3.2. This recipe has been used in previous studies and has demonstrated repeatability in its ability to create NW topologies. The effect of etch time variation can be seen in figure 3.6. A consistent scale reference of 2 μm has been included in each SEM image to aid with comparison, and the average NW height, h, across each sample has been determined and placed into table 3.2. Using the information shown in figure 3.6 and table 3.2, it is possible to determine NW height, h, as a function of etch time, t_e. This data is shown in figure 3.7.

It can be seen that, for the recipe used here (as in section 3.2.3.2), the etch rate, $h'(t_e)$, is linear at a rate of 0.261 μm/minute. This means that one can expect the height of the NWs to reach 1 μm at four minutes, 2 μm at eight minutes, and 3 μm at 12 minutes[4]. The data in figure 3.7 also includes the height information for every one of the 10 samples created for the corresponding etch times. This yields a total of 40 samples overall. As one would expect there is some divergence between sample height for constant t_e. This is due to slight deviations between the solution make–up between different samples. In the case of MACE, the solution needs to be purged and restored between etches; it cannot be reused due to the deterioration of $AgNO_3$ under ambient lighting conditions. Crucially, this introduces an element of error through variability in chemical composition. Such errors are unavoidable when recomposing the solution from scratch for each etch. In making multiple samples for each required etch time, as has been done here, this error is minimised and an average can be taken across the entire set to determine a more accurate etch rate.

On switching perspectives to a top–down view, as done in figure 3.8, the bunching properties of b-Si NWs in relation to the etch time, and subsequently to their respective heights, are noticeable. Clearly, it can be seen that for shorter NWs, this bunching effect, predominantly seen at the very top of the wires, is minimised. However, the

[4]Data for 12 minutes is extrapolated from the experimental dataset.

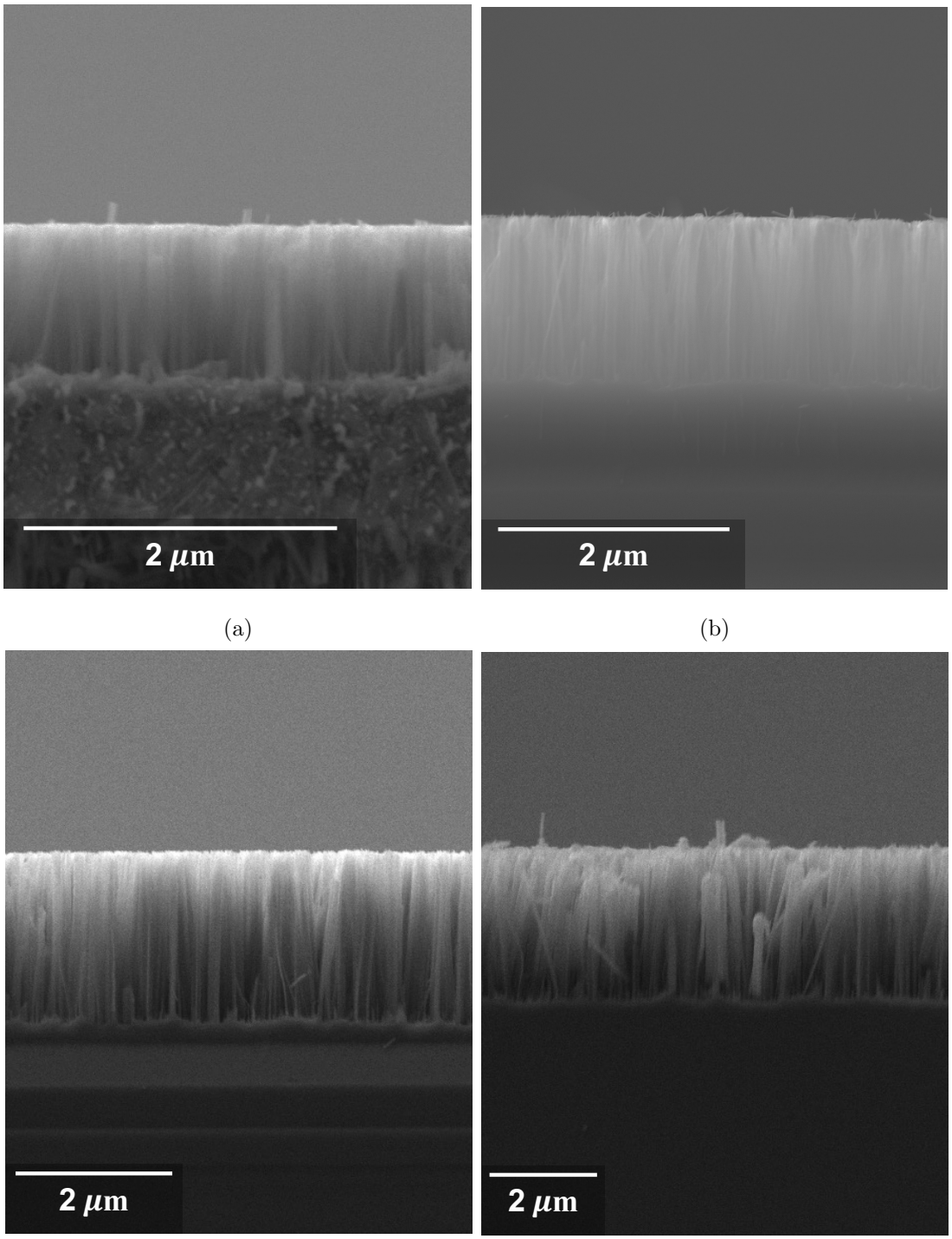

(a) (b)

(c) (d)

Figure 3.6: Visualising the effect of etch time, t_e, on resultant NW height for durations of four (a), six (b), eight (c), and 10 minutes (d) using SEM. The scale of each image is displayed with respect to 2 μm to prevent loss of resolution and aid comparison.

Table 3.2: An overview of the NW heights against etch time as recorded for the samples made for the work reported here.

Etch Time (Minutes)	**Nanowire Height (μm)**			
	Minimum	Maximum	Range	Mean
4	0.84	1.25	0.41	1.09
6	1.35	1.73	0.38	1.47
8	1.96	2.35	0.39	2.09
10	2.40	2.75	0.35	2.55

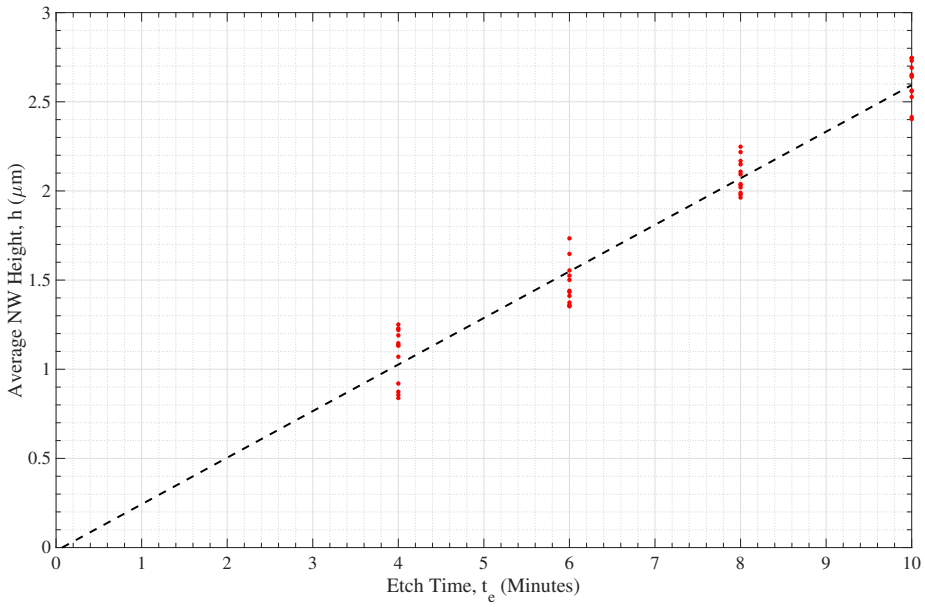

Figure 3.7: Mapping the average NW height, h, as a function of etch time, t_e, for 40 b-Si samples made in accordance with the MACE process workflow in section 3.2.3.4. Differential analysis shows the NW etch rate as $h'(t_e) = 0.261$ μm/minute.

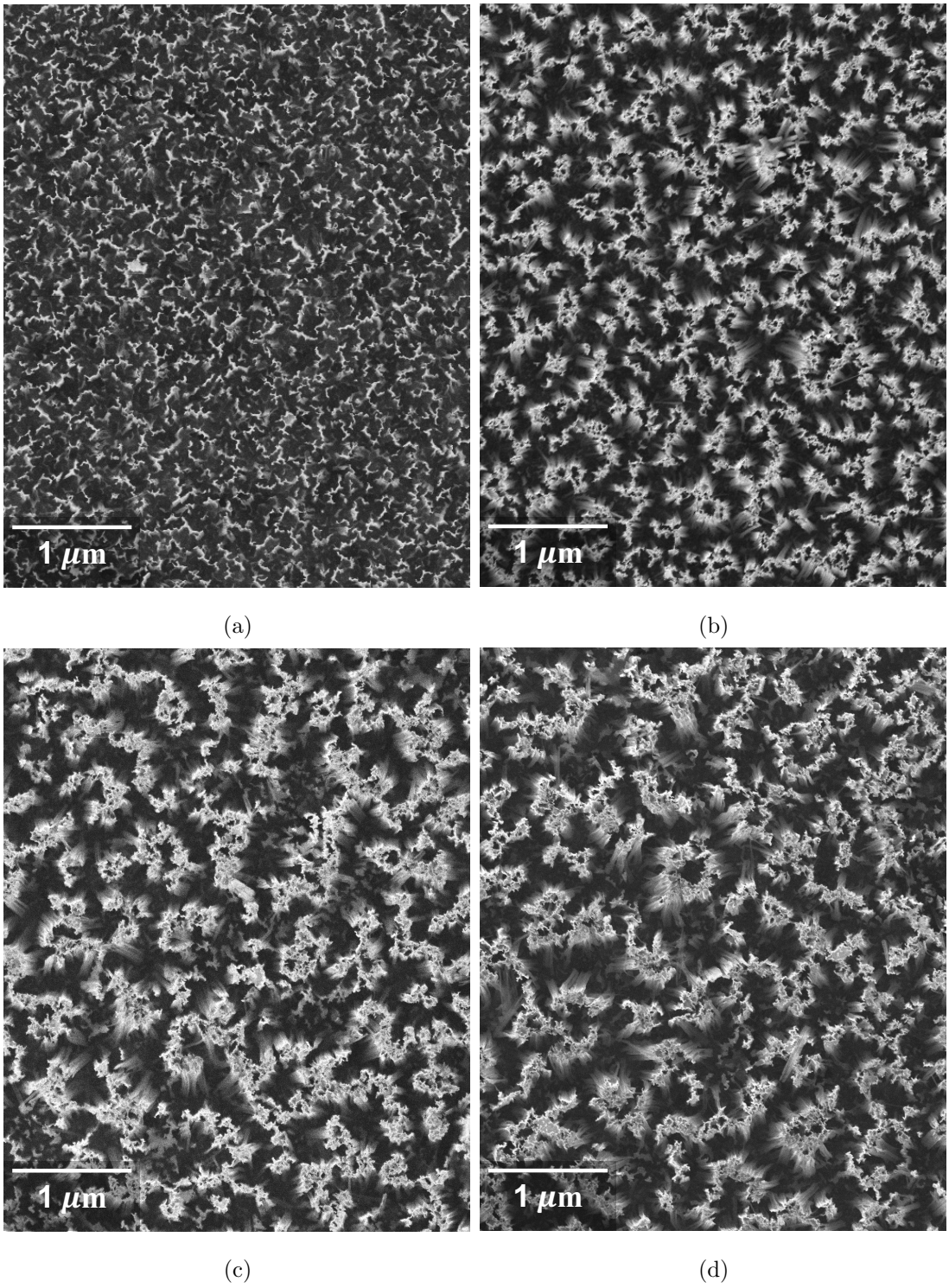

(a) (b)

(c) (d)

Figure 3.8: Visualising the effect of NW height, and subsequently etch time, t_e, on resultant NW distibution from a top–down perspective. The samples shown here were etched for durations of four (a), six (b), eight (c), and 10 minutes (d). The scale of each image is consistent to aid with cross–comparison.

taller they are etched, the greater the tendency for them to bunch together in greater numbers. This is far more visible from the top–down angles seen in figure 3.8. The implications on surface reflectance are studied in chapters 5 and 6. Uniformity, U, is instead looked at here, that is to say consistency of sample colour, as observed with the naked eye – the *apparent* uniformity.

Table 3.3: An overview of the surface uniformity for the b-Si samples as determined using the methodology outlined in section 3.2.4. The numerical value for U is calculated as shown in equation (3.6).

Etch Time, t_e (Minutes)	**Apparent Uniformity, U (1)**
4	0.822
6	0.876
8	0.911
10	0.923

Apparent uniformity, presented in table 3.3, is determined using the methodology outlined in section 3.2.4. In general, a positive correlation can be seen between NW height and surface uniformity. However, this relationship deteriorates as etch times of $t_e \geq 8$ minutes are reached. This is to be expected, given the graded refractive index behaviour of NWs; the longer they are, the further reduced the gradient between the air and Si substrate. This enables light to be directed toward the substrate with greater effectiveness, subsequently having a direct effect on the perceived darkness of the sample.

Increased etch time can also be attributed to decreasing the likeliness of planar regions, closing the relative gap between the heights of the NWs across the surface. As can be seen using the data shown in table 3.2, the range of NW heights recorded for each sample is relatively consistent (0.35 to 0.41 μm). Taking the value for the range of heights, it is possible to demonstrate this point by relating it to the mean height, h, recorded for each etch time, t_e. The range represents a relative proportion of h that is equal to 37.6%, 25.9%, 18.7%, and 13.7% for etch times of 4, 6, 8, and 10 minutes respectively. This demonstrates how, for longer etch times and, subsequently, taller NWs, the proportion of variability in individual NW height becomes less influential on the surface as a whole, contributing to greater apparent uniformity as supported by the data in table 3.3.

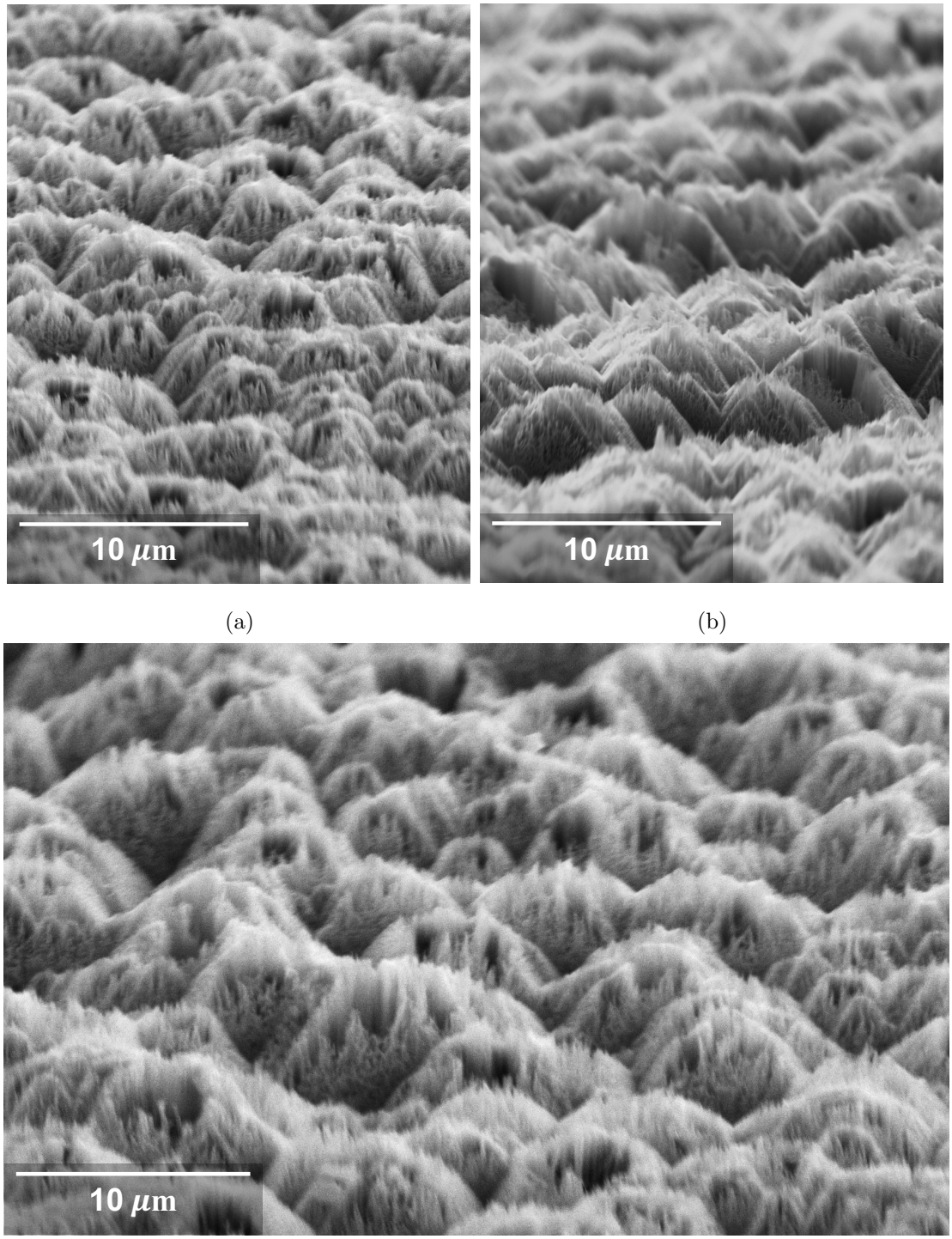

(a) (b)

(c)

Figure 3.9: Viewing the hb-Si surface textures from side–on after undergoing MACE for 4 (a), 6 (b), and 8 (c) minutes. The scale of each image is consistent to aid with cross–comparison.

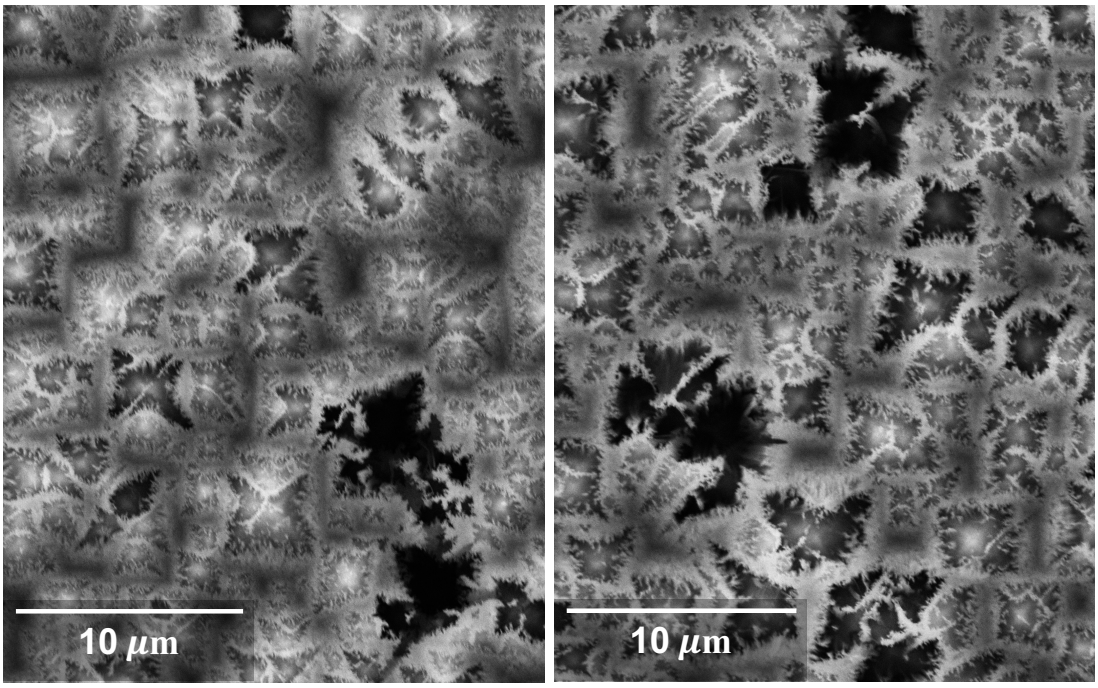

(a) (b)

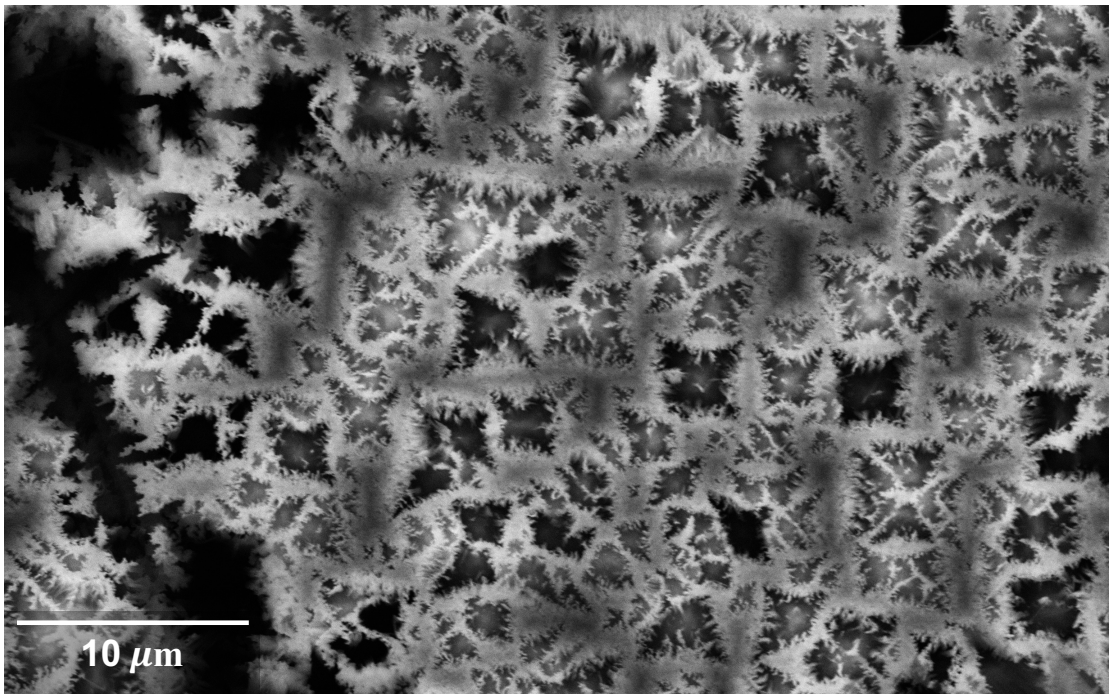

(c)

Figure 3.10: hb-Si textures from top–down after undergoing MACE for 4 (a), 6 (b), and 8 (c) minutes, demonstrating NW bend and bunching across pyramidal facets. The scale of each image is consistent to aid with cross–comparison.

3.3.3 Hybrid Black Silicon

Following the sequential etching sequence, whereby consistent pyramid–based textures are first created using the recipe described in section 3.2.2, followed by the use of the MACE recipe outlined in section 3.2.3.2 to create a coating of NWs, the creation of non–planar, hybrid black silicon is achieved. Scanning electron microscopy images are shown in figures 3.9 and 3.10, from side–on and top–down, respectively.

Table 3.4: Summarising the heights of the NWs against etch time when etched onto the facets of pyramids. The difference between these values and those for NWs on planar Si (table 3.2) are indicated in red.

Etch Time (Minutes)	**Nanowire Height (μm)**			
	Minimum	Maximum	Range	Mean
4	0.59	0.89	0.30	0.79 (-0.30)
6	1.01	1.37	0.36	1.17 (-0.30)
8	1.43	1.87	0.44	1.61 (-0.48)
10	–	–	–	–

In reference to the data in table 3.1, the average base size of these industry standard pyramidal textures is approximately 6.12 μm, and the average height is approximately 4.93 μm. By comparison, equivalent height information for the b-Si textures is shown in table 3.2. Note the mean height value for 8 and 10 minute etch times, being 2.09 and 2.55 μm, respectively. Excessively long NWs on the pyramids made here would simply cause disintegration of said pyramid, resulting in a disordered quasi–planar surface not indicative of hb-Si. On experimentation, it was found that, whilst 8 minute etches were sufficiently short to maintain pyramidal structures at this scale, 10 minute etch compromised the hb-Si topology and was not used going forward. 10 of each sample per etch time are manufactured, resulting in 30 samples forming the datasets shown forthcoming.

When cross–referenced against table 3.2, the data in table 3.4 shows hb-Si NWs come up smaller on average than NWs etched onto planar Si when etched for the same duration. Due to the existing surface texturing, the area of the sample surface, despite being cut to the same physical size, is considerably larger than that of planar Si. As such, there is a greater surface area for Ag particles to nucleate on, and a greater area in which the HF acid needs to act as a catalyst. One way of overcoming this difference is to increase the concentration of HF, and in the case of particularly large samples (not like

those used here), an increase in $AgNO_3$ would be particularly beneficial. Furthermore, the MACE process, much like the KOH etch, is anisotropic, meaning that the etch rate is directly related to, and effected by, the crystallographic orientation of the substrate itself. Complexities in the interface between an intricately textured surface and the solution in which it is submerged also comes into play here. Furthermore, the atomic density of the $< 111 >$ crystallographic plane that constitute the facets of the pyramids is greater than that of the $< 100 >$ crystallographic plane exposed in the planar b-Si samples. This increase in atomic density results in a slower etch rate along the $< 111 >$ plane. The etch rate for hb-Si texturing is approximately 0.205 μm/minute; around 21% slower than on planar Si.

Nanowire bunching is considerably different for hb-Si. Typically, bunching appears to occur more readily along the facet edges (facet–facet and facet–base). Lighter shades in these figures are indicative of NWs, whilst darker ones are weaker electron returns; pits or holes caused by NW divergence. As can be seen in figure 3.10, several distinct cross–like darker segments appear at the peak of each pyramid. It is these cross–like shapes that represent NW divergence, and this occurs where the very top point of the pyramid texture has been obliterated by the MACE process. An example of this is shown in figure 3.11.

Structural collapse occurs at the point where the width of the pyramid is matched by the ingress of b-Si NWs across a plane parallel to the base plane. The ingress caused as a result of the average NW height, as represented by h_n in equation (3.8), at a relative angle of θ_p to this plane can be determined through basic geometric analysis.

$$h_{\mathrm{p,lost}}(h_n) = h_n \frac{\tan(\theta_p)}{\cos(\theta_p)} \tag{3.8}$$

$$\begin{aligned} h_{\mathrm{p,etch}}(h_n) &= h_p - h_{\mathrm{p,lost}}(h_n) \\ &= h_p - \left(h_n \frac{\tan(\theta_p)}{\cos(\theta_p)} \right) \end{aligned} \tag{3.9}$$

Equation (3.9) allows us to relate the etched pyramid height ($h_{\mathrm{p,etch}}$), that is to say the average nanowire height (h_n) subtracted from the original pyramid height (h_p), to the NW height itself. This forms a ratio whereby the proportion of NW to pyramidal structure can be obtained and analysed against topological features. A detailed overview of the fundamentals for this analysis is shown in figure 3.12, where the NW coating is shown in red with the aforementioned divergence present in the obliterated section left behind at the top.

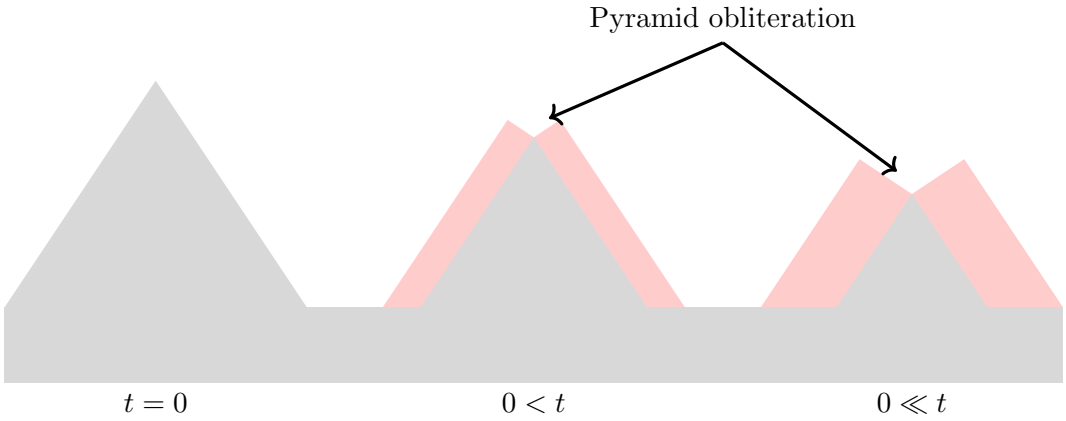

Figure 3.11: The process by which pyramid obliteration occurs. b-Si NWs, as shown in red, are etched into the pyramid causing the top to be etched away due to structural collapse. The pyramid angle, $\theta_p \approx 55.1$, as in table 3.1, is *not* drawn to scale here.

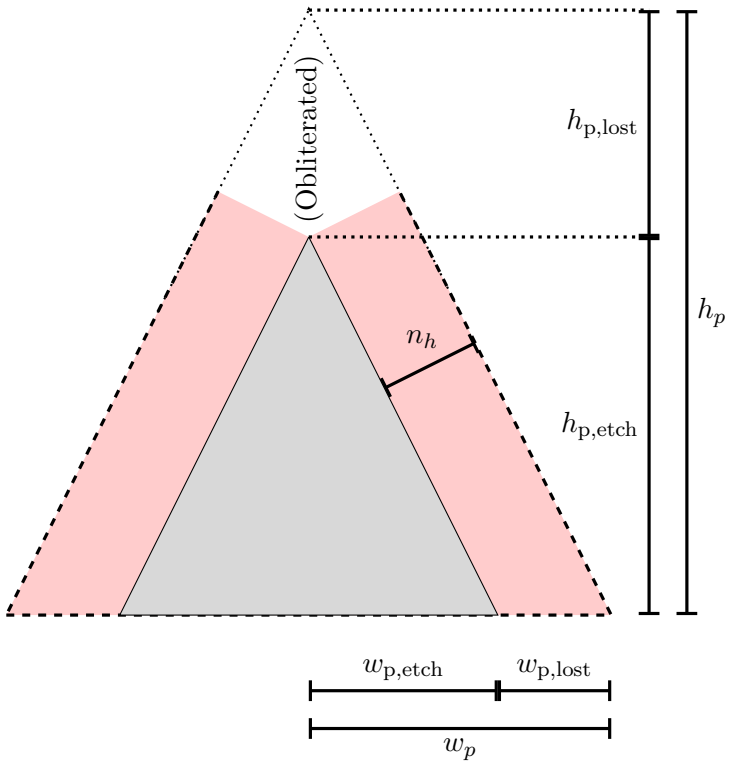

Figure 3.12: Indentifying the components of the hybrid b-Si nanostructures and their relationship to one another. Nanowire arrays are shown here in red, whilst the pyramid remaining post–etch is shown in grey, underneath the nanowires. Displayed components in relation to equations (3.8) and (3.8).

Table 3.5: An overview of the surface uniformity for the hb-Si samples as determined using the methodology outlined in section 3.2.4. The numerical value for U is calculated as shown in equation (3.6). The difference between these values and those for NWs on planar Si (table 3.3) are indicated in brackets.

Etch Time, t_e (Minutes)	**Apparent Uniformity, U (1)**
4	0.849 (+0.027)
6	0.884 (+0.008)
8	0.917 (+0.006)
10	–

In general, and as summarised by table 3.5, there is no considerable difference in apparent surface uniformity between b-Si and hb-Si, to be expected for samples of such dark appearance to begin with. However, there is a slightly greater measure for U in the case of shorter t_e when compared to the planar b-Si equivalent. This is likely due to the greater performance of hybrid nanostructures in trapping light over their planar counterparts. This is emphasised when the NWs are based on top of a pyramidal texture with complete surface coverage (where PF = 1).

3.4 Conclusions

In taking an industry–standard recipe for the anisotropic etching of microscale pyramids on c-Si wafers, alongside the silver–based metal–assisted chemical etching process, hybrid micro–/nano–scale surface textures consisting of pyramids coated with b-Si nanowires have been successfully manufactured. These such structures purportedly offer significant anti–reflectance through unique light trapping and redirection capabilities, predominately supported by their multiscale nature. This is somewhat supported by the data shown in tables 3.3 and 3.5, for b-Si and hb-Si, respectively, with surface uniformity above 80% for the former and 85% for the latter. Coupled with visual inspection, the significant lack of returning light, that is to say the darkness, is clearly apparent. Photographs of the b-Si samples, for each etch time, t_e, are shown in figure 3.13 to demonstrate this.

A differential in etch rate was recorded between the use of MACE on planar and textured surfaces, whereby the latter is notably slower ($\sim$ 21% slower). This is a result of the ambient occlusion derived directly from a non–planar surface interaction with the

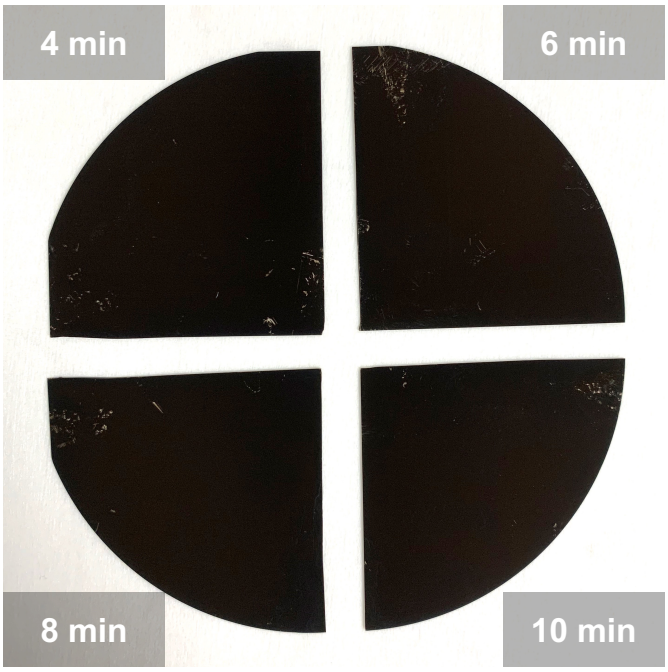

Figure 3.13: Exemplar b-Si samples showing resultant appearance to the human eye for all four etch times. Each sample was selected at random from the 10 of each available. Surface scratching is a result of significant handling during the characterisation of the samples using SEM.

etching solution, as well as a dependency on crystallographic plane orientation. Planes other than the $< 100 >$ plane are exposed by the KOH etch, meaning that Ag particles constituent of the metal–assisted chemical etch will need to etch through these planes in the creation of hb-Si. This is why the NWs etched on top of microscale pyramids are shorter given the same etch time.

Longer NWs, regardless of their foundation, can be attributed to a darker overall surface appearance, suggesting a subtle decrease in reflectance related to etch time. The rate of change in apparent darkness would seem to be non–linear, suggesting a point at which a sample's darkness will not continue to increase for increasing NW length. NWs of greater length are also difficult to passivate and prone to damage, where they can essentially be knocked–over with very little effort. Such assumptions are corroborated by the scanning electron micrographs in figure 3.6, paying particular attention to figure 3.6d, where damage can be more readily seen after the cleaving process.

Detailed optical characterisation is essential to understand the complexities behind the way each of these surfaces interacts with light incident on it, as well as how this relates to optical performance should it be applied as an anti–reflectance mechanism onto a solar

cell. A passivation layer, such as Al_2O_3 [135], is required on these structures to enable them to be used in solar cells. Such a coating has a prominent impact on the electrical characteristics of the resulting cell and a marginal impact on the optical characteristics (assuming this is a thin layer – as is typical). Given the focus of this work relates to optical studies, the inclusion of a passivation layer was not investigated.

Chapter 4

Angle-resolved Spectrophotometry

The work described here has been published in a journal paper

J. J. Tyson, T. Rahman, and S. A. Boden

"Angle–Resolved Spectrophotometry for the Optical Characterization of Material Surfaces"

IEEE Transactions on Instrumentation and Measurement, Volume 71

January 2022

DOI: 10.1109/TIM.2022.3146947

4.1 Introduction

4.1.1 Reflectance

Reflectance is an important property in the design of materials for specific applications. This property can be measured in several ways, which usually involve illuminating the sample at a single angle of incidence and collecting the light reflected in a particular direction, through the use of a detector mounted on an arm in a goniophotometry set-up, or the total reflected light (hemispherical reflectance) using an integrating sphere [137]. These single angle reflectance (SAR) approaches provide spectral information either through the use of a monochromator which scans the wavelength range at the input, or using a broadband light source and coupling the output to a spectrometer. SAR methods, despite being insightful, do not provide a complete picture of true reflectance characteristics, particularly for applications in which the angle of incidence varies. Many tools do not resolve hemispherical reflectance with respect to both incident angle, θ, and wavelength, λ, distributions simultaneously, as well as for different polarisations due to

the complexity of such measurements, particularly in an automated process with a high degree of control.

One exception to this was a tool developed by Parretta et al. known as the Reflectometer for Optical measurements in Solar Energy (ROSE) [138]. The ROSE system uses a series of portholes and a sample mounted on the side of the sphere to achieve variable angle incidence. This methodology, in comparison to that presented here, is limited in angular resolution by the positioning of the manufactured entrance portholes - 10° in this case. Resolution can only be increased with the use of a different (and larger) sphere featuring more entrance portholes at the required angles. By moving the light source instead of the sample, the number of portholes required directly increases the prominence of the general integration error by tarnishing the spherical nature of the sphere itself [136]. It should also be noted that the larger the integrating sphere, the lower the overall throughput of the system. This is because the reflected light must be integrated over a larger internal surface area from which only a small proportion is sampled. Many cases of custom-designed systems within laboratory settings have been reported as exceeding commercial, pre-built systems' performance and costs, often being far more applicable to their respective research applications as well [139, 140]. In the case of optical measurement devices, this has been increasingly reported in recent years [141–143].

Developed here is a broadband, angle–resolved, and elective linearly polarised hemispherical spectrophotometer capable of both enhanced SAR and variable angle reflectance (VAR) measurements. A photographic overview of the system is shown in figure 4.1. Hemispherical reflectance is where light is collected across the hemisphere encapsulating the illuminated surface and is demonstrated in figure 4.2. The use of a sample bypass beam, commonly referred to as the double beam approach, corrects errors introduced relating to the placement of a sample within the system's integrating sphere, providing accurate data regarding the optical response characteristics of a given surface. Outlined first are the design decisions behind the angle-resolved spectrophotometer (ARS), emphasising the key details behind the processing workflow, and highlighting the advantages and disadvantages of the methodology. The system then needed to be calibrated using thin film samples of known reflectance, comparing measurements to theory. Once calibrated, a range of other samples, such as coloured paints and a material designed to block light in the visible spectral range, are then characterised using the same workflow.

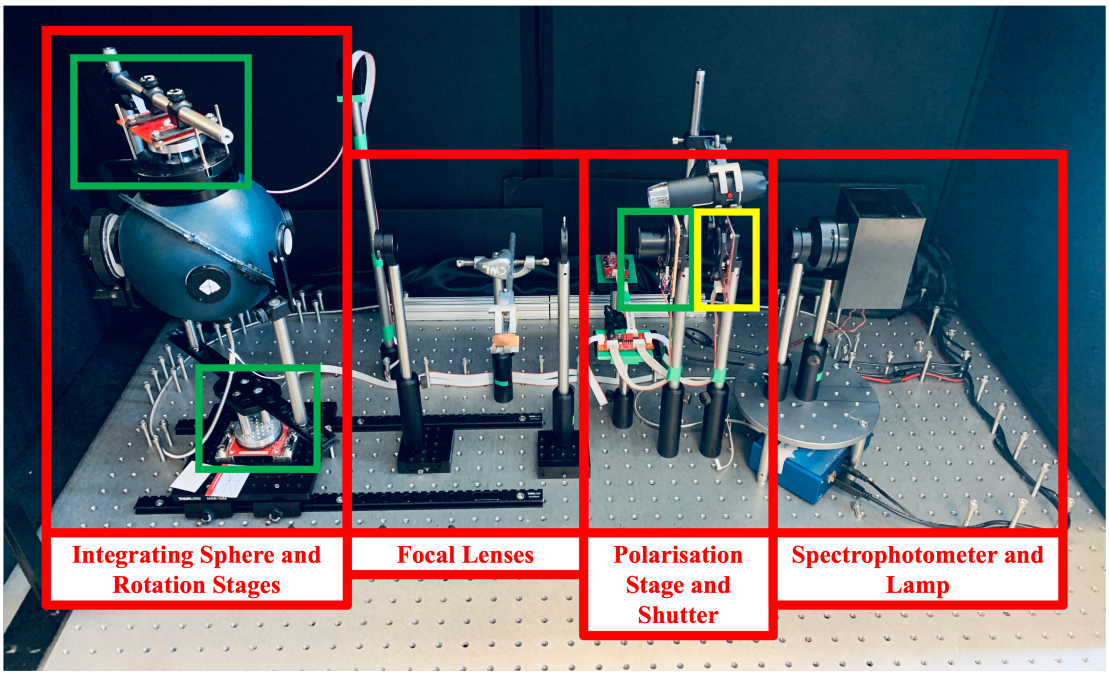

Figure 4.1: A side–on overview of the angle–resolved spectrophotometer discussed here. The three rotation stages are highlighted in green, and the linear translation stage (for the shutter) is highlighted in yellow.

There are two types of reflection: diffuse and specular. Specular reflection is the redirection of light away from a surface in accordance to the angle it came in at, creating a mirror image. All real surfaces have some component of specular reflection. Diffuse reflection is the process by which incident light is scattered away from a surface in many directions concurrently, leaving only disordered light reflected in the absence of any image. The appearance of such a reflection is best observed with matte coatings and materials; plain white paper being a highly diffuse reflector, for example. These types of reflections are illustrated in figure 4.3.

Advanced material characterisation includes a probability metric for specular and diffuse denoted by γ_s and γ_d respectively, where $\gamma_s + \gamma_d = 1$. By first conducting a specular included (SPIN) measurement, followed by a specular excluded (SPEX) measurement, these probabilities can be determined. For SAR, this is a rudimentary process and merely requires the specular component to be directed out of the system through a fixed port 16° across from the input port. For VAR, where a sample is mounted on a rotating stage in the centre of the sphere, this is far more convoluted and not feasible with most integrating spheres, save at 8° angles of incidence due to the fixed port location. It is possible to undertake SPEX measurements in variable angle goniophotometry, as opposed to an integrating sphere-based approach, but this not explored here. An

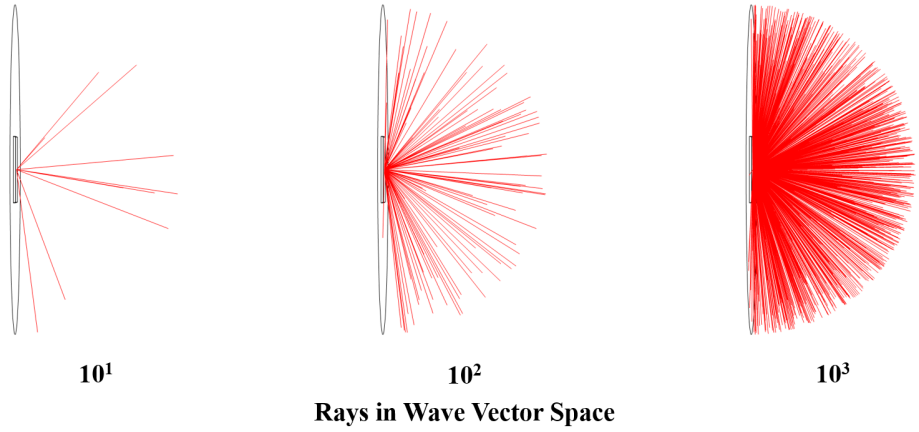

Figure 4.2: The hemispherical ray distribution about a sample of mixed diffuse and specular reflection. Here, the probability of such is $\gamma_d = 0.95$ and $\gamma_s = 0.05$ respectively.

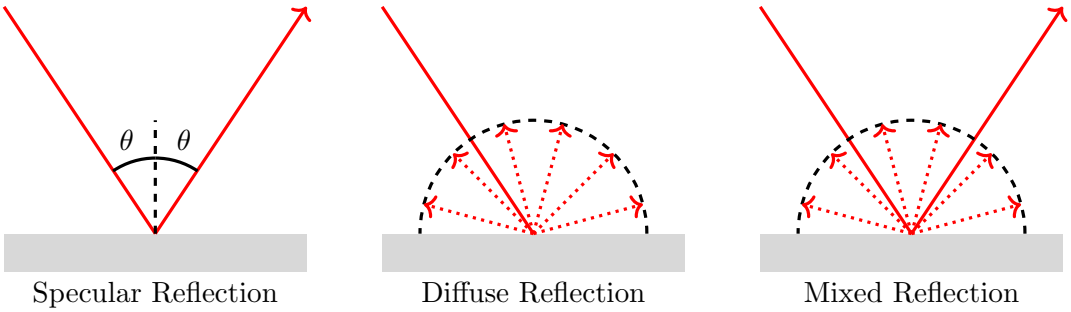

Figure 4.3: A graphical representation of specular, diffuse, and mixed surface reflections.

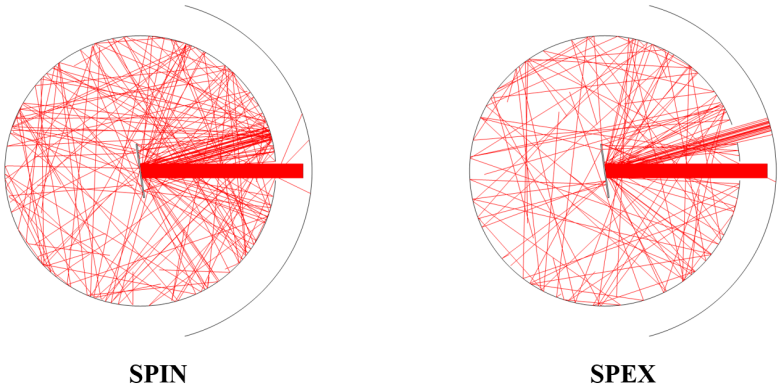

Figure 4.4: The effect of including (SPIN) and excluding (SPEX) the specular component of reflectance in VAR measurements for a given sample. Here, the probability of specular reflection is $\gamma_s = 0.3$. Particularly noticeable is the drop in ray density for SPEX measurements. These were simulated using optical ray tracing methods in COMSOL Multiphysics®† in a 2-D domain.

example of both SPIN and SPEX measurements using an integrating sphere with a sample fixed at 8° can be seen in figure 4.4.

4.1.2 The Integrating Sphere

4.1.2.1 Overview

Integrating spheres, also known as Ulbricht spheres [144, 145], are hollow spheres for which the internal wall is coated with a highly reflective, highly scattering material such as pressed barium sulphate ($BaSO_4$), smoked magnesium oxide (MgO), or polytetrafluoroethylene (PTFE) ($[C_2F_4]_n$) [146]. Light enters the sphere through a hole or 'port' on the side of the sphere. A sample is placed at a port on the opposite side of the sphere. A detector is placed at a third port, usually at the top or bottom of the sphere, and is shielded from light that has been reflected directly off of the sample by a baffle. This means that only the integrated light, that is to say the light reflected around the inside surface of the sphere, is incident on the detector. Ideally, the integrating sphere permits input light, directed at a sample to be reflected around the sphere without attenuation [147]. Such propagation of light causes the surface of the sphere to be illuminated uniformly with the light reflected off the sample, spatially integrating radiant flux. This can then be sampled by the detector and a value for reflectance calculated by comparing the signal to that from a surface of known reflectance.

Integrating spheres are never ideal, and subsequently various errors are introduced into a reflectometry system inclusive of one. Any one type of error may not be substantial enough to be detrimental to data accuracy; the combination of them will be. There are 10 different types, as reported by Clarke and Compton in 1986 [147], however only the most significant for this system will be explored here. These being single-beam sample absorption, general integration, diffuse reflectance screening, electronic dark, and detector recess errors.

$$\alpha(\lambda, t) = \frac{\tau_\alpha(t) R_c(\lambda)}{1 - R_c(\lambda)} \cong \frac{\bar{R}_c}{1 - \bar{R}_c} \qquad \text{for } \frac{\mathrm{d}}{\mathrm{d}t}\tau_\alpha \equiv 0 \tag{4.1}$$

$$\bar{R}_c \cong \frac{1}{701} \sum_{i=0}^{700} R_c\left(i + 3.50 \times 10^{-7}\right) \qquad \text{for } \lambda = 350 : 1,050 \text{ nm} \tag{4.2}$$

Figure 4.5 demonstrates how a real, non-ideal integrating sphere wall attenuates light on propagation. It is common that such wall coatings will have a reflectance of $R_c > 97\%$ over some proportion of the EM spectrum, and permits us to calculate a property known as relative integrating sphere efficiency, α. This property can be determined as shown

in equation (4.1), where τ_a is a time-based metric representing the integrity of the wall coating.

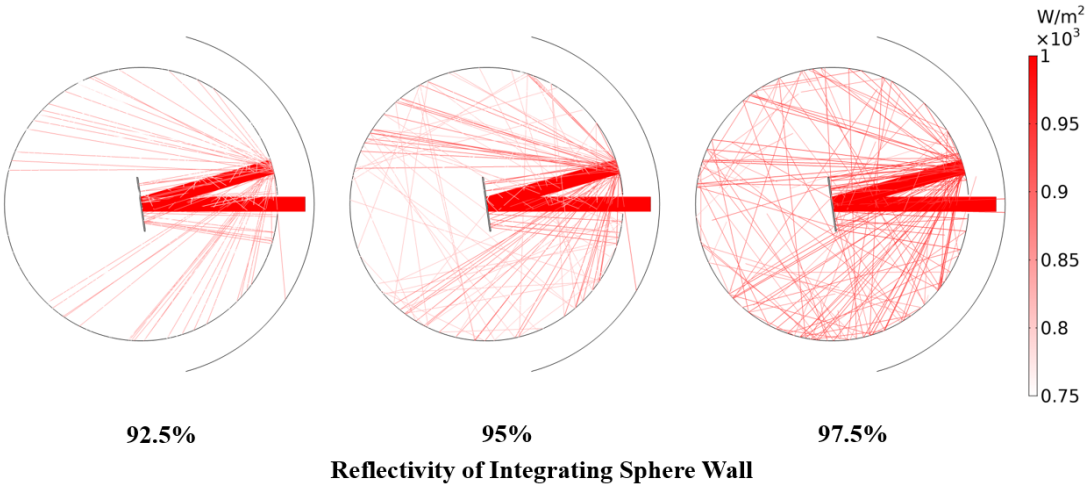

Figure 4.5: Real integrating sphere walls can exhibit significant transient light attenuation, as demonstrated here with three wall coatings of differing reflectance. The simulation period is 1.50 ns and wall reflectance is assumed to be independent of incidence angle. The sample is a perfect mirror to remove any non-wall related attenuation.

For a brand new coating, $\tau_a = 1$. For a properly maintained system with no permitted ingress of contaminants, this value will remain constant over time; the performance of the coating will not degrade, and $\tau_a'(t) = 0$, as shown in equation (4.1). Given the value of α tends towards 100%, wall-related attenuation errors can be negated as insignificant in causing deviation in the sample spectra taken using said sphere. Equation (4.2) shows how the average reflectance of the wall coating, $\bar{R}_c$, can be determined for the standard wavelength range used in solar PV applications - between 350 and $1,050$ nm.

4.1.2.2 Integration of Light

The physics supporting the use of the integrating sphere for spectrophotometric applications comes directly from the exchange of radiation between two predominantly diffuse surfaces. For instance, take two arbitrary diffuse surface areas, $\mathrm{d}A$, separated at their respective points of incidence by some distance, L. The exchange factor, $\mathrm{d}F$, that is to say the proportion of energy leaving the first surface that arrives at the second, is determined through the mathematical formulation shown in equation (4.3). Here, θ_n represents the angle of incidence on point P_n relative to the normal to the surface at which that point lays.

$$\mathrm{d}F_{12} = \frac{\cos(\theta_1)\cos(\theta_2)}{\pi L^2}\mathrm{d}A_2 \tag{4.3}$$

Relating this to any two points on the inner surface of a sphere, in this case an integrating sphere with a typical highly diffuse reflectance, presents a far simpler formulation. Take first the aforementioned scenario remapped for a spherical shape as shown in figure 4.6.

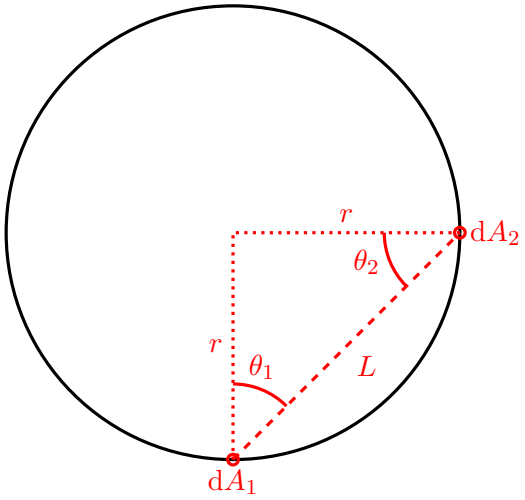

Figure 4.6: Taking two arbitrary points within a sphere of highly diffuse reflectance used in the determination of the exchange factor ξ, for integrating spheres.

From figure 4.6, it can be seen that, for any position of $\mathrm{d}A_1$ or $\mathrm{d}A_2$, $\theta_1 = \theta_2$. It can also be seen that $\frac{1}{2}L = r\cos(\theta)$, where r is the radius of the spherical medium. Taking this information, we can simplify equation (4.3) to obtain a relation for integrating spheres. This is shown in equation (4.7).

$$\mathrm{d}F_{12} = \frac{\cos^2(\theta)}{\pi L^2}\mathrm{d}A_2 \tag{4.4}$$

$$= \frac{\cos^2(\theta)}{\pi\left(2r\cos(\theta)\right)^2}\mathrm{d}A_2 \tag{4.5}$$

$$= \frac{\cos^2(\theta)}{4\pi r^2\cos^2(\theta)}\mathrm{d}A_2 \tag{4.6}$$

$$= \frac{\mathrm{d}A_2}{4\pi r^2} \tag{4.7}$$

Equation (4.7) shows how $\mathrm{d}F_{12}$ is independent of both angle, θ, and distance, L. With respect to integrating spheres, this means that regardless of the original source of surface reflection, $\mathrm{d}A_1$, the destination, $\mathrm{d}A_2$, receives a fraction of this reflection that is equal to the fractional surface area of the sphere held by that point. This shows how radiation is spread equally about the surface of an integrating sphere when applied with a sufficiently efficient diffuse reflectance coating, and demonstrates how they have the ability to quantify the reflectance, absorption, and transmission of different samples.

4.1.2.3 Determination of Sample Reflectance

Sample reflectance, R_x, as defined in equation (4.8), is determined through the ratio of two intensity spectra, S, measured as counts, and calibrating to a sample of known reflectance, R_y; a reflectance standard. The sample's intensity spectrum, S_x, is divided by the standard's, S_y, and a ratio is formed indicative of the *relative* difference between the two. To quantify this as *absolute* reflectance, as opposed to relative reflectance, this ratio must be multiplied by the true reflectance values for the standard, R_y, concerning the same angles, θ, wavelengths, λ, and polarisation, φ. R_y was determined by LabSphere® with an error of $\pm 0.71\%$.

$$R_x(\theta, \lambda, \varphi) = \frac{S_x(\theta, \lambda, \varphi)}{S_y(\theta, \lambda, \varphi)} R_y(\theta, \lambda, \varphi) \tag{4.8}$$

The single-beam sample absorption error occurs as a result of a sample with given reflectance, R_x, changing the average reflectance of the integrating sphere wall (for side–mounted samples) [148] or throughput of the sphere (for centre-mounted samples). In the case of systems with a centre–mounted sample, the throughput of the system changes as opposed to the reflectance of the wall. This error is counteracted using a second beam, whereby the sample or standard is removed from the path of the input light, but not removed from the sphere. Instead, the light first impacts the sphere wall, and secondary reflections are incident on the sample.

Taking the measured intensity for both the sample and standard under this condition, $S_{c,x}$ and $S_{c,y}$ respectively, a corrective factor can be determined and must be applied to equation (4.8) to counteract this error [149]. This is taken into account in equation (4.9), where the corrective factor is shown in red.

$$R_x(\theta, \lambda, \varphi) = \left(\frac{S_x(\theta, \lambda, \varphi)}{S_y(\theta, \lambda, \varphi)} \right) \left(\frac{S_{c,y}(\lambda, \varphi)}{S_{c,x}(\lambda, \varphi)} \right) R_y(\theta, \lambda, \varphi) \tag{4.9}$$

The electronic dark error is specific to spectrophotometers rather than integrating spheres, but must be considered when calculating reflectance. Electrical noise causes the pixels within spectrometers to sit at non-zero values even when the input light is off. A dark spectrum, S_d, must be taken and subtracted from every spectra shown in equation (4.9) to correct the zero error that would otherwise be present in the data. Given there is no input light, this correction is independent of angle of incidence but remains dependent on wavelength; each pixel in a spectrometer has its own noise and is tuned to a specific wavelength of light. This second corrective factor is also highlighted

as red in equation (4.10), a further expansion of equation (4.9).

$$R_x(\theta,\lambda,\varphi) = \left(\frac{S_x(\theta,\lambda,\varphi) - S_d(\lambda)}{S_y(\theta,\lambda,\varphi) - S_d(\lambda)}\right)\left(\frac{S_{c,y}(\lambda,\varphi) - S_d(\lambda)}{S_{c,x}(\lambda,\varphi) - S_d(\lambda)}\right) R_y(\theta,\lambda,\varphi) \tag{4.10}$$

4.1.2.4 The Negative Reflectance Problem

In a real spectrophotometric system, there will be a component of variance applied to each of the measured spectra, S, resulting from fluctuations in incident light intensity, sensor noise, and mechanical imperfections. Mechanical imperfections will typically relate to the diffraction grating; microscopic imperfections and, in the case of the monochromator, alignment error between the grating and slit. Vibration can also cause noise on top of a measured spectrum due to the interference it causes at the optical fibre coupling, though this is only particularly relevant for systems containing optical fibres and/or spectrometers, or dielectric-based sensors that are external to the optical system itself (introducing the need for a coupling between the two). While these factors are very difficult to apply to a discrete formulation, it is important to note one particular condition that will cause computational problems if not considered in advance.

Let us take S_x, S_y, and S_d. As in equation (4.10), we need to subtract the electronic dark spectrum from the measured spectra. Assume we are measuring a particularly dark sample, that is to say one of low reflectance. This would imply, regardless of the type of sensor used in the system, that $S_x \equiv S_d$. If the aforementioned variance causes significant enough noise on top of either S_x or S_d, there is a possibility that, for certain values of λ, $S_d > S_x$. This would result in negative reflectance – an impossibility as outlined by the laws of physics. This would be particularly true in regions of poor sensor resolution. Under such conditions, this is not a measure of reflectance, but instead an identifier of a *very* weak signal. Increasing the dynamic range of the sensor itself can reduce this risk, but is dependent on its quality and design.

$$R_x(\theta,\lambda,\varphi)\begin{cases} > 0 & \text{for } S_d(\lambda) < S_x(\theta,\lambda,\varphi) \\ = 0 & \text{for } S_d(\lambda) \equiv S_x(\theta,\lambda,\varphi) \\ = 0 & \text{for } S_d(\lambda) > S_x(\theta,\lambda,\varphi) \end{cases} \tag{4.11}$$

In computation, we can simply floor the reflectance value at a minimum of zero, in-line with theory, as opposed to permitting the calculated reflectance to drop below zero to a negative value. This is shown in equation (4.11).

4.2 Underlying Principles and System Design

4.2.1 Spectrophotometry

Spectrophotometers contain an entrance slit followed by a transmission grating. To understand the purpose of the entrance slit, and how light interacts with it, we must consider Huygen's principle. This states that a wavefront can be considered as an infinite number of points, each a source their own wavefront travelling in the same direction as of that from which they originated. At the instant of interaction between the original wavefront and the slit, spatially coherent light is diffracted in all directions simultaneously. Assuming the distance between the source of light and the slit is far greater than the width of the slit itself, such an interaction will create a Fraunhofer diffraction pattern. These patterns feature a central intensity maximum, surrounded by much lower intensity peaks. These lower intensity peaks are either discarded, or more commonly collimated by a series of focal mirrors to prevent unnecessary degradation of signal intensity within the spectrometer itself.

Once the light input through the entrance slit has been collimated, it is incident, either directly or through a series of lossless mirrors, onto a diffraction grating. This splits the input light into individual wavelengths, creating a rainbow-like pattern that is incident on the CCDs within the device. It is the CCDs that then convert this light, now incident on each CCD as a narrow band of wavelengths, into a digital signal measured as an intensity. Each CCD is often referred to as a pixel, where the relationship between the diffraction grating and the wavelength measured at each pixel is outlined by the features of the grating itself. This information is typically provided by the manufacturer at the point of construction, as spectrophotometers can be fit with a wide variety of different gratings to fit various applications.

Here, a high-resolution B&W Tek Glacier-X BTC112E-ST1 linear CCD spectrophotometer is used, connected to an integrating sphere via a ThorLabs BFL200LS02 round-to-linear (RTL) optical fibre bundle. The BTC112E-ST1 detects light within the sphere across its certified wavelength sensitivity range of 350 to $1,050$ nm with a resolution of ~ 0.5 nm/pixel. It contains an 11-bit sensor array for a total number of $2,048$ light sensitive pixels. Each pixel, n, is calibrated to be sensitive to a specific wavelength with a 16-bit dynamic range, yielding a total number of $65,536$ discrete intensity levels to which each wavelength can be quantified. Of these $2,048$ pixels, $1,777$ are used to quantify light intensity, I, between the aforementioned wavelengths, whilst the remain-

ing 271 are 'dummy' pixels – not used in the acquisition of spectral data. These are assigned as such due to the previously mentioned swappability of the grating. In the system, the grating offers insufficient signal integrity across these wavelengths, and as such the pixels corresponding to them are unused. Those remaining are used to sample light spectra are outlined in equation (4.12) alongside their absolute wavelengths in equation (4.13).

$$254 \leq n \leq 2,030 \tag{4.12}$$

$$349.5 \text{ nm} \leq \lambda \leq 1,050.4 \text{ nm} \tag{4.13}$$

A mathematical formulation, linking each pixel number, n, to their respective detected wavelength, λ_d, is outlined in equation (4.14). The *detected* wavelength is not the same as *absolute* wavelength, λ, due to the presence of a wavelength conversion error, λ_e, within the spectrophotometer. This error varies across the absolute wavelength spectrum and can be accurately approximated to an exponential curve of the form outlined in equation (4.15). Absolute wavelength can then be determined using both λ_d and λ_e, as shown in equations (4.16) and (4.17).

$$\lambda_d(n) = a_0 + a_1 n + a_2 n^2 + a_3 n^3 \tag{4.14}$$

$$\lambda_e(n) = b_0 \left(e^{b_1 n} - e^{b_2 n} \right) \tag{4.15}$$

$$\lambda(n) = \lambda_d(n) - \lambda_e(n) \tag{4.16}$$

$$\therefore \lambda(n) = a_0 + a_1 n + a_2 n^2 + a_3 n^3 - b_0 \left(e^{b_1 n} - e^{b_2 n} \right) \tag{4.17}$$

Here, the wavelength calibration and error coefficients, a and b respectively, are certified by the manufacturer or derived from their data. The curve showing the relationship between pixel number and detected wavelength can be seen in figure 4.7a. From this data it is also possible to quantify sensitivity based on the number of pixels per-unit detected wavelength. A higher value will be indicative of increased sensitivity within that respective detected wavelength range. This data is shown in figure 4.7b, and the values of each coefficient in equation (4.17) are outlined in table 4.1.

It is also important to realise the presence of a differential between actual wavelength, λ, and detected wavelength, λ_d, where the latter is the value for wavelength reported by the spectrophotometer. Equation (4.15) represents this differential as a function of wavelength. This data is visualised in figure 4.8, and, although very small, should be considered in the evaluation of reflectance for all of the samples. The accurate

Table 4.1: Outlining the wavelength calibration, a, and error, b, coefficients.

Coefficient	a_0	a_1	a_2	a_3	b_0	b_1	b_2
Value	218.821	0.529	-5.536	-1.651	-3.104	-5.061	-5.062
Multiplier	1	1	10^{-5}	10^{-9}	10^{4}	10^{-3}	10^{-3}

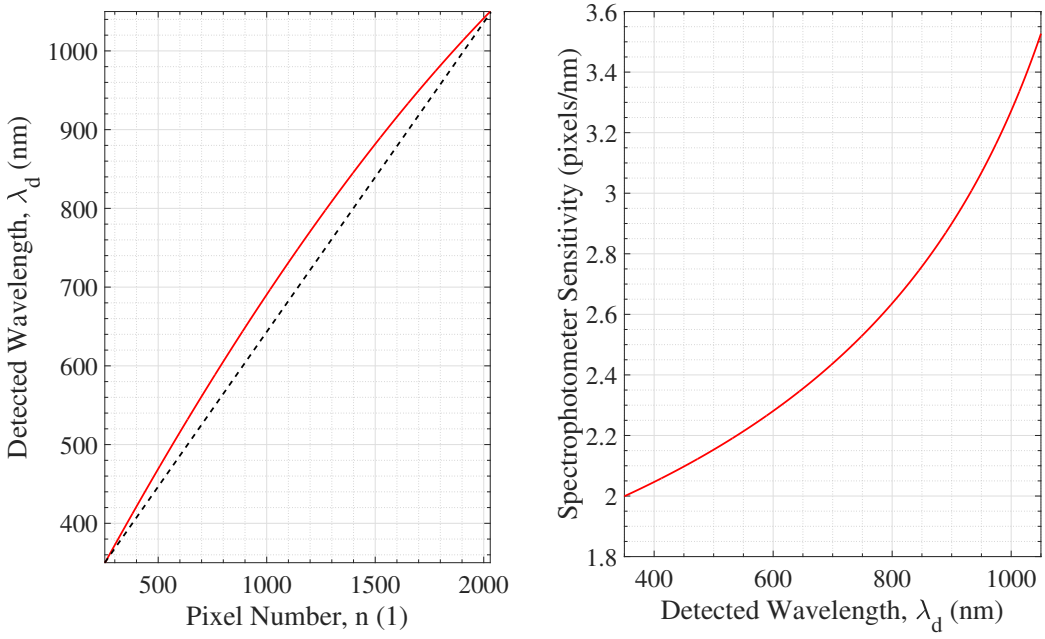

(a) (b)

Figure 4.7: The pixel to wavelength relation for the system's spectrophotometer (a), showcasing a minimum detected wavelength of 350 nm and a maximum of 1,050 nm, as well as the sensitivity variation across this wavelength range (b). The dashed line in (a) is indicative of uniform wavelength sensitivity, whereby divergence above this line shows greater sensitivity, and divergence below shows lesser. In this case, the spectrophotometer is more sensitive to wavelengths in the visible to NIR range (600 to 850 nm).

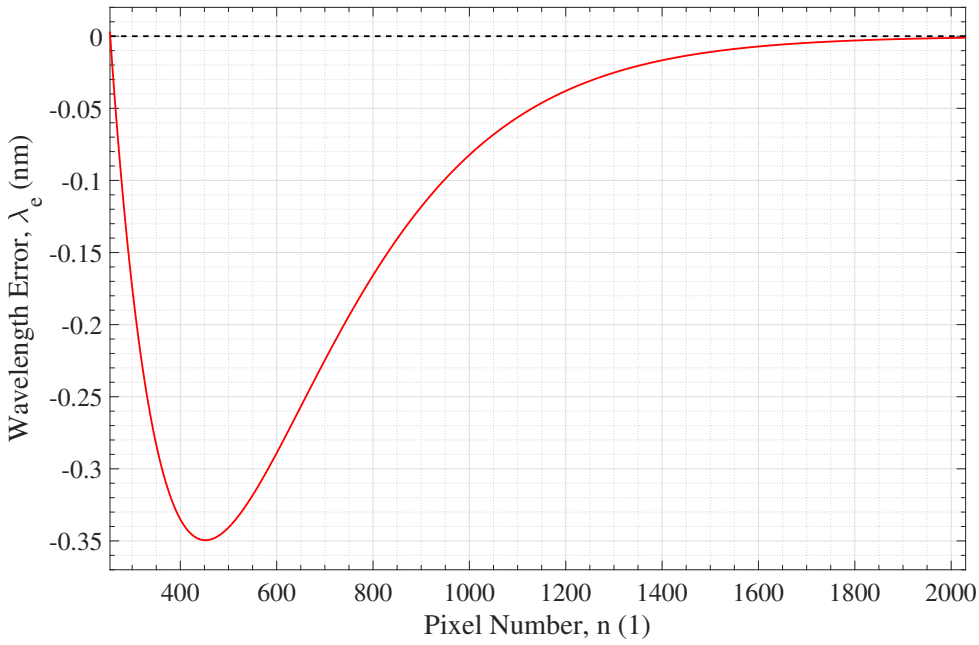

Figure 4.8: The certified wavelength error, λ_e, for the B&W Tek Glacier-X BTC112E-ST1 spectrophotometer in accordance with a known standard.

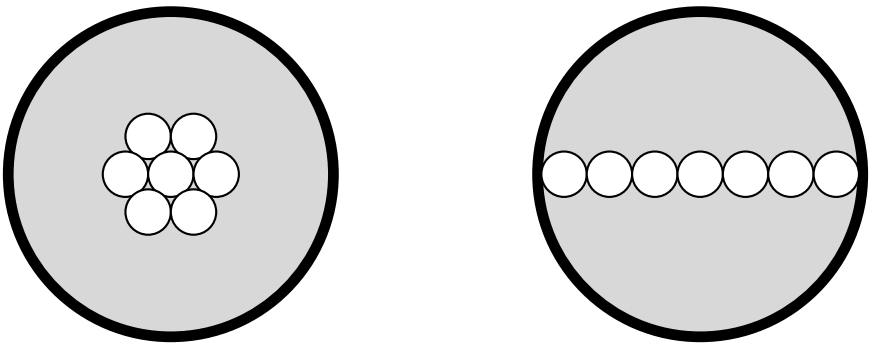

Integrating Sphere Side Spectrophotometer Side

Figure 4.9: A cross-sectional view of the optical couplings at either end of the BFL200LS02 RTL fibre bundle. The outer conduit (black) is shown alongside the internal shielding (grey) and optical fibre cores (white).

determination of reflectance demands the appropriate alignment of the BFL200LS02 RTL fibre optic cable with the entrance slit of the spectrophotometer. This type of fibre has a round bundle of seven optical fibres on the integrating sphere side of the system, and brings them to a linear formation on the spectrophotometer side. This is shown in figure 4.9. This fibre was chosen to serve as the optical coupling between sphere and sensor because this fibre dispersal pattern aligns far better with slit on the spectrophotometer. This is because the entrance slits are, likewise, arranged in a linear formation. The use of a round coupling against slits such as these is permissible, but will result in a lossy signal as light forwarded to the spectrophotometer must ricochet around the coupling mechanism before being aligned appropriately to pass through.

4.2.2 Spectral Irradiance

The ARS uses a quartz-halogen lamp, with a steady-state power dissipation of 100 W, configured as a point light source. This is achieved using a series of plano-convex lenses employing Köhler illumination. Köhler illumination is used to ensure only a uniformly distributed circular spot of light is incident on the illuminated sample, free from any optical aberration, rather than an image of the filament within the lamp. This principle is outlined in figure 4.10. A Glan-Thompson polariser is also used to switch between S- and P- polarisations and can be dropped out of the system entirely for unpolarised measurements. Such illumination is more indicative of the natural lighting conditions from a variety of sources, including the Sun. The LabSphere RT-060-SF is the integrating sphere used within the ARS. This sphere has a diameter of 15 cm and has a Spectraflect® diffuse reflectance coating with an operational range of between 300 and 2,400 nm.

A reflectometer will, commonly, illuminate a sample with only one wavelength of light at a time using a monochromator. Such systems are said to work under monochromatic illumination. The ARS, however, works under polychromatic illumination; seldom seen in reflectometry systems. All light from the light source is permitted to enter the integrating sphere simultaneously. No two light sources will have identical emission spectra, though due to the use of a reflectance standard, as in equation (4.10), this does not have any effect on measurements taken with different lamps. The output from such a light source can be approximated to a black body emission spectrum. By displaying the output from the spectrophotometer when the sphere is illuminated without any sample present, it is possible to determine the spectral sensitivity of the spectrophotometer.

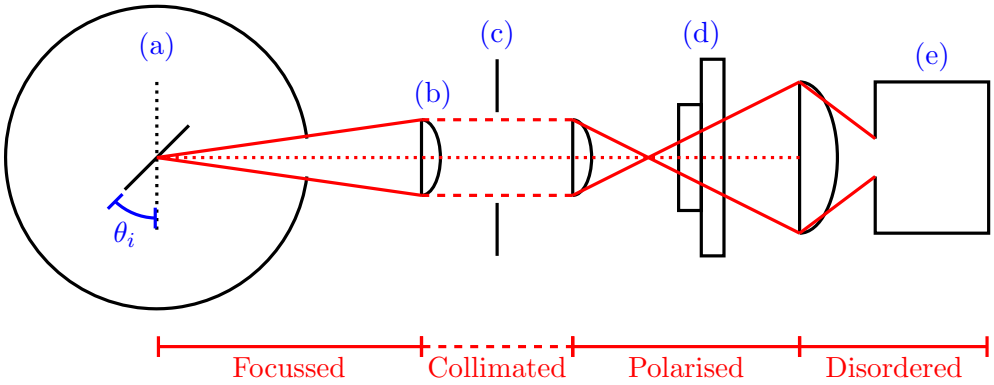

Figure 4.10: The system outline for the ARS. Labelled are the integrating sphere and centre-mounted sample (a), focal lenses (b), optical shutter (c), Glan-Thompson polariser (d), and the quartz halogen light source (e). The detector is situated at the bottom-centre of the sphere (below the intersection between the dotted and solid sample lines within the integrating sphere (a).

This data is shown in figure 4.11.

The ARS has a low irradiance below 450 nm. This is appropriate to prevent the solarisation of the RTL optical fibres that are rated for a minimum wavelength of 400 nm. Wavelengths approaching and below the NUV region of the spectrum have excessively high energy levels that can damage optical fibres with low hydroxyl ion content, particularly when exposed for extended periods of time. Damage by solarisation causes the glass to become translucent with an orange tint, as opposed to being transparent, prompting it to attenuate light propagation asymmetrically. Quartz-halogen lamps do not have high spectral radiance in the NUV, instead peaking at $\sim$ 960 nm as seen in figure 4.11.

Despite this system being designed foremost for angular-resolved reflectance measurements, it can also be used to do traditional side–mounted SAR and transmission measurements. This configuration requires the integrating sphere to be moved along the beam path, bringing the focal point from the centre to the back (for reflectance) or to the front (for transmission). The system incorporates three rotational stages and one linear stage, each driven by dual or single tuned piezoelectric resonance coil assemblies, respectively. The rotation stages incorporate opto-electronic and magnetic sensors to determine at which angle, between 0 and 360°, the stages are situated with a resolution of 0.0025°. The electromechanical stages used in the ARS are driven by ThorLabs Elliptec™ based coils. These are low-power, robust, and versatile devices capable of

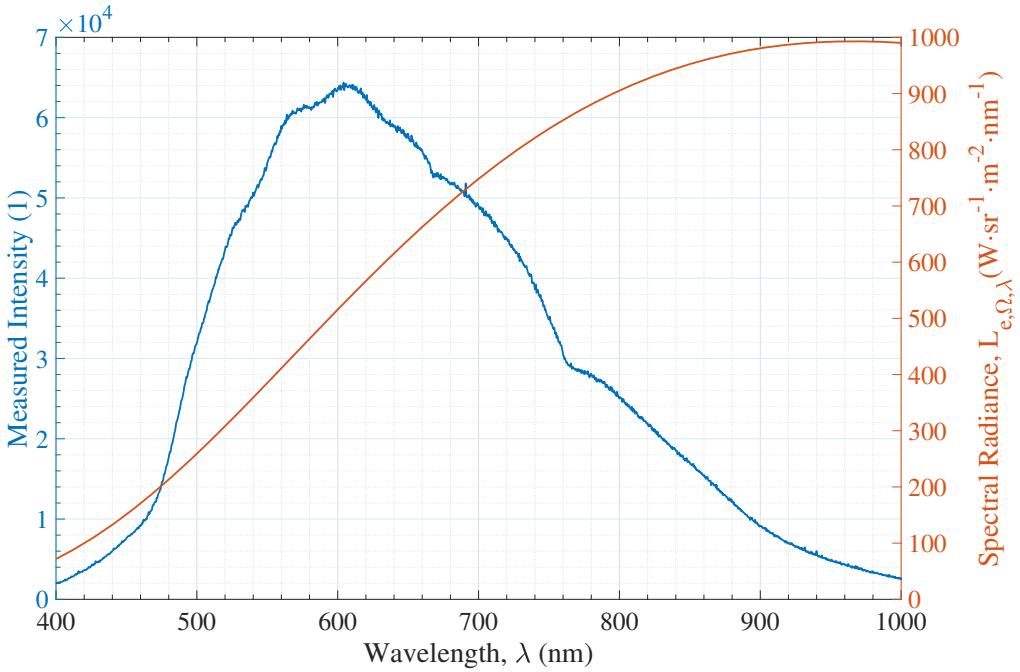

Figure 4.11: The polychromatic irradiance detected for the light source alongside its calculated black body emission spectrum. Black body spectral radiance data is calculated for a light source with colour temperature 3,000 K (the colour temperature of the lamp) using SpectraPlot [150].

being used in a variety of OEM applications thanks to their open serial communication protocols. A detailed cross-sectional schematic of the integrating sphere component of the ARS system can be seen in figure 4.12.

4.2.3 System Automation and Software

4.2.3.1 Code Availability and Declarations

The software shown here, developed by the author and named OptiComp, is open–source and available to download, redistribute, and modify in line with the terms of the Creative Commons Attribution 4.0 International (CC BY 4.0) licence[1]. A software repository[2] for this project has been created and can be accessed by request to the author. Proprietary component(s) used for the interface to specific hardware elements will be excluded from this report and online repositories in line with the terms enacted by the vendor(s). Specific segments of (open–source) code that are referenced in this section can be viewed in the supporting materials (section D).

[1] https://creativecommons.org/licenses/by/4.0/
[2] https://github.com/JackTyson/OptiComp

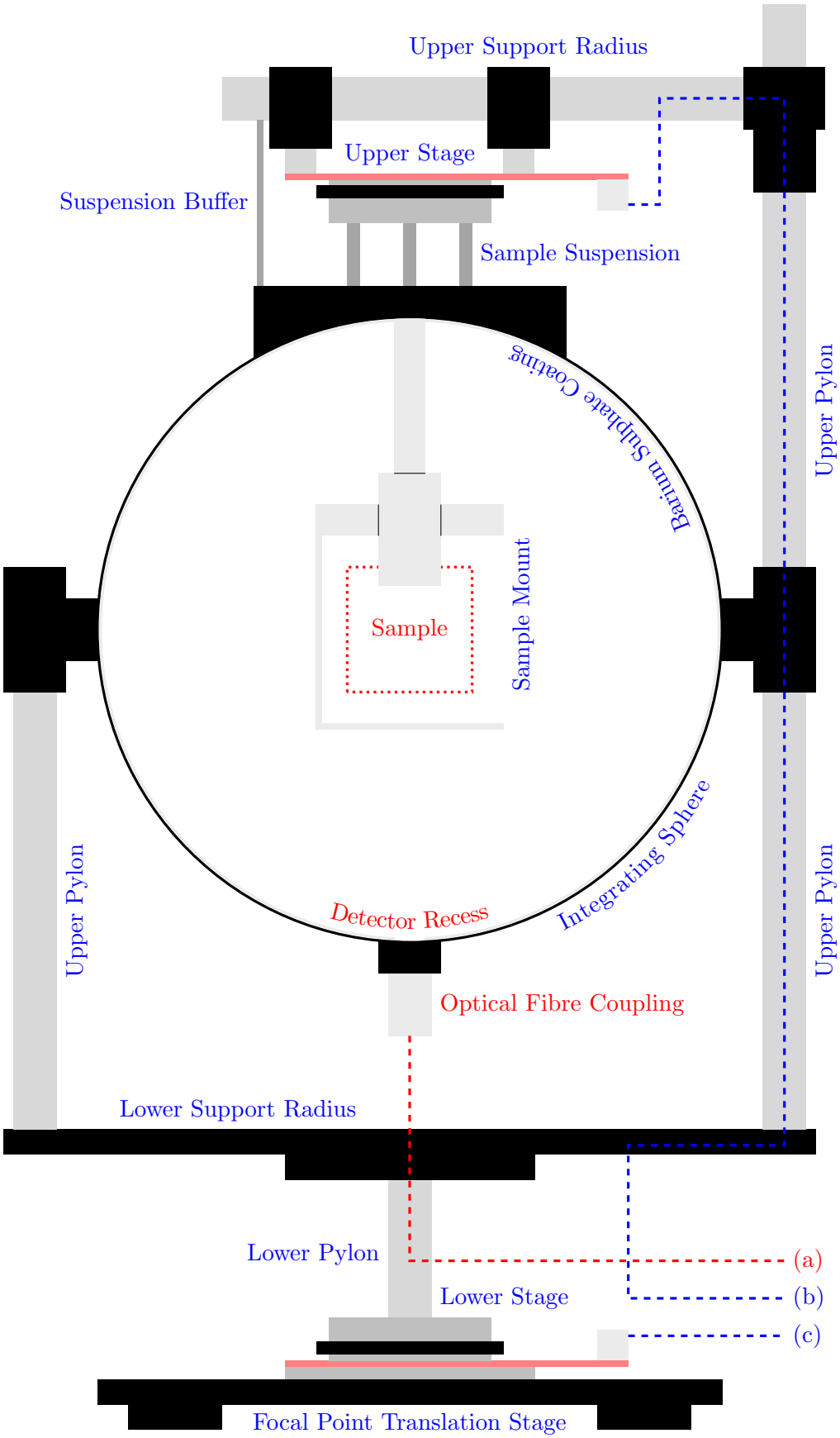

Figure 4.12: Cross-sectional schematic of the integrating sphere configuration, showing the optical fibre (a), upper stage (b), and lower stage (c) connections.

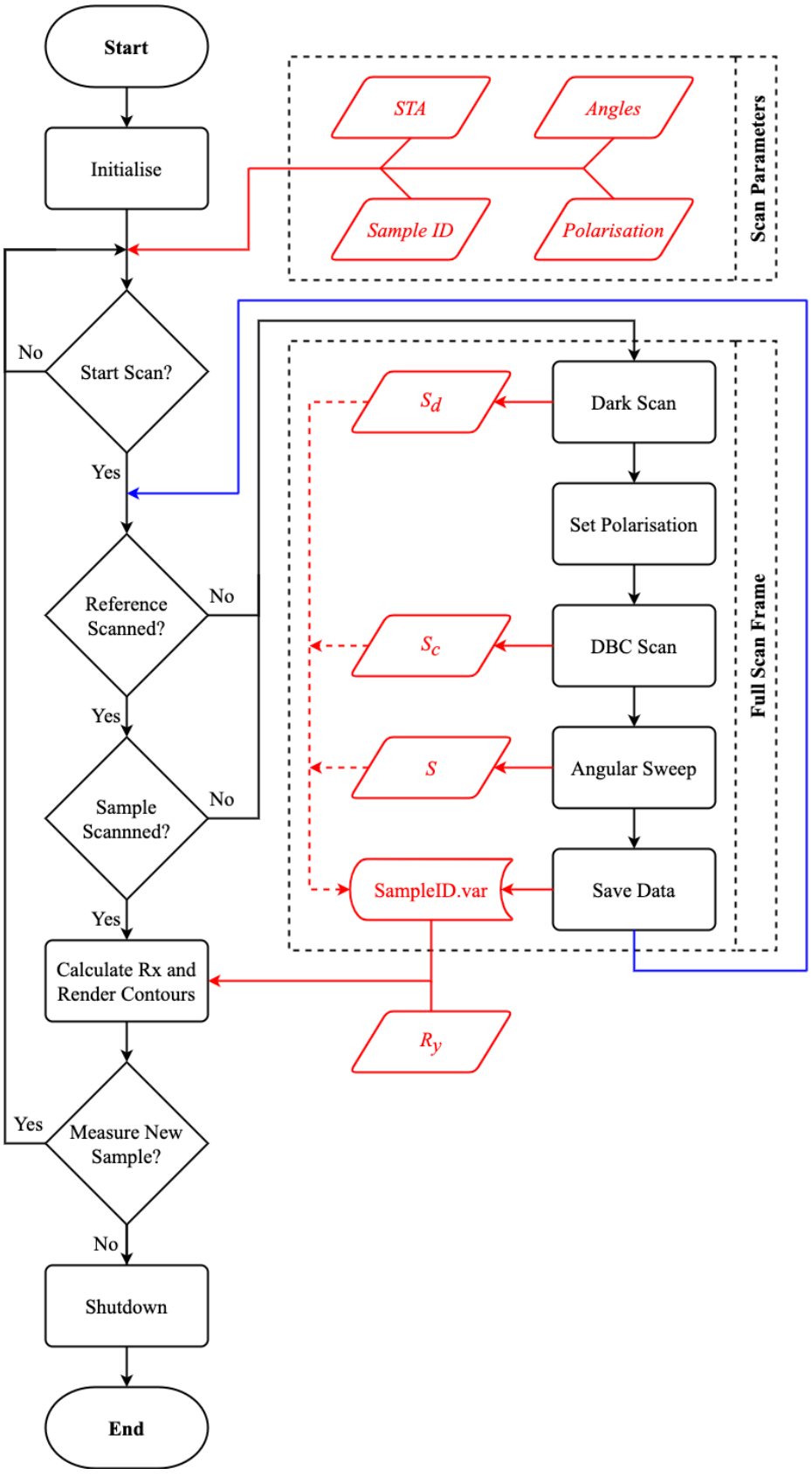

Figure 4.13: A flowchart-based view representing the process of taking centre-mount measurements using the ARS. Parts highlighted in red represent data operations, whilst the blue shows the return line from the main scanning subroutine.

4.2.3.2 Overview

All aspects of the system, save moving the porthole cover for double beam correction measurements, have been automated to significantly reduce the probability of human error during the extensive measurement process and to speed up the collection of results. A standard operating procedure (SOP), in the form of a flowchart, has been made to visualise the measurement process concisely and can be seen in figure 4.13. The system's automation is governed by tailor–made open–source software written in Python 3.9 against the aforementioned SOP. The software utilises several open source libraries to provide its functionality. A graphical user interface (GUI) is written using the Tkinter, Matplotlib, Numpy, and Python Imaging Library (PIL) frameworks. Each framework focuses on a particular area within the software. For example, Tkinter renders the main window, as well as providing elements to which the user can interact (buttons, sliders, tabs, and dropdown menus). These are referred to as Tkinter widgets. Matplotlib and Numpy work together in the collection, processing, and displaying of data acquired from the B&W Tek spectrophotometer, whilst the PIL maintains the stream from the system's internal camera.

4.2.3.3 Graphical User Interface and Control

The base GUI is first created as a Tkinter window object by invoking the command sequence shown in figure D.1. It is subsequently populated with Tkinter widgets including buttons, sliders, drop–down menus, a PIL streaming window, and a live data readout zone. This zone shows the current intensity measurement with respect to wavelength as read directly from the BTC112E spectrophotometer using the proprietary B&W Tek software development kit (SDK), which will not be shown here. The chosen layout for this main window, consisting of all these elements, can be seen in figure 4.14.

As shown in figure 4.14, three core control areas were placed across the main window: software, system, and hardware control. The software control area manages user login, gives access to the standard operating procedure (SOP), and enables basic data management functionality. The hardware control area primarily deals with the display of system status, scan progress, and scan mode selection controls. Centre–stage is the system control area, permitting the user to input scan parameters such as angular range, scans to average (STA), reflectance standard selection, and polarisation. Each of these variables undergo validation prior to any scans being taken. This is accomplished using a gatekeeper subroutine that is called when a scan sequence is started. The subroutine

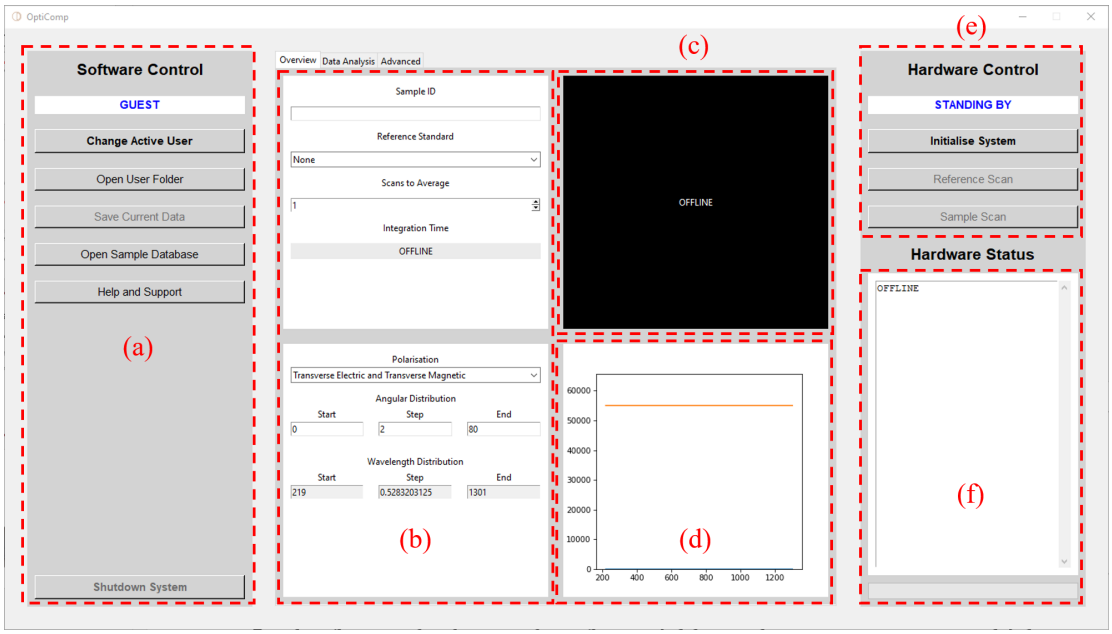

Figure 4.14: The main screen of the reflectometer's user interface showing the software controls (a), scan settings (b), system camera (c), live data readout (d), scan controls (e), and the system console (f).

written for this is shown in figure D.2. Alongside these controls are the internal camera live–stream (upper–right quadrant), and the live data readout (lower–right quadrant); a design decision made to give the user a greater idea of what is currently happening with the system. A progress bar, along with estimated time remaining, is also included at the bottom of the hardware control area, below the hardware status readout.

In checking the input parameters using the gatekeeper subroutine, the angular distribution requires particular attention, as entering the incorrect sequence of values here can cause the system to behave erratically, and possibly over–exert the fragile BFL200LS02 RTL optical fibre. As shown in figure 4.12, this cable is connected to the integrating sphere from the bottom, where, at excessive lower stage rotation angles, it can get easily wound around the lower support radius and become damaged as a result of torsion. The criteria for a valid entry under this heading requires the following:

- the start angle must be greater than or equal to zero and be less than the end angle;
- the step size must be greater than or equal to 1°;
- the end angle must not be greater than 80° and be greater than the start angle.

Failing any of these criteria will throw an exception within the program, and prevent a

scan from starting until the problem(s) is(are) remedied. Note that if the step size is greater than the difference between the start and end angles, then only these two angles will be measured, and if the start and end angles are the same value, then only this angle will be measured regardless of the step size input.

A higher value of STA, N, smooths much of the noise measured in a single spectrum. Typically, $3 \leq N \leq 5$ is adequate for most measured samples. However, darker samples require a higher value here to counteract the slightly more dominant electrical dark noise due to a decrease in the signal-to-noise ratio (SNR). For such samples, the STA should be set in–line with $5 \leq N \leq 10$. For $N > 10$, scan time is proportionately increased for little gain in noise reduction. As well as reducing sample throughput, longer scans can result in changing properties in optically less-stable samples and so should be avoided where possible. The number of spectra required per sample, n_S, is determined by the STA (N), the number of polarisation modes, n_φ, and the total number of angles scanned, n_θ, which are all user-defined input parameters. This is shown arithmetically by equation (4.18).

$$n_S = 2Nn_\varphi n_\theta + 1 \tag{4.18}$$

Here, the single dark scan is added on, and the sample scans are multiplied by two to take account of the reference scans (mirroring the sample scans). The number of polarisation modes, n_φ, can be either two or one depending on whether S and/or P modes are selected, respectively. If no polarisation is desired, that is to say hybrid mode, then $n_\varphi = 1$. Let us assume that we wish to take five STA, for both S- and P-polarisations, and for an angular distribution of $\theta = 8 : 1 : 80°$. Using equation (4.18) we can determine that the system must take $n_S = 877$ spectra – a considerable amount of data to manage and process.

To make a comparative statement, let us assume the integration time, t_i, the period over which the system accumulates light for a discrete intensity measurement, is 2 s. Now, in a manually-controlled system, the operator will need to adjust the system to a new angle, polarisation, and/or configuration dependent on the stage in the process workflow. Let us assume that these interactions would take an average of 10 s each. We can then determine that the time to fully complete a reference and sample scan with a manual system would be $\sim$ 3 hours. Taking the automated system, with an average hardware response time, t_r, of 0.5 s between measurements, this processing is reduced to just over 37 min – almost 5$\times$ faster. This also takes into account the four occasions

the operator must interact with the automated system throughout the measurement process to change the port covers. The time for a complete measurement, t_m, as shown here, can be calculated using equation (4.19). Note that the time to switch over the port covers is denoted by t_p.

$$t_m = t_i t_r n_S + 4t_p \tag{4.19}$$

$$= 2t_i t_r N n_\varphi n_\theta + 4t_p + 1 \tag{4.20}$$

A sequencing subsystem provisions custom-made frameworks for the correct and reliable operation of the system hardware. To correctly sequence such a convoluted series of measurements, a process needed to be drafted in software to better visualise the succession of both the virtual and physical events required to take place, as well as outline their inter-dependencies. This is employed on top of the gatekeeper subroutine shown previously, which in of itself only prevents accidental parameter entry, not ensuring reliable system operation.

For example, the integration time of the spectrophotometer needs to be calibrated to the reference sample at the point of highest reflection. Failure to correctly set the integration time at this point will cause the erroneous clipping of spectra to be measured later. This highlights the importance of selecting a suitable reflectance standard for a given sample; one that is more reflective than the sample itself by around 10 to 15%. For data resolved against angle and polarisation, the point of highest reflectance is at an incident angle of 80° under S-polarisation. This polarisation mode is used for this calibration due to its monotonically increasing magnitude for increasing angles of incidence. On non-textured samples, P-polarised light does not behave like this, and instead dips to a minimum before rising again, due to the presence of Brewster's angle.

4.2.3.4 Data Handling and Storage

Upon completion of a measurement series, all spectral data is stored in a composite data matrix of a consistent structure, saved with the suffix `.var`. These matrices are created and saved using open-source frameworks, enabling it to be opened and processed in other software packages in lieu of the built-in alternative. Such a file structure enables us to store all the required information for the determination of sample reflectance, R_x, in one ordered file. The structure of this data matrix is shown in figure 4.15.

Within the composite data matrix there are sub-matrices, **A** and **B**, containing spectral

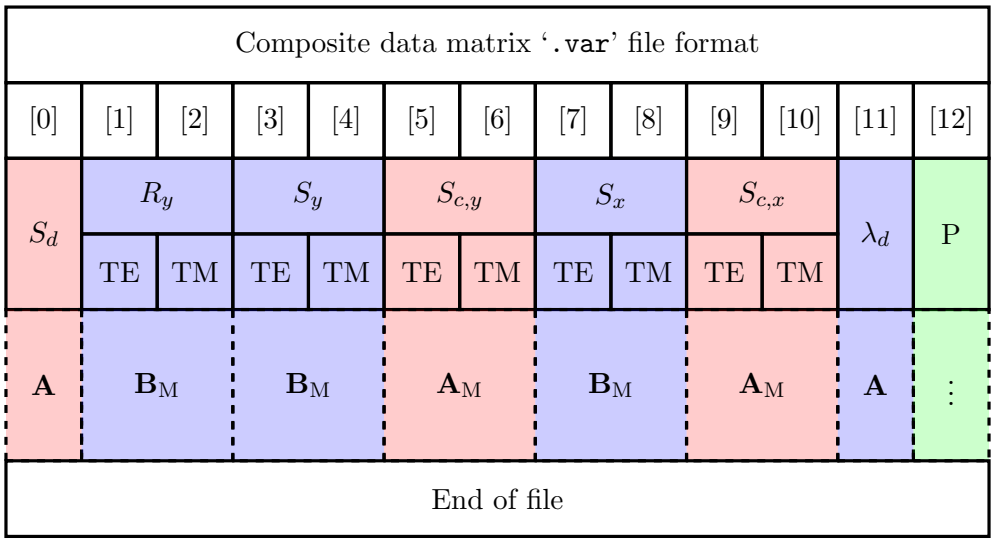

Figure 4.15: The format for all composite data matrices saved through the OptiComp software. Red represents error correction variables, whilst blue is for reflectance determination variables, and green shows sample-specific parameters stored within the data file. The sub-matrices, **A** and **B**, are 1- or 2-D respectively, containing spectral data linked to the index in which they are stored.

data, S, acquired using the spectrophotometer. These matrices have a format as shown in equations (4.21) and (4.22), respectively. Here, $n_{(\min)} = 254$ and $n_{(\max)} = 2,030$, whilst $\theta_{(\min)}$ and $\theta_{(\max)}$ are user defined, but must comply with the relationship $0 \leq \theta_{(\min)} \leq \theta_{(\max)} \leq 80$. In the case where SAR measurements are requested, that is to say $\theta_{(\min)} = \theta_{(\max)}$, then sub-matrix **B** will compress into the same format as that of **A**.

$$\mathbf{A_M} = \begin{pmatrix} I_{n(\min)} \\ \vdots \\ I_{n(\max)} \end{pmatrix}_M \tag{4.21}$$

$$\mathbf{B_M} = \begin{pmatrix} I_{n(\min),\theta(\min)} & \cdots & I_{n(\min),\theta(\max)} \\ \vdots & \ddots & \vdots \\ I_{n(\max),\theta(\min)} & \cdots & I_{n(\max),\theta(\max)} \end{pmatrix}_M \tag{4.22}$$

The minimum and maximum values for n are statically defined in accordance to information shown in equation (4.12) as to which pixels relate to the certified wavelength range of this system, whilst negating the previously mentioned 'dummy' pixels. In figure 4.15, P represents parameter data stored at data index 12. This contains important information regarding the selected scan parameters for that sample, including (but not

necessarily limited to): STA, selected polarisation(s), wavelength distribution, angular distribution, selected reflectance standard, and the sample name.

4.3 Limitations

Although VAR measurements are enlightening, there are some innate limitations to this form of reflectometry that should be mentioned. There are four types of measurement that this system is capable of, each requiring a slightly different configuration of the integrating sphere and sample stage. These configurations are: center-mount standard angle reflectance (CMSAR), center-mount VAR (CMVAR), side-mount standard angle reflectance (SMSAR), and side-mount standard angle transmission (SMSAT).

The data forthcoming showcases the distinctiveness of this reflectometry system and are therefore recorded by means of the CMVAR configuration. Note that the ARS employs the double-beam correction measurement for all reflectance modes. The use of a center-mount sample stage, in of itself, introduces certain margins within which the spectrophotometer must operate. These margins relate to how the sample and spot of light correlate to one another in free space. There are two primary concerns here: spot translation and aberration. As the center-mount sample stage rotates, it does so about its own central rotational axis. If this axis is not aligned to the incident light beam and the sample surface, then the spot of light will move across the surface of the sample as the angle of incidence is changed. This means that we would be measuring the reflectance for different parts of the sample surface as the angle of incidence increases. Spot translation can be negated, with the delicate alignment of the collector, field, and condenser lenses, with respect to the sample stage.

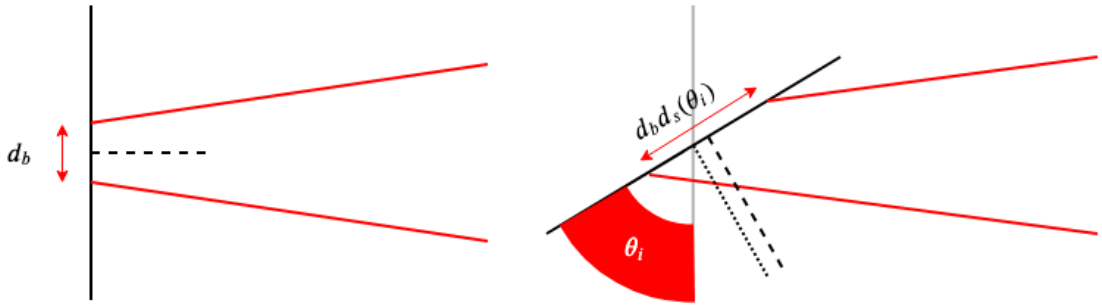

Figure 4.16: Displaying the effect of spot translation and aberration when a sample is rotated to higher angles of incidence against a typical focussed beam of light.

A more significant concern is spot aberration. This occurs in any system where the relative angle between a fixed plane (the sample surface) and some incident light is

changing. While the input power remains unchanged, the power density at the surface of the sample is reduced as the spot encompasses a greater area of that surface. Similarly, this means that different parts the sample surface are included in any measured data over variable angles, meaning that both spot aberration and translation are dependent on angle, not wavelength or polarization. Two key points arise from this observation: the sample must be of a minimum size to ensure the beam of light remains incident on the sample, not skirting the edges and partially impacting the integrating sphere wall directly, and to ensure the spot size is focused to a diameter small enough to ensure the prominence of aberration is limited. Both spot translation and aberration are visualised in figure 4.16.

4.4 Advanced Characterisation

Colorimetric analyses are an advanced form of optical characterisation relating to the *perceived* colour of an object by the human eye. Due to the apparent deceptive nature of perception, colorimetry is an inherently difficult area of optics to study. Introducing perceptive variance, inclusive of colour blindness and a divergent white point, adds further dependencies in the creation of an accurate colorimetric profile. Such measurements form a branch of spectrophotometry, since the process of acquiring the data needed to complete such analyses remains identical. Instead, the same data is interpreted in a different way to that of VAR measurements, for example. Indicative of the same theory explored here with regard to VAR, surface colours will appear differently at varying incident angles on a surface. It is possible to utilise VAR data, as measured with the ARS using the same SOP as shown in figure 4.13, to determine colour resolved against incidence angle. This has particularly interesting implications for manufacturers of PC displays, mobile phones, high–end TVs, specialised paints, and even artists.

$$X = \int [S(\lambda, \theta)\bar{x}(\lambda)]\,\mathrm{d}\lambda \tag{4.23}$$

$$Y = \int [S(\lambda, \theta)\bar{y}(\lambda)]\,\mathrm{d}\lambda \tag{4.24}$$

$$Z = \int [S(\lambda, \theta)\bar{z}(\lambda)]\,\mathrm{d}\lambda \tag{4.25}$$

The approach employed here to convert the intensity spectra, S, into a perceived colour, requires the use of CIE standard illuminant D65 [151]. This standard allows us to map wavelengths against their contributions to certain colours. The human eye has three types of sensors, known as 'cones'; one sensitive against red, X, green, Y, and blue, Z.

The standard contains colour matching functions that outline the wavelength sensitivity of each cone, and subsequently the colour sensitivity of each. These matching functions are $\bar{x}$, $\bar{y}$, and $\bar{z}$ for red, green, and blue, respectively. X, Y, and Z, as outlined in equations (4.23), (4.24), and (4.25), also respectively, represent the tristimulus values. These are analogous to RGB colour codes used in western electronic displays, but instead represent the colour perceived. It is from these values, as weighted against the matching functions outlined in the CIE standard illuminant, that permit us to derive colour as would be seen by the human eye (assuming no colour blindness is present).

4.5 Confirmation Studies

4.5.1 Overview

Prior to use on samples such as b-Si, the reflectometry system needed to be qualified by carrying out confirmation studies. Here, two thin film-coated Si wafer samples of theoretically determinable reflectance were placed within the system and processed in accordance with the system's standard operating procedure as shown in figure 4.13. Two 500 μm thick c-Si based samples were used, with ARCs consisting of 80 nm of SiN_x and 110 nm of SiO_2, respectively, deposited by plasma-enhanced chemical vapour deposition. The thickness of these films were confirmed prior to measurement using ellipsometry. The spectral reflectance for such coatings can be determined using simple TMM calculations, however the theoretical data presented here were sourced from the optical simulator, OPAL 2 [29].

4.5.2 Creating Multi-variant Reflectance Standards

There were no regular reflectance standards resolved against both wavelength and angle simultaneously. To address this, new standards needed to be made and certified by a third party – LabSphere in this case. A single piece of polished c-Si is taken, with dimensions of 3 cm $\times$ 3 cm $\times$ 500 μm, along with three solid blocks of $[C_2F_4]$n with dimensions of 3 cm $\times$ 3 cm $\times$ 1 cm. The three $[C_2F_4]$n blocks have an average reflectance of approximately 99, 50, and 10%, respectively, and were modelled as Lambertian reflectors. Such reflectors exhibit identical reflectance characteristics at any angle. Therefore, the blocks' reflectance, as certified by LabSphere at 8°, can be inferred across the angular distribution. Conversely, the uncoated DSP c-Si has variable reflectance as defined by theory, related to polarisation and angle as defined through the Fresnel equations and

explained by Kasap in 2013 [152] as in equations (4.26) and (4.27).

$$R(\theta) = \left(\frac{\cos(\theta) - \sqrt{\left(\frac{n_2}{n_1}\right)^2 - \sin^2(\theta)}}{\cos(\theta) + \sqrt{\left(\frac{n_2}{n_1}\right)^2 - \sin^2(\theta)}} \right)^2 \qquad \text{for S polarisation} \tag{4.26}$$

$$R(\theta) = \left(\frac{\sqrt{\left(\frac{n_2}{n_1}\right)^2 - \sin^2(\theta)} - \left(\frac{n_2}{n_1}\right)^2 \cos(\theta)}{\sqrt{\left(\frac{n_2}{n_1}\right)^2 - \sin^2(\theta)} + \left(\frac{n_2}{n_1}\right)^2 \cos(\theta)} \right)^2 \qquad \text{for P polarisation} \tag{4.27}$$

Equations (4.26) and (4.27) represent the reflectance of light between two media of refractive indices n_1 and n_2 with respect to the polarisation of said light [152]. Here we are trying to determine reflectance at the air-silicon barrier; $n_1 = 1$ and n_2 is wavelength dependent. Substituting this information into equations (4.26) and (4.27) yields equations (4.28) and (4.29), respectively.

$$R(\lambda, \theta) = \left(\frac{\cos(\theta) - \sqrt{(n_2(\lambda))^2 - \sin^2(\theta)}}{\cos(\theta) + \sqrt{(n_2(\lambda))^2 - \sin^2(\theta)}} \right)^2 \qquad \text{for S polarisation} \tag{4.28}$$

$$R(\lambda, \theta) = \left(\frac{\sqrt{(n_2(\lambda))^2 - \sin^2(\theta)} - (n_2(\lambda))^2 \cos(\theta)}{\sqrt{(n_2(\lambda))^2 - \sin^2(\theta)} + (n_2(\lambda))^2 \cos(\theta)} \right)^2 \qquad \text{for P polarisation} \tag{4.29}$$

The refractive index, n_2, in equations (4.28) and (4.29) is that of Si. The values for this have been sourced from Schinke *et al.* [153]. The data shown in figure 4.17 forms the R_y component of equation (4.10) for the relevant polarisation, φ.

In relation to the three remaining standards, that is to say the $[C_2F_4]$n blocks, theoretical calculations were not required. Instead, LabSphere certified the reflectance of each using the following control conditions:

- angle of incidence fixed at 8° – a typical SAR measurement;
- wavelength distribution was from 250 to 2,450 nm;
- light was of hybrid mode polarisation.

Given the aforementioned wavelength limitations of the ARS, only the wavelength range of 400 to 1,000 nm is shown here. The reason for this range, over the 350 to 1,050 nm mentioned previously, is to remove areas of the spectrum where noise is overly dominant. This is the same as the theoretical determination of reflectance carried out previously and shown in figure 4.17. Furthermore, the data for the $[C_2F_4]$n standards is shown in a 2-D data plot, as opposed to the 3-D contours used for the planar Si. This is

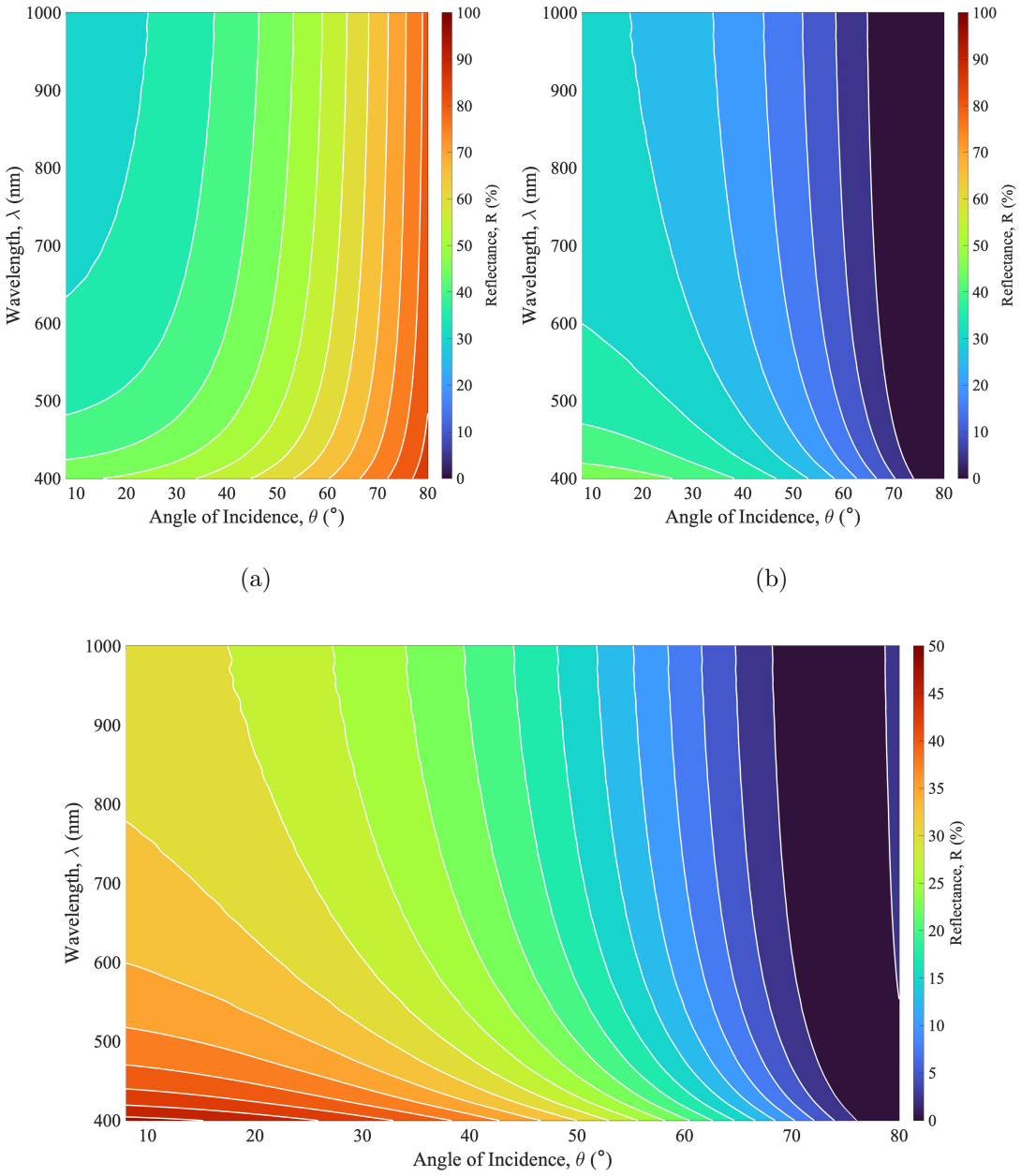

Figure 4.17: The theoretical TE (a), TM (b), and TEM (c) reflectance of polished silicon in air at variable angles, calculated using equations (4.28), (4.29), and (4.10) respectively.

because, under the assumption that these are ideal Lambertian reflectors, reflectance becomes angle-independent and is assumed identical for all angles of incidence where $0 \leq \theta < 90°$. The data for these tailor–made reflectance standards is shown in figure 4.18.

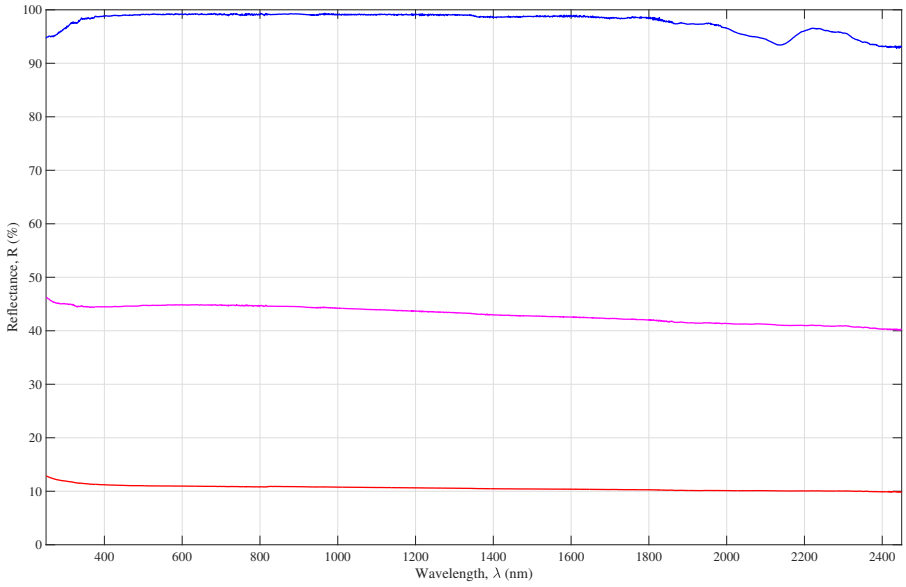

Figure 4.18: The certified absolute reflectance for the 10, 50, and 99% $[C_2F_4]n$ reflectance standards. Measured and certified by LabSphere.

4.6 Results and Analysis

4.6.1 Thin Film Anti–reflectance Coatings

4.6.1.1 Standard Angle Reflectance

Shown here are the SAR measurements, specifically both the CMSAR and SMSAR measurements, compared against the theoretical reflectance at 8°, for 80 nm SiN_x and 110 nm SiO_2 thin film ARCs. The 50% PTFE diffuse standard was used to collect the data for the samples in this section. As can be seen in figures 4.19 and 4.20, the low broadband difference in reflectance between theory and measurement is clearly visible.

Both of these datasets (figures 4.19 and 4.20) show slight differences to theory over the broadband spectrum. SiN_x deposited by chemical vapour deposition can vary in chemical content from silicon–rich to nitrogen–rich, depending on the relative concentrations and flow rates of the precursor gases used. In practice, there will also be spatial non–

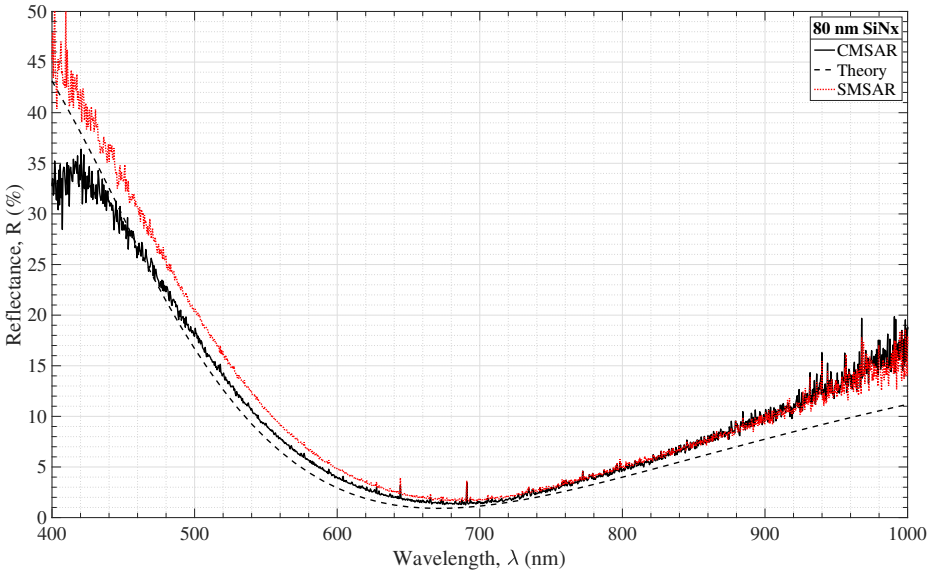

Figure 4.19: CMSAR and SMSAR measurements, alongside the theoretical reflectance, taken on the 80 nm SiN_x thin film ARC sample.

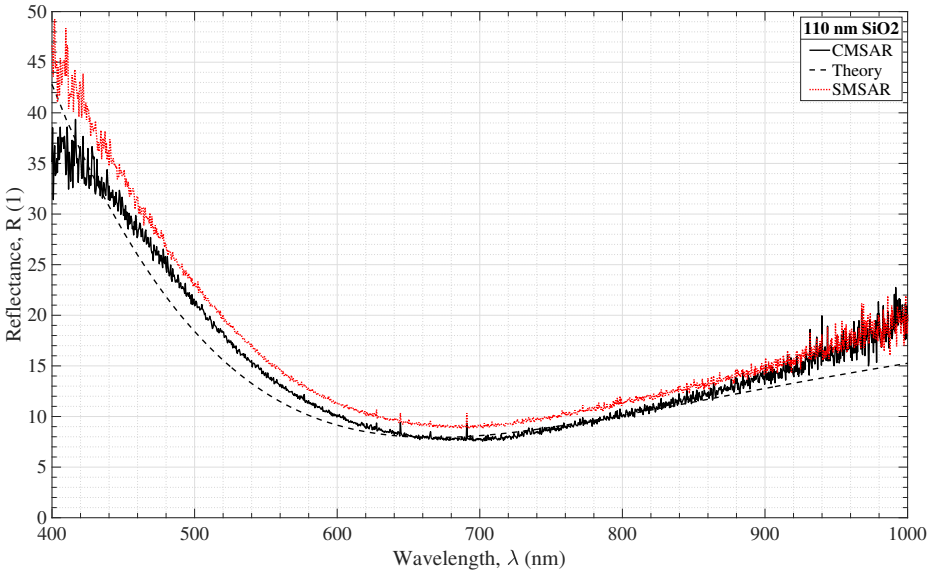

Figure 4.20: CMSAR and SMSAR measurements, alongside the theoretical reflectance, taken on the 110 nm SiO_2 thin film ARC sample.

uniformities in the deposited film. Given the system's sample illumination surface area is $\sim$ 30 mm^2, this would imply that the same surface area of the SiN_x sample being illuminated is not uniform. These factors explain the differences between measurement and theory for $650 \leq \lambda \leq 850$ nm with CMSAR shown in figure 4.19. This can also be seen looking at the SAR spectrum for SiO_2 in figure 4.20. Deposited SiO_2 coatings are more uniform and their optical properties are less sensitive to differences in deposition conditions. Consequently, the difference between theory and measured reflectance is smaller for the most part, topping out at $\pm 0.2\%$ for $650 \leq \lambda \leq 850$ nm in the CMSAR configuration.

Deviation between CMSAR and SMSAR can be seen for $\lambda \leq 450$ nm. Although these two measurements, in theory, should be identical, the difference seen here can be explained when we examine the structure of the samples. These ARCs are single–side polished c-Si, meaning that they are planar on the front surface and rough on the back. When in center-mount configuration, both of these surfaces, as well as the sides of the sample, are exposed to the light integrated by the sphere. The ratio between sample and reference standard in CMSAR configuration, therefore, encompasses differences in the rear and the sides, as well as the front. On the contrary, when side mounted, only the front surface contributes to the integration of light. This is the cause of the differences between the results from the two measurements in this spectral region.

In the theoretical data shown here, back-reflections were not accounted for. Such reflections occur when light passes through the front surface of the sample and subsequently reflects off of the back surface. This light then returns to the front surface and leaves the sample, contributing to overall reflectance measured. These reflections are prevalent at the longer wavelengths in the NIR response, and actively contribute to the difference between measured and theory in these cases. Specifically, note how measured reflectance is always higher than theory for CMSAR measurements. In reference back to figure 4.11, the spectral radiance of the light source against the spectrophotometer's sensitivity readout, above this wavelength measured intensity decreases steadily. This, coupled with the low (sub-15%) reflectance at this point, dramatically decreases the SNR ratio, which in turn causes electrical noise to become more dominant in the determination of R_x. The same is not observed in the NUV region as reflectance is much higher, resulting in a greater signal intensity, and thus a greater SNR. This effect can be seen with greater clarity when we look at VAR instead of SAR.

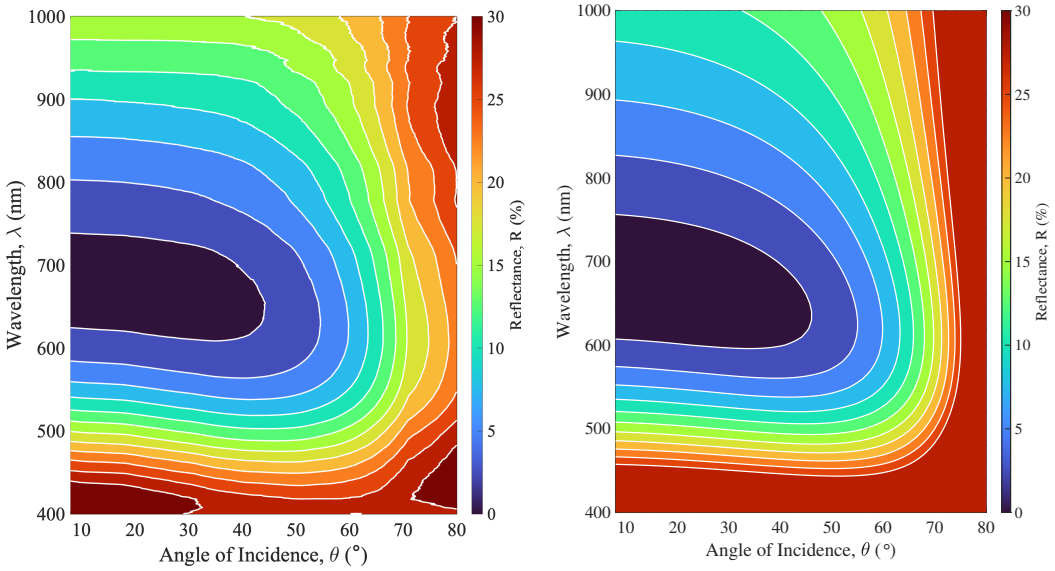

(a) (b)

Figure 4.21: VAR contours as measured (a) and according to theory (b) for an 80 nm thick coating of SiN_x on planar Si. Reflectance is represented by a colour scale as a percentage. The reflectance scale is identical between figures 4.21 and 4.22 to aid with comparison.

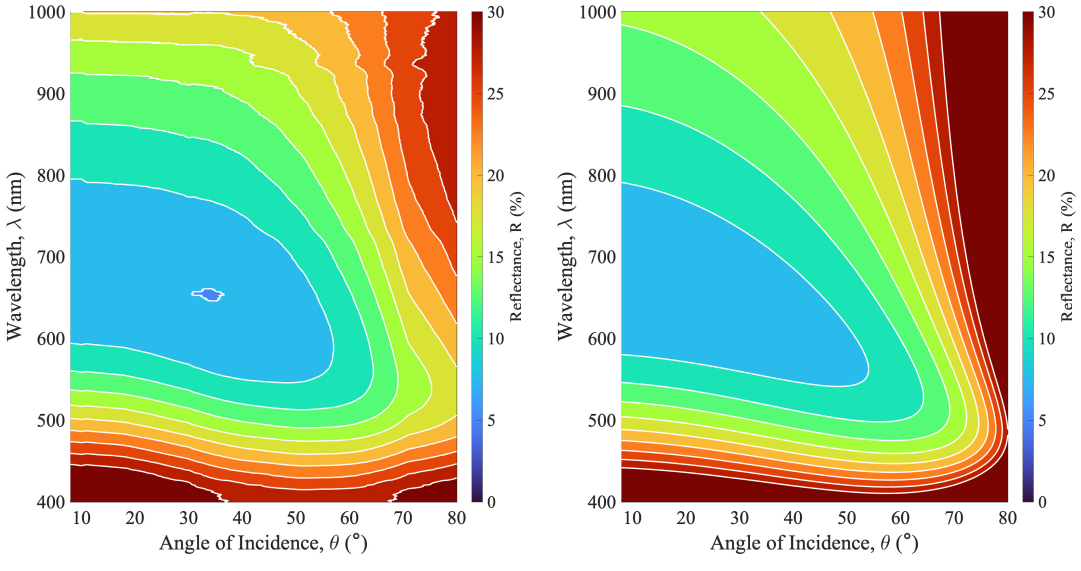

(a) (b)

Figure 4.22: VAR contours as measured (a) and according to theory (b) for an 110 nm thick coating of SiO_2 on planar Si. Reflectance is represented by a colour scale as a percentage. The reflectance scale is identical between figures 4.21 and 4.22 to aid with comparison.

4.6.1.2 Variable Angle Reflectance

Plots of reflectance versus wavelength and angle of incidence for the thin film ARC samples, measured in CMVAR mode, are shown in figures 4.21 and 4.22, alongside the results that are obtained in theory. The reflectance of these samples rises steadily as the angle of incidence, θ, increases. This is to be expected for optical interactions at a dielectric interface due to the presence of specular reflection. Note how the average broadband reflectance increases over the angle, tending toward values of 20%–25% beyond angles of 70°, particularly in the visible and NIR spectral regions. Reflectance in the NUV remains relatively constant due to silicon's ability to reflect very high energy light.

Constant reflectance with respect to increasing angle, that is to say angle independent reflectance, would be depicted in VAR contour data with perfectly horizontal lines. Conversely, reflectance that is wavelength independent would show in the contour plot as vertical lines. In the case of the SiN_x sample, with measured data as shown in figure 4.21a, it can be seen that for an approximate wavelength range of 600 to 700 nm, the latter holds true. This shows how the tuned wavelength minima for this typical single–layer ARC, as outlined in section 1.4.1.1 with equations (1.7) and (1.8), is also angle-independent. The same can be said for its theoretical data, as shown in figure 4.21b, though to a slightly lesser degree; the minima in this data shifts slightly downwards toward 500 nm from the initial ~ 600 nm.

Table 4.2: SAR and VAR measured average reflectance for the two thin film samples investigated here.

Sample	$\bar{R}_x(8°)$	$\bar{R}_x(\theta, \lambda, \varphi)$	$\Delta\bar{R}_x$
80 nm SiN_x	13.65%	18.76%	+5.11%
110 nm SiO_2	17.74%	22.21%	+4.47%

Average sample reflectance, $\bar{R}_x$, usually taken with respect to only wavelength in SAR measurements, can now also be taken over wavelength, angle, and polarisation. The difference between calculating this value for SAR and VAR measurements is outlined in table 4.2. The white contour lines plotted and shown in 4.21 and 4.22 allow for easy comparison of measurement with theory and reveal a good match between the two.

4.6.2 Variable Angle Colorimetry

Given the validity of the VAR data for thin films, with a cross–comparison to theory confirming the ARS is operating as expected, the reflectance of two generic paint samples, red and blue, as well as that of a black optical insulating material manufactured by ThorLabs, was measured. Unlike with the thin films, there is no way of theoretically determining the reflectance of these samples, and no data on this topic was available from the manufacturers. This is primarily due to the scarcity of VAR measurement systems resulting in a lack of current uptake in the industry. Furthermore, all of these samples are highly diffuse reflectors, and as such, no reflected image can be seen at any angle.

Both red and blue paints, as shown in figures 4.23 and 4.24, respectively, demonstrate how the reflected light changes with angle of incidence. Notably, each colour paint reflects highly in the region of the visible spectrum that is associated with that colour: the red paint can be seen to reflect noticeably higher above 550 nm, and the blue paint does the same below 550 nm. Figure 4.24 also shows how, at the upper end of the visible spectrum, the reflectance of the blue sample also increases. The sample remains apparently blue because of the reflectance dominance in the sub-550 nm region. Reflection far toward the NIR end of the visible spectrum, ($\lambda > 650$ nm) has implications on the material's thermal properties rather than its optical performance.

The reflectance of both these paints remains reasonably consistent even at high angles of incidence. This is due to the diffuse/matte nature of the paint surface, where the angle at which the light impacts the surface has a reduced significance on the subsequent scattering of light in all directions simultaneously. This is unlike specular reflection, where the angle of incidence has a dominant effect on ensuing surface reflection at that same angle. With both the red and blue paints, the reflectance spectra, in the ranges representative of their color, both expand to encompass surrounding wavelengths at high angles of incidence ($\theta \geq 50°$).

Figure 4.24 shows a peak reflectance for $440 \leq \lambda \leq 515$ nm at low angles of incidence, expanding to $410 \leq \lambda \leq 550$ nm in the wide angle. This indicates that the colour of these paints changes when illuminated from these wider angles. By combining the VAR data with information about illumination conditions and the photopic response of the human visual system, it is possible to plot perceived colour as a function of angle of incidence. This branches into an area of optics known as colorimetry, and was

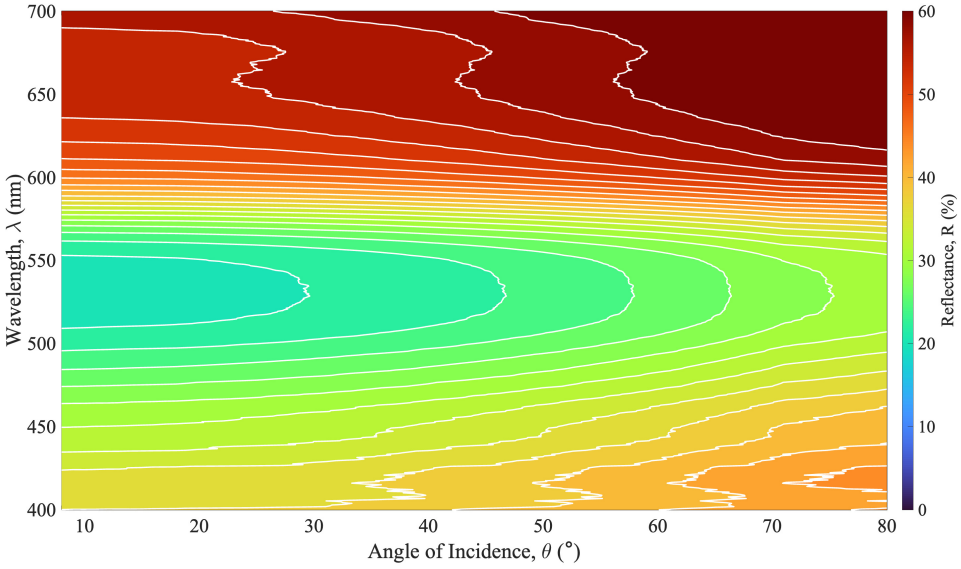

Figure 4.23: VAR measurements of generic red wall paint. The wavelength range for the data shown here has been limited to $400 \leq \lambda \leq 700$ nm in–line with the visible portion of the EM spectrum. The reflectance scale is identical between figures 4.23 and 4.24 to aid with comparison.

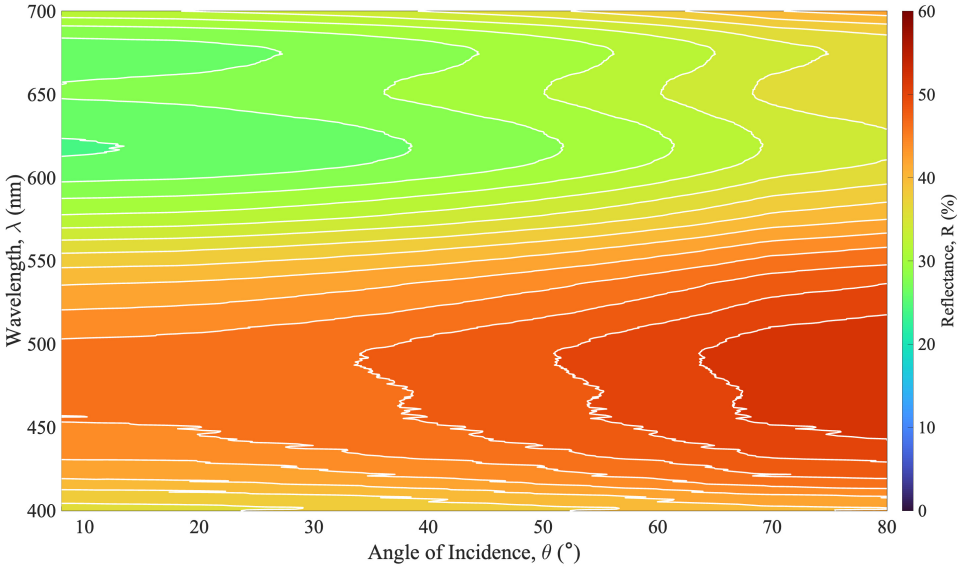

Figure 4.24: VAR measurements of generic blue wall paint. The wavelength range for the data shown here has been limited to $400 \leq \lambda \leq 700$ nm in–line with the visible portion of the EM spectrum. The reflectance scale is identical between figures 4.23 and 4.24 to aid with comparison.

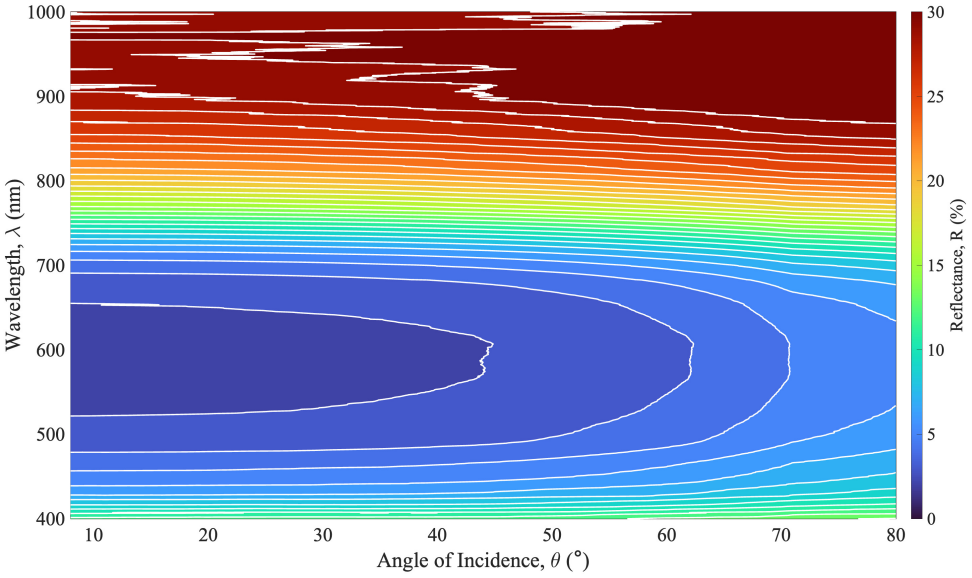

Figure 4.25: VAR measurements of the matte black optical insulating material. Unlike in figures 4.23 and 4.24, where the sample's optical properties are only important in the visual portion of the EM spectrum, the full wavelength range is presented here (inclusive of the NIR region).

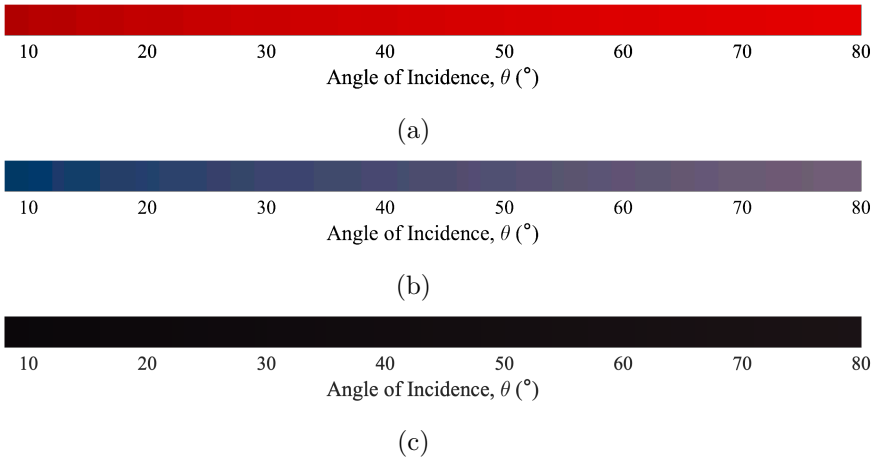

Figure 4.26: Perceived colour as a function of angle for the red (a) and blue (b) paints, alongside the perceived colour of the optical insulator made by ThorLabs (c).

introduced as an advanced characterisation mechanism off the back of VAR data in section 4.4. Using the CIE standard illuminant D65 [151], often used in colormetry, the optical colour variance as a result of the changing angle is determined. Although only slight, the colour of both paints does vary with angle of incidence. This is more apparent with the red paint 4.26a than the blue 4.26b, where a more significant ingress of both violet and blue light can be seen beyond the 60° mark. The higher reflectance from the red wavelengths also diverges outward into the yellow area of the visible spectrum.

Figure 4.25 shows that, in the NIR spectral region, the optical insulator also acts as a thermal insulator. Infra-red radiation is transmitted primarily as heat and therefore, high reflection in this region would equate to heat being reflected as well. There is no significant component of visual reflection here, as one would expect from a sample that appears black to the naked eye. As with the samples shown in figures 4.26a and 4.26b, the colour of this material becomes lighter at higher angles of incidence, although this increase is not as noticeable as that seen in largely specular reflectors, such as the two thin film samples shown in figures 4.21a and 4.22a.

4.7 Conclusions

In summary, a novel and enlightening methodology in the determination of material reflectance has been shown. Resolution over angular and wavelength distributions provides a more complete picture regarding the true optics of a given sample. Two thin film ARCs were measured, with the results showing a good match with theory, and any differences observed were sufficiently explained. The highly common SMSAR configuration was also demonstrated with the ARS, as shown in figures 4.19 and 4.20, with the pitfalls of such an approach outlined.

VAR measurements offer a more comprehensive picture of the overall reflectance properties of a sample, which is of particular interest for applications where surfaces operate under varying illumination conditions. It was demonstrated how, under constant angle, reflectance can be determined as either higher or lower than that calculated over variable angles, with implications on the design of material surfaces for glass, paint, and solar PV. The colour of samples can also be extracted from these datasets, with implications on the manufacturing of paints and coatings for visual consistency over varying illumination angles. Angle-resolved reflectance measurements, although more complicated than traditional reflectometry, are beneficial to both academic studies and industry-

based research and development. The likelihood of human error is significantly reduced using this approach, which is highly automated, and permits a significant increase in the throughput of samples with a rapid turnover of data.

Chapter 5

Applied Spectrophotometry for Evaluation of Solar Photovoltaics

The work described here has been published in a journal paper

J. J. Tyson, T. Scheul, T. Rahman, and S. A. Boden

"Characterising the broadband, wide–angle reflectance properties of black silicon surfaces for photovoltaic applications"

OPG Optics Express, Volume 31

August 2023

DOI: 10.1364/OE.496448

5.1 Introduction

As reported in chapter 4, the variant incidence angle of light plays a critical role in the determination of true optical performance in the real–world. Planar, single layer ARC samples were characterised and demonstrated the applicability of the measurement technique across multiple areas of study. However, we now return to the pyramids, b-Si, and hb-Si samples manufactured as part of the work shown in chapter 3. The optical performance of textured anti–reflectance coatings for solar PV is far more difficult to quantify effectively with typical RAT measurement systems. (CM/SM)SAR and SM-SAT are unable to showcase how the interaction of light with nanoscale textures is fundamentally different to that of relatively larger topologies.

The measurement and quantification of optical performance for samples of applicability

to solar PV is a crucial determinant in their effectiveness for use in such systems. On employing the power of the ARS characterisation methodology, a new perception of these solar anti–reflectance coatings is showcased, enabling a far more thorough analysis. Other than simply observing the relation between the reflection from a surface of a solar cell and its angle dependency, it is shown that VAR data can be further enhanced when used to relate the surface optical response to a moving source respective of time: the Sun. Taking some geographical location, solar irradiance with respect to that location, and transient daylight hours for the same across a given year, it is possible to transition from angle–dependant reflectance, to time– and seasonal–dependant reflectance, extrapolating anticipated optical performance when a topology is applied to the underlying PV cell. This data and all of its dependencies is taken, and used to create a single optical figure of merit; the weighted reflectance (WR).

5.2 Angle–resolved Spectrophotometry for Solar Cells

Mere silicon–based samples with surface texturing or ARCs are insufficient in the determination of performance under real–world conditions. True solar modules are formed of at least two more layers that will affect optical performance, including the encapsulant and glass front panel as a minimum. A passivation layer is also required for a solar cell to function electronically, but has a far lesser overall effect on the cell's optical performance than the encapsulant and glass layers. Let us take common material choices for each of these layers: ethylene–vinyl acetate (EVA) and borosilicate glass, respectively, and visualise them in a basic solar cell structure. This can be seen in figure 5.1.

Figure 5.1: A basic overview of the typical structure representative of a full solar cell system with exemplar materials alongside in brackets.

Textured silicon samples were encapsulated with these two constituent components and complete an analysis on the resultant optical performance. This enables us to quantify the effect of introducing these layers in a real–world setting. Not outlined in figure 5.1 is the presence of electrical contacts. These contacts allow for the collection of charge carriers for passing through an external load as current. However, there are also significant optical implications of these structures as well. The cheaper, more typical front contact solar cells contain crossed busbars and electrical contacts. Despite these being very thin, the fact they sit between the substrate and glass layers will cause some degree of self–shading. This is where the busbars and contacts block light from passing into the substrate underneath, reflecting it back and increasing overall surface reflectance. The interdigitated back contact (IBC) solar cell structure eliminates this concern by placing all of the electrical contacts at the rear of the cell, out of the path of sunlight. In bifacial systems, that is to say solar panels that can absorb light incident on either side of the panel, this advantage is mute, but exploration into this very novel type of cell goes beyond the scope of this work. To ignore self–shading effects that would otherwise be present with the busbars, it is assumed that the ARCs and textures explored here are built onto such IBC cells.

5.3 Experimental Methodology

As reported across chapters 3 and 4, there were four types of samples fabricated ahead of characterisation: a standard random pyramidal texture using an anisotropic potassium hydroxide (KOH) based chemical etch, the same with an 80 nm SiN_x single–layer ARC, several b-Si nanotextures of various heights, and hb-Si nanotextures, also of various heights. The average height against etch time for these b-Si and hb-Si textures are tabulated in tables 3.2 and 3.4, respectively. Scanning electron micrographs of each textured sample can be seen in section 3.3. The ARS is used to perform high resolution CMVAR scans on these samples, with a diffuse reflectance standard of 50% used as a reference. The ARS scan parameters were: $\lambda = 400 : 1000$ nm, $\theta = 8 : 80°$, where S– and P–polarisations were averaged together over five consecutive scans.

Subsequent to these measurements being taken, two of the best performing samples are then encapsulated in Norland Optical Adhesive (NOA) 61[1] and 1.5 mm thick borosilicate glass, based on the structure shown in figure 5.1. NOA 61 offers $> 95\%$ transmission of light between wavelengths of 400 nm and 1.8 μm – covering the range of interest

[1] norlandprod.com/adhesives/NOA%2061.html

explored using the ARS system and completely covering the typical operating range of Si–based solar cells. This transmission spectra can be seen in figure 5.2. The NOA 61 encapsulant layer is applied in the centre of each 3×3 cm sample, ensuring coverage does not exceed half the area of that sample. The borosilicate glass layer is then placed on top of this, causing the NOA 61 encapsulant to spread across the sample surface underneath the glass for complete surface area coverage. Samples were cured in an ultraviolet light irradiance box for a period of one minute, in–line with the manufacturer's specifications. Prior to completing any optical measurements, the encapsulated samples were inspected to confirm the absence of any visible air bubbles.

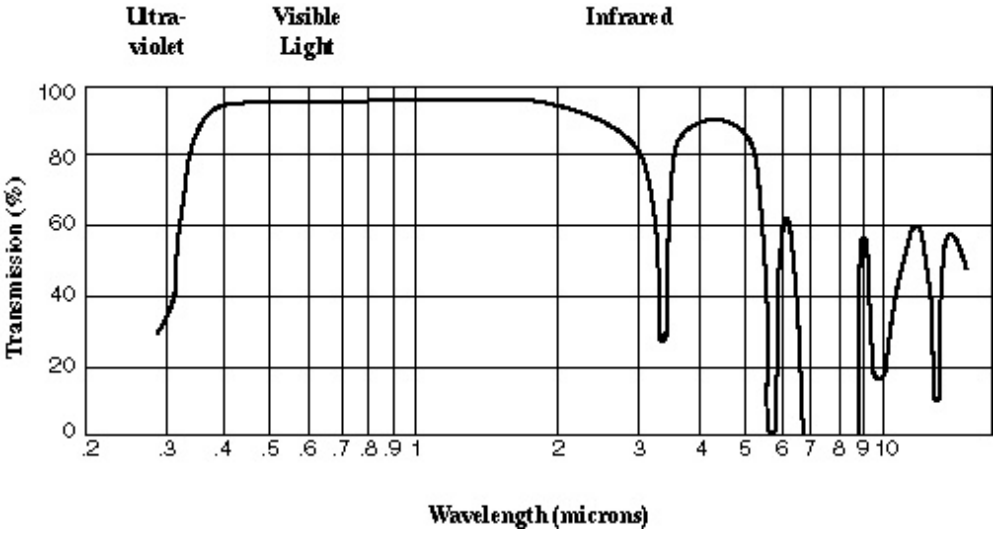

Figure 5.2: The transmission spectrum for NOA 61 as outlined in the material specifications. This data is provided courtesy of Norland Products[1] (2022).

In order to understand the process by which VAR data can be related to real–world equivalent scenarios, it is first important to evaluate how the Sun moves relative to the solar panel over the length of the solar day, i.e. the proportion of a 24 hour period where the Sun is above the horizon. The solar day length is affected by several factors, such as specific geographical location (latitude and longitude), the height of the terrain above sea level (elevation), and whether the location is in the northern or southern hemisphere. The change in solar elevation throughout the year can be visualised by taking the two solstices (shortest and longest days of the year); all days in–between will have solar elevations situated between these two curves. Solar elevation data is calculated using NREL's solar position algorithm (SPA). For this work, the parameters used in the SPA are tailored for Southampton, UK, having geographic coordinates of $50^\circ\ 54'\ 9.126''$ N (latitude) and $1^\circ\ 24'\ 15.0804''$ W (longitude), with an elevation of 2 m. Solar elevation against hour for both solstices can be seen for this location in figure 5.3,

calculated using the SPA. Even when the Sun is below the horizon, light can still reach the solar panel indirectly. As such, negative values of elevation, that is to say when the Sun is below the horizon, are only included in situations whereby the SPA indicates a significant component of scattered light throughout the atmosphere.

In a polar coordinate system, instead of referencing a point object using x, y, and z coordinates, radius, elevation, and azimuth are used. Polar coordinate systems are far more efficient when working with spherical spatial geometries. The position of the Sun is readily represented using such methods. Take the example geometry as shown in figure 5.4. In the case of solar PV, the radius, that is to say the distance between the centre point (the solar panel) and the Sun, need not be considered. Given the distance between any point on Earth and the Sun, this factor becomes insignificant and we can assume that solar irradiance is consistent, attenuated only by local weather patterns.

Using spectral irradiance data, weighted average reflectance can be determined for a given sample. In typical, single angle reflectance measurement systems, this weighted average reflectance (WAR) is a single figure of merit weighted against the AM1.5 spectrum to provide a more valuable insight into the true reflectance implications for solar PV technologies. WAR is determined for single angle reflectance as shown in equation (5.1), where R_x is the sample's surface reflectance, λ is wavelength, and $F_{\mathrm{AM1.5}}$ is the AM1.5G spectral irradiance curve.

$$\mathrm{WAR} = \frac{\sum[R_x(\lambda)F_{\mathrm{AM1.5}}(\lambda)]}{\sum[F_{\mathrm{AM1.5}}(\lambda)]} \tag{5.1}$$

In the case of variable angle reflectance, determination of a weighted reflectance must be done with respect to two variables simultaneously: wavelength and angle. Variable angle of incidence will require different irradiance spectra, F_{VAR}, to be weighted against, given the difference in air mass through which the light must pass before being incident on the surface of the samples. In this case, F_{VAR} can be determined using Bird and Hulstrom's Solar Irradiance Model [155, 156]. This takes into account both direct and diffusely incident light and enables predictions of day–to–day optical performance of the anti–reflective surfaces, should they be employed in a real solar PV system. The definition of WAR, as in equation (5.1), can be expanded to include this angle–dependency of VAR measurements as shown in equation (5.2).

$$\mathrm{WAR} = \frac{\sum[R_x(\theta,\lambda)F_{\mathrm{VAR}}(\theta,\lambda)]}{\sum[F_{\mathrm{VAR}}(\theta,\lambda)]} \tag{5.2}$$

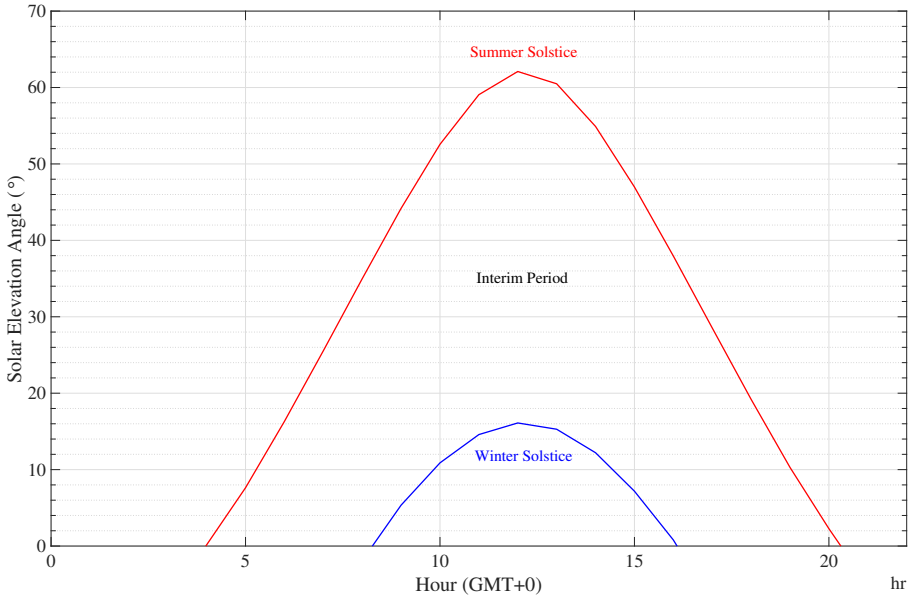

Figure 5.3: An overview of the variation in solar elevation angle with respect to the hour of the day for a given season. Shown here are the longest and shortest days of the year for Southampton, UK. Data is calculated using the NREL solar position algorithm [154] and averaged over all days within the given month.

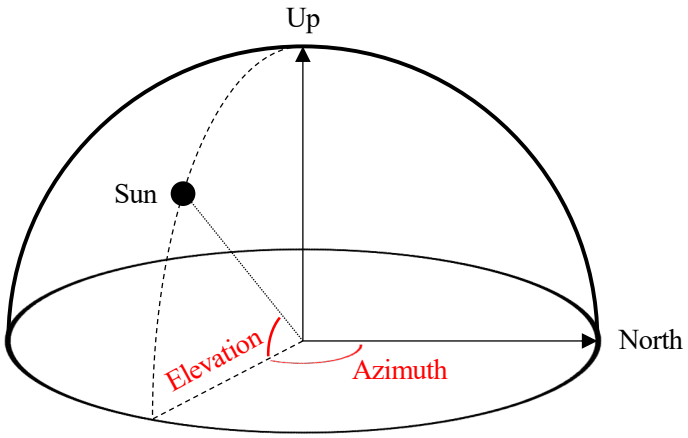

Figure 5.4: The Sun's position as represented using the polar coordinate system. Only the upper (positive) hemisphere is shown here.

The location of deployment for the model is Southampton, UK, where the panel is held at a fixed tilt of 35° from the horizontal and is south facing (as is optimal for use in the UK)[2]. Ozone levels are determined using the Heuklon model [157] and pressure is as typical at sea level (14.7 PSI). Direct light has an intensity linked directly to the angle of incidence, θ, meaning that it is only considered when the Sun is within the front facing hemisphere about the incident surface. When the Sun is either below the horizon, or illuminating the panel from behind, the direct illumination component is zero. Atmospheric scattering between these points, respectively, causes some degree of indirect (diffuse) illumination. To account for this component, all non–zero values for diffuse irradiance over the course of the whole day, as determined using Bird and Hulstrom's Solar Irradiance Model [155,156], were averaged and divided through by the number of hours of direct irradiance for that day. This value could then be added to the values for direct irradiance, yielding total irradiance for the day as a whole.

It should be noted that the minimum direct solar elevation angle is always zero. The only situation when this is an incorrect statement is at either of the poles, where the Sun can remain below or above the horizon for months at a time. The solar elevation angle alone cannot be linked directly to the angle of incidence measured using the ARS. The angles present in the VAR contour plots are relative to the surface normal for that sample. For example, when light from the Sun is incident on the panel parallel to the surface normal, this relates to an ARS angle of 0°. The angular distribution of the scans are limited to between 8 and 80°. In order to ensure full spectral coverage in the theoretical determination of performance on a solar panel, this range needs to go from the minimum to maximum possible angles of incidence (0 and 90°, respectively). This is readily achieved through the careful extrapolation of the VAR data. When light approaches any sample at an angle tending toward 90° relative to the surface normal, reflectance will tend toward unity. Meanwhile, at angles close to normal incidence, data has shown that reflectance is typically only wavelength dependent; changes to angle of incidence do not significantly change the reflectance measured at a given wavelength. This means that the VAR data can be extended from the original distribution of 8 to 80° to between 0 and 90° whilst maintaining validity by assuming spectral reflectance is the same for all values of θ below 8° ($R_x(0 \leq \theta < 8°, \lambda) = R_x(\theta = 8°, \lambda)$), and also assuming reflectance increases linearly towards 100% for all values of θ above 80° ($\lim_{\theta \to 90°} R_x(\theta, \lambda) = 1$). Here, R_x is the sample's surface reflectance, θ represents angle

[2] As reported by Spirit Energy and Viridian Solar for roof–mounted panels in the UK. This angle varies throughout the year, but 35° is an effective compromise for tilt–invariant systems.

of incidence (with respect to the surface normal), and λ is wavelength.

Spectral irradiance data was calculated for each hour of the day, across every day of the month, over every month of the year. Each of these spectra were averaged with their counterparts from the same month, creating an average solar day indicative of that month. This average day can then be taken to assess the optical performance of the samples for each hour in said day, yielding 12 data points representing expected optical performance for a typical day within each month of the year. WR is a single optical figure of merit for each month of the year, representing the average response across that month. This can also be averaged across a larger timescale, for example the whole year, to determine the same over a given year for a specific location.

5.4 Results and Analysis

5.4.1 Samples Prior to Encapsulation

5.4.1.1 Pyramidal Textures

As is expected, bare, uncoated pyramids perform relatively poorly. Figure 5.5a shows how the pyramidal structures maintain an almost linearly-increasing reflectance over increasing angles. The point of lowest reflectance lies between 600 and 750 nm at the minimum angle (8°), where the reflectance drops to approximately 11.7%. The reflectance peaks at 30% at high angles of incidence in the near infra-red (NIR) and near ultra-violet (NUV) spectral regions, but holds slightly lower at around 25% in the visible. In reference to figure 5.5b, when a 80 nm thin film coating of SiN_x is applied to the same pyramids, the reflectance minima shifts considerably into the visible spectrum at a wavelength of approximately 550 nm. The reflectance minima at 8° is only 1.35%, a mere $\sim$ 15% of the minima seen in figure 5.5a for uncoated pyramids when the wavelength shift is ignored. Taking the reflectance of the uncoated pyramids at 550 nm (not the minima for that sample), the reflectance of the ARC coated sample is approximately 10% that prior – a considerable optical performance boost. Furthermore, the minima for the sample shown in figure 5.5b does not shift up or down the wavelength spectrum, remaining almost constant throughout the angular distribution.

5.4.1.2 Black Silicon and Hybrids

The ARS data for planar b-Si textures, which can be seen in figure 5.6, reveals that there is a noticeable difference between the optical response when compared to either of

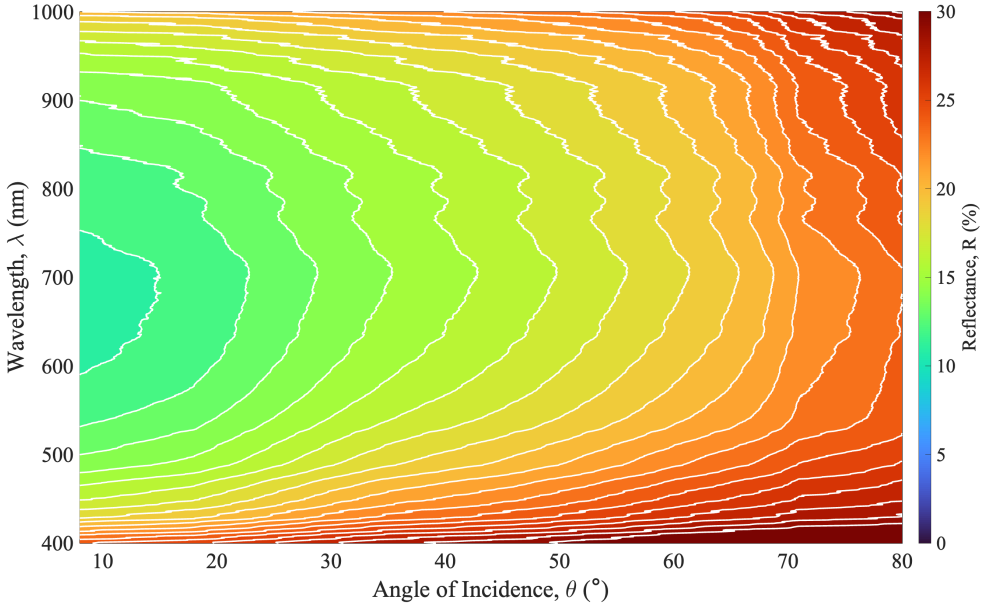

(a)

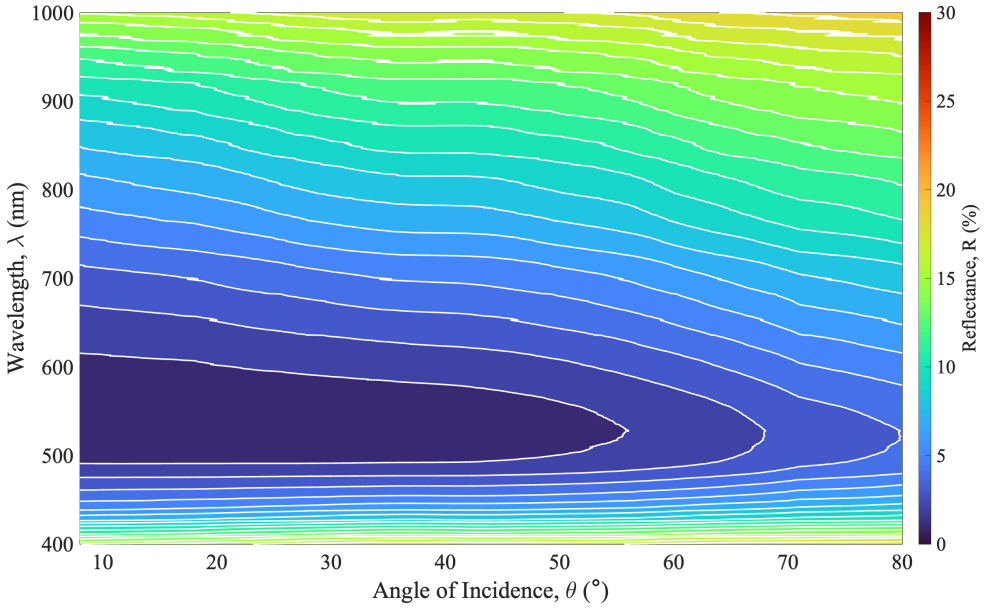

(b)

Figure 5.5: The VAR data for the pyramidal samples both without (a) and with (b) an 80 nm SiN_x ARC. The reflectance scale is identical between figures 5.5, 5.6, and 5.7 to aid with comparison.

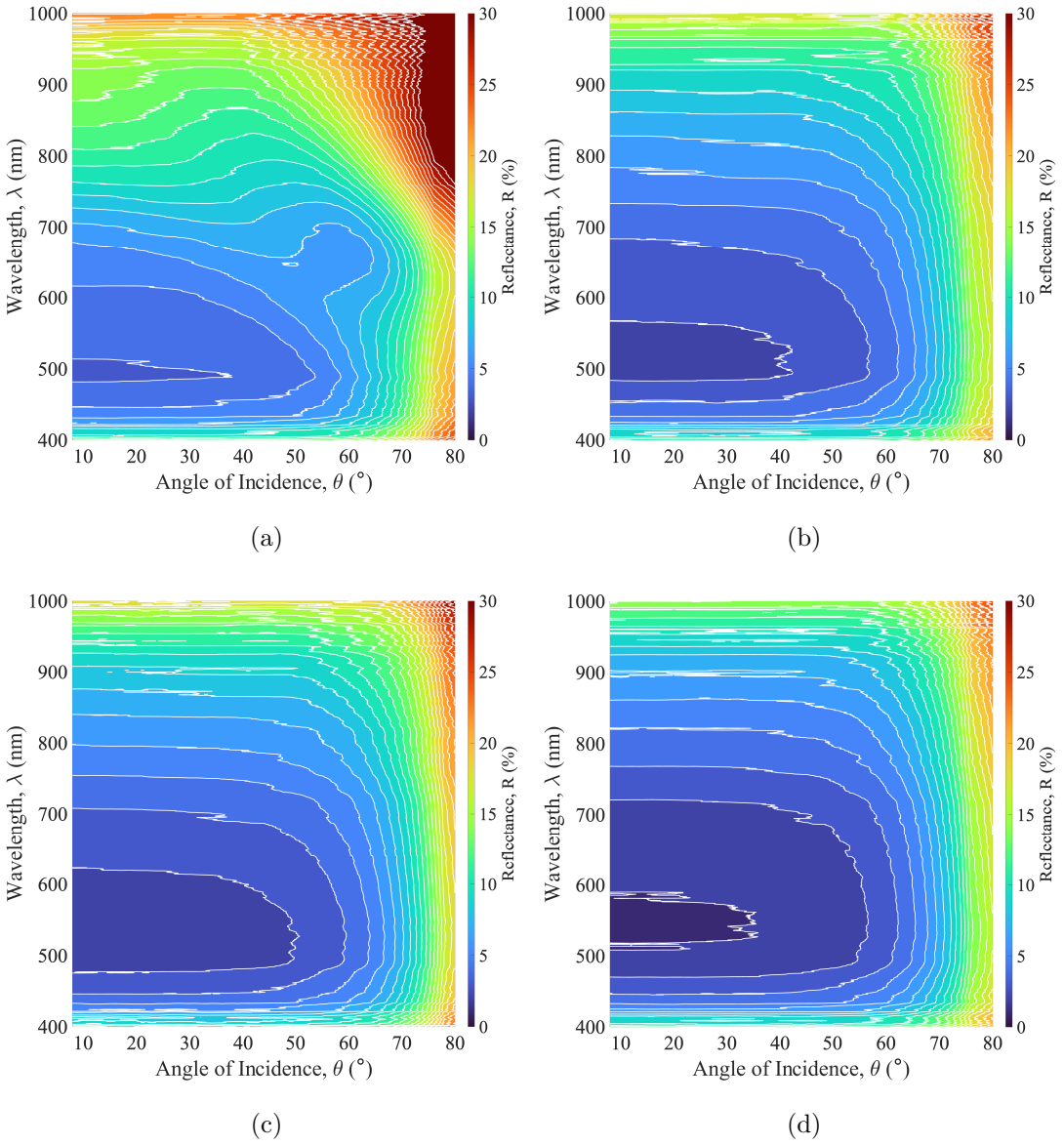

Figure 5.6: The VAR data for the b-Si samples for etch times of 4 (a), 6 (b), 8 (c), and 10 (d) minutes. The reflectance scale is identical between figures 5.5, 5.6, and 5.7 to aid with comparison.

the pyramid–based textures in figures 5.5a and 5.5b. A combination of both vertical and horizontal lines, applicable in different areas of the wavelength and angular distribution, demonstrates wavelength or angle independence that in itself is dependant on both of these properties. For example, reflectance can be seen to remain constant regardless of incidence angle up to between 40° and 60°, with the latter applicable for wavelengths in the NIR and NUV, and the former for the visible spectrum. A distinct rectangular pattern is created by this characteristic for a subset within the reflectance data, for each of the etch times shown, but with greater prominence for $t_e > 4$ minutes (figures 5.6b, 5.6c, and 5.6d). In the case of $t_e = 4$ minutes (figure 5.6a), this feature is slightly more obscured but still remains visible through higher values of reflectance.

Crucial to note, in the case of all samples as in figure 5.6, reflectance in the visible spectrum, $400 \leq \lambda \leq 700$ nm, is consistently the lowest throughout the angular sweep, holding even up to very high incidence angles of 80°. Reflectance for these samples is, in terms of absolute reflectance, generally 5 to 10% higher than the visible region in the NIR above 60°.

For longer etch times, and thus taller NWs, the low reflectance contour regions can be seen to grow and expand to fill the VAR data plots. Nanostructured b-Si surfaces create a graded refractive index effect between the superstrate (air) and substrate (Si). The taller the NWs are the shallower this gradient is, resulting in a smoother transition between the two media, and hence a better anti–reflective effect. This is why longer etch times produce b-Si surfaces with decreasing levels of reflectance. The reflectance minimum for the 4 minute sample represented in figure 5.6a is located at approximately 500 nm and shifts toward 650 nm suddenly about an incidence angle of 60°. The reflectance at these points is 3.8% and 18.9%, respectively. As the etch time is increased through to 10 minutes, this minima shifts upward toward 550 nm but remains in position regardless of incidence angle. This data for all the b-Si samples is summarised in table 5.1.

The maximum reflectance, sample irrespective, is at 80° and in the NIR – the top right corner of each contour plot. This is mirrored in the NUV, where Si is highly reflective by default. Planar b-Si surface texturing can be seen to make significantly better use of the NIR and NUV when compared to pyramids inclusive of an ARC. On comparison of figures 5.5b and 5.6, the low reflectance region of the pyramid–based sample stretches to the right, however the same region for b-Si is instead stretched diagonally upwards to the right, permitting a far greater area coverage outside the

Table 5.1: Summarising how the reflectance minima varies in both wavelength, λ, and reflectance, R_x, on the lower and upper sides of the angular distribution for the b-Si samples.

Etch Time, t_e (Minutes)	**Reflectance Minima**			
	Lower (8°)		Upper (80°)	
	λ	R_x	λ	R_x
4	500 nm	3.8%	650 nm	18.9%
6	525 nm	2.8%	525 nm	17.4%
8	535 nm	2.5%	535 nm	18.5%
10	550 nm	1.9%	550 nm	16.8%

visible spectrum. Despite this, the data in figure 5.5b does show how pyramids, when coupled with an ARC, can outperform b-Si in terms of minimum reflectance levels. In order for b-Si to reach an equivalent level of reflectance, the NWs would need to be excessively tall – a hindrance for solar applications given the increasing complexity of passivating a surface with disproportionate features (far taller structures than they are wide, for example).

Moving to hb-Si textures, there is once again a clear jump in optical performance across the spectrum. Figure 5.7 shows the data for hb-Si samples etched using the MACE process for periods of 4, 6, and 8 minutes. Immediately apparent is the shift in minima between 500 and 550 nm for planar b-Si, to $\sim$ 650 nm in the case hb-Si.

On taking the worst performing hb-Si sample ($t_e = 4$ minutes), the substantially lower reflectance minima at both 8° and 80° when compared to even the best performing b-Si sample ($t_e = 12$ minutes) is clear. At 8°, the 4 minute hb-Si sample has less than 50% the reflectance of the 12 minute b-Si sample. Notably, the wavelength position of the reflectance minima at shallow angles of incidence remains the same between all the datasets in figure 5.7. Table 5.2 summarises this data for the hb-Si samples. Moreover, the hb-Si samples are shown to exhibit a broader anti–reflective effect over both wavelength and angle ranges compared to the planar b-Si samples.

5.4.1.3 Average Reflectance

Table 5.3 contains the tabulated average CMSAR, $\bar{R}_x(8°)$, and CMVAR, $\bar{R}_x(\theta, \lambda, \varphi)$, values for all the samples shown across figures 5.5, 5.6, and 5.7. This data is *not* weighted

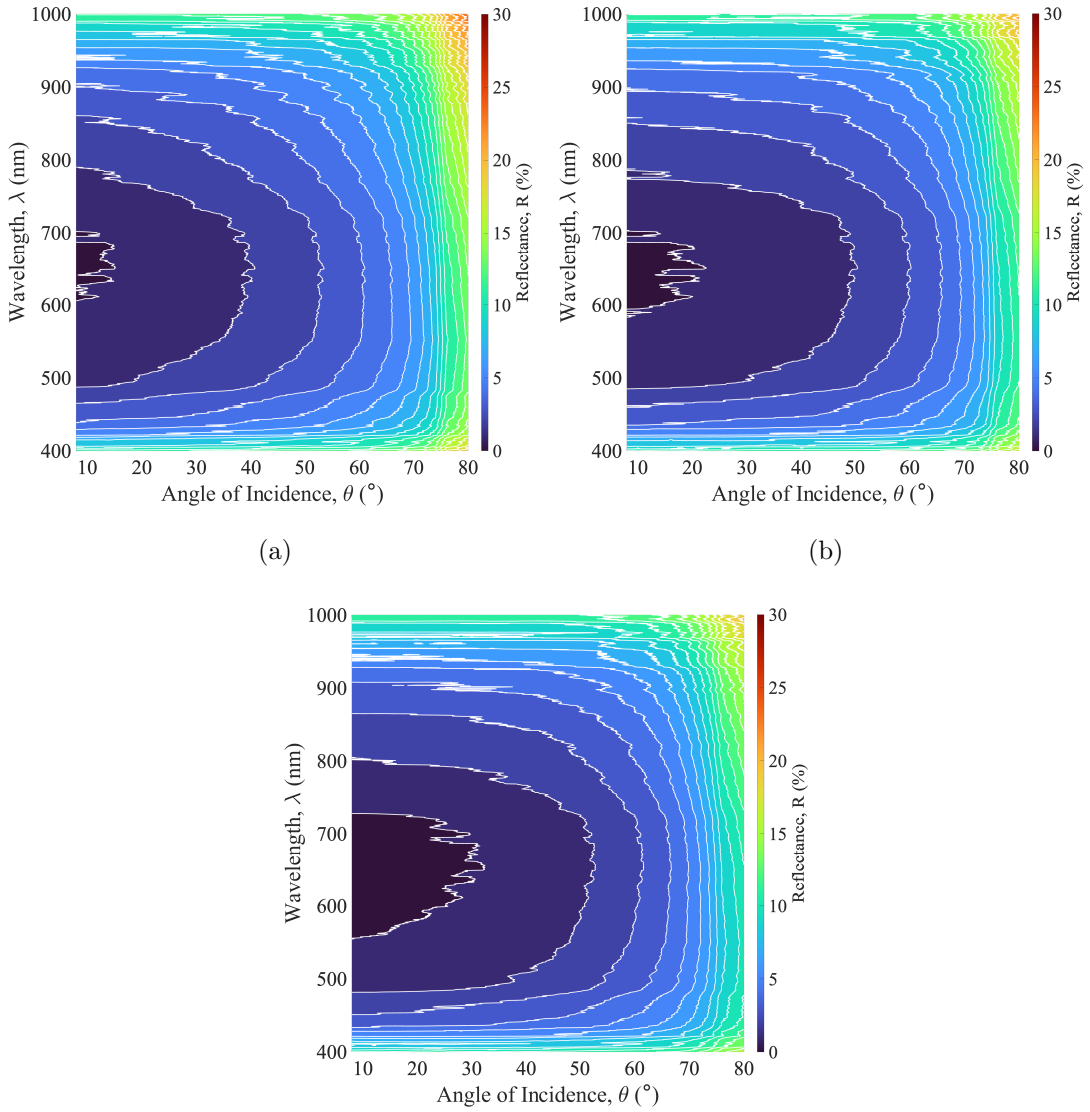

Figure 5.7: The VAR data for the hb-Si samples with etch times of 4 (a), 6 (b), and 8 (c) minutes. The reflectance scale is identical between figures 5.5, 5.6, and 5.7 to aid with comparison.

Table 5.2: Summarising how the reflectance minima varies in both wavelength, λ, and reflectance, R_x, on the lower and upper sides of the angular distribution for the hb-Si samples.

Etch Time, t_e (Minutes)	**Reflectance Minima**			
	Lower (8°)		Upper (80°)	
	λ	R_x	λ	R_x
4	650 nm	0.9%	650 nm	14.0%
6	650 nm	0.9%	650 nm	12.0%
8	650 nm	0.7%	650 nm	10.9%
10	–	–	–	–

against the AM1.5 spectrum shown in figure 1.14, and is instead a standard average taken over both directions of each empirical dataset. As identified in the creation of the ARS, reporting the SAR alone as a quantitative metric for optical performance does not provide a true indication of such performance. This can be seen side–by–side here; every sample has an average CMVAR value considerably higher than the equivalent CMSAR value. The implication of this is that SAR data will always yield a lower average reflectance than VAR. This is understandable given the tendency for lower reflectance at shallower angles of incidence as proven by the Fresnel equations in equations (4.26) and (4.27), for either S– or P– polarisation, respectively. As a result of this, only VAR will be cited going forward.

In summary of the data shown in table 5.3, notable is how effective the use of any ARC topology, be it b-Si NWs or a thin film, dramatically decreases the default reflectance of uncoated pyramids. The use of the common SiN_x coating essentially halves this value, from 20.8% to only 10.6% – a 49% relative decrease. When this is replaced with a coating of NWs, the effect is even more pronounced. Relative drops in reflectance between bare pyramids and hb-Si range from 60 to 65% as the height of the NWs is increased. The worst performing hb-Si sample has a reflectance metric over 2% (absolute) lower than the typical PV ARC implementation. However, and as previously mentioned in chapter 1, the applicability of these textures to solar PV must be considered here.

Surface passivation, usually through the deposition of a thin film of a dielectric material, is essential for solar cells to function effectively. However, the introduction of nanoscale surface texturing can hinder the application of a uniform passivation layer across the entire surface, as is required for high performance. The deposition of a passivation layer,

Table 5.3: SAR and VAR measured average reflectance for all nine of the samples measured across figures 5.5, 5.6, and 5.7. These values are not weighted against the AM1.5 spectrum. Samples highlighted in blue are carried forward for advanced analysis.

Sample	$\bar{R}_x(8°)$	$\bar{R}_x(\theta, \lambda, \varphi)$	$\Delta\bar{R}_x$
Pyramids (Bare)	15.7%	20.8%	+5.1%
Pyramids + 80 nm SiN_x	8.5%	10.6%	+2.1%
b-Si (4 Minutes)	13.3%	15.7%	+2.4%
b-Si (6 Minutes)	9.7%	11.5%	+1.8%
b-Si (8 Minutes)	9.6%	11.3%	+1.7%
b-Si (10 Minutes)	8.0%	9.8%	+1.8%
hb-Si (4 Minutes)	5.9%	8.4%	+2.5%
hb-Si (6 Minutes)	5.8%	7.6%	+1.8%
hb-Si (8 Minutes)	5.5%	7.2%	+1.7%

in the case of b-Si or hb-Si, needs to result in conformal coverage of each individual NW. This is possible through atomic layer deposition methods [66, 67], but is increasingly more difficult to achieve the taller and more complex the texture features are. The results in figure 5.7 show that there is only a small decrease in reflectance for increasing NW height for the hb-Si samples, in contrast to the larger decreases in reflectance seen for the equivalent b-Si samples. As such, it is possible to compromise on overall reflectance and select the hb-Si sample with shorter NWs for application onto a solar cell, whilst still maintaining exceptional levels of optical performance and good compatibility with existing passivation methods.

5.4.2 Samples After Encapsulation

On applying an encapsulant (NOA 61) layer and glass (borosilicate) layer to the samples, the VAR characteristics of the samples fundamentally change to correspond with what would be expected for real–world deployment. It is assumed that the electrical contacts would be mounted on the rear of the cell (that is to say an IBC) to ignore any self–shading effects. The updated VAR contours for the two encapsulated samples can be seen in figure 5.8.

The general patterns for both textures in figure 5.8 are more consistent with one another than shown in previous plots without the inclusion of any encapsulant layers. Take the pyramids inclusive of the single–layer ARC, for example. When unencapsulated (figure

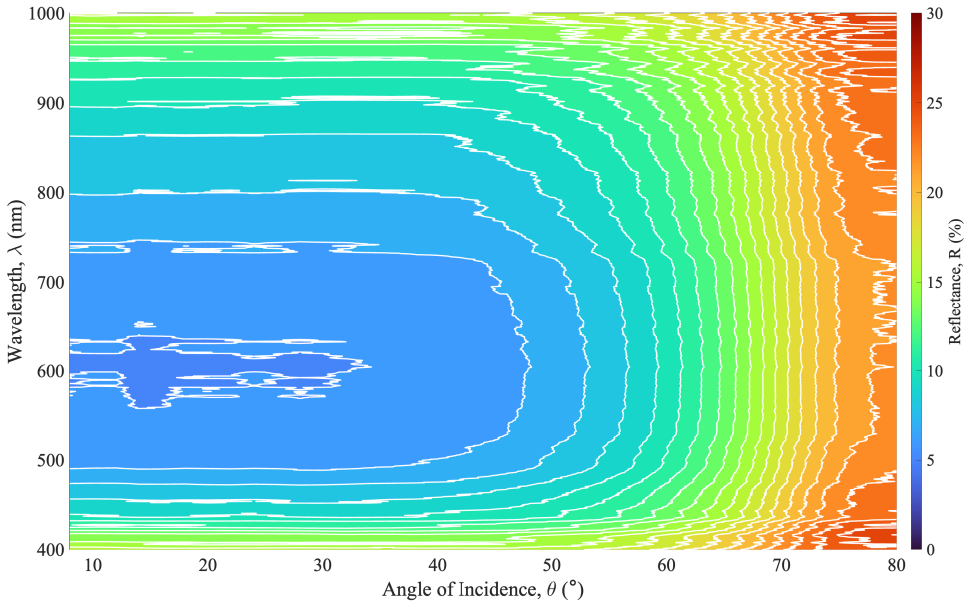

(a)

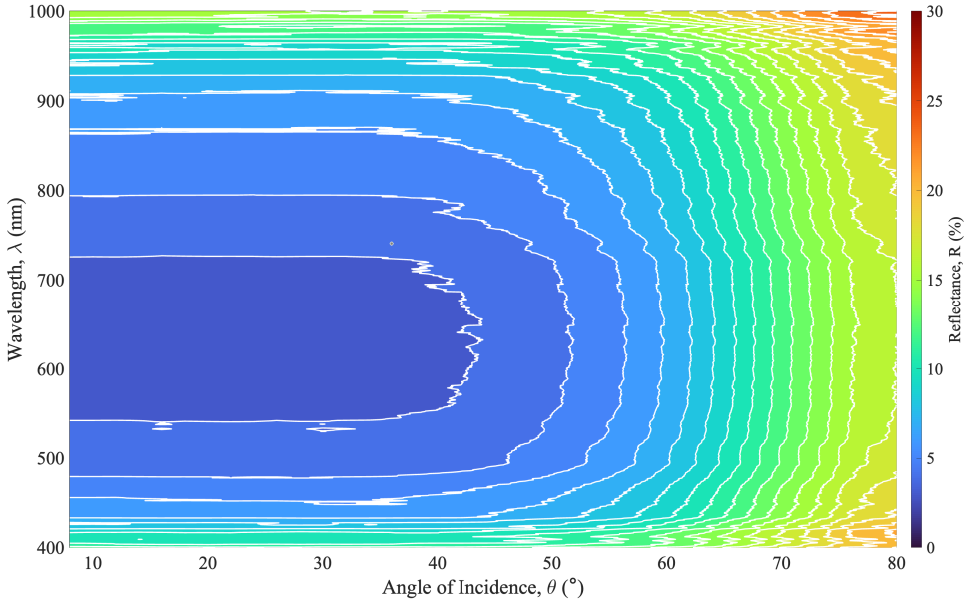

(b)

Figure 5.8: The VAR data for the pyramidal sample with an 80 nm SiN_x ARC (a) as well as the 4 minute hb-Si sample (b), now encapsulated with the same physical structure as in figure 5.1.

5.5b), this texture exhibits a distinct low–reflectance band formed along the angular distribution between wavelength of 500 and 600 nm, extending all the way up to an 80° incidence angle. When encapsulated (figure 5.8a), the reflectance contours form a pattern similar to that of the hb-Si, and the uncoated pyramids as seen in figure 5.5a. Data compared from each of these figures (5.5a, 5.5b, and 5.8), as well as figure 5.7, suggests that similar base structures, in this case pyramids, illicit similar spectral reflectance curves under the same incident lighting conditions, whereby the magnitude of reflectance is dictated by the coating (if any) applied to such structures.

Both textures, as to be expected, exhibit increased reflectance minimum resulting from the greater number of optical interfaces present. Each interface, according to the Fresnel equations, will both transmit and reflect a certain quantity of light. There will also be loss resulting from absorption in the encapsulant layers, reducing the total energy available for e-h pair generation. The VAR reflectance minima for the hb-Si and pyramidal samples shown in figure 5.8 are 3.7% and 5.9%, respectively. This represents an increase of 3% and 4.6%, respectively. Reflectance levels in the NUV and NIR are noticeably lower for the sample shown in figure 5.8a when compared to the same sample without encapsulation. This apparent optical improvement is due to the increased refractive index steps between the air and silicon that help to steer the light inward toward the normal through refraction. Pyramids see the biggest improvement in these spectral regions as their ARC topography does not create the graded refractive index seen with nanostructures like Si NWs.

Conformity between the NOA 61 encapsulant and surface texturing is an influential factor on optical performance requiring discussion. Typically, microscale textures such as pyramids allow the encapsulant layer, applied as a liquid, to conformally coat the Si substrate surface with no trapped air bubbles. However, nanoscale textures like the hb-Si structures, with very small gaps between each nanowire or nanowire cluster, make it difficult for the encapsulant to conform well to the Si material. As a result of the viscosity of NOA 61, coupled with the nanoscale pores exhibited by hb-Si, it is likely that the encapsulant is unable to seep into these gaps – instead simply sitting on top of the NW structures. This creates pockets of air situated between the encapsulant, NWs, and substrate surface, affecting the smooth graded refractive index seen previously and will contribute to the measured reflectance for such samples.

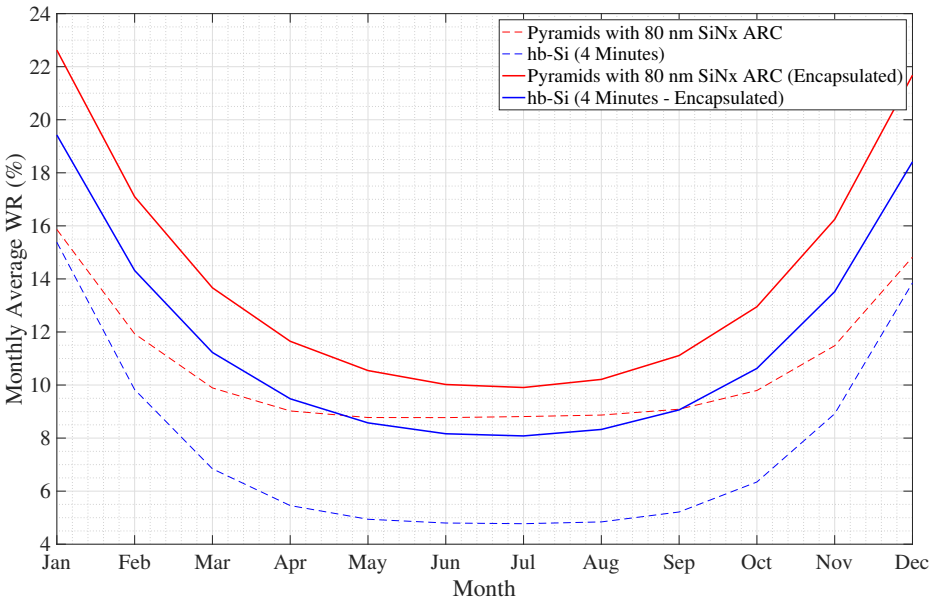

Figure 5.9: The WOR determined for both the pyramidal (red) and hb-Si (blue) samples, with VAR as shown in figures 5.8a and 5.8b, respectively. The data shown here is for Southampton, UK.

Table 5.4: An overview of the key data statistics for the samples shown in figure 5.9.

Sample	**WR (%)**		
	Min.	*Max.*	*Mean*
Pyramids with 80 nm SiN_x ARC	8.8%	15.9%	10.6%
Pyramids with 80 nm SiN_x ARC (Encapsulated)	9.9%	22.6%	14%
hb-Si	4.8%	15.4%	7.6%
hb-Si (Encapsulated)	8.1%	19.4%	11.6%

5.4.3 Weighted Reflectivity

The pyramids featuring an 80 nm layer of SiN_x and the 4 minute hb-Si sample are carried forward for further analysis. For reference, the average height of the NWs on the 4 minute hb-Si samples is 790 nm. The WR for the samples shown in figures 5.5b and 5.7a can be seen in figure 5.9 as a function of the month in the year. For both anti–reflective surfaces, it can be seen that WR is higher in the winter months. This is to be expected given the lower average elevation of the Sun during winter. At and around the winter solstice, the Sun maintains a far lower elevation, and thus a larger angle with the surface normal, for the majority of the solar day. By contrast, the Sun is much higher in the sky throughout the summer months, resulting in a smaller angle of incidence and hence a lower reflectance.

The sample consisting of pyramids with an ARC coating, a standard for c-Si solar PV, performs well and consistently throughout the year. At its worst, this scheme exhibits a WR of approximately 15.9%. This drops down to a value of just 8.8% in the high–elevation summer months, with the best performing month being June. The mean WR across the entire year is 10.6%. On the other hand, hb-Si performance varies more than the pyramids, starting only slightly lower in winter and swinging much lower in the summer. The WR for hb-Si ranges between 15.4% and 4.8% over the year, with an average WR of 7.6%. This shows the hb-Si surface as the best overall performer, with significant performance improvements over conventional texturing in the summer months, and slightly better relative performance in the winter months. This data showcases points made previously, whereby weighted average reflectance measurements are crucial to *fully* understanding the implications of solar cells, particularly those with nanoscale texturing that behave very differently to their microscale counterparts under incident illumination.

Re–evaluating the WR for encapsulated samples brings a considerable change in theoretical performance when located in Southampton. Figure 5.9 shows how peak performance, once again, can be obtained during peak summer usage with the longest days, and highest solar elevation. However, optical losses are much higher than in the absence of encapsulation. The lowest WR for these samples are 8.1% and 9.9% for hb-Si and coated pyramids, respectively. It is once again highest in the winter months, hitting highs of 19.4% and 22.6%, respectively, with average weighted reflectivities of 11.6% and 14%. These key statistical points for the WR presented in figure 5.9 are summarised in table 5.4 for reference. This figure, coincidentally, showcases the advantage of hybrid

structures when used over the whole year, with a consistently better performance across every month of the year. When encapsulated, the shape of both WR curves become very similar, with only an apparent translational difference along the y–axis. This is subtly different to when the samples were unencapsulated, where the curves have slightly differing shapes to one another.

5.5 Conclusions

We have employed the versatility of the ARS for angle–resolved reflectance measurements on several nanoscale textures such as b-Si and hb-Si, alongside traditional anti–reflectance mechanisms such as microscale pyramidal textures that are both bare and coated with an ARC. Theoretical calculations are applied to extrapolate the performance of these anti–reflectance methodologies should they be applied to all back contacted silicon solar cells inclusive of their encapsulation and glass layers. Bare pyramids are initially used as the baseline sample, with every subsequent sample outperforming it. The VAR performance of b-Si generally sat behind that of the coated pyramids, with the only exception being the longest etch time of 10 minutes, which equated to NWs with an average height of 2.55 μm. This optical efficiency is visibly proportional to NW height as a result of the gradient in refractive index created by these nanostructures. A similar effect could be seen with hb-Si samples that comprised of longer NWs; reflectance steadily decreased with increasing NW height, but to a far smaller degree than planar b-Si due to the already substantially low levels of reflectance.

Consideration was made regarding the applicability of these textures to solar applications. Excessive NW height makes these surfaces difficult to passivate effectively – a considerable drawback to the approach. In finding the appropriate balance between height and optical performance, hybrids containing NWs under 1 μm were selected, being the 4 minute etch. This decision was supported by literature on the subject as well as the optical performance quantified in figure 5.7a. This hybrid black silicon sample was carried forward to be compared with its primary competitor: pyramids coated with an ARC.

When encapsulant and glass layers were applied and the VAR and WR analyses were re–run, hb-Si was shown to be highly effective and performed better than its pyramidal counterpart. WR ranged from 8.1% to 19.4% over the year. In comparison, the WR of pyramids inclusive of these encapsulant and glass layers varied from 9.9% to 22.6% under

the same conditions. Hb-Si textures are shown to perform notably better than pyramids with NIR and NUV responses considerably lower when unencapsulated. This difference in performance is still present but notably less when both are encapsulated, where the encapsulant layers reduce the angular range of incident light through refraction towards the normal.

This work demonstrates how obtaining the full spectral and angular reflectance characteristics of a surface can be used to compare anti–reflective schemes for applications where broadband light is incident at varying angles, using crystalline silicon photovoltaics as an example. The approach is extendable to other photovoltaic technologies and to other applications in optics for which the illumination conditions change over time.

Chapter 6

Computational Physics for Stochastic Nanostructures

The work described here has been published in a journal paper

J. J. Tyson, T. Rahman, and S. A. Boden

"A New Mathematical Interpretation of Disordered Nanoscale Material Systems for Computational Modelling"

Computer Physics Communications, Volume 255

October 2020

DOI: 10.1016/j.cpc.2020.107399

6.1 Introduction

As with the aforementioned stochasticism of b-Si, it is not possible to create a truly succinct model indicative of its inherently unpredictable nature. Herein, the applicability of the FEM in the accurate modelling of planar b-Si, aiming to simulate the surface optical response. A 3-D model of planar Si was created with EM waves incident directly on the top surface of the Si substrate; that is to say the boundary present between the air and Si domains. On confirmation that determined reflectance was as theory states, implying the correct physics parameters have been applied, b-Si NW textures are applied to this boundary with varying degrees of pseudo-randomisation. These degrees are defined in terms of levels, whereby level zero is indicative of periodic NW arrays, level one includes the pseudo-randomisation of NW heights, radii, bending, and pitch, and level two introduces bunching. Level three, the most complex of the levels, is identical to the previous, only with non-cylindrical footprints as opposed to modelling NWs as cylindrical structures.

6.2 Computational Methodology

6.2.1 Statistical Mathematics for Heterogeneity

6.2.1.1 Implications on Reflectance

Effective pseudo-randomisation requires a high degree of sequential mathematical processing, to which a substantial number of 'random' functions, logical switches, and iterative calculations must be employed before any geometry is realised. The b-Si model was inclusive of three pre-processing stages, listed respectively of their execution order: pseudo-randomisation, generation, and meshing.

$$R_t(\lambda) \cong \bar{R}_n(\lambda, S) = \frac{1}{n}\sum_{i=1}^{n_c} R_i(\lambda, S) \tag{6.1}$$

$$[R_t(\lambda)]_M \cong \left[\bar{R}_n(\lambda, S)\right]_M = \left[\frac{1}{n}\sum_{i=1}^{n_c} R_i(\lambda, S)\right]_M \tag{6.2}$$

By generating enough different iterations, i, of the geometry, each with a different random seed, S, each can be simulated whilst taking a summing average to more accurately obtain the target property. Here, surface reflectance, R, was taken as the property of interest. Equation (6.1) shows that $\bar{R}_n(\lambda, S) \equiv R_t(\lambda)$ for $n \to \infty$, where R_n is the average reflectance of n NW surfaces and $R_t(\lambda)$ is the reflectance of an entire b-Si surface, essentially made-up of all these iterations. In FEM-based EMWO, light can be simulated in one of two discrete modes; TE or TM. To represent these discrete modes, both sides of equation (6.1) are subscripted as shown in equation (6.2), where M is the mode. The average of these two modes, TEM, can also be calculated as being more indicative of ambient irradiance.

Post-processing was limited to a single step process, whereby the number of geometry iterations, n, required for convergence could be distributed appropriately for the system architecture. On a multi-parallel computer system, that is to say a network consisting of multiple individually addressable multi-thread compute nodes, this can be done immediately should the point of convergence, n_c, be known. For serial or low-powered computer systems, this would run in the form of a closed loop; one iteration after another. This results in a very extensive simulation runtime. The point of data convergence is a crucial study that must be carried out prior to simulation on parallel-execution systems for a given simulation geometry to be modelled accurately and efficiently. This takes the form of a single parameter simulation run with multiple geometries and averaging on the result of each.

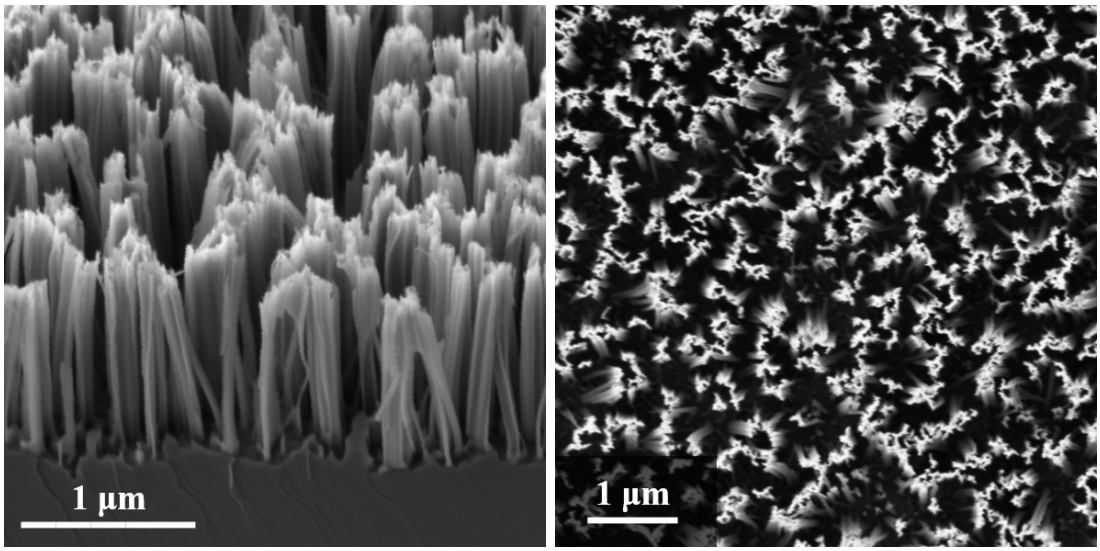

(a) (b)

Figure 6.1: Scanning electron microscopy images of a Si surface decorated with vertically-aligned NWs from side-on (a) and top-down (b).

Theory outlines that a point must be reached where an individual simulation result does not cause large deviation from the summed average of those before it; this is the point of convergence as in equation (6.1). On serial or low-powered computer systems however, this study is not required as the solver sequence can determine convergence after each iteration. Once guidelines for the desired geometry of the model are known, static parameters are input outlining specific properties of the surface being modelled. Here, where a surface covered with b-Si NWs was recreated, scanning electron microscopy (SEM) images were used as a basis for these parameters. Examples of these images are shown in figure 6.1.

6.2.1.2 Black Silicon

Average values for the silicon NWs of the model geometry are used as a point-of-reference to which randomisation can be applied. For instance, taking the images shown in figure 6.1, the silicon NWs can be observed as having an approximate height, h, of 1 μm, approximate average separation (pitch, g) of 180 nm and diameters, d, of up to 160 nm. Each NW is different, though this approximates the average values for these properties across the entire surface. Using this information, some degree of pseudo-randomisation could be applied to each individual NW within the model geometry. These properties

were varied on a per-NW basis using the following formulation:

$$z(S) = z_0 + \Delta z(S) \tag{6.3}$$

Here, z is the randomised parameter, z_0 is the average value for that parameter as described previously, and Δz is some random variation to be applied depending on a given input seed, S. Each parameter has an individual range in which it can be varied. This is carried out by defining Δz as a random function with a mean of zero and a range of some finite amount. The model reported here applied the variation limits shown in table 6.1. For these parameters, uniform distributions were employed over that of Gaussian to enable greater control and predictability in their subsequent variation.

Table 6.1: Variations applied to the key parameters of each Si NW.

Parameter, $z(S)$	**Average Value, z_0**	**Applied Variance, $\Delta z(S)$**
Radius, $0.5d$	50 nm	-30 nm $\leq \Delta z \leq 30$ nm
Height, h	1 μm	-15 nm $\leq \Delta z \leq 15$ nm
Pitch, g	180 nm	-56 nm $\leq \Delta z \leq 56$ nm

The values outlined in table 6.1 were derived from observations of real Si NW structures (see chapter 3). Commonly, little deviation is observed in height given a well-executed etching process. However, pitch and radius vary considerably more than this, and subsequently larger magnitudes of applied variance were permitted for these properties. It is difficult to quantify these variances exactly, however average variances as observed through imaging the samples have been applied here. Generating NWs in the geometry is a multi-step process consisting of several sub-elements. Notably, a footprint, spine, and extrusion needed to be created for each individual NW generated within their respective 4×4 array. Experimental observations of real variants of these surfaces have demonstrated how such structures may not be modelled accurately simply as cylinders. In fact, Scheul et al. [158] have demonstrated that many Si NWs have unpredictable outlines presenting an additional area for randomisation.

$$x_w(S) = r_{0.5d}(S)\cos(2\pi s)\left[1 + \frac{1}{10}\sum_{i=-N}^{N}\left(i^{-b} r_g(i,S)\cos(2\pi i s + r_u(i,S))\right)\right] \tag{6.4}$$

$$y_w(S) = r_{0.5d}(S)\sin(2\pi s)\left[1 + \frac{1}{10}\sum_{i=-N}^{N}\left(i^{-b} r_g(i,S)\cos(2\pi i s + r_u(i,S))\right)\right] \tag{6.5}$$

Random footprints for these NWs were generated using a modified random function coupled with a parametric curve element. This curve defaulted to unity at the scale set for the model; the nanometre range here. Subsequently, the parametric curves were initially generated about an approximate radius of 1 nm. This was scaled-up to the correct size as defined by the static radius parameter, $0.5d$, by multiplying the two together. This mathematical method is shown for both the x and y components of the curve in equations (6.4) and (6.5), where S is the input seed, r_u is a uniform random distribution, r_g is a Gaussian random distribution, N is the spatial frequency resolution, and b is the spectral exponent. The values used in equations (6.4) and (6.5), in order to create the random footprints reported in figure 6.2 were $N = 10$ and $b = 0.7$. For the uniform random distribution, r_u, a mean of zero and a standard deviation of π was used, whilst for the Gaussian distribution, r_g, a mean of zero and a standard deviation of one was used.

Figure 6.2a demonstrates the relationship between the statically defined radius, $0.5d$, and the randomised parametric curve about it after using the radius as a multiplier. In this form, it is important to realise that the curve is simply a boundary, and subsequently cannot be extruded into 3-D NW domain directly. Instead, the convert-to-solid method within COMSOL Multiphysics®† was used to fill the area enclosed by this curve and subsequently visualise it as a surface instead. The use of this method required the implementation of a separate work plane, consisting of the newly-created surface, mapped to the original 3-D domain. This meant that each Si NW footprint was not created within the original coordinate system but could be referenced from it. The work plane had a 2-D Cartesian coordinate system denoted by x_w and y_w and held the footprints for all NWs within the array, inclusive of their variable pitch as shown in figure 6.2b.

The 3-D extrusion of the surfaces shown in figure 6.3b is achieved externally from the work plane in the core simulation domain. These surfaces can be addressed individually and formed into NWs using a quadratic Bézier polygon as a basis for extrusion. It is to this curve where the variation of height, h, must be applied, as well as any bend/bunching properties. In reference back to figure 6.1, it is clearly visible that these nanoscale structures bend towards one another at sufficient height. Being able to recreate this in simulation enables a further increased level of accuracy and allows us to observe how this effect changes other properties of the surface. An imaginary line is configured to be drawn between any two parallel edges of the model. Shown in figure 6.3b is this

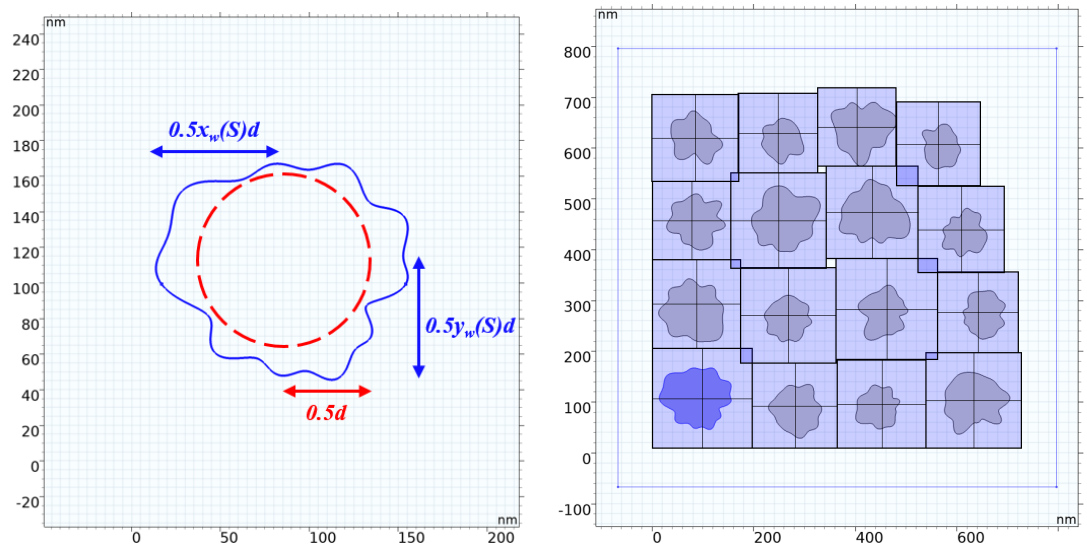

(a) (b)

Figure 6.2: The domain-mapped 2-D work plane hosting an exemplar single parametric curve-based boundary (a), and a 4×4 array of Si NW faces demonstrating variable pitch, g, and radius, $0.5d$ (b).

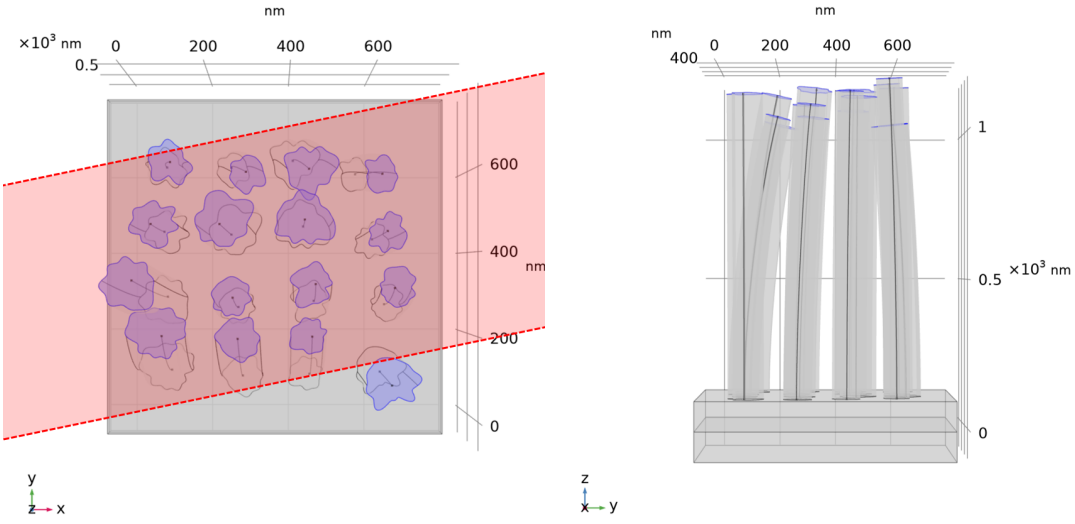

(a) (b)

Figure 6.3: Demonstrating how bending and bunching is achieved between the bottom and the top (highlighted in blue) of each silicon NW. The tops can be seen to have the same shape as their respective footprints but have been translated toward a bunching zone shown in red (a) following their Bézier polygon spines (b).

line bearing right whilst originating from the left. Using this line as a basis, a radius around it can be drawn to create an area of oblong proportions; this is the bunching zone. Any one of the 16 silicon NWs created here, whose top rests within this zone after the influence of bending is applied, will be shifted towards this zone with varying magnitude and directionality.

6.2.2 Meshing

COMSOL Multiphysics®† is a finite element analysis tool, used in the completion of this work, employing various direct and/or iterative solvers to compute discretised partial differential equations (DPDEs). PDEs are infinitely regressive and representative of real physical geometries existing in both space and time. Analytically near-impossible to solve, discretisation needs to be introduced to these systems to ensure that there are only a finite number of elements making up an infinitely complex geometry. Conversion from a PDE to a DPDE makes the problem solvable in real-time. The solution accuracy for such DPDEs is highly dependent on the level of discretisation used within a given solver sequence.

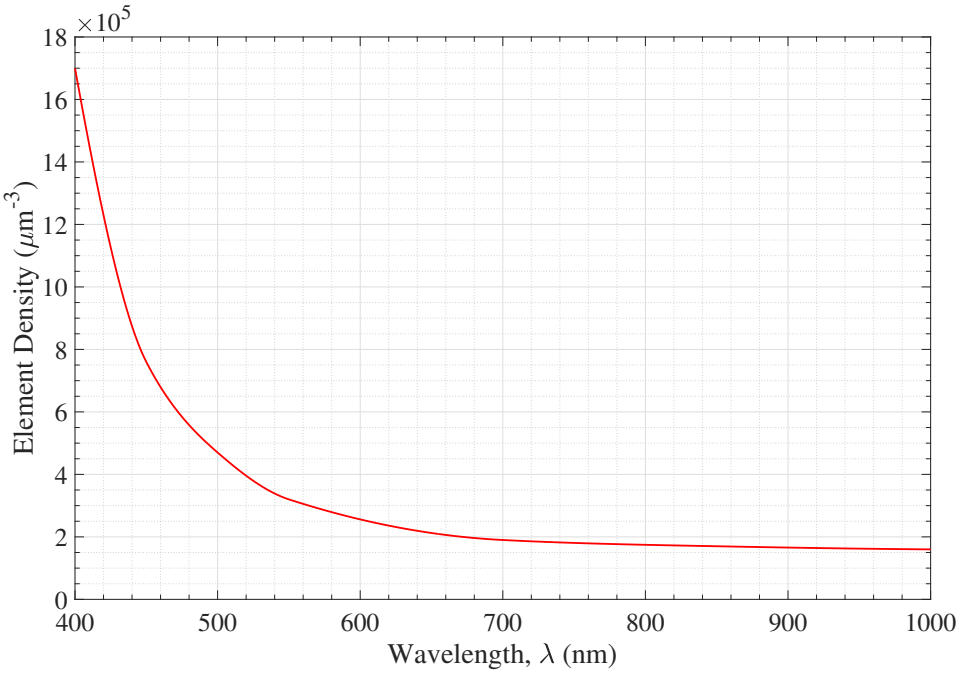

Figure 6.4: Quantifying how the adaptive mesh is dependant on the wavelength of light input, λ.

Employed here is an adaptive meshing strategy, whereby the mesh and inclusive elements were automatically scaled based on the wavelength of light input within the model. The

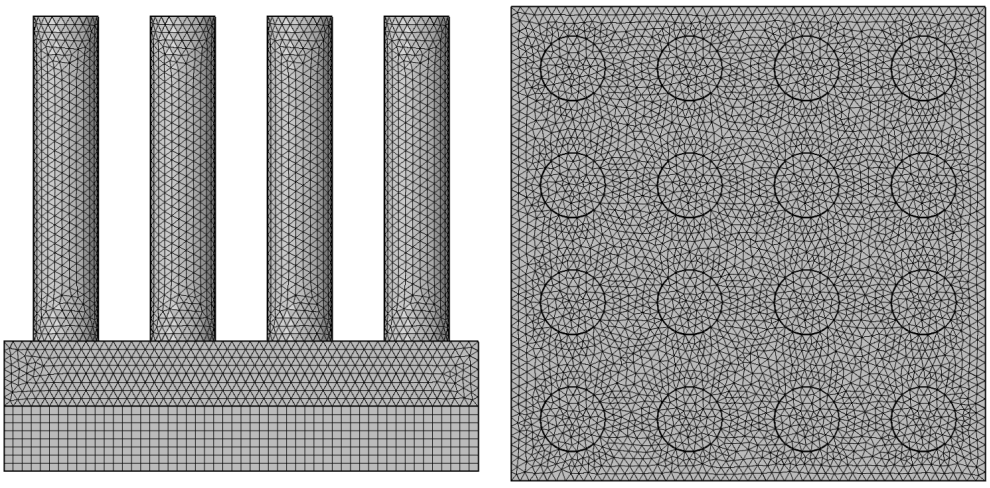

(a)

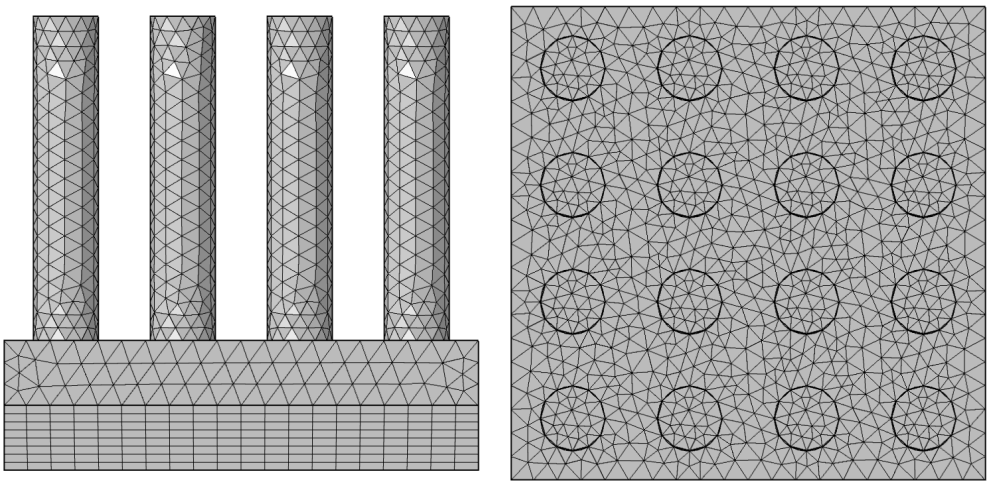

(b)

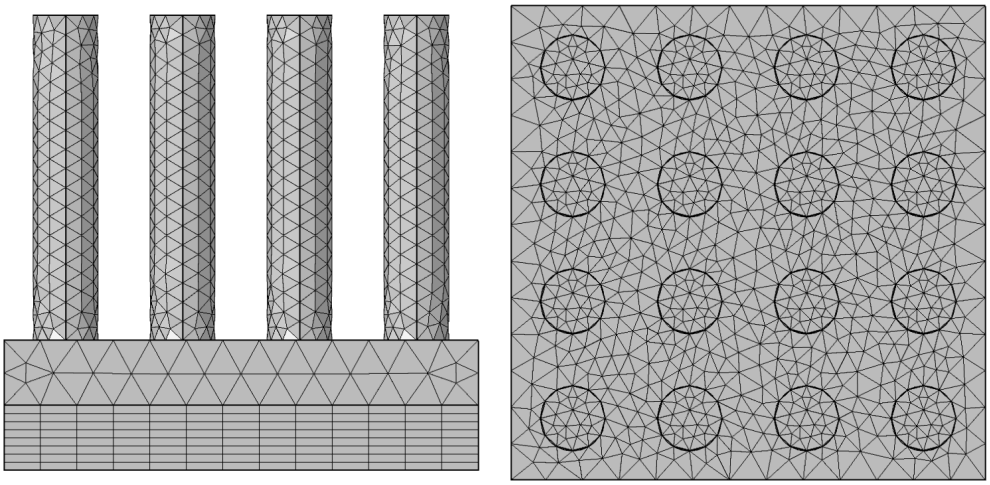

(c)

Figure 6.5: Showcasing how the adaptive meshing strategy responds to input wavelengths, λ, of 400 (a), 700 (b), and 1000 (c) nm. Although the geometry shown here is a 4×4 periodic array, the meshing strategy works identically for non-periodic arrays.

absolute maximum element size must be at least five times smaller than the wavelength being simulated[1]. For example, an input of $\lambda = 400$ nm would require all mesh elements to be 80 nm or smaller. This model set the maximum element size to be 10 times smaller than this wavelength to act as both an optimised physics buffer and to prevent aliasing larger details rendered on each NW. A quantitative summary on what this means to the mesh's element density is shown in figure 6.4. It can be seen here that, for $\lambda > 700$ nm, the density of the mesh does not drop considerably and essentially becomes independent of wavelength entirely. There are two key points taken from this information at wavelengths beyond 700 nm; simulation runtime will remain constant[2] and the maximum size of mesh elements is limited to preserve geometric entities. Figure 6.5 further demonstrates what is shown in figure 6.4, where very little difference in mesh density can be seen between larger wavelengths, particularly from a top-down viewpoint.

6.2.3 Solution Sequencing

Once the entire geometry is meshed it is possible to simulate it. Here, the EM waves frequency domain (EWFD) interface within the Wave Optics module of COMSOL Multiphysics®† was employed to determine the reflectance of the geometries. A FEM model exhibiting such a high level of mathematical dependency on extra-geometrical components requires a considerable number of pre- and post-processing steps. As stated previously, the model was broken-down into key processing stages and executed in the appropriate sequence. It was designed to be as accurate and efficient as possible. The randomisation of individual geometric features could be done anywhere in the pre-processing sequence. Despite this, it was crucial for all randomisation to occur before any rendering took place; this significantly saves on computational resources and time. The implication here being that rendering a non-randomised geometry, only to then have it randomised and subsequently re-rendered, was undesirable, particularly on computer systems that lacked any graphics processing units (GPUs). Incidentally, this simulation is tailored to run remotely on the IRIDIS 5 supercomputer that notably lacks any form of GPU on its standard compute nodes. A system-wide overview was drawn-up to ensure the potentially resource heavy simulation was designed to utilise the strengths of each system involved within the simulation sequence.

It is clear from the information shown in figure 6.6 that the local and remote systems

[1] As outlined in the COMSOL Multiphysics®† Wave Optics module user guide.

[2] Assuming identical runtime conditions and resources.

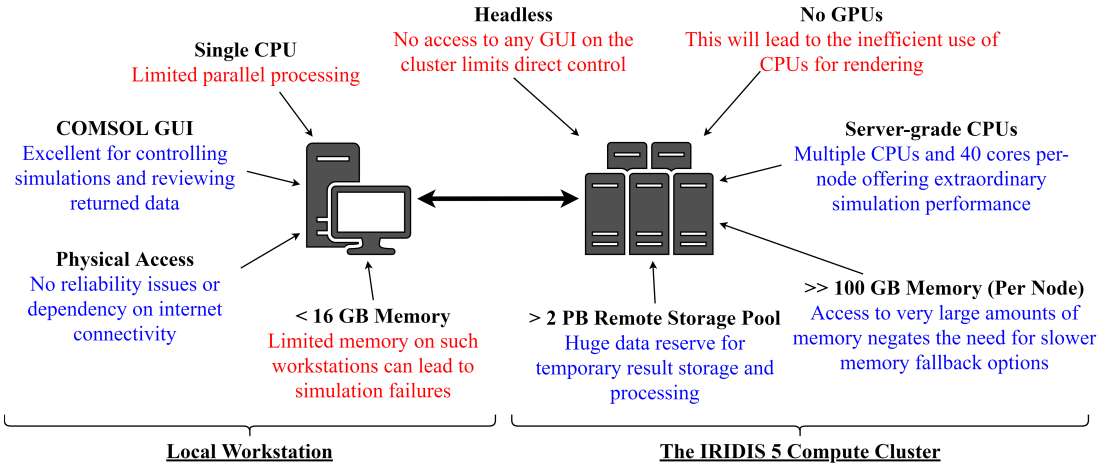

Figure 6.6: An overview of system specifics in preparation for the optimised modelling workflow, where blue indicates an advantage, and red indicates a drawback.

each have their own strengths and weaknesses in general. By using each to showcase their advantages, and play-down their disadvantages, a simulation sequence suitable for both systems could be realised. The only real disadvantages of using the cluster computer – no GPUs, and no user interface. All simulations with a 3-D geometry, particularly a complex one, should both be rendered and meshed using a GPU. It is important to note that CPUs can be used for these tasks, but are not optimised to perform them, and subsequently can easily introduce unnecessary runtime and memory consumption, potentially crashing the solver mid-simulation. Given the local workstation had a GPU, it was decided to complete all rendering on this system, before passing it across to IRIDIS 5 for computation.

Simulations were configured to run using the parallel direct sparse solver (PARDISO), ensuring that out-of-core mode (OCM) was switched off. This is because the nodes on IRIDIS 5 do not have any directly accessible local storage space, and subsequently OCM would cause the simulation to crash on the event of a memory overload. Even if the nodes had local storage space, it is generally inadvisable to use the OCM. Writing data from memory to solid state or mechanical storage, and recalling it when needed, adds substantial delays to the solver sequence. It also can cause serious degradation to solid state storage devices, potentially leading to early component failure. This can simply be bypassed by preventing the solver from using OCM from the beginning, though it is essential to have a system with a significant amount of memory before disabling this mode. Each node on the cluster used here has 768 GB of high-speed memory – adequate for the simulation of even the most complex geometries explored here.

COMSOL®† offers a wide variety of options when it comes to solving remotely. Two software components needed to be configured for this sequence to run successfully; invoking commands and queue management. For COMSOL®† to invoke commands remotely, the "Remote Computing" preferences needed to be configured according to the cluster's setup. The local workstation ran a Windows®‡ 10 operating system not native to the secure shell (SSH) environment used by Linux systems such as the one on IRIDIS 5. A third party program, PuTTY[3], was used to interface with the cluster via SSH. IRIDIS 5 employs the SLURM®§ queuing system which, by default, COMSOL®‡ will not correctly interface with to provide the maximum amount of resources available on each node. Additional scheduler arguments needed to be added to ensure that all 64 cores on each node were available to the remote COMSOL®‡ kernel, and that the 'walltime' was set appropriately. Simulation 'walltime' is simply the amount of time the node will be available for use, and the simulation must subsequently finish within this time allocation. Furthermore, the queue name, 'highmem' as defined here, needed to be set to place the simulations in-line for the correct nodes within IRIDIS 5.

A study first needed to be completed outlining how many different model geometries needed to be simulated in order to see convergence in the results. This took the form of a cluster sweep where the input seed, S, was varied from one to 50 in increments of one. The shortest wavelength to be simulated, a wavelength of 400 nm, was injected into each geometry and the surface reflectance was calculated. The shortest wavelength takes the longest to settle and converge, given the greater number of elements in the model at such wavelengths (as in figure 6.5a). Each of these values for reflectance were then averaged together and the cumulative average plotted against the number of geometries forming that average. The point of convergence, n_c, could be seen when the cumulative average stabilised within a relative tolerance of $\pm 2.5\%$.

Taking this value forward, a full wavelength sweep of $\lambda = 400 : 25 : 1000$ nm would be performed on each of the geometries formed by the input seed, S, representative of values between one and n_c in increments of one. For instance, if the point of convergence, n_c, was found to be 15, then the reflectance response of 15 geometries would be averaged together with input seeds of one to 15. Four levels of randomness were simulated so the effect of heterogeneity on the reflectance of a given surface could be determined. Graphical representations of these levels can be seen in figure 6.7. Note that, for purely periodic geometries, the point of convergence is irrelevant and only one geometry needs

[3]PuTTY: a free SSH and Telnet client by Simon Tatham.

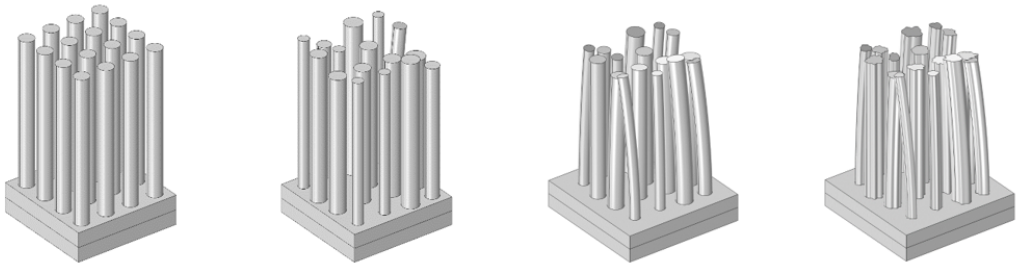

Figure 6.7: Demonstrating how the different levels of randomness are characterised as discrete levels and how they appear in the form of Si NWs.

to be simulated due to a lack of any randomisation. This is the only type of geometry that is completely independent of the input seed, S. For each of the levels shown in figure 6.7, simulation statistics such as runtime, memory usage, total element count and absolute error are noted and compared to identify which is the best compromise between accuracy and resources available.

6.3 Results and Analysis

It can be seen from the data shown in figure 6.8 that convergence in the reflectance data is dependent on the average height of the NWs. Interestingly, the shorter NWs take slightly more geometric iterations before stabilising adequately at a value of $n_c = 20$. For the longer NWs this value was $n_c = 15$. It was at these points where the data held a consistent relative tolerance of approximately $\pm 2\%$; below the magnitude of 5% ($\pm 2.5\%$) as stated in the simulation methodology. This represented an acceptable degree of error in the simulation results and was carried forward into the forthcoming geometric studies.

The point of convergence can be shown as being dependent on the geometric complexity of the model; lower for less complex geometries, and higher for more complex ones. For this reason, the convergence data presented in figure 6.8 is for the most complex geometry, randomness level three. Unfortunately, given the random nature of the geometries being simulated here, it is not conceivable to predict the convergence point mathematically. Implementations of such heterogeneity must have a corresponding study to find this point, ensuring that further data extracted from simulations has in fact converged.

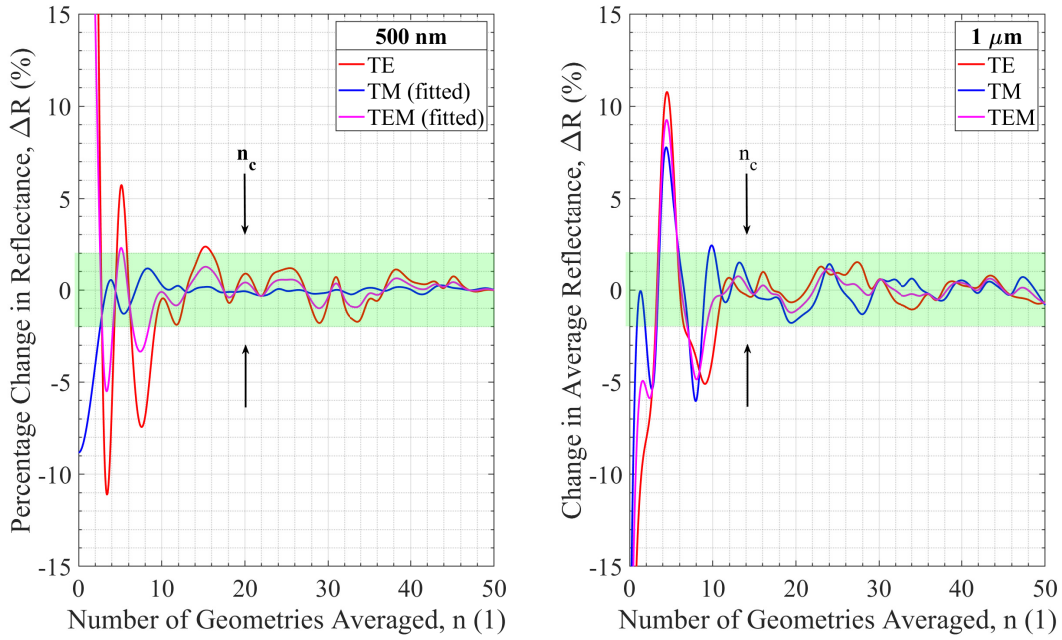

(a) (b)

Figure 6.8: Convergence studies showing stable reflectance for b-Si with randomness level three at $\lambda = 400$ nm, and NWs of average height 500 nm (a) and 1 μm (b).

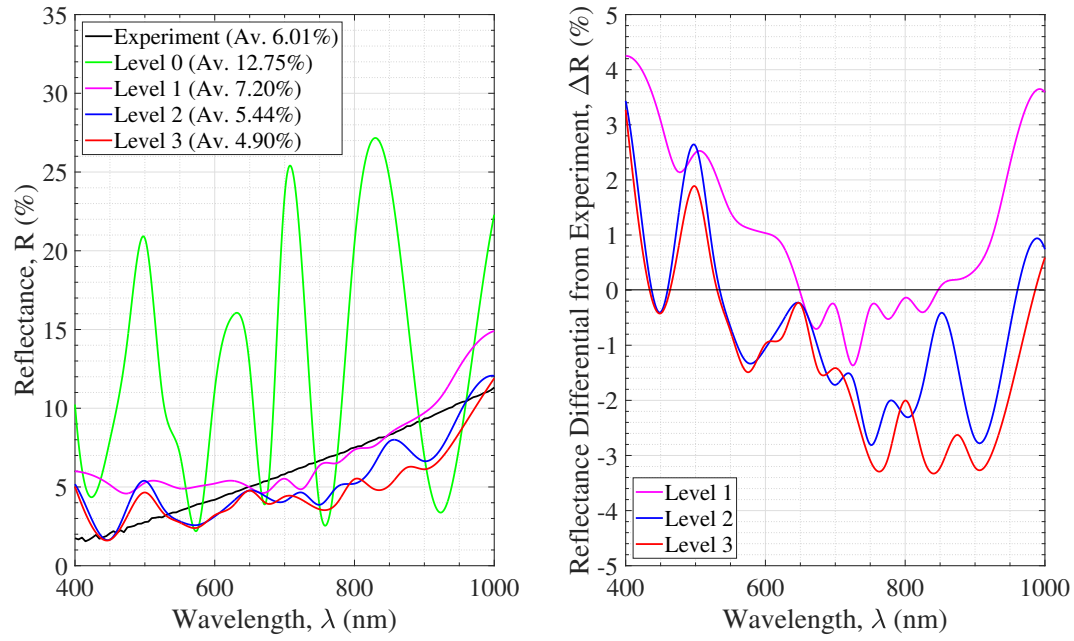

(a) (b)

Figure 6.9: The simulated reflectance for each randomness level against an equivalent real b-Si sample (a), and the difference between simulated and experimental data for levels one, two, and three (b). Broadband average (Av.) reflectance is also noted.

In summary of the reflectance data gathered from the simulations, and in comparison to an equivalent real sample, figure 6.9a showcases the immediately noticeable inaccuracy of taking a purely periodic approach to creating a Si NW geometry. Real silicon NWs are highly anti-reflective due to their unique ability to create many different EM interference modes. In periodic structures, these interference patterns are not substantial enough to cancel one another out, to give a relatively flat-line response. Instead, only a few modes are apparent and their subsequent interference patterns are much more noticeable. On the introduction of a slight degree of randomness, as seen with level one where each NW exhibits varying pitch, radius, height, and bend, there is a considerable decrease in this oscillatory effect.

On the addition of bunching effects, as with level two, a slight drop toward the NUV region of the EM spectrum can be seen, but a sudden rise in the visible to NIR region. Figure 6.9a also goes on to demonstrate that, when using non-cylindrical NWs, there is no better match to the experimental data. A substantial and somewhat unexpected finding, representative of the data shown in figure 6.9b, was that randomness level one appeared to be the most accurate of all the geometries studied here. A greater level of randomness within the simulation geometry is indicative of a closer match between theory and structures observed. There are several possible reasons behind why the results appear to show the opposite, the first being that each randomised property is constrained within specific variance tolerances (see table 6.1). Further sources of error include the generation of the model 'by eye' using figure 6.1, which introduces human error, and the possibility of some arbitrary degree of mesh inadequacy.

It is likely that the error between simulation and experimental data, regardless of the randomness level, is derived from the use of an SEM image of real silicon NWs to generate an accurate model of structures with similar heights amongst other properties. When transposing data from this imagery to the simulation domain, many of the properties were assumed to be approximate to certain values. These values were chosen based on the observations and experience manufacturing such structures on c-Si. Whilst the height of these structures is relatively uniform, their pitch and radius tend to be far more variable. This led to the implementation of the limits outlined for this work. The issue that arises from this is that properties such as radius and pitch are very difficult to quantify specifically, and the variation limits are very much approximated based on only a small unit-area represented within the image. Further variance and non-uniformities to a real Si NW surface may be present elsewhere in the sample, where

these variation limits are not strictly constant across the whole sample. Also, given that these variation limits are defined as a proportion of the property they are varying, in opposition to a more statistical approach from real data, an element of systematic error is also introduced here.

Mesh inadequacy, whereby the mesh density is insufficient to produce comprehensible data, is a common source of problems in modern simulation methods, particularly the FEM. Before commencing the reflectance studies, sufficient mesh density was confirmed to validate the data and rule this out as a potential cause for any differences observed between simulated and measured. Figure 6.10 demonstrates how, after a total element count of approximately $600,000$, convergence on a reflectance value of 8.4% is apparent. On further increases to the element count, simulation accuracy changes very little but runtime continues to rise linearly. The implication here is that for any further increase in mesh density, only the runtime is extended, yielding exactly the same data. It should be noted that for an element count of $800,000$ and above, denoted here as 'excessive', the simulation becomes highly unstable and crashes frequently due to its memory demands.

It is noticeable that there is a strong correlation between the number of elements within a model, that is to say the mesh density, and the subsequent memory usage during the solution process. In fact, change in the differences between the levels as shown in figure 6.11a yields an essentially linear relationship. The implication here being that memory usage per-element appears to be independent of the element's size, and subsequently it is possible to extrapolate an approximate memory requirement for much larger models under the same meshing strategy. The data here shows a memory requirement of approximately 150 kB/element. For the case of a slightly larger 5×5 Si NW periodic geometry with an identical mesh, approximately 156% larger than the equivalent 4×4, this would yield a memory requirement somewhere in the region of 58 GB. Simulation runtime does not have quite as strong a correlation, and that of the level three geometry took considerably longer to simulate given the requirements in comparison to the others.

The trends shown in figure 6.11b have interesting implications for this investigation. The higher error of what was expected to be the most accurate representation of a silicon NW surface (randomness level three), showed that the effort and higher resource requirements for this level of randomisation actually damages the accuracy of the model. Standard deviation metrics appear to showcase a greater level of convergence for level

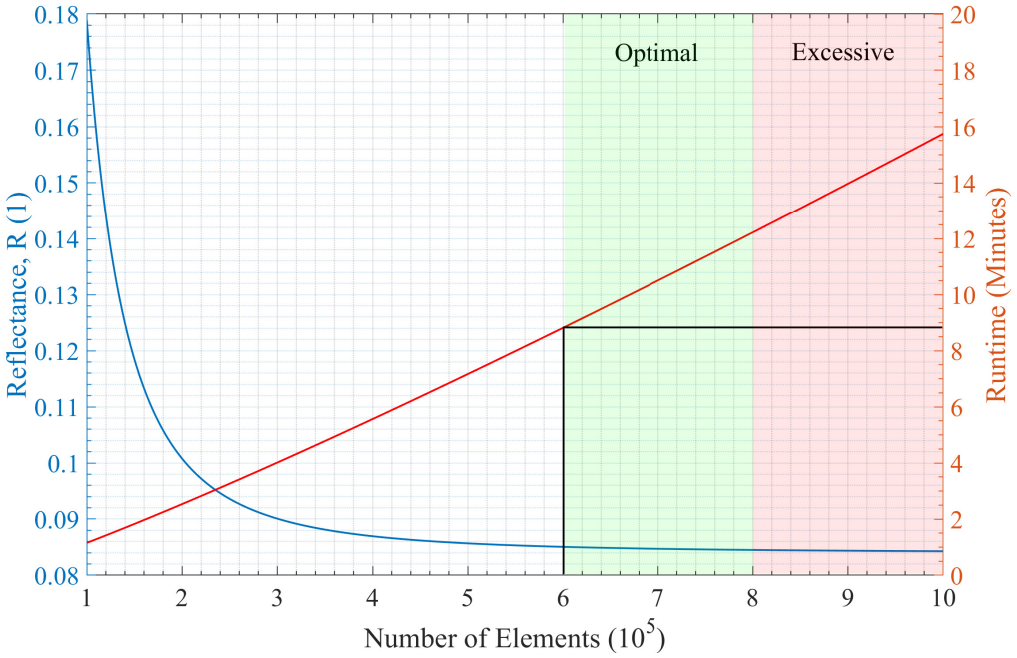

Figure 6.10: Data showcasing how the simulated reflectance for randomness level three varies given different mesh densities.

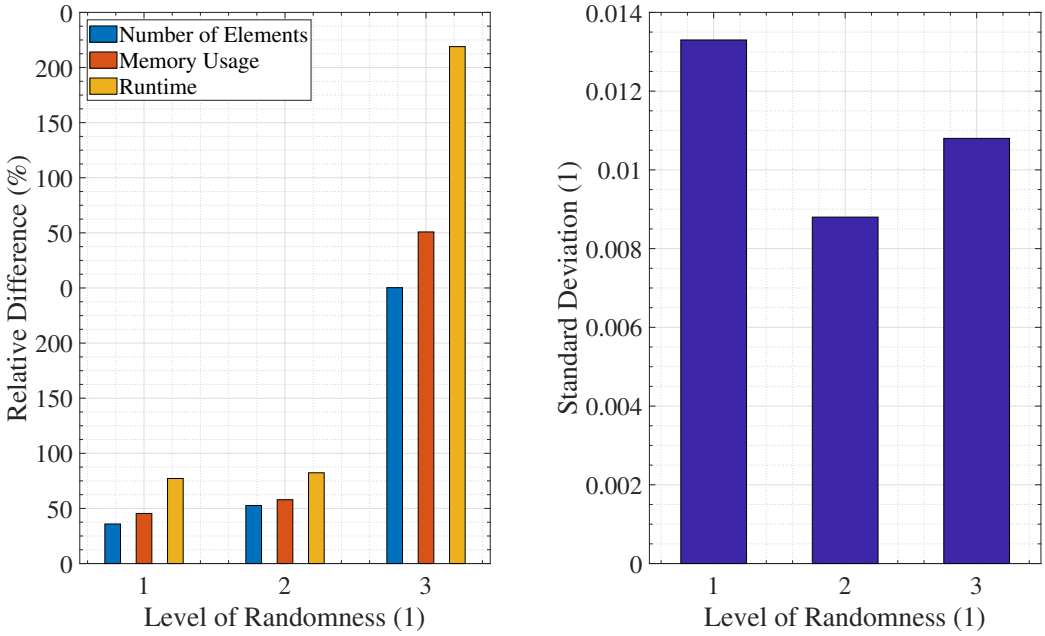

(a) (b)

Figure 6.11: Demonstrating four key metrics for each randomness level, where level zero had 279, 579 elements, 35.31 GB of memory usage, and a runtime of 41.57 minutes. Levels one, two, and three are reported relative to these values (a) as well as the standard deviation of the geometries' results (b) for a single wavelength.

two against its average as shown in figure 6.9. This supports the argument that the properties of this particular geometry, notably the bunching tendencies, cause greater convergence on a specific reflectance value regardless of the state of the geometry. In effect, what can be inferred from this data is that bunching minimises the effect of heterogeneity on reflectance for small surface areas and causes greater uniformity in spectral response over a larger area. The distribution of individual simulation results can be seen for both of these levels in figure 6.12.

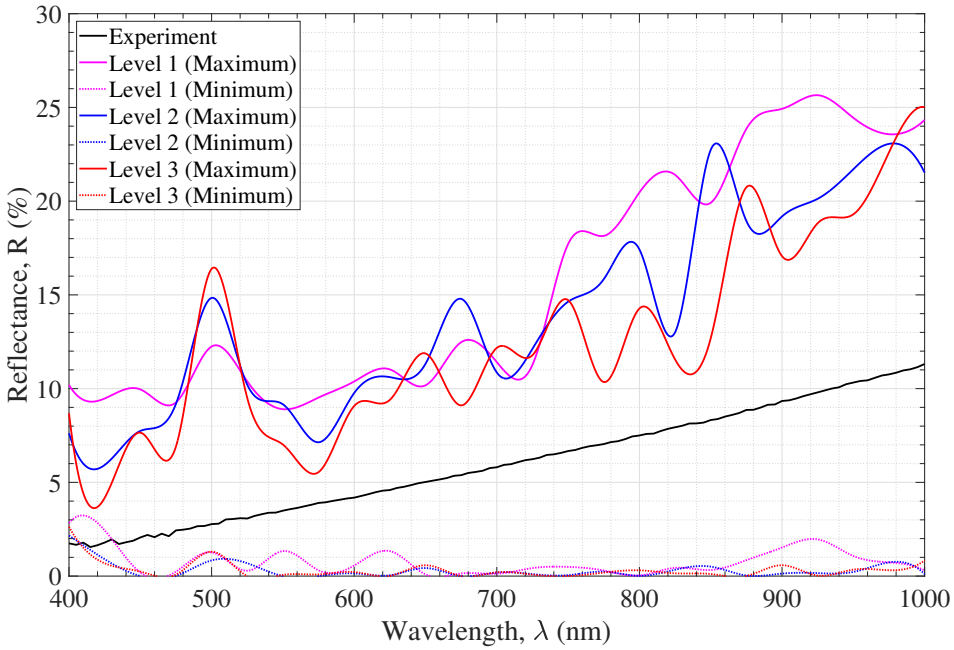

Figure 6.12: Demonstrating how the distribution of single simulation results varies between levels one, two, and three.

The most accurate simulation model however, was that of randomness level one. Mid-range wavelengths from approximately 750 to 900 nm exhibited a match to experimental data within 0.50%, a first for the optical simulation of such structures. However, the shortfall of level one is apparent in the short and long wavelengths in the sweep, where both show a far higher reflectance than expected, overshooting by as much as 5.00% in these regions. In contrast, despite being slightly less accurate overall, levels two and three demonstrated a significant improvement in these regions, with errors of as little as 0.25% in the NUV and 1.00% in the NIR. This implies a possible mixture of bunched and non-bunched Si NWs on the measured surface, and showcases the effect of bunching on surface reflectance outside the visual range.

Simulation efficiency is a measure of overall resource usage over time. A higher efficiency

is symbolic of a simulation that uses as much of the resources made available to it for as much of its total runtime as possible. This is often an important factor when requesting to use supercomputer time, and models with a greater efficiency are more desirable on such large scale, high power systems like that of IRIDIS 5 used here. The efficiency of the model was relatively high, holding consistently at a value of approximately 73%.

6.4 Conclusions

This b-Si model has helped showcase the dependencies of random variations within nanoscale structures on optical modelling. Furthermore, it has demonstrated an effective method of creating far more advanced levels of randomisation within what would otherwise be limited to static geometries. The most comparable work to that demonstrated here was conducted by Altermatt et al. in 2009 [123]. Their work reported a slightly different method of pseudo-randomisation used to achieve semi-accurate recreations of Si NWs that had not been explored prior. Due to the limited computational resources available, alongside a less diverse modelling ecosystem, the level of geometric pseudo-randomisation as demonstrated in this work was not possible. A modern and refreshed approach to recreating these geometries is explored here in comparison to their work, enabling us to vary more than just pitch, radius and tilt, but also bend, shape and bunching as well. This has opened a new possibility for identifying the influential factors of nanoscale surface properties on EM wave propagation.

Interestingly, it is apparent from the data obtained here that, although increasing levels of heterogeneity demonstrates a significant impact on the accuracy of the data, extending this randomisation does not strictly result in a better agreement with experimental data. Overly complex models, such as the randomisation level three, turned out to be less accurate than its simpler counterparts. This shows that there is a balance required, at least for silicon NWs, between model complexity and reality, supporting the use of simplified models where intricate features seem to have little impact on the outcome of the study whatsoever.

Aside from this specific geometry, the mathematical methods used to generate it are applicable to a wide range of different structures other than those explored here. For example, protein design and structure prediction, material or environmental feature growth and weather pattern simulation. Using the same mathematical methods, more variation can be added or even removed from an arbitrary geometry as required, making

this a robust and versatile method of pseudo-randomisation. Shown here is how the bunching of silicon NWs affects reflectance, and also how inducing variations between surface features yields a more accurate response in this case. Despite also varying the shapes of the NWs, little improvement was seen at the cost of a substantial increase of 300% in simulation runtime, alongside a 150% increase in resources, leading to the conclusion that randomisation, much like mesh density, has its limits.

There are disadvantages associated with this method however, which relate to the dependency on the FEM. This modelling methodology is notoriously resource and process intensive, making this level of randomisation only available for models created with access to sufficiently powerful hardware to run it within an acceptable amount of time. Furthermore, though the process workflow has been optimised for supercomputers here, some tweaking may be required in order to get higher efficiencies between different systems; the implication being that this is far from a simple plug–and–play program, and the mathematics must be carefully integrated into a study.

Chapter 7

Conclusions and Future Work

7.1 Overview

In summary of the work contained herein, an optically–efficient, micro–/nano–scale texture for application to c-Si PV technologies is reported. Showcased was the industry adopted standard of microscale pyramids with nanoscale black silicon nanowires etched into their facets, creating a hybrid nanostructure dubbed hybrid black silicon. Chapter 3 gave an overview of the processes employed to create these textures. The pyramids were formed using an industry standard heated potassium hydroxide etch, while the nanowires were etched using a silver–based metal assisted chemical etch. The etch time was varied and its effect on resultant surface topology was studied for both of these etches. Longer etch times created larger–scale structures in both cases. However, it was shown that, in the case of creating hybrid structures, excessively long nanowires coupled with sufficiently small pyramids will cause them to be obliterated. Such obliterated structures appear as holes or pits on the surface of the underlying substrate and exhibit poor optical performance. A good quality hybrid etch requires the appropriate balance between these two etches, and was determined prior to performing advanced optical analyses.

In chapter 4, a new optical characterisation system, called the angle–resolved spectrophotometer, was designed and implemented, capable of studying the reflectance variations of a given sample over varying angles, polarisations, and wavelengths, as opposed to the current standard of only varying wavelength. This was achieved using a centre–mount sample holder built into an integrating sphere permitting rotation without the removal of or interaction with the sample being measured. This enables a great degree

of automation in the measurement process, minimising the risk of human and systematic error. Studies performed against samples of known or theoretically determinable reflectance were required to confirm the system was accurately measuring reflectance prior to measuring unknown samples like hybrid black silicon. Measurements taken of silicon nitride and silicon dioxide coatings on top of a silicon substrate demonstrated a high degree of accuracy in the measurement process and reflectance calculations. In demonstrating the system's effectiveness across multiple applications, as opposed to only photovoltaics, various paint samples were analysed including an optical insulating material. The variable angle reflectance spectra clearly identified the colour of each, and permitted an advanced colorimetric analysis. This meant, for the first time, colour change with respect to incident angle could be quantified and recreated during the post–processing data analysis.

The angle–resolved spectrophotometer was then used to perform similar optical studies on the photovoltaic anti–reflectance textures created in chapter 3. Chapter 5 takes pyramidal textures, both bare and coated with a layer of silicon nitride, planar black silicon, and hybrid black silicon, forming a cross–comparison between each of them. It was shown how bare pyramidal textures exhibited the greatest average reflectance across both wavelength and angle of incidence. Planar black silicon textures greatly improved on this, but failed to reach the low levels of reflectance exhibited by the remaining two textures: coated pyramids and hybrid black silicon. The hybrid samples performed the best overall, with reflectance as low as 7.18% for the 8 minute etch, and 8.36% for the 4 minute etch. The pyramids with an 80 nm coating of silicon nitride had an average reflectance of 10.61%.

Nanowire length has an implication on the ability to passivate a substrate that in–turn causes the electrical efficiency of the cell to vary. Despite electrical characterisation not being a focus of this work, it remained crucial to consider this for photovoltaic applications. Work reported in chapter 2 outlined how, with increasingly complex surface topologies in the nanoscale size range, uniform passivation becomes difficult and results in a careful balance required between optical and electrical performance. In this case, the shortest nanowires etched onto pyramids were taken forward and compared with the coated pyramids – a fair comparison given the widespread use of the latter as a standard form of anti–reflectance in commercial solar cells. This hybrid sample represented the easiest to passivate of the three lengths, though it should be noted that this would still be more complex than the passivation of coated pyramids. Using the solar position

algorithm created by NREL [154], coupled with the measured variable angle reflectance data, it was possible to estimate the optical performance of these two surface textures when applied to a solar panel deployed in a real location around the world. Calculating solar elevation angles, as well as diffuse and direct irradiance spectra for Southampton, a weighted optical response was determined for such panels across a typical year. The two textures were also encapsulated, measured again, and the weighted optical response was recalculated. The inclusion of this encapsulant layer makes for a more accurate determination of optical performance when applied to photovoltaic technologies, as no solar panel can be without this critical protective layer when exposed to weather conditions. Similar to before, the hybrid nanostructures outperformed the coated pyramids in all situations, with and without an encapsulant layer. It was seen, however, that the inclusion of this layer results in a higher average reflectance and weighted optical response.

The mix–and–matching of pyramid size and nanowire lengths for experimental optimisation is time–consuming, expensive, and inefficient. Chapter 6 attempts to address this issue by creating a computer model designed to simulate the electromagnetic wave interaction with nanoscale structures. In particular, a novel method of simulating heterogeneous structures was reported whereby a large surface was broken down into smaller unit–cells, simulated individually, and averaged to determine a response indicative of the entire surface. Electromagnetic wave optics requires small simulation areas due to the dense mesh required for accurate simulation. These dense meshes are computationally expensive to simulate, and thus the IRIDIS 5 supercomputer was employed to handle distributed, multi–parallel black silicon surface simulations. Despite the use of a supercomputer, the simulation of hybrid nanostructures and variable angle incidence is not feasible for this work due to the limited computational resources available, and the complexity and size of such a simulation being beyond our capabilities at the time of writing. Despite this, a hybrid black silicon model was developed as part of this work, and is reported here as an area of future work.

The planar black silicon model developed in this project enables the determination of the optical response of a stochastic geometry given approximate parameters and appropriate variation. Reported was a recreation of a planar black silicon sample's reflectance spectrum, as imaged using scanning electron microscopy and optically measured using a standard angle monochromatic spectrophotometry system. On average, the reflectance was successfully matched through the use of the model to an accuracy of within 1% for

the infra–red spectral region, and 0.25% down towards the ultraviolet spectral region. Various levels of pseudo–randomisation were explored, from no randomisation at all, to the inclusion of inter–nanowire bunching. An optimum level was found, whereby the inclusion of the latter resulted in decreased accuracy, and increased runtime, but slightly less randomisation across geometric elements yielded greater accuracy for a decreased runtime. Such determinations are crucial to realise for efficient experimentation and a reduction in computational expense.

The importance behind developing such a model lies foremost in the ability to rapidly simulate surface topographies for their optical performance without the need to fabricate samples with limitless feature combinations. This presents a considerable cost saving within the research and development pipeline, and can be readily adapted to quantify other crucial metrics related (or not related) to solar photovoltaic systems. It is possible to simulate with the inclusion of passivation and encapsulation layers and to include a full cell structure. The latter, however, requires the rework of the existing model. If front contacts are to be included, then either a larger simulation area is required (not desirable for electromagnetic wave optics as previously stated) or to have a small number of unit–cells making up the entire model consist predominantly of structures relating to the presence of a front contact or busbar.

7.2 Implications and Conclusions

Hybrid black silicon textures have been shown to be very effective in the reduction of front surface optical losses, with photovoltaics being a key beneficiary. Within the scope outlined in section 1.6, these structures would be well–received within the industry, though overshadowed by an important consideration. Coated pyramids, currently being the go–to standard for optimising optical efficiency on silicon–based solar cells, offer a good level of anti–reflectance when compared to hybrid structures, though constantly falling short of that provided by hybrids. Despite this, the pyramids may prove advantageous at a system–level perspective, where electrical performance becomes a considerable factor.

As outlined in section 2.2.2.3, the complex nanostructures such as black silicon nanowires are noticeably more complex to passivate uniformly than microscale textures. This can lead to a high degree of surface recombination triggered by unpassivated dangling bonds left behind after sawing through the crystalline structure of silicon during the wafer

manufacturing process that are usually treated effectively on larger surface textures. Atomic layer deposition has been shown to passivate black silicon nanowires to a high degree of uniformity, though it should be noted that this was not on hybrid structures that would introduce additional topographical complexities to overcome.

Conversely, pyramidal texturing is much easier to passivate effectively. A chemical vapour deposition process is used that is fast, cheap, and sufficient in creating high quality thin films on planar or textured samples (without a significant degree of complexity in their formation). A bonus is presented in the fact that a typical anti–reflectance coating for pyramids also acts as a passivation layer, condensing two layers into one layer that does two jobs simultaneously. This gives pyramidal textures incorporating an anti–reflectance coating a unique selling point, from a manufacturability and performance perspective. It also presents a major advantage over hybrid nanotextures.

However, throughout the advanced analysis performed in chapter 5, the hybrid textures outperformed the optics of coated pyramids, even under encapsulation. This was an important factor to consider in the analyses, given that uncoated pyramids are not applicable in solar photovoltaic systems. The inclusion of such data, relating to when these textures are not encapsulated, is important to include for the other applications that hybrid black silicon textures would be useful for; specifically photodetectors. These devices require a consistent (and low) reflectance across the area of the electromagnetic spectrum for which their application is specific to. The same must hold true across the angular range as well for ultra–wide angle sensing applications; camera sensor arrays, for example.

7.3 Future Work

Despite the clear advantages of hybrid black silicon surfaces, there is clear scope for further work prior to the widespread adoption of the textures by the energy industry. For instance, a thorough analysis of the electrical properties of a full hybrid black silicon based interdigitated rear contact cell is crucial for further development and applicability of the technology. Being outside the focus of the work reported here, the electrical properties rely heavily on the ability to uniformly passivate the front surface, minimising carrier recombination. Interdigitated rear contacts are suggested for hybrid textures to avoid damaging the front surface on the application of front contacts, and to ensure the optical performance of the textures remains as high as possible – front contacts sig-

nificantly increase surface reflectance and induce self–shading effects, decreasing overall efficiency. Such problems are avoided with the use of rear contacts, which leave the front surface completely exposed to incident light. This is indicative of the samples manufactured and characterised throughout chapters 3, 4, and 5.

Variable angle reflectance measurements have been shown to be useful in the determination of optical properties from a variety of different surfaces, for a range of different applications. The wavelength range in the ARS is bound to the upper near ultraviolet, visible, and lower near infra–red spectral regions, as defined by the slit size and diffraction grating within the B&W Tek Glacier-X BTC112E-ST1 linear CCD spectrophotometer. The resolution of this spectrometer was noted as approximately 0.5 nm/pixel. Solar (not just silicon–based), glass, and sensor applications also benefit from optical investigations beyond this range. To enable future investigations deeper into the near infra–red, a second spectrophotometer, namely an Ocean Insight FLAME-NIR+ spectrophotometer, was obtained and is to be investigated forthcoming.

The work presented in chapter 5 offers a vast area for continued research. the studies were limited to the application of hybrid black silicon and coated pyramids in the UK, but further work can be done on a vast array of different solar technologies beyond silicon, as well as adapting the algorithm to include electrical performance (when such studies have been sufficiently completed). It is also possible to map the applicability of technological variants around the world. As seen in figure 1.2, places such as Chile, Australia, and Argentina have very high levels of solar irradiance. All technologies have a negative temperature coefficient. Typically, as the temperature of a solar panel rises, the efficiency decreases. This effect is exacerbated with very low levels of surface reflectance. Greater quantities of electromagnetic energy are absorbed into the substrate when surface reflectance is low, as can be seen in equation (2.3) when transmission, T, is assumed to be negligible for panels of sufficient thickness. Given this fact, the application of highly anti–reflective solar panels can be detrimental in such areas of high irradiance, requiring the use of active cooling in some cases, subsequently resulting in a loss of energy generated that cannot be used outside of the photovoltaic system. the algorithm offers the chance to test for such applicability, and will offer insight, in–line with the drive to renewable energy generation, into the deployment of appropriate solar cells around the world.

Bibliography

[1] M. Kameda, S. Sakai, M. Isomura, K. Sayama, Y. Hishikawa, S. Matsumi, H. Haku, K. Wakisaka, M. Tanaka, S. Kiyama, S. Tsuda, and S. Nakano, "Efficiency evaluation of a-si and c-si solar cells for outdoor use," in *Conference Record of the Twenty Fifth IEEE Photovoltaic Specialists Conference - 1996*, IEEE, 1996.

[2] J. F. Leaver, K. Durose, and J. D. Major, "CdTe-based photovoltaics using a CdTe/CdSe/CdTe absorber layer structure," in *2022 IEEE 49th Photovoltaics Specialists Conference (PVSC)*, IEEE, jun 2022.

[3] S. Niki, S. Ishizuka, K. ichiro Sakurai, K. Matsubara, H. Tampo, H. Komaki, Y. Kamikawa-Shimizu, K. Maejima, T. Yoshiyama, K. Mizukoshi, A. Yamada, H. Nakanishi, and N. Terada, "Progress in CIGS solar cell technologies," in *LEOS 2008 - 21st Annual Meeting of the IEEE Lasers and Electro-Optics Society*, IEEE, nov 2008.

[4] R. Usmani, M. Asim, and M. Nasibullah, "In roads to OPV design perspective: limitations and optimum parametric characterization," in *2022 2nd International Conference on Emerging Frontiers in Electrical and Electronic Technologies (ICEFEET)*, IEEE, jun 2022.

[5] O. Coddington, J. L. Lean, P. Pilewskie, M. Snow, and D. Lindholm, "A solar irradiance climate data record," *Bulletin of the American Meteorological Society*, vol. 97, pp. 1265–1282, July 2016.

[6] W. Bludau, A. Onton, and W. Heinke, "Temperature dependence of the band gap of silicon," *Journal of Applied Physics*, vol. 45, pp. 1846–1848, Apr. 1974.

[7] S. Rühle, "Tabulated values of the Shockley–Queisser limit for single junction solar cells," *Solar Energy*, vol. 130, pp. 139–147, June 2016.

[8] M. A. Green, E. D. Dunlop, G. Siefer, M. Yoshita, N. Kopidakis, K. Bothe, and X. Hao, "Solar cell efficiency tables (version 61)," *Progress in Photovoltaics: Research and Applications*, vol. 31, pp. 3–16, nov 2022.

[9] Y. Delannoy, "Purification of silicon for photovoltaic applications," *Journal of Crystal Growth*, vol. 360, pp. 61–67, dec 2012.

[10] R. K. Jones, J. H. Ermer, C. M. Fetzer, and R. R. King, "Evolution of multijunction solar cell technology for concentrating photovoltaics," *Japanese Journal of Applied Physics*, vol. 51, p. 10ND01, Oct. 2012.

[11] M. J. Ludowise, R. A. LaRue, P. G. Borden, P. E. Gregory, and W. T. Dietze, "High-efficiency organometallic vapor phase epitaxy AlGaAs/GaAs monolithic cascade solar cell using metal interconnects," *Applied Physics Letters*, vol. 41, pp. 550–552, Sept. 1982.

[12] S. Essig, C. Allebe, J. F. Geisz, M. A. Steiner, B. Paviet-Salomon, A. Descoeudres, A. Tamboli, L. Barraud, S. Ward, N. Badel, V. LaSalvia, J. Levrat, M. Despeisse, C. Ballif, P. Stradins, and D. L. Young, "Boosting the efficiency of III-V/Si tandem solar cells," in *2016 IEEE 43rd Photovoltaic Specialists Conference (PVSC)*, IEEE, jun 2016.

[13] K.-H. Lee, K. Araki, and M. Yamaguchi, "Analyzing the cost reduction potential of III-V/Si hybrid concentrator photovoltaic systems," in *2017 IEEE 44th Photovoltaic Specialist Conference (PVSC)*, IEEE, jun 2017.

[14] D. Benmoussa, D. Tidjani, and F. Mostefa, "The influence of limiting factors on the multi-junction mixed mode," in *2019 International Conference on Power Generation Systems and Renewable Energy Technologies (PGSRET)*, IEEE, aug 2019.

[15] G. Masson, *Snapshot of Global Photovoltaic Markets (1992-2015).* International Energy Agency Photovoltaic Power Systems Programme, 2016. p. 6.

[16] S. Carattini, M. Péclat, and A. Baranzini, "Social interactions and the adoption of solar PV: evidence from cultural borders." Centre for Climate Change Economics and Policy Working Paper 339/Grantham Research Institute on Climate Change and the Environment Working Paper 305. London: London School of Economics and Political Science, Nov. 2018.

[17] C. Lotz and K. Schneider, "Annual report 2017/18," tech. rep., Fraunhofer Institute for Solar Energy Systems ISE, Heidenhofstrasse 2, 79110 Freiburg, Germany, 2018.

[18] M. O'Neill, A. J. McDanal, H. Brandhorst, K. Schmid, P. LaCorte, M. Piszczor, and M. Myers, "Recent space PV concentrator advances: More robust, lighter, and easier to track," in *2015 IEEE 42nd Photovoltaic Specialist Conference (PVSC)*, IEEE, jun 2015.

[19] T. Li, C. Jiang, C. Sheng, H. Lu, L. Hou, and X. Hang, "Research on new technologies of photoelectric conversion efficiency in solar cell," in *2010 International Conference on Mechanic Automation and Control Engineering*, IEEE, jun 2010.

[20] "Electricity generation costs 2020," tech. rep., Department for Business, Energy, and Industrial Strategy, 2020.

[21] "Levelized costs of new generation resources in the annual energy outlook 2022," tech. rep., Energy Information Administration, 2022.

[22] R. S. Ohl, "Light–sensitive electric device including silicon," May 1941. US2443542A.

[23] M. A. Green, "The path to 25% silicon solar cell efficiency: history of silicon cell evolution," *Progress in Photovoltaics: Research and Applications*, vol. 17, pp. 183–189, May 2009.

[24] M. A. Woodhouse, B. Smith, A. Ramdas, and R. M. Margolis, "Crystalline silicon photovoltaic module manufacturing costs and sustainable pricing: 1H 2018 benchmark and cost reduction road map," tech. rep., National Renewable Energy Laboratory, Feb. 2019.

[25] S. J. Ling, W. Moebs, J. Sanny, G. Friedman, S. D. Druger, A. Kolakowska, D. Anderson, and D. Bowman, *University physics*, vol. 2. OpenStax, Feb. 2016.

[26] F. J. J. Clarke and D. J. Parry, "Helmholtz reciprocity: its validity and application to reflectometry," *Lighting Research & Technology*, vol. 17, pp. 1–11, Mar. 1985.

[27] R. Dai, J. C. Fritchman, Q. Liu, Y. Xiao, H. Yu, and L. Bao, "Assessment of student understanding on light interference," *Physical Review Physics Education Research*, vol. 15, p. 020134, oct 2019.

[28] M. R. Vogt, *Development of physical models for the simulation of optical properties of solar cell modules*. PhD thesis, Gottfried Wilhelm Leibniz Universität Hannover, 2015.

[29] K. R. McIntosh and S. C. Baker-Finch, "OPAL 2: Rapid optical simulation of silicon solar cells," in *2012 38th IEEE Photovoltaic Specialists Conference*, IEEE, June 2012.

[30] T.-M. Kuan, C.-C. Huang, L.-G. Wu, and C.-Y. Yu, "High efficiency large-area multi-crystalline silicon solar cells using reactive ion etching technique," in *2013 IEEE 39th Photovoltaic Specialists Conference (PVSC)*, IEEE, jun 2013.

[31] E. D. Palik, *Handbook of optical constants of solids*, vol. 1. Elsevier Science and Technology, Dec. 1985.

[32] M. J. Dodge, "Refractive properties of magnesium fluoride," *Applied Optics*, vol. 23, p. 1980, jun 1984.

[33] R. S. Bonilla, K. O. Davis, E. J. Schneller, W. V. Schoenfeld, and P. R. Wilshaw, "Effective antireflection and surface passivation of silicon using a SiO2/a-t iOx film stack," *IEEE Journal of Photovoltaics*, vol. 7, pp. 1603–1610, nov 2017.

[34] J. Henrie, S. Kellis, S. M. Schultz, and A. Hawkins, "Electronic color charts for dielectric films on silicon," *Optics Express*, vol. 12, p. 1464, apr 2004.

[35] T.-Y. Wang, W.-J. Lih, C.-Y. Cheng, J.-Y. Liu, and W.-H. Lin, "Surface treatment for multi-crystalline silicon wafer sliced by diamond wire saw," in *2016 IEEE 43rd Photovoltaic Specialists Conference (PVSC)*, IEEE, June 2016.

[36] X. Ye, S. Zou, K. Chen, J. Li, J. Huang, F. Cao, X. Wang, L. Zhang, X.-F. Wang, M. Shen, and X. Su, "18.45%-efficient multi-crystalline silicon solar cells with novel nanoscale pseudo-pyramid texture," *Advanced Functional Materials*, vol. 24, pp. 6708–6716, Aug. 2014.

[37] S. Zou, X. Ye, C. Wu, K. Cheng, L. Fang, R. Tang, M. Shen, X. Wang, and X. Su, "Complementary etching behavior of alkali, metal-catalyzed chemical, and post-etching of multicrystalline silicon wafers," *Progress in Photovoltaics: Research and Applications*, vol. 27, pp. 511–519, Apr. 2019.

[38] S.-C. Shiu, S.-B. Lin, and C.-F. Lin, "Reducing Si reflectance by improving density and uniformity of Si nanowires fabricated by metal-assisted etching," in *Confer-*

ence on Lasers and Electro-Optics 2010, OSA, May 2010.

[39] B. Dieng, M. Beye, A. S. Maiga, M. Toure, and D. Kobor, "Fabrication and characterization of silicon nanowires for photovoltaic applications," in *2018 Thirteenth International Conference on Ecological Vehicles and Renewable Energies (EVER)*, IEEE, Apr. 2018.

[40] A. M. Gouda, N. K. Allam, and M. A. Swillam, "Facile omnidirectional black silicon based on porous and nonporous silicon nanowires for energy applications," in *2016 Photonics North (PN)*, IEEE, May 2016.

[41] B. Iandolo, M. Plakhotnyuk, R. S. Davidsen, E. Stamate, O. Hansen, and S. Nunomura, "Towards solar cells with black silicon texturing passivated by a-Si:H," in *2018 IEEE 7th World Conference on Photovoltaic Energy Conversion (WCPEC) (A Joint Conference of 45th IEEE PVSC, 28th PVSEC and 34th EU PVSEC)*, IEEE, jun 2018.

[42] C. Honsberg and S. Bowden, "Equations for photovoltaics," 2019.

[43] J. F. Geisz, R. M. France, K. L. Schulte, M. A. Steiner, A. G. Norman, H. L. Guthrey, M. R. Young, T. Song, and T. Moriarty, "Six-junction III-V solar cells with 47.1% conversion efficiency under 143 Suns concentration," *Nature Energy*, vol. 5, pp. 326–335, Apr. 2020.

[44] "Tables for reference solar spectral irradiances: Direct normal and hemispherical on 37 tilted surface."

[45] M. A. Green and M. J. Keevers, "Optical properties of intrinsic silicon at 300 K," *Progress in Photovoltaics: Research and Applications*, vol. 3, no. 3, pp. 189–192, 1995.

[46] L. Tsakalakos, "Application of micro- and nanotechnology in photovoltaics," in *Comprehensive Renewable Energy*, pp. 515–531, Elsevier, 2012.

[47] T. Markvart and L. Castañer, "Principles of solar cell operation," in *Practical Handbook of Photovoltaics*, pp. 7–31, Elsevier, 2012.

[48] Y. Jestin, "Down-shifting of the incident light for photovoltaic applications," in *Comprehensive Renewable Energy*, pp. 563–585, Elsevier, 2012.

[49] J. Szlufcik, S. Sivoththaman, J. F. Nijs, R. P. Mertens, and R. V. Overstraeten, "Low-cost industrial technologies for crystalline silicon solar cells," in *Practical Handbook of Photovoltaics*, pp. 129–159, Elsevier, 2012.

[50] B. Prasad, S. Bhattacharya, A. K. Saxena, S. R. Reddy, and R. K. Bhogra, "Performance enhancement of mc-Si solar cells due to synergetic effect of plasma texturization and SiNx:h AR coating," *Solar Energy Materials and Solar Cells*, vol. 94, pp. 1329–1332, aug 2010.

[51] M. A. Zahid, M. Q. Khokhar, E.-C. Cho, Y. H. Cho, and J. Yi, "Impact of anti-reflective coating on silicon solar cell and glass substrate : a brief review," *Current Photovoltaic Research*, 2020.

[52] P. Campbell and M. A. Green, "Light trapping properties of pyramidally textured surfaces," *Journal of Applied Physics*, vol. 62, pp. 243–249, jul 1987.

[53] P. Campbell and M. A. Green, "High performance light trapping textures for monocrystalline silicon solar cells," *Solar Energy Materials and Solar Cells*, vol. 65, pp. 369–375, jan 2001.

[54] A. W. Smith and A. Rohatgi, "Ray tracing analysis of the inverted pyramid texturing geometry for high efficiency silicon solar cells," *Solar Energy Materials and Solar Cells*, vol. 29, pp. 37–49, feb 1993.

[55] P. Mena, "Optimization of a nanostructured moth-eye antireflective coating in RSoft," resreport, Synopsys, Aug. 2018.

[56] S. A. Boden and D. M. Bagnall, "Moth–eye antireflective structures," in *Encyclopedia of Nanotechnology*, pp. 1467–1477, Springer Netherlands, 2012.

[57] W.-K. Kuo, J.-J. Hsu, C.-K. Nien, and H. H. Yu, "Moth–eye–inspired biophotonic surfaces with antireflective and hydrophobic characteristics," *ACS Applied Materials and Interfaces*, vol. 8, pp. 32021–32030, nov 2016.

[58] M. R. Lotz, C. R. Petersen, C. Markos, O. Bang, M. H. Jakobsen, and R. Taboryski, "Direct nanoimprinting of moth–eye structures in chalcogenide glass for broadband antireflection in the mid–infrared," *Optica*, vol. 5, p. 557, may 2018.

[59] S. Kubota, K. Kanomata, B. Ahmmad, J. Mizuno, and F. Hirose, "Optimized design of moth eye antireflection structure for organic photovoltaics," *Journal of Coatings Technology and Research*, vol. 13, pp. 201–210, nov 2015.

[60] R. R. Singh, N. Malviya, and V. Priye, "Parametric analysis of silicon nanowire optical rectangular waveguide sensor," *IEEE Photonics Technology Letters*, vol. 28, pp. 2889–2892, Dec. 2016.

[61] I. Khodadad, N. Dhindsa, and S. S. Saini, "Refractometric sensing using high-order diffraction spots from ordered vertical silicon nanowire arrays," *IEEE Photonics Journal*, vol. 8, pp. 1–10, Apr. 2016.

[62] Y. D. Almoallem, M. J. Moghimi, and H. Jiang, "Black silicon based iris with reduced light scattering and reflection," in *2017 International Conference on Optical MEMS and Nanophotonics (OMN)*, IEEE, Aug. 2017.

[63] R. B. Sadeghian, "An e-nose concept based on semiconductor-assisted field ionization and gaseous discharge on arrays of whiskered nanowires," in *2013 35th Annual International Conference of the IEEE Engineering in Medicine and Biology Society (EMBC)*, IEEE, July 2013.

[64] Z. X. Chen, H. Y. Yu, N. Singh, N. S. Shen, R. D. Sayanthan, G. Q. Lo, and D.-L. Kwong, "Demonstration of tunneling FETs based on highly scalable vertical silicon nanowires," *IEEE Electron Device Letters*, vol. 30, pp. 754–756, July 2009.

[65] S. K. Srivastava, D. Kumar, P. K. Singh, and V. Kumar, "Silicon nanowire arrays based "black silicon" solar cells," in *2009 34th IEEE Photovoltaic Specialists Conference (PVSC)*, IEEE, June 2009.

[66] H. Savin, P. Repo, G. von Gastrow, P. Ortega, E. Calle, M. Garín, and R. Alcubilla, "Black silicon solar cells with interdigitated back-contacts achieve 22.1% efficiency," *Nature Nanotechnology*, vol. 10, pp. 624–628, May 2015.

[67] T. Rahman, R. S. Bonilla, A. Nawabjan, P. R. Wilshaw, and S. A. Boden, "Passivation of all-angle black surfaces for silicon solar cells," *Solar Energy Materials and Solar Cells*, vol. 160, pp. 444–453, Feb. 2017.

[68] A. G. Nassiopoulou, V. Gianneta, and C. Katsogridakis, "Si nanowires by a single-step metal-assisted chemical etching process on lithographically defined areas: formation kinetics," *Nanoscale Research Letters*, vol. 6, Nov. 2011.

[69] S. Grigoropoulos, "Highly anisotropic silicon reactive ion etching for nanofabrication using mixtures of SF_6/CHF_3 gases," *Journal of Vacuum Science & Technology B: Microelectronics and Nanometer Structures*, vol. 15, p. 640, May 1997.

[70] X.-L. Han, G. Larrieu, P.-F. Fazzini, and E. Dubois, "Realization of ultra dense arrays of vertical silicon nanowires with defect free surface and perfect anisotropy using a top-down approach," *Microelectronic Engineering*, vol. 88, pp. 2622–2624, Aug. 2011.

[71] A. Y. Vorobyev and C. Guo, "Antireflection effect of femtosecond laser-induced periodic surface structures on silicon," *Optics Express*, vol. 19, p. A1031, July 2011.

[72] S. H. Zaidi, D. S. Ruby, and J. M. Gee, "Characterization of random reactive ion etched-textured silicon solar cells," *IEEE Transactions on Electron Devices*, vol. 48, pp. 1200–1206, June 2001.

[73] G. Su, X. Dai, K. Tao, H. Sun, R. Jia, Z. Jin, X. Liu, H. Liu, S. Liu, C. Xu, Y. Cao, Y. Zhao, H. Qu, B. Liu, and B. Chen, "The study of the defect removal etching of black silicon for diamond wire sawn multi-crystalline silicon solar cells," *Solar Energy*, vol. 170, pp. 95–101, Aug. 2018.

[74] T. Daniels-Race, *Nanolithography: the art of fabricating nanoelectronic and nanophotonic devices and systems*, ch. 12, pp. 399–423. Woodhead Publishing Limited, Feb. 2014.

[75] C. Li, K. Fobelets, C. Liu, C. Xue, B. Cheng, and Q. Wang, "Ag-assisted lateral etching of Si nanowires and its application to nanowire transfer," *Applied Physics Letters*, vol. 103, p. 183102, Oct. 2013.

[76] A. M. Gouda, M. Elsayed, N. K. Allam, and M. A. Swillam, "Black silicon based on simple fabrication of mesoporous silicon nanowires for solar energy harvesting," in *2016 IEEE 43rd Photovoltaic Specialists Conference (PVSC)*, IEEE, June 2016.

[77] K. A. Gonchar, A. A. Zubairova, A. Schleusener, L. A. Osminkina, and V. Sivakov, "Optical properties of silicon nanowires fabricated by environment-friendly chemistry," *Nanoscale Research Letters*, vol. 11, Aug. 2016.

[78] X. Liu and Q. Hu, "Preparation of silicon nanowire arrays via electroless metal deposition," in *2010 3rd International Nanoelectronics Conference (INEC)*, IEEE, Jan. 2010.

[79] M. W. Amdemeskel, C. Dam-Hansen, B. Iandolo, R. S. Davidsen, O. Hansen, G. A. dos Reis Benatto, N. Riedel, P. B. Poulsen, S. Thorsteinsson, and A. Thorseth, "Indoor measurement of angle resolved light absorption by black

silicon," in *2017 IEEE 44th Photovoltaic Specialist Conference (PVSC)*, IEEE, June 2017.

[80] M. Rahmani and C. Jagadish, "Light–matter interactions on the nanoscale," *Beilstein Journal of Nanotechnology*, vol. 9, pp. 2125–2127, Aug. 2018.

[81] W. Jooss, I. Melnyk, C. Lai, J. Jung-Koenig, A. Teppe, S. R. Madugula, O. Voigt, P. Fath, B. Hu, I. Wang, P. Tian, A. Yang, and T. Wang, "Process development for MCCE textured solar cells on multicrystalline DWS wafer," in *2018 IEEE 7th World Conference on Photovoltaic Energy Conversion (WCPEC) (A Joint Conference of 45th IEEE PVSC, 28th PVSEC & 34th EU PVSEC)*, IEEE, June 2018.

[82] Z. Ying, M. Liao, X. Yang, C. Han, J. Li, J. Li, Y. Li, P. Gao, and J. Ye, "High-performance black multicrystalline silicon solar cells by a highly simplified metal-catalyzed chemical etching method," *IEEE Journal of Photovoltaics*, vol. 6, pp. 888–893, July 2016.

[83] F. Cao, K. Chen, J. Zhang, X. Ye, J. Li, S. Zou, and X. Su, "Next-generation multi-crystalline silicon solar cells: diamond-wire sawing, nano-texture and high efficiency," *Solar Energy Materials and Solar Cells*, vol. 141, pp. 132–138, Oct. 2015.

[84] S. Koynov, M. S. Brandt, and M. Stutzmann, "Black nonreflecting silicon surfaces for solar cells," *Applied Physics Letters*, vol. 88, p. 203107, May 2006.

[85] S. Koynov, M. S. Brandt, and M. Stutzmann, "Black multi-crystalline silicon solar cells," *Physica Status Solidi (RRL) – Rapid Research Letters*, vol. 1, pp. R53–R55, Mar. 2007.

[86] P. Hoyer, M. Theuer, R. Beigang, and E.-B. Kley, "Terahertz emission from black silicon," *Applied Physics Letters*, vol. 93, p. 091106, Sept. 2008.

[87] Z. Xiao, C. Feng, P. C. H. Chan, and I. Hsing, "Formation of silicon nanopores and nanopillars by a maskless deep reactive ion etching process," in *TRANSDUCERS 2007 - 2007 International Solid-State Sensors, Actuators and Microsystems Conference*, IEEE, June 2007.

[88] E. P. Ivanova, J. Hasan, H. K. Webb, G. Gervinskas, S. Juodkazis, V. K. Truong, A. H. F. Wu, R. N. Lamb, V. A. Baulin, G. S. Watson, J. A. Watson, D. E.

Mainwaring, and R. J. Crawford, "Bactericidal activity of black silicon," *Nature Communications*, vol. 4, Nov. 2013.

[89] X.-L. Liu, S.-W. Zhu, H.-B. Sun, Y. Hu, S.-X. Ma, X.-J. Ning, L. Zhao, and J. Zhuang, ""Infinite sensitivity" of black silicon ammonia sensor achieved by optical and electric dual drives," *ACS Applied Materials & Interfaces*, vol. 10, pp. 5061–5071, Jan. 2018.

[90] T.-H. Her, R. J. Finlay, C. Wu, S. Deliwala, and E. Mazur, "Microstructuring of silicon with femtosecond laser pulses," *Applied Physics Letters*, vol. 73, pp. 1673–1675, Sept. 1998.

[91] T.-H. Her, R. J. Finlay, C. Wu, and E. Mazur, "Femtosecond laser-induced formation of spikes on silicon," *Applied Physics A: Materials Science & Processing*, vol. 70, pp. 383–385, Apr. 2000.

[92] C. H. Crouch, J. E. Carey, J. M. Warrender, M. J. Aziz, E. Mazur, and F. Y. Génin, "Comparison of structure and properties of femtosecond and nanosecond laser-structured silicon," *Applied Physics Letters*, vol. 84, pp. 1850–1852, Mar. 2004.

[93] T. Baldacchini, J. E. Carey, M. Zhou, and E. Mazur, "Superhydrophobic surfaces prepared by microstructuring of silicon using a femtosecond laser," *Langmuir*, vol. 22, pp. 4917–4919, May 2006.

[94] M. Barberoglou, V. Zorba, E. Stratakis, E. Spanakis, P. Tzanetakis, S. H. Anastasiadis, and C. Fotakis, "Bio-inspired water repellent surfaces produced by ultrafast laser structuring of silicon," *Applied Surface Science*, vol. 255, pp. 5425–5429, Mar. 2009.

[95] A. Y. Vorobyev and C. Guo, "Direct femtosecond laser surface nano/microstructuring and its applications," *Laser & Photonics Reviews*, vol. 7, pp. 385–407, Aug. 2012.

[96] H. Jansen, M. de Boer, R. Legtenberg, and M. Elwenspoek, "The black silicon method: a universal method for determining the parameter setting of a fluorine-based reactive ion etcher in deep silicon trench etching with profile control," *Journal of Micromechanics and Microengineering*, vol. 5, pp. 115–120, June 1995.

[97] D. Murias, C. Reyes-Betanzo, M. Moreno, A. Torres, A. Itzmoyotl, R. Ambrosio, M. Soriano, J. Lucas, and P. R. i Cabarrocas, "Black silicon formation using

dry etching for solar cells applications," *Materials Science and Engineering: B*, vol. 177, pp. 1509–1513, Sept. 2012.

[98] Y. Inomata, K. Fukui, and K. Shirasawa, "Surface texturing of large area multicrystalline silicon solar cells using reactive ion etching method," *Solar Energy Materials and Solar Cells*, vol. 48, pp. 237–242, Nov. 1997.

[99] G. Su, R. Jia, X. Dai, K. Tao, H. Sun, Z. Jin, and X. Liu, "The influence of black silicon morphology modification by acid etching to the properties of diamond wire sawn multicrystalline silicon solar cells," *IEEE Journal of Photovoltaics*, vol. 8, pp. 937–942, July 2018.

[100] K. N. Nguyen, P. Basset, F. Marty, Y. Leprince-Wang, and T. Bourouina, "On the optical and morphological properties of microstructured black silicon obtained by cryogenic-enhanced plasma reactive ion etching," *Journal of Applied Physics*, vol. 113, p. 194903, May 2013.

[101] B. Bosovic, A. Smajkic, M. Muratovic, M. Kapetanovic, M.-H. Kim, and K.-H. Kim, "Simulation and validation of pressure rise in a HV circuit breaker with SF6 and alternative interrupting media," in *2017 4th International Conference on Electric Power Equipment - Switching Technology (ICEPE-ST)*, IEEE, oct 2017.

[102] J. Zha, T. Wang, C. Pan, K. Chen, F. Hu, X. Pi, and X. Su, "Constructing submicron textures on mc-Si solar cells via copper-catalyzed chemical etching," *Applied Physics Letters*, vol. 110, p. 093901, feb 2017.

[103] F. Flory, L. Escoubas, J. L. Rouzo, and G. Berginc, "Nanophotonics: from fundamental research to applications," in *Micro- and Nanophotonic Technologies*, pp. 1–28, Wiley-VCH Verlag GmbH & Co. KGaA, mar 2017.

[104] C. Zheng, H. Shen, T. Pu, Y. Jiang, Q. Tang, W. Yang, C. Chen, C. Rui, and Y. Li, "High-efficient solar cells by the Ag/Cu-assisted chemical etching process on diamond-wire-sawn multicrystalline silicon," *IEEE Journal of Photovoltaics*, vol. 7, pp. 153–156, Jan. 2017.

[105] S. Li, W. Ma, Y. Zhou, X. Chen, Y. Xiao, M. Ma, W. Zhu, and F. Wei, "Fabrication of porous silicon nanowires by MACE method in HF/H2O2/AgNO3 system at room temperature," *Nanoscale Research Letters*, vol. 9, p. 196, Apr. 2014.

[106] H. Omar, M. J. Salifairus, S. A. H. Alrokayan, H. A. Khan, A. M. M. Jani, M. Rusop, and S. Abdullah, "Effect of temperature to the structure of silicon nanowires

growth by metal-assisted chemical etching," in *2015 IEEE Student Conference on Research and Development (SCOReD)*, IEEE, Dec. 2015.

[107] S. Nichkalo, A. Druzhinin, and M. Chekaylo, "Morphology of nanowire arrays produced by metal-assisted chemical etching on Si wafers of different types: comparative analysis," in *2019 IEEE 39th International Conference on Electronics and Nanotechnology (ELNANO)*, IEEE, Apr. 2019.

[108] J. Oh, H.-C. Yuan, and H. M. Branz, "An 18.2%-efficient black-silicon solar cell achieved through control of carrier recombination in nanostructures," *Nature Nanotechnology*, vol. 7, pp. 743–748, Sept. 2012.

[109] K. Chen, T. P. Pasanen, V. Vahanissi, and H. Savin, "Effect of MACE parameters on electrical and optical properties of ALD passivated black silicon," *IEEE Journal of Photovoltaics*, vol. 9, pp. 974–979, July 2019.

[110] F. A. Fernandez, "Recent developments in finite element analysis of optical and microwave devices," in *Proceedings of 1995 SBMO/IEEE MTT-S International Microwave and Optoelectronics Conference*, IEEE, July 1995.

[111] F. L. Teixeira, "Time-domain finite-difference and finite-element methods for maxwell equations in complex media," *IEEE Transactions on Antennas and Propagation*, vol. 56, pp. 2150–2166, Aug. 2008.

[112] B. M. A. Rahman, "A review on the characterization of photonic devices using the finite element method," in *Proceedings of 8th Mediterranean Electrotechnical Conference on Industrial Applications in Power Systems, Computer Science and Telecommunications (MELECON 96)*, IEEE, May 1996.

[113] A. Arjmand and D. Mcguire, "Complete optoelectronic simulation of patterned silicon solar cells," *Optical and Quantum Electronics*, vol. 46, pp. 1379–1384, Feb. 2014.

[114] T. Rahman and S. A. Boden, "Optical modeling of black silicon for solar cells using effective index techniques," *IEEE Journal of Photovoltaics*, vol. 7, pp. 1556–1562, Nov. 2017.

[115] G. Lifante, "Effective index method for modelling sub-wavelength two-dimensional periodic structures," *Physica Scripta*, p. 72, Jan. 2005.

[116] P. S. Ivanov, A. V. Kublik, I. V. Guryev, A. V. Dyogtyev, and S. I. Petrov, "Validity of the effective index model fop. analisys of photonic crystal fibers," in *5th International Workshop on Laser and Fiber-Optical Networks Modeling, 2003. Proceedings of LFNM 2003.*, IEEE, Sept. 2003.

[117] S. A. Schulz, A. H. K. Park, I. Deleon, J. Upham, and R. W. Boyd, "Better than the effective index method: improved simulation of photonic crystal waveguides," in *2015 Photonics North*, IEEE, June 2015.

[118] P. Roy, P. Das, and S. Tallur, "Hybrid numerical-analytical effective index method for designing large geometry ridge waveguides," in *2018 IEEE Photonics Conference (IPC)*, IEEE, Sept. 2018.

[119] J. Buus, "The effective index method and its application to semiconductor lasers," *IEEE Journal of Quantum Electronics*, vol. 18, pp. 1083–1089, July 1982.

[120] R. Rao and T. Tang, "Study on the maximum effective refractive index of single interface surface plasmon-polariton waveguide," in *International Conference on Communications and Electronics 2010*, IEEE, Aug. 2010.

[121] A. Polemi, A. Alu, and N. Engheta, "Guidance properties of plasmonic nanogrooves: comparison between the effective index method and the finite integration technique," *IEEE Antennas and Wireless Propagation Letters*, vol. 10, pp. 199–202, Mar. 2011.

[122] J. J. Tyson, T. Rahman, and S. A. Boden, "Optical simulation of black silicon surfaces using geometric randomisation and unit-cell based averaging," in *15th Photovoltaic Science, Application and Technology Conference*, pp. 81–84, Apr. 2019.

[123] P. P. Altermatt, Y. Yang, T. Langer, A. Schenk, and R. Brendel, "Simulation of optical properties of Si wire cells," in *2009 34th IEEE Photovoltaic Specialists Conference (PVSC)*, IEEE, June 2009.

[124] D. Wu, X. Tang, K. Wang, and X. Li, "An analytic approach for optimal geometrical design of GaAs nanowires for maximal light harvesting in photovoltaic cells," *Scientific Reports*, vol. 7, Apr. 2017.

[125] K.-Y. Zhou, S.-W. Jee, Z.-Y. Guo, Y. Xiao, S. A. Moiz, S.-T. Liu, and J.-H. Lee, "Plasmonics induced absorption enhancement in silicon nanowires coated with

metallic nanoparticles," in *2011 37th IEEE Photovoltaic Specialists Conference*, IEEE, June 2011.

[126] L. Zou, B. Zhang, J. Li, Y. Song, Q. Shen, and L. Li, "A comparative analysis of the 'transmittance' method between using integrating sphere and filter holders for measuring light absorption by aquatic particles," in *2012 IEEE International Geoscience and Remote Sensing Symposium*, IEEE, jul 2012.

[127] Y. Karamavus, H. B. Celebi, Y. Uludag, and M. Ozkan, "Design of a new optic probe for diffuse reflectance spectroscopy," in *2015 23nd Signal Processing and Communications Applications Conference (SIU)*, IEEE, may 2015.

[128] M. Radke, H.-P. Roser, and A. Demircan, "Bidirectional reflectance measurements using a CCD-line-camera on a rotating device," in *IEEE 1999 International Geoscience and Remote Sensing Symposium. IGARSS'99 (Cat. No.99CH36293)*, IEEE, July 1999.

[129] M. Janecek and W. W. Moses, "Optical reflectance measurements for commonly used reflectors," *IEEE Transactions on Nuclear Science*, vol. 55, pp. 2432–2437, aug 2008.

[130] J. Cipar, T. Cooley, and R. Lockwood, "Measurements of seasonal changes in vegetation reflectance spectra," in *2008 IEEE International Geoscience and Remote Sensing Symposium*, IEEE, 2008.

[131] M. Shafique, J. P. Phillips, and P. A. Kyriacou, "A novel non-invasive trans-reflectance photoplethysmographic probe for use in cases of low peripheral blood perfusion," in *2009 Annual International Conference of the IEEE Engineering in Medicine and Biology Society*, IEEE, sep 2009.

[132] S. Anand and N. Sujatha, "Effects of probe placement on tissue oxygenation levels during reflectance measurements for different types of tissues in a clinical setting," in *2015 International Conference on BioPhotonics*, IEEE, may 2015.

[133] J. J. Tyson, T. Rahman, and S. A. Boden, "Angle–resolved spectrophotometry for the optical characterisation of material surfaces," *IEEE Transactions on Instrumentation and Measurement*, vol. 71, pp. 1–8, 2022.

[134] J. J. Tyson, "Dataset: Characterising the broadband, wide–angle reflectance properties of black silicon surfaces for solar photovoltaic applications," 2023.

[135] T. E. Scheul, *Metal-assisted chemically etched black silicon: morphology and light interaction*. PhD thesis, University of Southampton, 2020.

[136] T. E. Scheul, E. Khorani, T. Rahman, M. D. Charlton, and S. A. Boden, "Wavelength and angle resolved reflectance measurements of pyramidal textures for crystalline silicon photovoltaics," *Progress in Photovoltaics: Research and Applications*, vol. 28, pp. 1248–1257, jul 2020.

[137] A. Parretta, A. Sarno, P. Tortora, H. Yakubu, P. Maddalena, J. Zhao, and A. Wang, "Angle-dependent reflectance measurements on photovoltaic materials and solar cells," *Optics Communications*, vol. 172, pp. 139–151, Dec. 1999.

[138] A. Parretta, A. Sarno, and H. Yakubu, "Non-destructive optical characterization of photovoltaic modules by an integrating sphere.," *Optics Communications*, vol. 161, pp. 297–309, mar 1999.

[139] E. Lopez-Fraguas, J. M. Sanchez-Pena, and R. Vergaz, "A low-cost LED-based solar simulator," *IEEE Transactions on Instrumentation and Measurement*, vol. 68, pp. 4913–4923, dec 2019.

[140] J. Xu, Y. Liu, and Y. Wu, "Automatic defect inspection for monocrystalline solar cell interior by electroluminescence image self-comparison method," *IEEE Transactions on Instrumentation and Measurement*, vol. 70, pp. 1–11, 2021.

[141] X. Tao, Z. Zhang, F. Zhang, and D. Xu, "A novel and effective surface flaw inspection instrument for large-aperture optical elements," *IEEE Transactions on Instrumentation and Measurement*, vol. 64, pp. 2530–2540, sep 2015.

[142] F. Carpignano, G. Rigamonti, G. Mazzini, and S. Merlo, "Low-coherence reflectometry for refractive index measurements of cells in micro-capillaries," *Sensors*, vol. 16, p. 1670, oct 2016.

[143] V. Bello, A. Simoni, and S. Merlo, "Spectral interferometric detection of NIR optical resonances of rectangular microcapillaries for refractive index sensing," *IEEE Transactions on Instrumentation and Measurement*, vol. 70, pp. 1–9, 2021.

[144] R. Ulbricht, "Die bestimmung der mittleren räumlichen lichtintensität durch nur eine messung," *Elektrotech*, vol. 21, pp. 595–597, 1900.

[145] J. Palmer, *The art of radiometry*. Bellingham, Wash: SPIE Press, 2010.

[146] "Integrating sphere fundamentals and applications," tech. rep., Newport Corperation, 2021.

[147] F. J. J. Clarke and J. A. Compton, "Correction methods for integrating-sphere measurement of hemispherical reflectance," *Color Research & Application*, vol. 11, no. 4, pp. 253–262, 1986.

[148] S. L. Storm, A. Springsteen, and T. M. Ricker, "The use of center mount sample holders in reflectance spectroscopy," Jan. 1998.

[149] S. A. Boden, *Biomimetic nanostructured surfaces for antireflection in photovoltaics*. Phd thesis, University of Southampton, May 2009. p. 166.

[150] C. S. Goldenstein, V. A. Miller, R. M. Spearrin, and C. L. Strand, "SpectraPlot.com: integrated spectroscopic modeling of atomic and molecular gases," *Journal of Quantitative Spectroscopy and Radiative Transfer*, vol. 200, pp. 249–257, Oct. 2017.

[151] J. J. Hsia, "CIE standard illuminants for colorimetry," 1999.

[152] S. O. Kasap, *Optoelectronics & photonics: principles & practices*. Pearson Education Limited, second ed., 2013.

[153] C. Schinke, P. C. Peest, J. Schmidt, R. Brendel, K. Bothe, M. R. Vogt, I. Kröger, S. Winter, A. Schirmacher, S. Lim, H. T. Nguyen, and D. MacDonald, "Uncertainty analysis for the coefficient of band-to-band absorption of crystalline silicon," *AIP Advances*, vol. 5, p. 067168, June 2015.

[154] I. Reda and A. Andreas, "Solar position algorithm for solar radiation applications," *Solar Energy*, vol. 76, no. 5, pp. 577–589, 2004.

[155] R. E. Bird and R. L. Hulstrom, "A simplified clear sky model for direct and diffuse insolation on horizontal surfaces," tech. rep., Solar Energy Research Institute, 1981.

[156] R. E. Bird and C. Riordan, "Simple solar spectral model for direct and diffuse irradiance on horizontal and tilted planes at the Earth's surface for cloudless atmospheres," tech. rep., Solar Energy Research Institute, 1984.

[157] T. K. Van Heuklon, "Estimating atmospheric ozone for solar radiation models," *Solar Energy*, vol. 22, pp. 63–68, Aug. 1978.

[158] T. E. Scheul, E. Khorani, T. Rahman, and S. A. Boden, "Characterization of atomic layer deposited alumina thin films on black silicon textures using helium ion microscopy," in *9th International Conference on Crystalline Silicon Photovoltaics*, Apr. 2019.

Supporting Material

D Code Snippets

```
31 # Initialise a Tkinter window object
32 window = tk.Tk()
33 # Set window properties and base theme
34 name = 'OptiComp'
35 framePadding = 30
36 frameHeight = 740
37 elementPadding = 10
38 fontTitleText = 'Helvetica 16 bold'
39 fontBoldText = 'Helvetica 11 bold'
40 fontStandardText = 'Helvetica 11'
41 # Apply window title
42 window.title(name)
43 # Set shutdown protocol
44 window.protocol("WM_DELETE_WINDOW",quit)
45 # Disable window resizing
46 window.resizable(0,0)
47 # Override window manager
48 window.overrideredirect(True)
```

Figure D.1: Creating the base window object to host the software for the ARS. Source file: `ui.py:31`.

```
53 def getscanparameters(tkmb,interface):
54     # Get the current sample ID (entered in GUI)
55     sampleID = interface.getsamplename()
56     # Get reflectance standard (entered in GUI)
57     standard = interface.getreflectancestandard()
58     # Get scans to average
59     sta = interface.getscanstoaverage()
60     # Check for valid sample ID and get angular resolution
61     if(len(sampleID) > 0):
62         # Ensure valid angular resolution
63         state,start,step,stop = interface.getangularresolution()
64         if(not state):
65             msg = "Error: Invalid angular resolution entered."
66             notify(tkmb,2,msg)
67         else:
68             msg = "Warning: No sample ID has been set."
69             notify(tkmb,1,msg)
               # Abort if not sample ID has been set and reset values
70             state = False
71             sampleID = start = stop = step = None
72     # Obtain optical mode if SID and angular resolution are valid
73     if(state):
74         mode = interface.getopticalmode()
75     else:
76         mode = None
77     return state,sampleID,sta,start,step,stop,mode,standard
```

Figure D.2: Sanity-check on all user input parameters to ensure a valid scan sequence has been programmed. Source file: `softwaremanager.py:53`.

```
60 def correctwavelengtherror(lambda_d):
61     # Set active pixels
62     n = np.arange(254,2031,1)
63     # Determine wavelength error
64     lambda_e = B0*(exp(np.multiply(B1,n))-exp(np.multiply(B2,n)))
65     # Return true wavelength
66     return lambda_d - lambda_e
```

Figure D.3: Code applying the wavelength correction factors. Source file: `datamanager.py:60`.

ORCID: 0000-0002-3112-5899

This thesis is written in LaTeX as maintained by The LaTeX Project.

[†]COMSOL Multiphysics is a registered trademark of COMSOL AB.

[‡]Windows is a registered trademark of the Microsoft Corporation.

[§]SLURM is a registered trademark of SchedMD LLC.

[¶]MATLAB is a registered trademark of The MathWorks Inc.

Final word count: 59,965